The effects of fibre architecture on fatigue life-time of composite materials

Hansen, Jens Zangenberg; Østergaard, Rasmus

Publication date:
2013

Document Version
Publisher's PDF, also known as Version of record

The effects of fibre architecture on fatigue life-time of composite materials

Jens Zangenberg Hansen
Technical University of Denmark
DTU Wind Energy PhD-0018 (EN)
September 2013

DTU Wind Energy
Department of Wind Energy

THE EFFECTS OF FIBRE ARCHITECTURE ON FATIGUE LIFE-TIME OF COMPOSITE MATERIALS

PhD thesis

Jens Zangenberg Hansen

September, 2013
DTU Wind Energy
Technical University of Denmark

Prepared by:
Jens Zangenberg Hansen

Main supervisors:
Povl Brøndsted, Professor
Technical University of Denmark
DTU Wind Energy, Section of Composites and Material Mechanics
Mail: pobr@dtu.dk

Rasmus Østergaard, Senior Manager
LM Wind Power Blades
Materials and Process, Composite Mechanics
Mail: rcoe@lmwindpower.com

Technical University of Denmark
DTU Wind Energy, Section of Composites and Material Mechanics
Risø Campus
Frederiksborgvej 399
4000 Roskilde
Denmark
Tel +45 4677 5085
Mail: info@vindenergi.dtu.dk
Web: http://www.vindenergi.dtu.dk/

Publication reference data
Jens Zangenberg Hansen
The effects of fibre architecture on fatigue life-time of composite materials
PhD thesis
Technical University of Denmark
DTU Wind Energy, Section of Composites and Material Mechanics
September 2013
DTU Wind Energy PhD-0018 (EN)
ISBN: 978-87-92896-48-3

Preface

This thesis is submitted to the Technical University of Denmark in candidacy for a degree of Doctor of Philosophy, PhD, in applied mechanics. The work is prepared in accordance with the regulations regarding the industrial PhD programme in Denmark.

The topic treated is tension fatigue damage of unidirectional glass fibre reinforced composite materials with emphasis on the fibre architecture. The application in focus is composite materials used for the load-carrying main laminate of a wind turbine rotor blade. Basic knowledge on mechanics, composite materials, wind turbine rotor blade design, and microscopy are assumed. The work presented was carried out in collaboration between the Technical University of Denmark, Department of Wind Energy, Section of Composites and Material Mechanics (formerly known as Risø National Laboratory for Sustainable Energy); LM Wind Power Blades, Materials and Process, Composite Mechanics; and the University of Delaware, Center for Composite Materials during the period April 2010 to September 2013.

Research funding was provided from the Danish Council for Strategic Research via the Danish Centre for Composite Structures and Materials for Wind Turbines (DCCSM) (contract number 09-067212). The project has been supervised by Professor Povl Brøndsted (DTU Wind Energy), Senior Manager Rasmus Østergaard (LM Wind Power), and Professor John Gillespie, Jr. (University of Delaware).

Jens Zangenberg

Risø, Denmark
September 2013

"En Kraftkilde har Landet dog, som er mere end rigelig nok, naar den ellers var tilstrækkelig let at øse af, nemlig Vindkraften; men til dennes anvendelse er der knyttet to Ulemper, at Vinden kun kan udføre et meget ujævnt Arbejde, når det blæser, og at det til Tider aldeles ikke blæser. I vore Dage er der imidlertid fysisk Mulighed for at komme ud over begge disse Ulemper."

Folk high school teacher and wind power pioneer Poul la Cour, Ingeniøren, 1895.

Acknowledgements

Starting from a background in civil engineering, and moving on to write a PhD thesis within fatigue of fibre reinforced composites, is a challenging task. Luckily, a lot of people have kindly offered their guidance during the years, and this section expresses my gratitude.

Without the kind support from the Danish Council for Strategic Research via the Danish Centre for Composite Structures and Materials for Wind Turbines (DCCSM) (contract number 09-067212), the project would not have come into consideration, and the financial aid is appreciated.

First of all, I would like to give a special thank to my supervisor Povl Brøndsted for encouraging and inspiring me to become a PhD candidate within composite materials and provide fruitful discussions, in addition to pleasant company. Also, a great thank goes to Rasmus Østergaard from LM Wind Power Blades and John Gillespie from the University of Delaware who both have given valuable input and support to my project.

Many thanks to my co-authors Michael Koefoed, Jesper Larsen, Povl Brøndsted, Rasmus Østergaard, and John Gillespie for providing valuable input to the work. Furthermore, Torben Jacobsen has provided valuable insight, and I would like to thank you for the support.

I owe personal thanks to my office mates both at LM Wind Power and DTU Wind Energy for interesting collaboration, great friendship, comfortable working environment, and your enjoyable company. I am indebted to the composite mechanics team at LM Wind Power Blades and the Section of Composites and Materials Mechanics at DTU Wind Energy for a providing an excellent daily working life as well as valuable discussions and technical assistance with the experiments. A special thank to my former office mate Lonnie Andersen at the Danish Technological Institute for assistance regarding micro computed tomography.

Part of the work done in the thesis was conducted abroad during a research stay at the University of Delaware, Center for Composite Materials. The stay would not have been possible without the entry provided by Mala Nagarajan from Owens Corning, thanks. Furthermore, I express my gratitude to John Gillespie for giving me the opportunity to

join a world recognised research institution. Friendly greetings go to Cedric Jacob, Raymond McCauley, and Subramani Sockalingam for making the stay an excellent personal experience and being great friends. Also thanks to the rest of the staff at the Center for Composite Materials for giving me a helping hand whenever it was needed.

Finally, heartfelt thanks go to Maya and Robert for all your love and support as well as reminding me that there are more important things in life besides fatigue of composite materials.

Abstract

Wind turbine rotor blades are among the largest composite structures manufactured of fibre reinforced polymer. During the service life of a wind turbine rotor blade, it is subjected to cyclic loading that potentially can lead to material failure, also known as fatigue. With reference to glass fibre reinforced composites used for the main laminate of a wind turbine rotor blade, the problem addressed in the present work is the effect of the fibre and fabric architecture on the fatigue life-time under tension-tension loading.

Fatigue of composite materials has been a central research topic for the last decades; however, a clear answer to what causes the material to degrade, has not been given yet. Even for the simplest kind of fibre reinforced composites, the axially loaded unidirectional material, the fatigue failure modes are complex, and require advanced experimental techniques and characterisation methodologies in order to be assessed. Furthermore, numerical evaluation and predictions of the fatigue damage evolution are decisive in order to make future improvements.

The present work is focused around two central themes: fibre architecture and fatigue failure. The fibre architecture is characterised using real material samples and numerical simulations. Experimental fatigue tests identify, quantify, and analyse the cause of failure. Different configurations of the fibre architecture are investigated in order to determine and understand the tension-tension fatigue failure mechanisms. A numerical study is used to examine the onset of fatigue failure. Topics treated include: experimental fatigue investigations, scanning electron microscopy, numerical simulations, advanced measurements techniques (micro computed tomography and thermovision), design of test specimens and preforms, and advanced materials characterisation.

The results of the present work show that the fibre radii distribution has limited effect on the fibre architecture. This raises the question of which fibre radii distribution ensures optimum mechanical properties, damage tolerance, and fatigue performance. The experimental fatigue results and analyses identify and explain the onset of tension fatigue failure. It is documented that improvements of the fibre architecture and specimen design are needed in order to provide next generation of fatigue resistant composite materials for wind turbine rotor blades.

Resumé

Vindmøllevinger er blandt de største strukturer fremstillet af fiber-forstærket polymer. En vindmøllevinge er gennem dens levetid udsat for cyklisk belastning, som over tid kan lede til brud - også kendt som udmattelse. Med henblik på glasfiber-forstærket kompositter til brug i hovedbjælken i en vindmøllevinge, undersøger det foreliggende arbejde effekten af fiber- og væv-arkitekturen på udmattelseslevetiden ved træk-træk belastning.

Udmattelse af kompositmaterialer har været et centralt forskningsemne gennem de seneste årtier. Dog er de entydige svar på hvad der forårsager denne materialedegradering endnu ikke givet. Selv for den simpleste type af fiber-forstærket komposit, det aksialt belastede ensrettede materiale, er udmattelsesbruddet komplekst, og kræver avancerede eksperimentelle teknikker og karakteriseringsmetodikker for at blive vurderet. Ydermere er numerisk evaluering og forudsigelse af skadesudbredelsen i udmattelse afgørende for fremtidige forbedringer.

Det nærværende arbejde fokuserer på to centrale emner: fiber-arkitektur og udmattelsesbrud. Fiber-arkitekturen er karakteriseret ved hjælp af materialeprøver og numeriske simuleringer. Eksperimentelle udmattelsesforsøg identificerer, kvantificerer, og analyserer årsagen til brud. Forskellige konfigurationer af fiber-arkitekturen er undersøgt med henblik på at klarlægge og forstå de grundlæggende brudmekanismer i træk-træk udmattelse. Et numerisk studie benyttes til at undersøge initiering af udmattelsesbruddet. Relevante emner i relation til arbejdet er: eksperimentel undersøgelse af udmattelse, skanning elektron mikroskopi, numerisk simulering, avancerede måleteknikker (mikro røntgen tomografi og thermovision), design af testprøver og væv samt avanceret materialekarakterisering.

Resultaterne af det foreliggende arbejde viser, at fiber radius-fordelingen har begrænset effekt på fiber-arkitekturen. Dette leder til spørgsmålet hvilken fiber radius-fordeling sikrer optimale mekaniske egenskaber, skades-tolerance og udmattelsesegenskaber. De eksperimentelle udmattelsesresultater og -analyser identificerer og forklarer initiering af udmattelsesbruddet ved træk belastning. Ydermere fremhæves nødvendigheden af forbedringer i både fiber-arkitekturen og test-geometrien for at kunne levere næste generation af modstandsdygtige kompositmaterialer til fremtidens vindmøllevinger.

Publications

List of publications appended to the thesis in App. A.

[P1] Zangenberg J., Larsen J.B., Østergaard R.C., and Brøndsted P. Methodology for characterisation of glass fibre composite architecture, *Plastics, Rubber and Composites*, **41(4/5)**, pp. 187-193 (2012).

[P2] Zangenberg J. and Brøndsted P. Quantitative study on the statistical properties of fibre architecture of genuine and numerical composite microstructures, *Composites Part A: Applied Science and Manufacturing*, **47**, pp. 124-134 (2013).

[P3] Zangenberg J. and Brøndsted P. Determination of the minimum size of a statistical representative volume element from a fibre-reinforced composite based on point pattern statistics, *Scripta Materialia*, **68**, pp. 503-505, (2013).

[P4] Zangenberg J., Brøndsted P., and Gillespie J.W. Jr. Fatigue damage propagation in unidirectional glass fibre reinforced composites made of a non-crimp fabric, *Journal of Composite Materials*, **Accepted**, (2013).

[P5] Zangenberg J., Brøndsted P., and Koefoed M. Design of a fibrous composite preform for wind turbine rotor blades, *Materials & Design*, **Submitted**, (2013).

Contents

Nomenclature

Abbreviations

CDF	Cumulative distribution function	
CoE	Cost of energy	[$/kWh]
CoI	Cost of installation	[$]
CoI	Cost of maintenance	[$]
CoT	Cost of turbine	[$]
CT	Computed tomography	
CTE	Coefficient of thermal expansion	
FVF	Fibre volume fraction	
FWF	Fibre weight fraction	
HAWT	Horizontal axis wind turbines	
MMA	Methyl methacylate	
NCF	Non-crimp fabric	
PDF	Probability density function	
PET	Polyethylene terephthalate	
PP	Power produced	[kWh]
PS	Polystyrene	
PUR	Polyurethan	
PVC	Polyvinyl chloride	
SAN	Styreneacrylonitrile	
UD	Unidirectional	
VARTM	Vacuum assisted resin transfer moulding	

Greek symbols

α	Global in-plane fibre undulation angle	[deg]
α_i	Coefficients of thermal expansion in principal material directions $i = 1, 2$	[1/K]
α_L	Length ratio between backing and axial fibre bundles	[-]
α_t	Thickness ratio between backing and axial fibre layers	[-]
β	Global out-of-plane fibre undulation angle	[deg]
β	Length reduction factor	[-]
$\Delta\sigma_i$	Amplitudes of the principal stress in material directions $i = 1, 2$	[Pa]
δz	Increment in z-direction	[-]
ε	Strain	[-]
λ	Eigenvalue	[-]
μ	Mean value	[pending]
μ	Micron, typically a length scaling factor	$[10^{-6}]$
ν	Poisson's ratio	[-]
ϕ	Local in-plane fibre misalignment angle	[deg]

ρ	Density	[kg/m³]
σ	Standard deviation	[pending]
σ	Stress	[Pa]
θ	Local out-of-plane fibre misalignment angle	[deg]

Roman symbols

A	Area	[length^2]
a	Power law scaling coefficient	[pending]
A_w	Area weight of fabrics	[g/m²]
b	Indication of backing layer in non-crimp fabric	[-]
m	Power law exponent	[-]
C	Compliance	[1/Pa]
C_p	Specific heat capacity	[J/kg K]
c_v	Coefficient of variation	[-]
ΔT	Temperature oscillation	[K]
E	Young's modulus	[Pa]
f	Frequency	[Hz]
L	Geometry, length	[length]
L_d	Linear density (typically of fibre roving)	[tex]
m	Number of repetitions of plies in a laminate	[-]
N	Number of cycles	[-]
N	Number of image slices	[-]
n	Number of plies in a laminate	[-]
R	Ratio between minimum and maximum cyclic stress $\left(\frac{\sigma_{\min}}{\sigma_{\max}}\right)$	[-]
r	Radius, typically fibre radius	[length]
s	Crack spacing	[length]
T	Temperature	[K]
t	Thickness	[length]
T	Transpose of vector or matrix	[-]
tex	Unit of linear density	[g/km]
V_f	Fibre volume fraction	[-]
x	Coordinate axis, abscissa	[-]
y	Coordinate axis, ordinate	[-]
z	Coordinate axis, perpendicular to the xy-plane	[-]

Vectors and matrices

a	Random vector
D	Scaled identity matrix
d	Displacement vector for fibre misalignment
I	Identity matrix
$\mathbf{U}_i$	Direction vectors of main fibre undulation, $i = 1,\ 2,\ 3$
u	Random vector
V	Variance-covariance matrix
v	Random vector
g	Matrix associated to the centre of mass of a point cluster
X	Coordinate matrix

Chapter 1

Introduction

This chapter gives an introduction to the topics treated in the thesis, and explains the motivation and objectives of the study. A background survey regarding the themes of the work is found in Chapter 2.

1.1 Problem statement and motivation

In modern society, energy is considered a fundamental and vital resource, and it is basically the foundation for our way of life. Without the constant access to energy, society as we know it today, would not exist. Future prospects indicate that the demand for energy will increase, and as the access to fossil fuels is getting more complicated, the cost of energy, CoE, for non-renewable energy resource, will also increase. This means that renewable energy sources like wind, water, and solar have the potential of cost competitive alternatives. The environmental aspects are also of concern, and renewable energy sources have an obvious benefit compared to fossil fuels. Fig. 1.1 illustrates the wind power production in EU from 2000-2008 with estimations on future trends, which is also a simple measure for the supply-and-demand estimate for the future energy consumption.

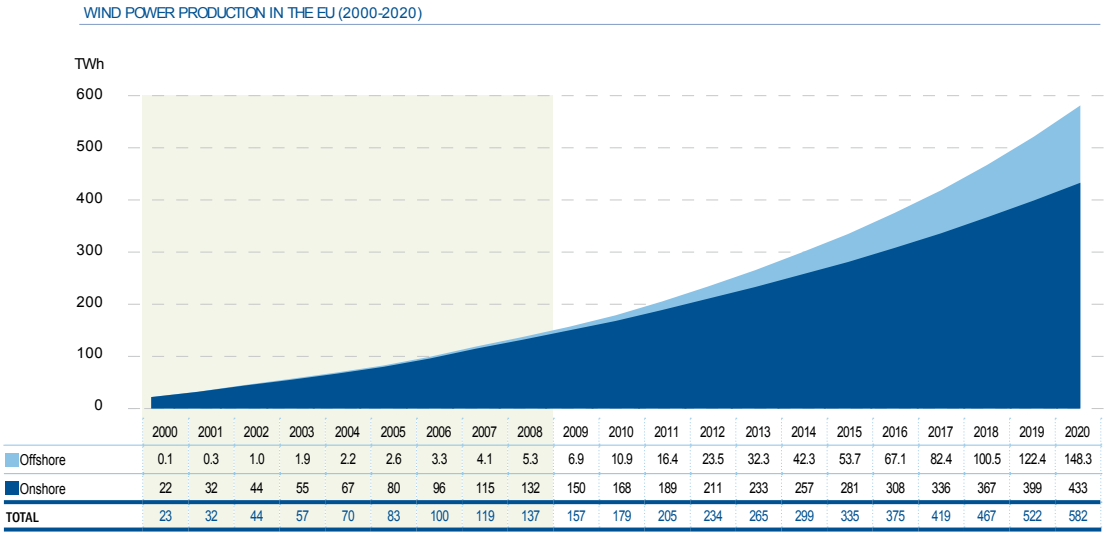

	2000	2001	2002	2003	2004	2005	2006	2007	2008	2009	2010	2011	2012	2013	2014	2015	2016	2017	2018	2019	2020
Offshore	0.1	0.3	1.0	1.9	2.2	2.6	3.3	4.1	5.3	6.9	10.9	16.4	23.5	32.3	42.3	53.7	67.1	82.4	100.5	122.4	148.3
Onshore	22	32	44	55	67	80	96	115	132	150	168	189	211	233	257	281	308	336	367	399	433
TOTAL	23	32	44	57	70	83	100	119	137	157	179	205	234	265	299	335	375	419	467	522	582

Figure 1.1: Offshore and onshore wind energy production in the EU. Current status and future projections, [1].

As seen from Fig. 1.1, it is estimated that the wind power production is tripled within the next decade, which means that the market for wind turbines is growing. Still, in order for wind energy to be cost competitive and reach the grid parity, meaning the price of producing wind power is equal to or less than the market purchase price, the CoE must be reduced. Lowering the CoE has been a central focus point and driver within the wind industry for the past years. The CoE, meaning the cost to produce energy (kWhs) during the life-time of the wind turbine, is defined as, [2]:

$$\mathrm{CoE} = \frac{\mathrm{CoT} + \mathrm{CoI} + \mathrm{CoM}}{\mathrm{PP}} \tag{1.1}$$

where

CoT:	Cost of Turbine (foundation + tower + machinery + nacelle + blades).
CoI:	Cost of Installation and transportation.
CoM:	Cost of operation and Maintenance during the life-time of the turbine.
PP:	Power Produced during the turbine life-time.

From an industrial perspective and in order to be cost-competitive, it is desirable to lower the cost of energy. This can be done by affecting the different factors in Eq. (1.1): either by lowering the numerator, or increasing the denominator. From a wind turbine rotor blade manufacturers point of view, the objective is to decrease the CoT and increase the PP. Since the power output scales with the swept area of the rotor, the PP is predominantly related to the blade length. A direct up-scaling of existing blade geometry will not lead to a lower CoE, sooner on the contrary. Extending the life-time of the blade will increase the total amount of produced power; thus, increasing the PP. Current challenges are more related to decrease the CoT, and can, in relation to the rotor blades, be divided into two parts, [2]:

a) Allow the design limit of the blade material to be closer to the actual strength based on an improved understanding of failure mechanisms and damage tolerance. In turn, material savings are introduced and lighter blades are produced.

b) Increasing materials and process performance in a cost-effective manner.

The current work is linked to the first point, and can be illustrated as shown in Fig. 1.2. From a material perspective, Fig. 1.2 shows the design space available in order to avoid failure, in basic: material strength larger than the applied stress (load).

In order to reduce the probability of material failure, the stress and strength distributions should be separated as far as possible (increasing the design margin). Nonetheless, if the distributions are far apart, the material design is conservative. The distributions can be separated by translation or change of shape. In relation to the material stress, it is difficult to change the shape of the distribution due to the coupling to the random nature of the wind. However, there are two ways to translate the stress distribution in order to reduce the load: either by adding material to the component, or by improved smart component design. The first option is the obvious, but adds unwanted additional weight

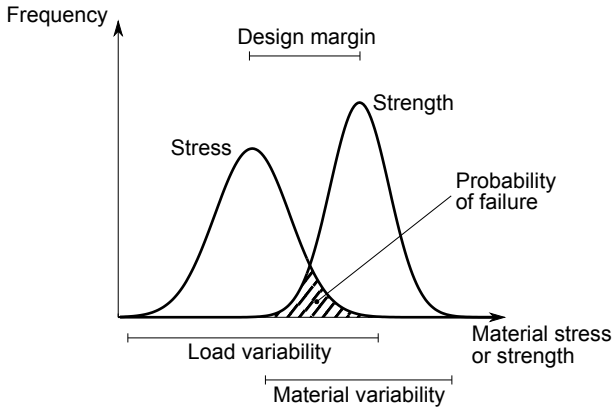

Figure 1.2: Sketch of the material design space available for composite material used in wind turbine rotor blades.

and cost to the component. The latter requires an optimisation of the structure, and can be beneficial in the long term. In any case, changing the location of stress distribution is a difficult task. On the other hand, the strength distribution can both change shape and location. A translation is achieved by materials with improved mechanical properties, which may add additional cost and save weight. The shape of the strength distribution can be altered by improved material understanding to reduce the material variability. In terms of cyclic damage (fatigue), the present project aims at providing an increased material understanding, thus increase the design margin by reducing the material variability. Fatigue of composites for wind turbine blades is an essential part of the design that is not yet explored and understood in detail.
The present thesis can contribute to lowering the CoT in terms of increased fatigue performance through a more profound understanding of the damage mechanisms in the materials. The material cost can be reduced as a result of the current study, leading to a lower CoE. Also, if fatigue damage mechanisms are well understood and described, the life-time of the blade can be extended, meaning increasing the PP and contributing to a lower CoE. Improved material understanding enables a design closer to the limit, and thus desirable weight savings in the blade. In turn, lighter blades reduce the CoI due to smaller loads on the remaining turbine components.

1.2 Scientific objectives and achievements

Composites are a wide-ranging family with a diverse selection of individual materials, microstructure, lay-up, and mechanical properties. On top of this, there are numerous different combinations of fatigue loading on the resulting structure, which must be considered. Therefore, in order to understand the effects of fibre architecture on the fatigue lifetime of composite materials, one would most likely do it in vain if all aspects should be considered. Hence, with reference to the application in focus (wind turbine rotor blades), the present study deals with unidirectional glass fibre materials embedded in a polyester matrix exposed to tension-tension fatigue loading. Focus will be put on the microstruc-

tural level and the interaction between fibre architecture and fatigue characteristics.

In order to gain a clearer understanding of composite material fatigue failure mechanisms, this project aims at providing tools and ideas for: identification, increased know-how, and improvements of composite materials for wind turbine blades. With special attention to the effect from fibre architecture, the final achievement is to understand and explain the tension fatigue damage mechanisms in composite materials used in the main spar of a wind turbine rotor blade.

The present work is a part of the Danish Centre for Composite Structures and Materials for Wind Turbines (DCCSM), which aims at providing methods to the industry for lighter and stronger wind turbine blade structures. This is achieved through improved material understanding covering all length scales from microscale to structural scale. The work package related to the present deals with the laminate scale, and the effect of fibre architecture on the mechanical performance.

1.3 Thesis overview

In Chapter 2, a survey is given regarding the different themes considered, and the application in focus. The next two chapters are the main emphasis of the thesis, and Chapter 3 presents different aspects and characteristics of the fibre architecture in unidirectional composites. In Chapter 4, the focus is on tension-tension fatigue damage and the effects from fibre architecture of unidirectional composites manufactured of non-crimp fabrics for the main laminate of a wind turbine blade. Chapter 5 completes the thesis with a conclusion and a future outlook. The thesis is supported by a number of published or submitted journal papers appended in App. A.

Chapter 2

Background

From the thesis title, three executive themes are distinguished: (i) composite materials, (ii) fibre architecture, and (iii) fatigue. This chapter briefly presents relevant information regarding each of the themes along with the application in focus: wind turbine rotor blades. The intention is to provide an overview and relevant references related to these fields. The chapter is divided into four sections dealing with each of the different themes and the application: composite materials, fibre architecture, wind turbine blades, and fatigue of composite materials.

2.1 Composite materials

A composite material (or just composites) is a combination of two or more different materials with diverse properties combined with a matrix at the interface to form a continuous material [3]. During the recent decades, composites have seen a huge increase in use, and today composites are everywhere in our daily life e.g. insulation materials, sporting equipment, civil engineering, energy application, medical science, aviation, automotive industry, shipping industry, etc. With this wide spreading field of applications, an increasing demand for better understanding of these materials has emerged. Composites are typically a two-fold material consisting of a ductile resin/matrix (adhesive) reinforced with stiff particles or filaments/fibres, illustrated in Fig. 2.1.

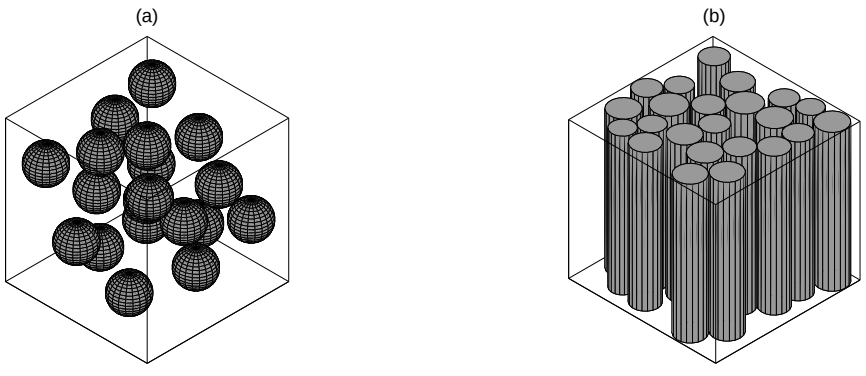

Figure 2.1: Typical reinforcements in composite materials. (a) Particulate composite. (b) Fibre composite.

Particulate composites, Fig. 2.1(a), are traditionally used to increase the fracture toughness whereas continuous fibre reinforcement is used to strengthen against specific actions. Fibre reinforced materials can be designed or tailored to suit a specific demand depending on the direction and magnitude of the action. Often for fibre reinforced composites, the fibres are woven or stitched together to form a fabric where the fibres are aligned according to a certain direction. Several fabrics or plies are stacked and infused using a resin to form a laminate. Depending on the direction of primary action on the structure, different lay-ups are used to produce the laminate. Processing of composites typically takes place in moulds where the dry fabrics (preforms) are placed, and infused using an appropriate resin. This type of manufacturing is unique for composites since the structure and material is the same unit, which is unlike traditional structures that are assembled of different materials and geometries. This material and structural coherence is one of the advantages of using composites for advanced structural applications. Some common applications and associated lay-ups for fibre reinforced composites are shown in Fig. 2.2.

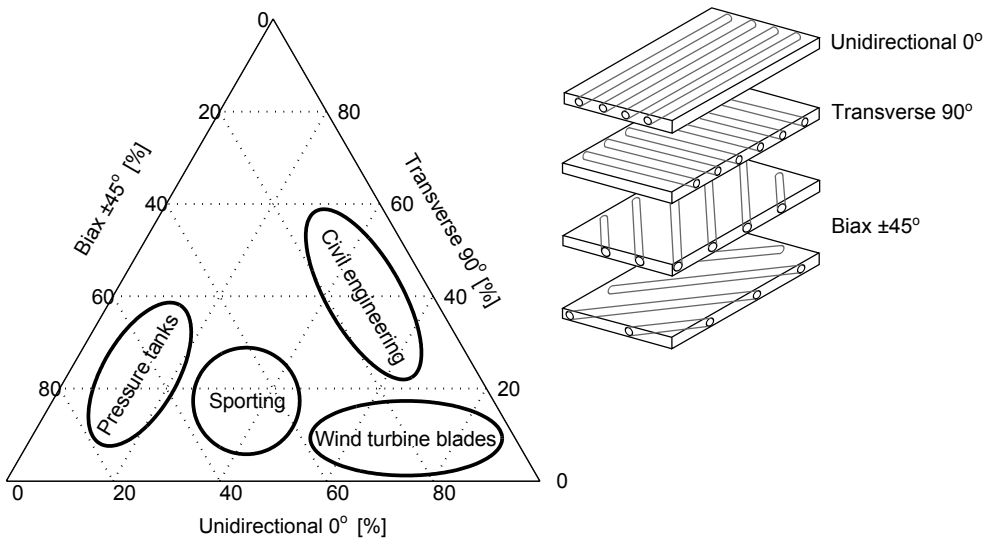

Figure 2.2: Instructive comparison and amount of composite lay-ups used in different applications. Inspiration from Jones, [4].

Unlike traditional structural materials, composites enable a large variety of options regarding the material tailoring, which makes it possible for the engineer to design the best suitable material for the purpose. Composite material design is far from trivial since it requires thorough knowledge of the fibre and resin materials used, their individual properties and mechanical performance, resistance to different loadings, etc. When the fibre material is mixed with a resin to form a composite, a completely new material is emerging, and the considerations regarding mechanical performance, resistance, etc. must be re-evaluated.

Classical introductory books with further information within composites are Jones [4], Bunsell & Renard [5], and Chou [6].

2.2 Fibre architecture

A fibre reinforced composite material can be manufactured in numerous ways using different reinforcement types, materials, fabrics and lay-ups, and processing techniques. Another important question is how to quantify the processed composite, and the most obvious and widespread parameter for characterisation of composite microstructures, is the fibre volume fraction. This is defined as the total fibre volume in relation to the volume of the entire material, and is often used as a control parameter for the composite. The effect of the fibre volume fraction on selected properties is sketched in Fig. 2.3.

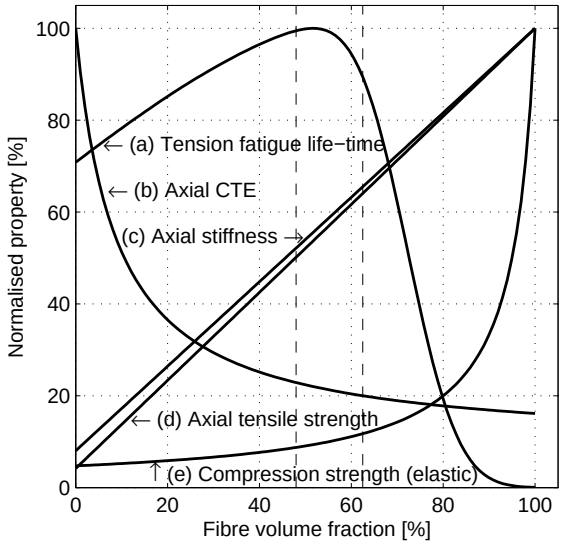

Figure 2.3: Sketch of the effect of fibre volume fraction on selected mechanical properties. The dashed lines mark the region where the FVF of wind turbine blades is typically found. Comments: (a) Deterministic, see e.g. Sec. 4.2. (b) Force equilibrium, see e.g. [7]. (c) Rule of mixtures, see e.g. [7]. (d) Rule of mixtures, see e.g. [7]. (e) Elastic kinking, see Rosen [8].

As illustrated in Fig. 2.3, composites are not just a coincidental mixture of A and B. It requires a thorough expertise in order to produce the material, and to be in control of the mechanical properties. It is noted that the simple estimates of the composite properties are not valid for the bulk materials where the FVF $\simeq 0$ (resin) and 100% (glass).

The role of the fibre architecture in fibrous composites is the theme of papers [P1-P3], and additional interesting references are Lopes [9], Ghosh et al. [10], Pyrz [11], or Summerscales [12]. [P5] considers the design process of a composite preform for a wind turbine blade.

2.3 Wind turbine rotor blades

The basic concept of a wind turbine is to transform a horizontal wind force into a turning moment (torque) of the rotor, thus producing energy using a generator. The most

common type of installed wind turbine systems today, is the three bladed horizontal axis wind turbines (HAWT) with an upwind rotor [13; 14; 15]. An example is shown in Fig. 2.4.

Figure 2.4: Example of a horizontal axis wind turbine.

During the last decades, wind energy has experienced an upturn in installed power and societal interest, [13; 14], see also Fig. 1.1. However, political decision, willingness, and subsidies are still of fundamental concern in order for wind technology to be cost-competitive. For a wind turbine, one way to raise the output gain is by increasing the swept area of the blades, i.e. the blade length. Consequently, wind turbine (blade) manufacturers pursue the development of longer and lighter blades. The evolution of the blade size during the recent years for LM Wind Power blades, is illustrated in Fig. 2.5.

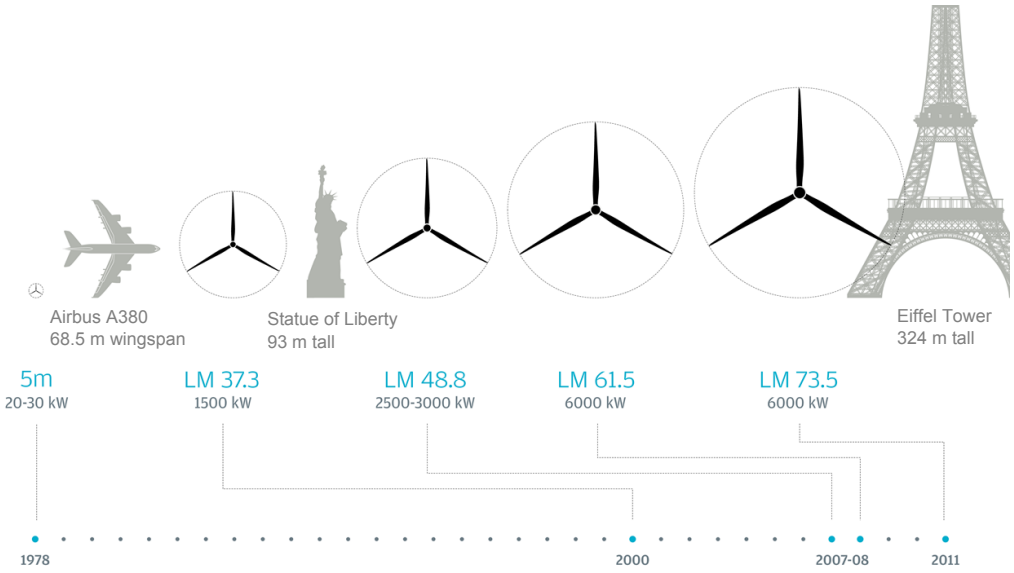

Figure 2.5: Size development of LM Wind Power blades during the last decades. The number LM XX denotes blade length in meters, and the number below, the associated rated power output from the turbine.

The increasing blade size, illustrated in Fig. 2.5, has been achieved through better materials knowledge and properties, improved manufacturing techniques, increased reliability

and understanding of the materials, optimisation, and innovation. The obvious way to increase the existing blade size is by a direct up-scaling of the geometry in all three spatial directions, which is far from an optimised solution (due to Galileo's square-cube law, [16]). Based on the above mentioned achievements, it has been possible to reduce the blade-length vs. -weight relation (for blade lengths less than 40m) to a power exponent of 2.66 (rather than 3), [17]. This means that the blade mass is reduced compared to the cubic up-scaling, and in turn the gravitational and centrifugal forces are decreased. Typical weight and cost components for a three-bladed HAWT turbine are given in Table 2.1.

Table 2.1: Cost and weight of different components for a wind turbine, [13].

Component	Weight [% of machine]	Cost [% of machine]
Rotor	10 - 14	20 - 30
Gearbox and drivetrain	5 - 15	10 - 15
Nacelle and machinery	25 - 40	25
Generator system	2 - 6	5 - 15
Weight on top tower	35 - 50	-
Tower	30 - 65	10 - 25

As observed from Table 2.1, the rotor blades have a significant contribution to the wind turbine, and a reduction in weight and/or cost is beneficial for the entire economy of the turbine unit. A reduced blade mass affects all other parts of the wind turbine, and in turn reduces the cost of energy, mentioned in Chapter 1.

Regarding the material selection for wind turbine rotor blades, three general requirements are governing, [17]: high material stiffness is required to maintain optimal aerodynamic performance and sufficient tower clearance, low density materials in order to reduce gravity forces, and long fatigue-life is needed to reduce material degradation. Composites have shown to suit all three of these requirements. In Denmark, the wind turbine blade industry is therefore the key industry regarding composites. Typical material combinations for wind turbine blades are presented in Table 2.2.

Table 2.2: Typical material selections and technologies for wind turbine blades, [2]. Current LM technologies are underlined.

Category	Options
Reinforcement	Glass fibre, carbon fibre, natural fibre
Matrix	Polyester, vinylester, epoxy, bio-based resins
Core	PVC, balsa, PET, PS, SAN, PUR, ...
Adhesives	Epoxy, vinylester, PUR, MMA
Surface protection	Gelcoat, epoxy/PUR paints, leading edge tapes
Process	VARTM, prepreg, winding

From a blade manufacturers point of view, the main focus over the last years has been on mastering some of the material combinations shown in Table 2.2 in order to get the best possible solution to a competitive price. At LM Wind Power, the expertise is a material system based on continuous glass fibres infused with a polyester resin. Skin panels are manufactured with a balsa core and sandwich beams with a PVC core. Joints are bonded with an epoxy adhesive. Gelcoat is used for the exterior surface of the blade.

In order to achieve an improved wind turbine blade design, skills within all length scales of the design must be possessed. The different characteristic length scales involved in wind turbine blade design are illustrated in Fig. 2.6.

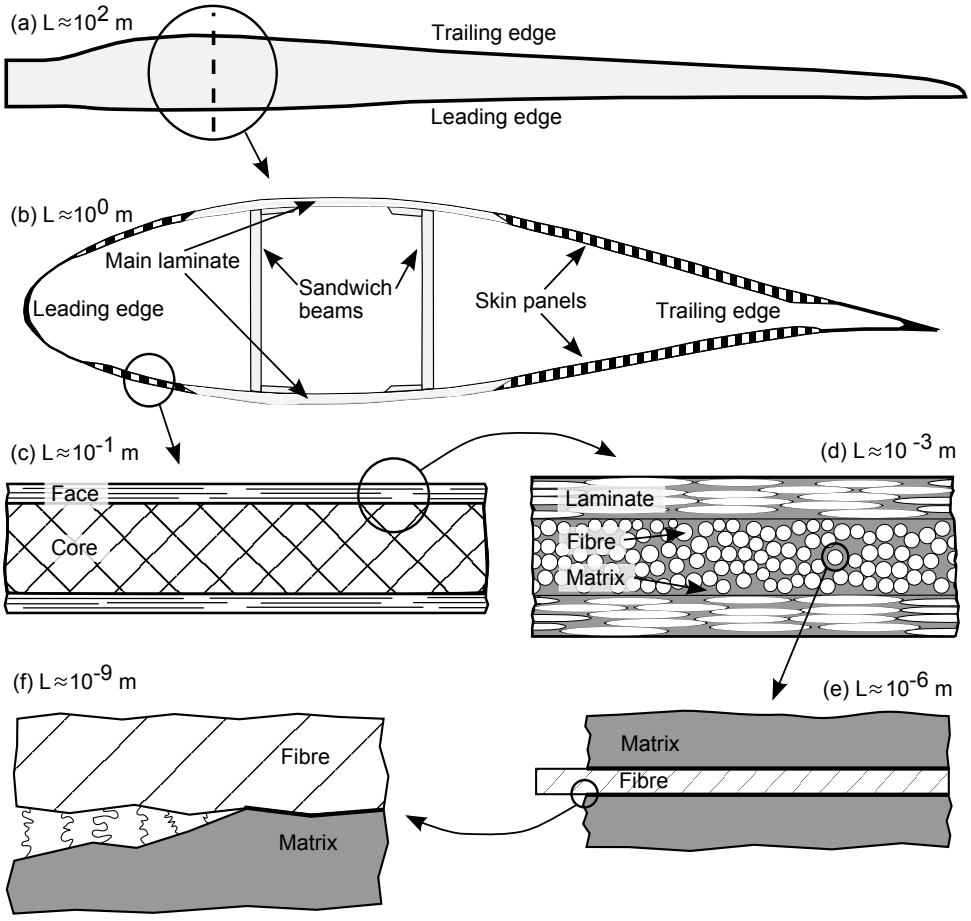

Figure 2.6: Characteristic length scales involved in wind turbine blade design. (a) Structural scale. (b) Sub-structural scale. (c) Component scale. (d) Laminate scale. (e) Micro-scale. (f) Nano-scale.

As illustrated in Fig. 2.6, the material design of a wind turbine blade is a complex and diverse task since all length scales must be evaluated. Each level affects the others, and changes on one length scale can have a dramatic impact on the overall performance of the blade. Not only in the material design process are the length scales important, but also in relation to material defects and imperfections that can influence the mechanical performance.

A lot of research is going on within the field of wind energy, both in the private, public, and academic sector. With regards to material research for future wind turbine blades, there is still many aspects to consider in order to manufacture more reliable, lighter, and longer blades, [13]:

- New material systems are needed, e.g. composite hybrids in the form intelligent combinations of carbon and glass.
- Fracture mechanical tools and databases are needed to design against delamination and fatigue crack propagation.
- Influence of creep, moisture, erosion, and temperature must be understood and described.
- Improved fatigue design and damage tolerance.
- Probabilistic design tools with respect to mechanical material performance.
- Influence of imperfections and defects on the mechanical properties.
- Improved understanding of process induced defects.

For recent presentations regarding the history, manufacturing, and design of wind turbine blades, the reviews of McGowan [13], Schubel & Crossley [15], Brøndsted et al. [17], or Veers et al. [18] should be addressed. Manwell et al. [19] is a comprehensive information source on several aspects of wind energy technology.

2.4 Fatigue of fibre reinforced composites for wind turbine blades

Wind turbine blades are designed to a 20 year life-time, and during this period the blades are exposed to a number of rotations in the order 10^8 to 10^9. This large number of load-cycles with time degrades the composite material, and the phenomenon is known as fatigue. Fatigue resistance is a key parameter for wind turbine blade material design. On top of the rotation of the blades is the stochastic behaviour of the wind, which causes an additional complex type of fatigue loading with varying load amplitude and wavelength. In order to handle the randomness of the loadings on the structure, the time series of the loading is recast into load blocks with constant mean and amplitude (varying frequency), e.g. using rainflow counting. This principle is known as constant amplitude fatigue. A basic assumption is that the damage is constant within each loading block, and the total damage during the life-time of the blade is obtained using damage accumulation rules like Miner's sum. An unsettled issue is whether there is a sequence dependency of the loading blocks on the resulting damage accumulation. Characterisation of the type of constant amplitude fatigue loading is expressed in terms of the load-ratio, R, defined as the minimum to maximum stress/strain in each load cycle: $R = \sigma_{\min}/\sigma_{\max}$ in terms of stresses. Different sinusoidal shaped stress waveforms are illustrated in Fig. 2.7 for typical load ratios, R.

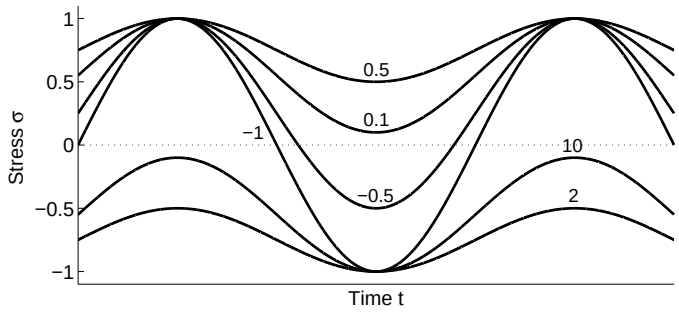

Figure 2.7: Constant amplitude sinusoidal shaped stress waveforms as a function of time for different stress ratios, R. Tension is considered positive.

It is seen from Fig. 2.7 that different types of fatigue loading are defined depending on the sign and magnitude of R. Different fatigue terminologies are used for varying ranges of R: $-\infty \leq R < 0$ tension-compression, $0 \leq R < 1$ tension-tension, and $1 < R < \infty$ compression-compression. A limitation in the definition of the stress ratio, is that $R = 1$ corresponds to two different experiments (static tension or compression) with various characteristics and failure modes. In addition to the stress ratio, R, the amplitude ratio, A, is often used. The amplitude ratio is defined as the ratio between the stress amplitude, σ_a, and the mean stress, σ_m, as:

$$A = \frac{\sigma_a}{\sigma_m} = \frac{\sigma_{\max} - \sigma_{\min}}{\sigma_{\max} + \sigma_{\min}} = \frac{1 - R}{1 + R}$$

The fatigue performance of composites used for wind turbine blades are typically evaluated for different values of R in order to get a proper material description. However, it is noted that certifying agencies like Germanischer Lloyd [20] do not prescribe actual fatigue testing, but the material design can be based on the static strength values in tension and compression.
Fatigue resistance of composites is traditionally done in terms of the Wöhler curve (or SN-curve) where the failure stress or strain, S, is plotted as function of cycles to failure, N. A flat Wöhler curve indicates a large resistance against fatigue, and a steep implies low resistance. For three values of R typical for wind turbine blade design, the associated Wöhler curves are plotted in Fig. 2.8 for a unidirectional glass-epoxy $[0]_4$ material.

It is observed from Fig. 2.8 that the tension-tension fatigue curve ($R = 0.1$) is most severe for the material since it is most steep, and have the lowest stress amplitude to failure in the high-cycle regime. Also, tension-tension fatigue is the dominant fatigue loading type on a blade structure, which arises as a consequence of the primary blade actions. Stiffness degradation is an additional documented fatigue phenomenon, and is addressed in [P4]. In blade design, the experimental Wöhler curves, Fig. 2.8, are transformed into constant life diagrams, which enable evaluation of the fatigue damage accumulation.

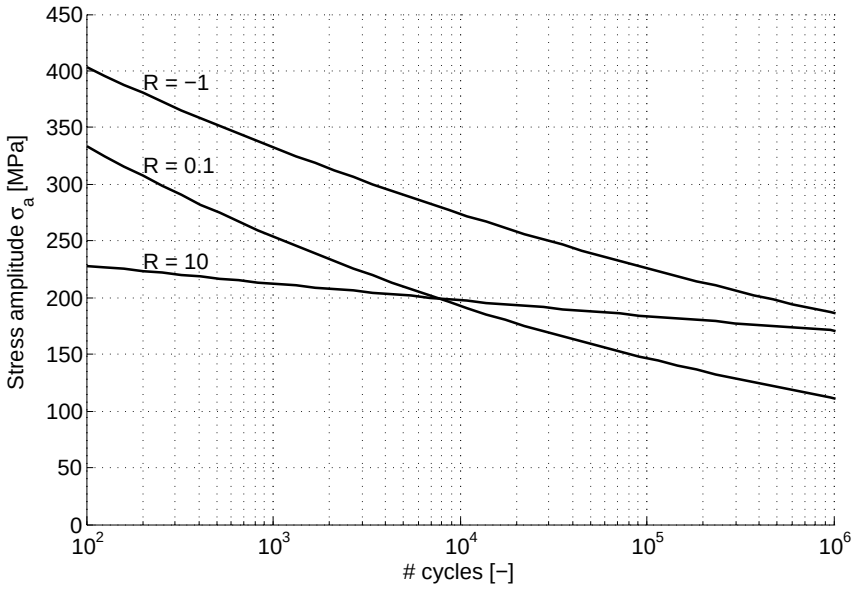

Figure 2.8: Wöhler curves for different stress ratios, R, and constant amplitude loading. Experimental data are taken from the OPTIDAT database, [21; 22], for a unidirectional glass-epoxy $[0]_4$ material and fitted to a power law behaviour. Fibre volume fraction for the samples considered: $(\mu,\, \sigma) = (52.1\%,\, 1.36\%)$.

Material imperfections, defects and inhomogeneities at all length scales affect the mechanical performance - both static and fatigue. In an experimental study, Mandell et al. [23] investigated the knock-down factors both statically and fatigue with respect to different imperfections and defects. They considered the commercially available Owens Corning fabrics A130 (warp woven unidirectional, $0°$) and D155 (weft stitched unidirectional, $90°$) embedded in a polyester resin, which are both common wind turbine blade materials. Knock-down factors for typical common composite material defects and design details are presented in Table 2.3.

Table 2.3 illustrates the dramatic influence of imperfections, design details, defects and inhomogeneities on the strength in both static and fatigue loading. In a blade design, the reason for these knock-down factors must be understood and managed in order to obtain an appropriate margin of safety. For instance, common geometric design details like ply-drops have a severe impact on the blade performance in terms of strength knock-down. Table 2.3 can be considered as a test matrix for future efforts on damage and failure mechanism in composite materials for wind turbine blades.

Lemaitra & Desmorat [24] give a general presentation of damage and fatigue whereas fatigue of composites used for wind turbine blades is addressed e.g. in Mandell et al. [23], Brøndsted et al. [25], Nijssen [26], Kensche [27], Marín et al. [28], and Mandell et al. [29]. Fatigue performance of composites in general has been subject to large research interest during the years. Selected works include: Talreja [30], McMeeking & Evans [31], El Kadi & Ellyin [32], Gamstedt & Talreja [33], Degrieck & Van Paepegem [34], Mao & Mahadevan [35], and Vassilopoulos & Keller [36].

Table 2.3: Experimentally determined knock down factors for static and fatigue loading of the A130 and D155 fabrics. The knock down factor, F, is the strength or 10^6 cycle fatigue strain in either tension (T) or compression (C) normalised with the undamaged material property, [23].

Detail	Sketch	Knock-Down Strength Factor, F			
		Static Strength		10^6 Cycle Fatigue	
		A130 fabric	D155 fabric	A130 fabric	D155 fabric
Simple coupon (straight material)		1.0	1.0	1.0	1.0
50 mm wide coupon with a 13 mm dia. hole		1.5 (T)	1.5 (T)	2.2 (T)	1.7 (T)
Bonded stiffener beam-web, (bending)			1.0		1.2
Time 100 to 1000 seconds at maximum stress	S time	1.3 (T)*	1.3 (T) 1.3 (C)		
Hot / Wet 50°C / Max. moisture	Ortho polyester 63 - AX - 051		1.0 (T) 1.5 (C)		1.0 (T) 1.9 (C)
Fiber waviness (in-plane) 0° fibers in loading direction	Mild		1.0 (T) 1.2 (C)		
	Severe		1.7 (T) 2.7 (C)		2.7 (C)
Single interior 0° ply drop			1.0 (T) F 1.4 (T) D		1.2 (T) F 2.5 (T) D
Double interior 0° ply drop	V_F <0.4	1.1 (T)	1.0 (T) F 3.0 (T) D 1.0 (C) F	1.25 (T)	1.6 (T) F 3.9 (T) D 4.0 (C) F
	V_F >0.4		1.05 (T)		1.0 (T)
Surface indentation (V_F increased, thickness reduced by 25%)	V_F = 45 - 52%, r = 6mm, V_F = 35 - 37%	1.0 (T) 1.2 (C)	1.0 (T) 1.4 (C)	2.3 (T) 1.0 (C)	2.5 (T) 1.4 (C)
Locally higher fiber content (2 - 90° plies in center)	V_F = 47%, V_F = 34%	1.0 (T) 1.1 (C)	1.0 (T) 1.5 (C)	2.1 (T) 1.0 (C)	1.5 (T) 1.4 (C)
Cracked transverse 90° patch			1.0 (T)		1.0 (T)
Sandwich panel (tension)	balsa	1.02 (T)		1.1 (T)	
Sandwich panel (tension) 30 degree closeout to thin laminate	balsa	4.0 (T) D 2.3 (T) F		3.4 (T) D 3.0 (T) F	

* (T) Tension Loading (R=0.1), (C) Compression Loading (R = 10), (F) Failure, (D) Delamination
Sandwich panel data are based on stress, and are compared to the facesheet material alone.
Delamination indicates conditions where delamination spreads completely across the specimen.

Chapter 3

Fibre architecture

The current chapter deals with investigations of the architecture and microstructure found in unidirectional fibre reinforced composite materials used for wind turbine rotor blades. Understanding of the material microstructure is the key for evaluation of the mechanical properties. The current status of characterisation of composite microstructures is outlined. Then, a practical example regarding hierarchical characterisation of the microstructure is presented. The chapter is closed with a preliminary study using micro computed tomography in order to characterise the three dimensional fibre misalignment. Journal papers relevant to the present chapter are [P1-P3] and partly [P5].

3.1 Literature survey

Proper characterisation of materials microstructure is essential in order to understand the mechanical behaviour, and provide valid information for materials modelling. This survey covers recent relevant literature in relation to the microstructure of composite materials used for wind turbine blade materials. Emphasis is on the fabric types referred to as non-crimp fabrics (NCF's) since these are the common selection for wind turbine blades. In NCF, straight fibrous layers with different orientation are placed on top of each other and stitched or knitted together to from a fabric. NCF's are dry fabrics and can be processed using autoclave, hot/cold pressing, or (vacuum assisted) resin transfer moulding with almost any kind of resin. [P1-P3] focus on the microstructure and fibre architecture inside the bundles of a NCF, and [P5] deals with the design process of a non-crimp composite preform.

Recent overviews regarding characterisation of microstructures containing isolated inhomogeneities (like fibres in resin) are found in the work of Torquato [37] and Kachanov & Sevostianov [38]. A comprehensive investigation of statistical analyses and microstructural descriptors applied to fibre reinforced composite materials, is found in the work of Lopes [9].

Classical measures for the microstructure of fibre embedded composite materials are for instance the fibre volume fraction, the nearest neighbour distance, the number of neigh-

bours, and the nearest neighbour orientation. Techniques for quantification of fibre misalignment, fibre spatial distribution and others are provided by Yurgartis [39] or Paluch [40]. More sophisticated statistical microstructural descriptors like the Ripley K-function (Ripley [41] and Dixon [42]) are often employed for composite materials. Pyrz [11; 43] presents interesting characterisation techniques including second order statistics of the microstructure of a composite material. Second order statistical analyses have been extensively used for characterisation by other researchers, e.g. Louis & Gokhale [44], Ghosh et al. [10] and later Shan & Gokhale [45] who used second order statistics in order to characterise and simulate the microstructure of fibre composites. Using Voronoi cells with fibre statistics from real composites, Swaminathan et al. [46] and Swaminathan & Ghosh [47] numerically investigated the response of representative volume elements. Numerical replication of composite microstructures in terms of representative unit cells has been a central research theme for some time, see [P2;P3] for further information.

The references provided above are more or less all centred around the microstructure of pure unidirectional filament wound laminates, and do not quantify the architecture of the entire laminate. Limited information is available regarding characterisation of hierarchical composite microstructures like NCF's used for wind turbine blades. To the authors knowledge, the only works dealing with characterisation of the internal hierarchical microstructure of NCF's are provided by Mattsson et al. [48] and partly Lomov [49]. Wei & Zhang [50] investigated variations of the microstructure in a stitched composite (like NCF's) in the vicinity of the stitching.
In relation to numerical modelling of the entire structure of the non-crimp material, the WiseTex software package, Verpoest & Lomov [51], provides automated generation of composite architectures for finite element analyses suitable for multiscale modelling strategies. Tessitore & Riccio [52] and Petriccione et al. [53] used a slightly different numerical methodology to generate and analyse the mechanical response of non-crimp materials.

3.2 Scaling effects and fibre volume fraction

3.2.1 Introduction

The fibre volume fraction (FVF) is the single most employed parameter for characterisation of the microstructure of fibre reinforced composites. For a hierarchical fibre reinforced composite like NCF's, the outcome of the fibre volume fraction is different depending on the length scale considered. The present study addresses changes in the composite microstructure in terms of the FVF at different length scales of a NCF. The FVF is chosen as a characterisation parameter of the different length scales due to its widespread use. Other selected interesting microstructural parameters are presented in [P1]. A NCF typically consists of filaments (fibres) arranged in bundles that are stitched to form the fabric. Several fabrics are stacked and infused to form the laminate. This length scale coherence is referred to as a hierarchical structure, and it is evident to describe the microstructure at each level in order to understand the resulting mechanical behaviour. The hierarchical structure of a NCF is sketched at different length scales in Fig. 3.1.

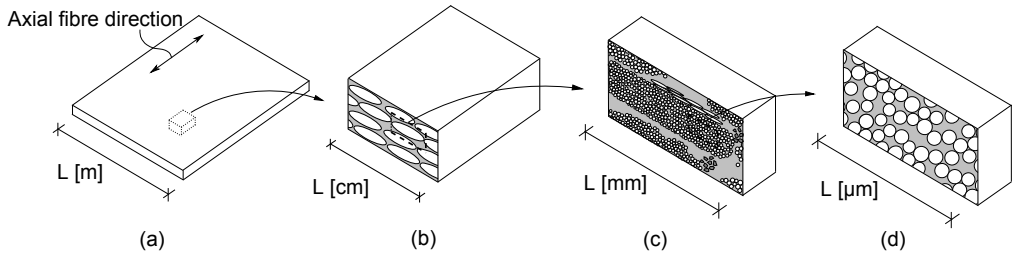

Figure 3.1: Hierarchical structure of a NCF, and associated length scales considered in the microstructural investigation. (a) Plate scale. (b) Laminate scale. (c) Bundle scale. (d) Fibre scale.

In the following, the composite microstructure is evaluated in terms of the FVF at the length scales: plate scale, laminate scale, bundle scale, and fibre scale. Different methodologies are used at the different length scales to determine the FVF. The investigation is carried out on a single specimen, and the material considered is a unidirectional NCF with backing, UD1322, employed in the main laminate of a wind turbine blade. The number 1322 refers to the amount (area weight) of unidirectional warp fibres. The fabric is shown in Fig. 3.2, and selected details are listed in Table 3.1.

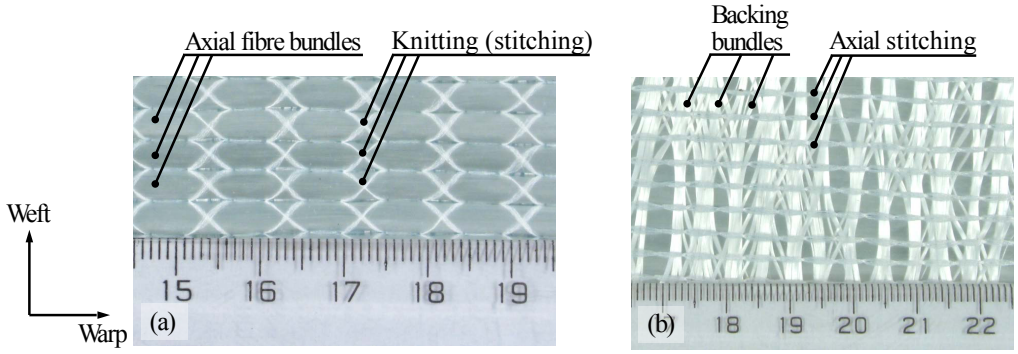

Figure 3.2: Fibre architecture of NCF UD1322. Scale bars in units of cm. Stitching pattern: double equal pillar tricot. (a) Axial face. (b) Backing face.

A 4-layered laminate is analysed with stacking sequence $[0/b, 0/b]_s$ where b indicates the position of the backing layer. The laminate is manufactured using a polyester matrix and the VARTM process.

Table 3.1: Selected fabric details for UD1322.

Category	Unit	Axial fibres	Backing fibres	Stitching thread
Orientation	[deg]	0 (warp)	$\pm$80 (weft)	N/A
Area weight	[g/m^2]	1322	60	15
Linear density (roving)	[tex]	2400	68	7.6
Material	[-]	H+ glass	E-glass	Polyester
Avg. filament diameter	[μm]	17	9	N/A

For the UD1322 fabric, two rovings are used to form each axial fibre bundle.

3.2.2 Plate scale [m]

At this scale, see Fig. 3.1(a), the laminated composite plate is considered as a continuum microstructure. The loss ignition method is used to determine the fibre *weight* fraction (FWF) and yields an average value of (mean/standard deviation) 70.9/0.25 %. Using the fibre and matrix densities, $\rho_f = 2.58\,\mathrm{g/cm^3}$ and $\rho_m = 1.19\,\mathrm{g/cm^3}$, the average value of the fibre *volume* fraction is determined as: FVF = 52.3%.

3.2.3 Laminate scale [cm]

At the laminate scale, see Fig. 3.1(b), it is possible to distinguish the different fabric layers and fibre bundles. The individual variations in the microstructure within the bundles are not considered. A typical transverse cross-section of the material reveals a brick-like structure of the fibre bundles, and a micrograph of the microstructure is shown in Fig. 3.3. Axial fibres are oriented out-of-plane.

The bundles are considered with uniform microstructure at this length scale, and the average FVF of the cross-section is calculated using a threshold analysis (see e.g. [P1]) where bright pixels are considered as fibre, dark as non-fibre. This yields that the FVF = 54.8% for the transverse cross-section shown in Fig. 3.3. Bundles 1 and 2 are analysed further at the next length scale.

3.2.4 Bundle scale [mm]

At this scale, the microstructure is analysed within the bundle, and the methodology outlined in [P1] is used to characterise the FVF. The number of contact points per fibre across the bundles is also evaluated to illustrate the fibre compactness. The investigation is performed using an incremental analysis with a moving frame across the bundle to determine the microstructural parameters within that specific frame. Data are stored for each frame, collected, and processed at the end of the analysis. Thereby, the microstructure can be characterised across the entire bundle. High-resolution micrographs of the two analysed bundles are shown in Fig. 3.4. Note that both stitching thread, backing fibres, and mould surface are present in regions close to the bundles considered.

It is seen from Fig. 3.4 that the microstructure inside the fibre bundles is similar to what is obtained in pure unidirectional composites e.g. made by filament winding. In such materials, the microstructure is uniform and the fibres are dispersed randomly across the entire laminate and not arranged in bundles. Analysis of the microstructure inside the bundles is the topic of [P2] and [P3] considering variations in generated microstructures, and the appropriate size of a volume element at this scale. The variation of the FVF and the number of contact points per fibre across the bundle are shown in Fig. 3.5. The tex value of the bundle is determined as the total fibre area multiplied with the fibre density. The average FVF of the bundle is found as the ratio between the total fibre area and the area of the bundle. The statistics for the variation of fibre diameters are shown in the figures as well, and it is observed that there is a slight variation in the mean fibre diameter for the two bundles considered.

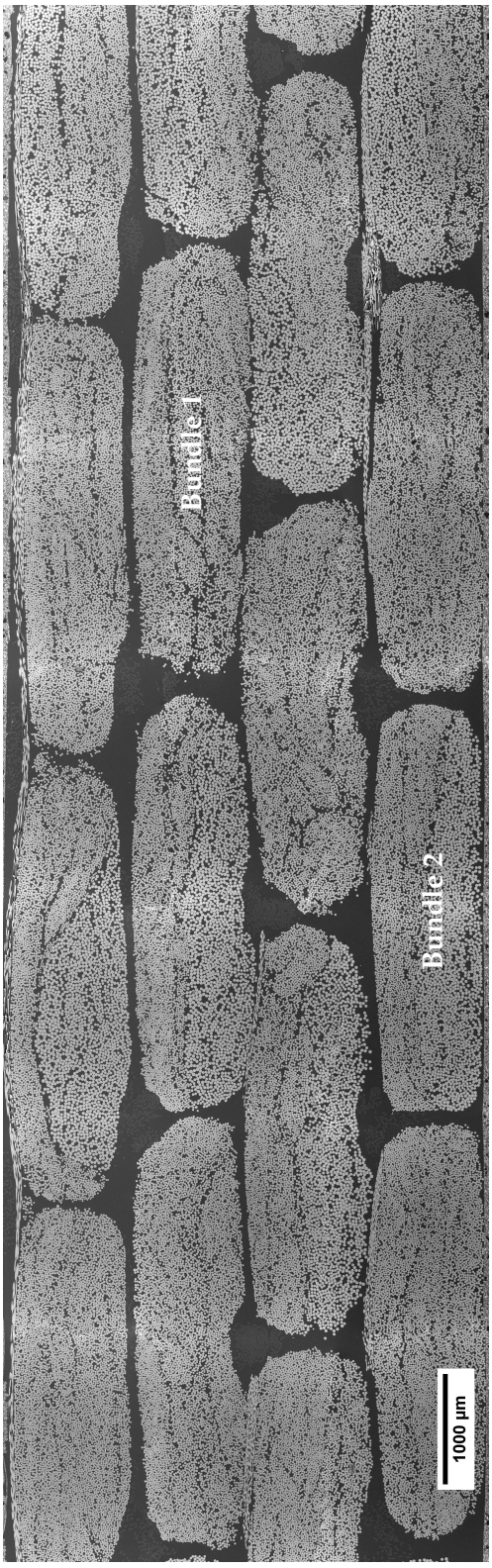

Figure 3.3: Transverse cross-section of bundle structure in unidirectional laminate manufactured of a NCF. The fabric considered is shown in Fig. 3.2. Bundles 1 and 2 are used for further analysis at the bundle scale, and magnified in Fig. 3.4.

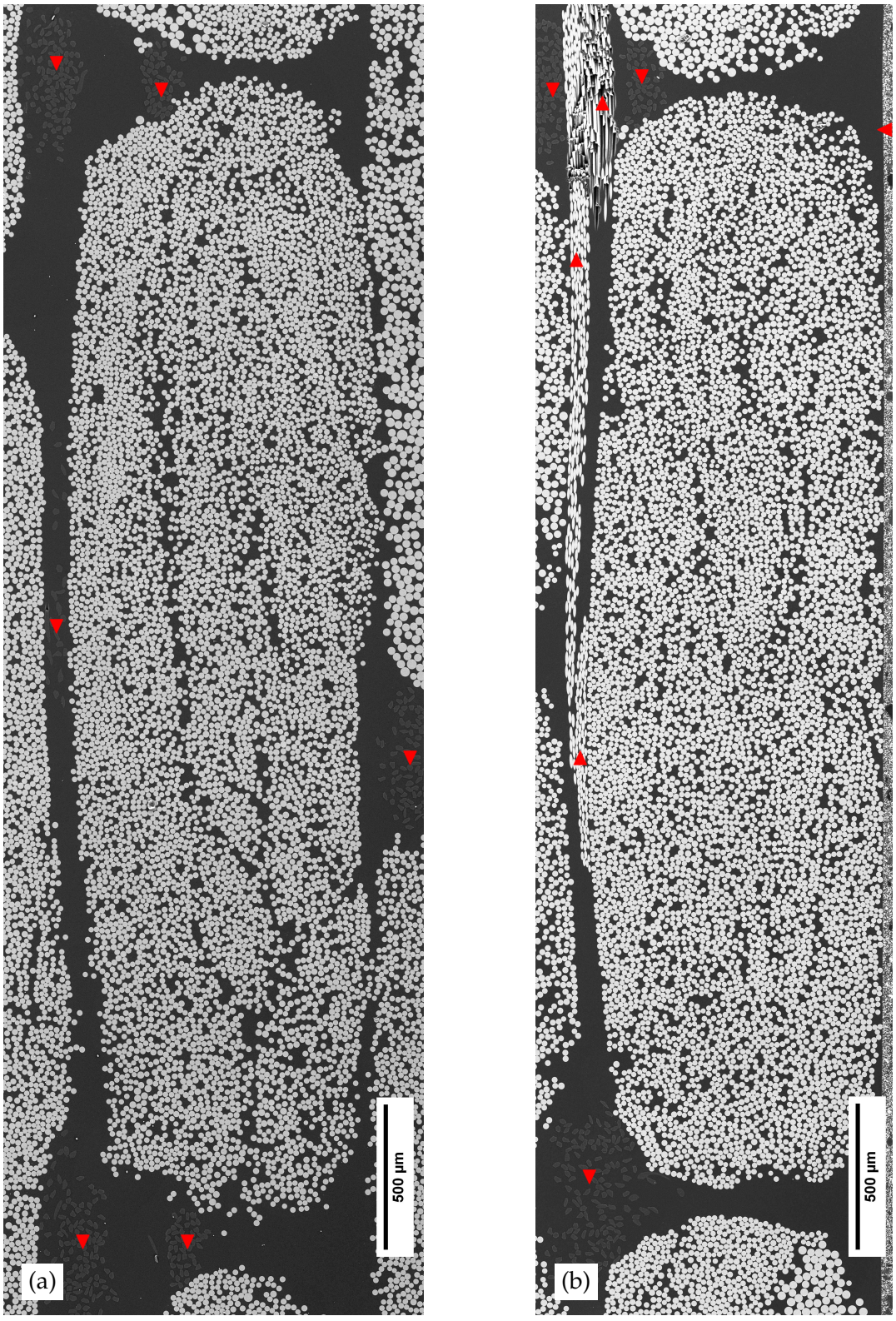

Figure 3.4: Magnification of the fibre bundles shown in Fig. 3.3. Markers denote: ▼ (stitching thread), ▲ (backing fibres), and ◄ (mould surface). (a) Bundle 1. (b) Bundle 2.

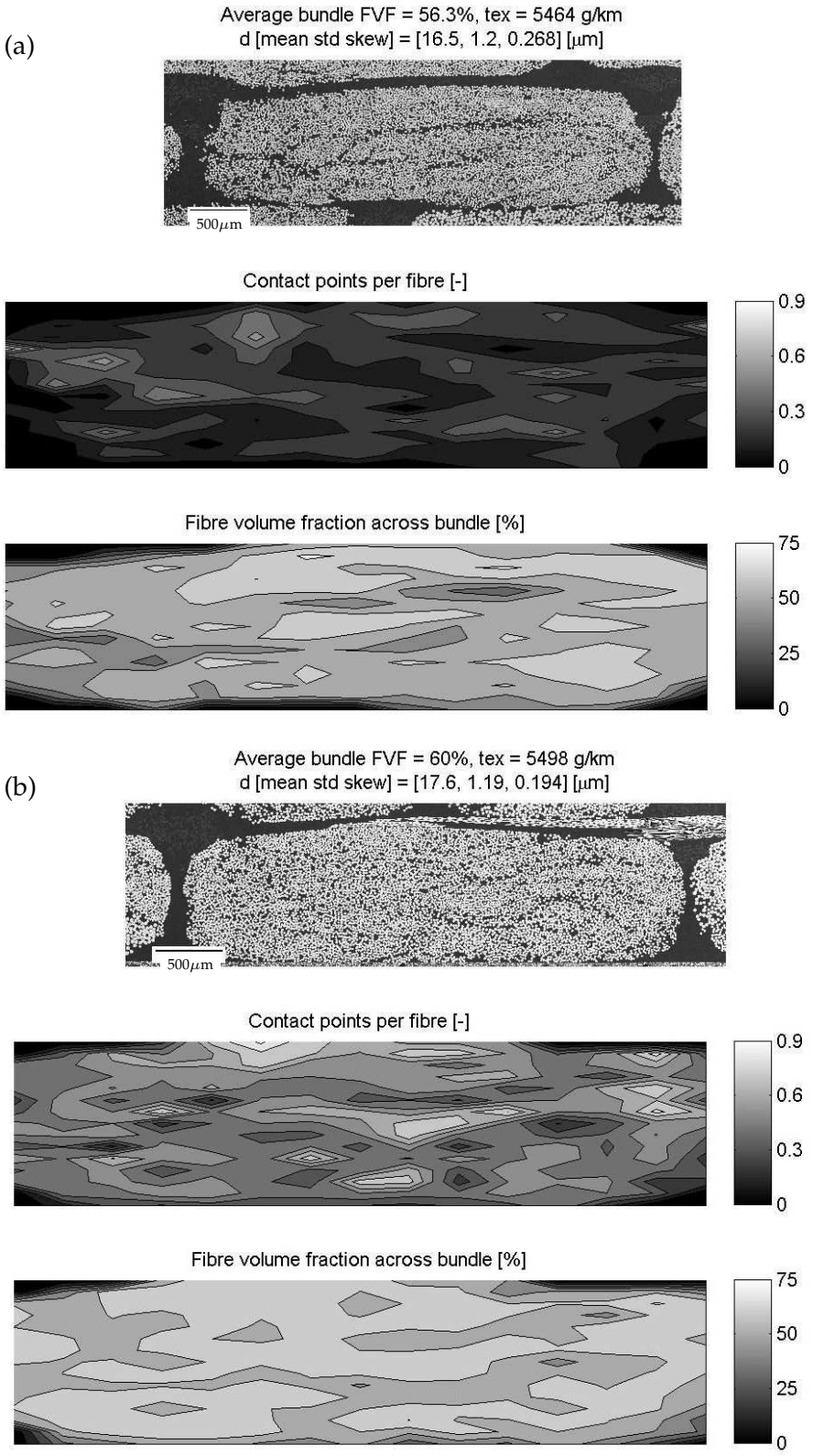

Figure 3.5: Result of image analysis of microstructure across fibre bundles at bundle scale. The locations of stitching thread, backing fibres, and mould surface are shown in Fig. 3.4. (a) Bundle 1. (b) Bundle 2.

For both fibre bundles in Fig. 3.5, it is noticed that there is a large scatter in the FVF and the number of fibre contact points across the bundle. In particular, the FVF is deviating from the average value across the bundle. For bundle 1, Fig. 3.5(a), it is seen that both the FVF and the number of contact points per fibre increase locally near the stitching thread due to the applied stitching tension. Similar observations can be made for bundle 2, Fig. 3.5(b), in addition that the microstructure is locally affected in contact to the backing fibres where both the FVF and the number of contact points are increased. Furthermore, for bundle 2, the axial fibres are more compacted near the mould surface reflected in the increase in FVF and the number of contact points.
It is documented that fibres in contact increase the local stress concentration between the fibres, see e.g. Kushch et al. [54], which may be a weak region with respect to crack initiation and propagation. One might imagine that there is an increased risk of damage in regions with a larger number of contact points. In the present material, the regions with increased number of fibre contact points are found in contact to the stitching thread or backing fibres. As reported in [P4], it is also in these regions that fatigue damage initiate.

3.2.5 Fibre scale [μm]

The final length scale considered in this analysis, is the fibre scale where individual resin encapsulated filaments are considered. A proper microstructural descriptor at this length scale is the Voronoi cell decomposition, see e.g. [P1]. The principle of the Voronoi decomposition and Delaunay triangulation of a typical fibre packing pattern is illustrated in Fig. 3.6.

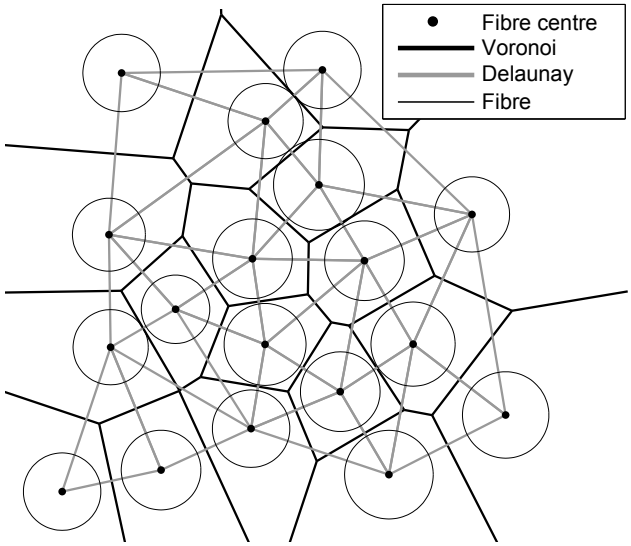

Figure 3.6: Example of Voronoi and Delaunay decomposition of a point pattern.

As seen from Fig. 3.6 each fibre has its own Voronoi cell with the property that any point inside the cell is closest to that particular fibre centre. This means that the extension of the Voronoi cell can be considered as the amount of matrix material belonging to each fibre.

The local FVF at this scale is therefore defined as:

$$\text{FVF} = \frac{A_{fibre}}{A_{voronoi}} \tag{3.1}$$

where A_{fibre} is the fibre area, and $A_{voronoi}$ is the area of the associated Voronoi cell. It is seen from Fig. 3.6 that unbonded Voronoi cells are present near the boundary, but these are disregarded due to their infinite area. Again, bundles 1 and 2 are considered for analysis, and the methodology outlined in [P1] is used to detect the fibre radius and position of each fibre in the bundle. Thereupon, the Voronoi decomposition is carried out, and Eq. (3.1) is used to determine the FVF across the bundle for each fibre detected. The results are shown in Fig. 3.7 for bundles 1 and 2. Each Voronoi cell is coloured according to the local FVF obtained from the respective cell.

Since the local FVF is determined on fibre scale, the resolution is larger, and it is possible to distinguish variations in the microstructure. As seen from Fig. 3.7(a), different regions are distinguished where fibres are separated or highly compacted. There is a noticeable variation in the local FVF across the bundle varying from 0-100% (the limits are not practically possible, and caused by un-bounded regions and fibers larger than the Voronoi cell). The average local FVF is approximately equal to the entire bundle volume fraction, which is also observed in [P2]. Bundle 2 seems to have a slightly larger average value for the local FVF, and the prevalence of the local FVF is more uniform compared to bundle 1. It is difficult to make any observations regarding the influence of the backing fibres, the stitching thread, or the specimen mould surface on the local FVF at this length scale.

3.2.6 Summary and discussion

The hierarchical microstructure of an unidirectional NCF has been investigated at different length scales in terms of the FVF. Variations are found for the FVF at the various length scales, and a summary is presented in Table 3.2.

Table 3.2: Summary of the variation in fibre volume fraction for a unidirectional non-crimp composite at different length scales.

Length scale and measure		FVF, average [%]	FVF, max [%]
Plate	[m]	52.3	N/A
Laminate	[cm]	54.8	N/A
Bundle	[mm]	56-60	$\simeq 75$
Fibre	[μm]	52-55	$\simeq 100$

From Table 3.2, it is obvious that there is a considerable difference on which length scale is examined for analysis of the FVF. This raises the question whether the FVF is a suitable parameter for description of the internal microstructure of a hierarchical material. For instance, if the FVF on plate scale is used as characterisation parameter for the composite, there is a major difference compared to the internal microstructure of the bundles. Furthermore, the microstructure is locally affected by the backing fibres and stitching thread causing a heavier fibre packing in these regions, which is reflected in terms of the maximum obtained FVF. In the study presented above, only a single specimen is considered

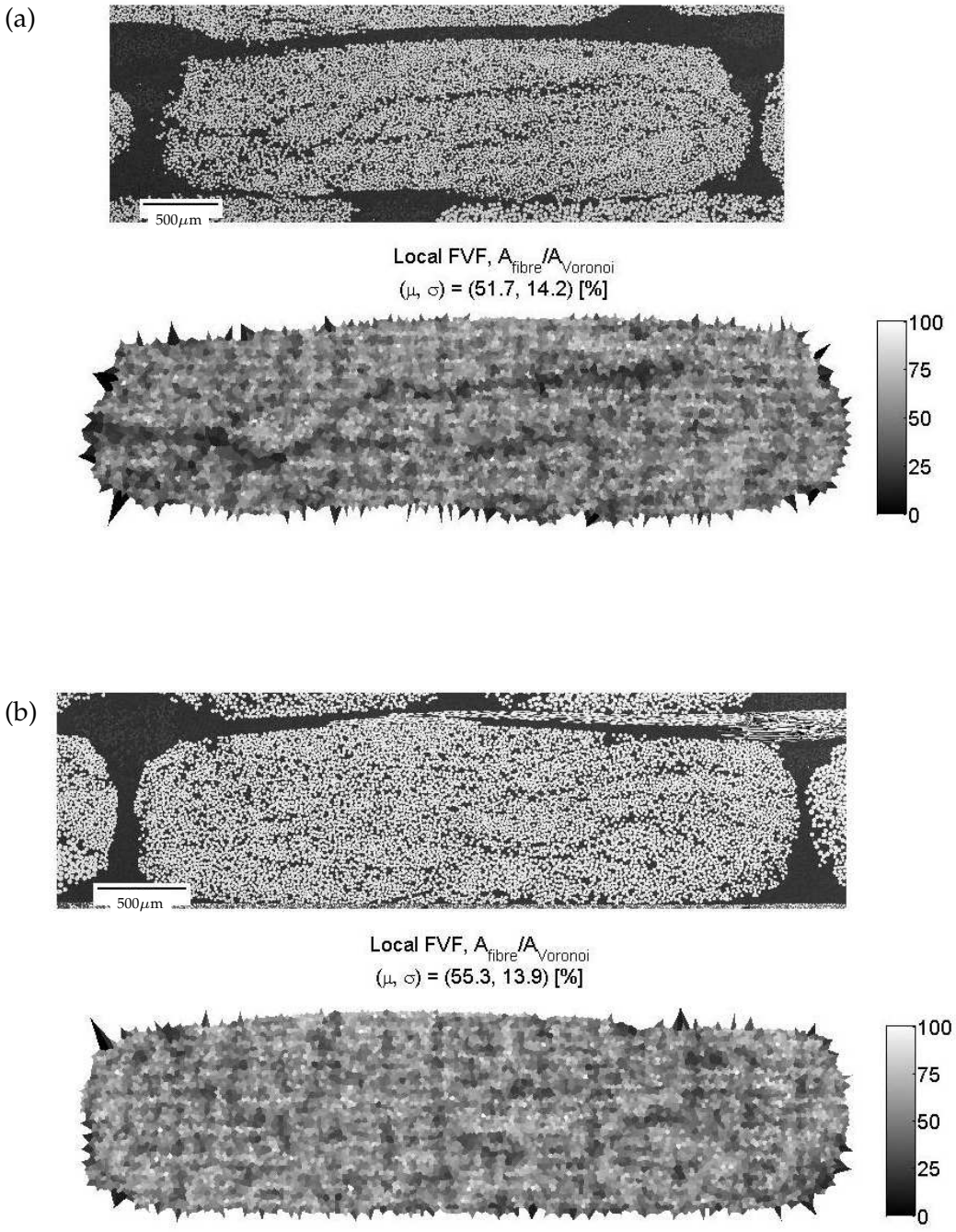

Figure 3.7: Result of image analysis of microstructure across bundles at fibre scale. (a) Bundle 1. (b) Bundle 2.

to illustrate the microstructural complexity associated with the hierarchical material. As seen from Table 3.2, there is a difference between the FVF at the length scales considered, and changing the FVF at the plate scale affects all of the remaining length scales. Additional interesting high-resolution examples of composite microstructures with varying FVF are shown in Fig. 3.8. The same fabric is used as above, but processed with a different vacuum pressure.

Depending on the vacuum pressure during processing, the FVF at the laminate scale is different and varies from 46.0 to 58.7%, see Fig. 3.8. Furthermore, the average FVF at the bundle scale changes as well, which in turn affects the local FVF at the fibre scale. An interesting observation is that the amount of fibres is the same in the micrographs shown in Fig. 3.8, and the only way to affect the FVF is by adding (or removing) resin from the composite. One design factor in wind turbine blade manufacturing, is stiffness (tip deflection and tower clearance). Since the composite stiffness is dominated by glass properties, the blade is basically designed with a fixed amount of glass to ensure the correct stiffness. Resin is added to bond the fibres together, and as seen from Fig. 3.8(b) there appears to be an upper limit for the fibre compaction. Also, there is a limit on how much the fibre bundles can be separated due to the stitching thread, and the resin enters between the fibrous layers and the bundles, Fig. 3.8(a). Decreasing the composite stiffness (lowering the FVF) can only occur if resin is added, which will cause a reduction in the composite density, but an increase in blade mass due to the required stiffness. All together with the current processing method, there is a narrow range around 55% (laminate scale) into which the FVF of composites used for wind turbine blades is usually found. Still, for this narrow range of FVF's, the understanding of the composite microstructure, and the effect on mechanical properties must be ensured at the different length scales within the composite. A way to numerically investigate the interplay between microstructure and damage progression of a NCF, is by hierarchical modelling. Here, mechanical and damage properties from one length scale are passed on to the next, e.g. to evaluate the damage evolution. A still unanswered question is what length scale that is suitable for evaluation of the mechanical and damage properties of NCF's.

3.3 Micro computed tomography

3.3.1 Introduction and motivation

Waviness and misalignment of load carrying axial fibres cause local stress concentrations and shear transfer at the interface between fibre and matrix, which may initialise or lead to failure. Fibre waviness and misalignment are of particular interest regarding the compressive strength of composites (e.g. Wisnom [55]) and in relation to kink-band formation (e.g. Budiansky & Fleck [56]). In (tension) fatigue, there is a risk of fibre debonding as a consequence of the cyclic stretching of a wavy fibre. With regards to characterisation of the 3D microstructure of fibre composite, measurements of the fibre misalignment are important in order to obtain a correct statistical material description. An accurate 3D description of the microstructure is useful for numerical predictions of the mechanical behaviour of the composite. Measurement and determination of the fibre misalignment have for instance been done by Yurgartis [57] and Paluch [40]. The present section deals with characterisation of the fibre misalignment based on the 3D microstructure of a NCF. The 3D microstructure is obtained using micro computed tomography (CT), and the methodology outlined in [P1] is used to map the individual fibres.

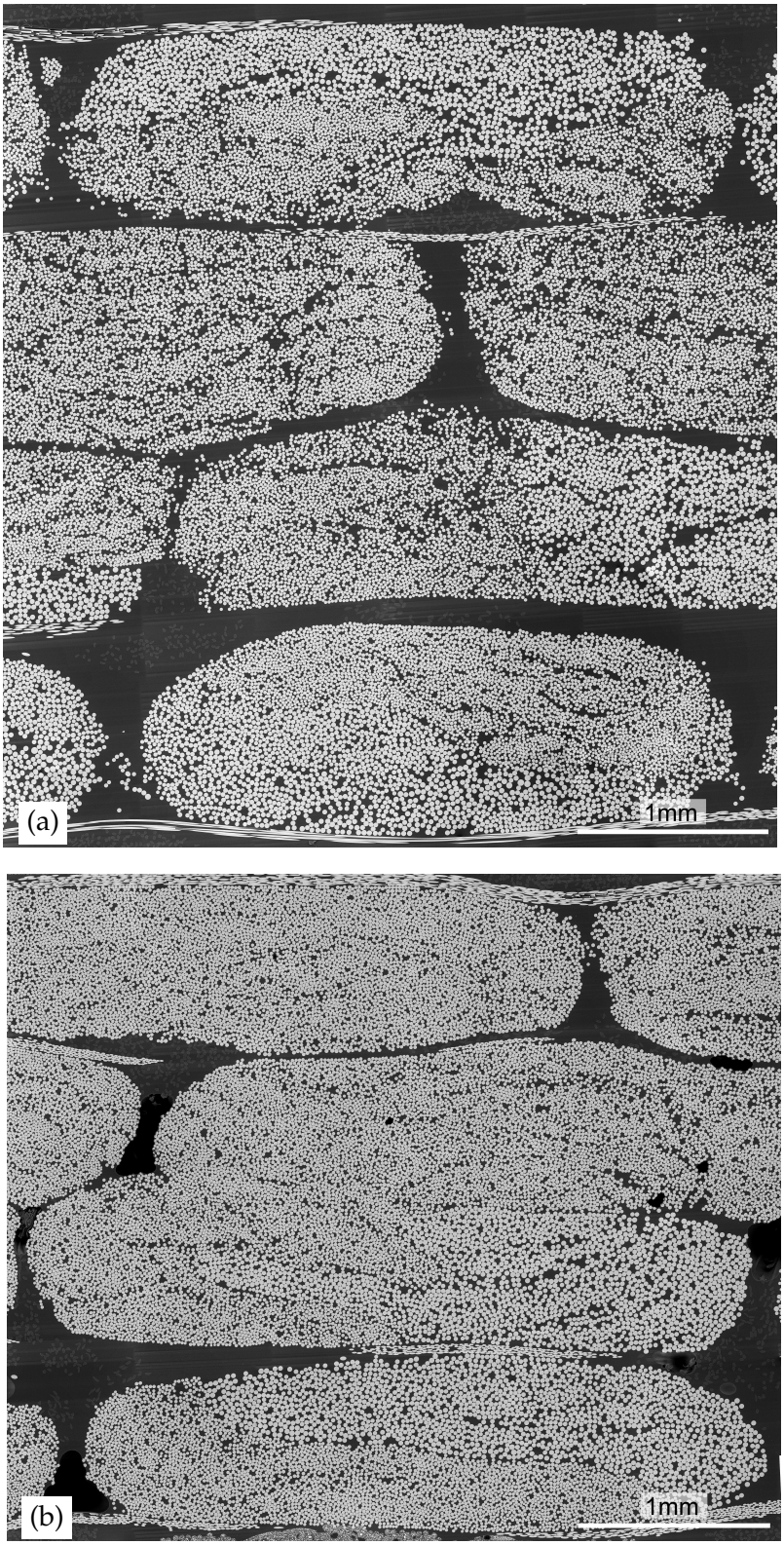

Figure 3.8: Additional high-resolution micrographs at laminate scale of UD1322 fabrics with varying fibre volume fraction. (a) FVF at laminate scale 46.0%. (b) FVF at laminate scale 58.7%.

3.3.2 Material and method

The material considered in the 3D misalignment investigation is the UD1322 fabric, illustrated in Fig. 3.2 on page 17. A laminate consisting of 4 layers is manufactured using the VARTM process and a polyester resin. A representative material sample is cut (approximately $4 \times 4 \times 4$mm) and analysed using a Skyscan 1172 micro CT-scanner. The CT-scanner used is kindly provided by the Danish Technological Institute. The 3D construction of the material sample is based on image stacking of 2D image slices captured along the principal fibre direction. Selected image slices are shown in Fig. 3.9 along with the considered volume of interest (VOI) that is used to detect the fibre misalignment. The view plane is analogous to Figs. 3.3 and 3.8.

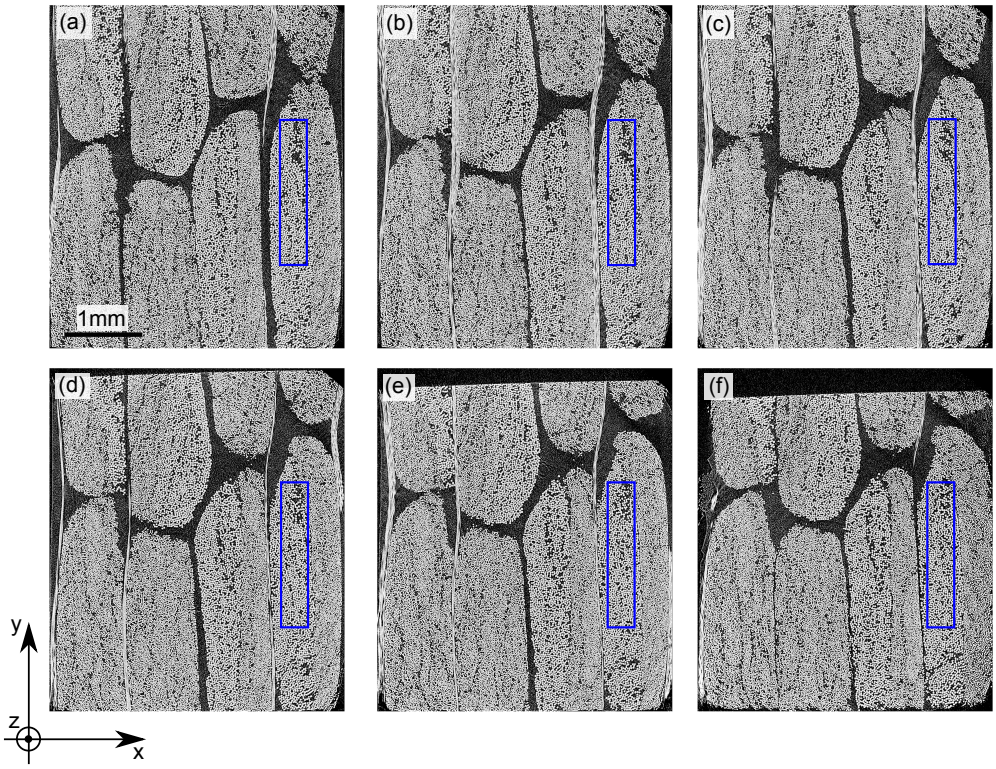

Figure 3.9: Selected image slices of the composite microstructure at different locations along the principal fibre direction (out-of-plane). The blue rectangles mark the volume of interest where the fibre misalignment is determined. A movie clip entitled `JZAN_CT_scan` showing the 3D construction of the image slices as function of z can be found from the DTU Research Information System, Orbit[1]. (a) $z = 0$. (b) $z = 0.2z_{\max}$. (c) $z = 0.4z_{\max}$. (d) $z = 0.6z_{\max}$. (e) $z = 0.8z_{\max}$. (f) $z = z_{\max} = 3.36$mm.

[1]To locate the file, follow the link `http://orbit.dtu.dk/en/`, and make a search on the thesis title 'The effects of fibre architecture on fatigue life-time of composite materials'. The movie clip appears under documents appended to the thesis.

It is seen from the image sequence, Fig. 3.9, along the principal fibre direction that the fibre bundles change both shape and location. Also, the transverse backing bundles are present between the axial fibre bundles at various locations. The reason for the skew top side of the images in Fig. 3.9(e) and (f) is due to the cutting of the sample. The VOI, marked in Fig. 3.9, is considered in the following to determine the fibre misalignment within that specific region. Fig. 3.10 shows the methodology adopted in order to detect the local fibre misalignment from two subsequent image slices separated by a distance δz. The terminology 'local angles' is used to refer to the slice-to-slice variation whereas 'global angles' are used for entire fibre undulation.

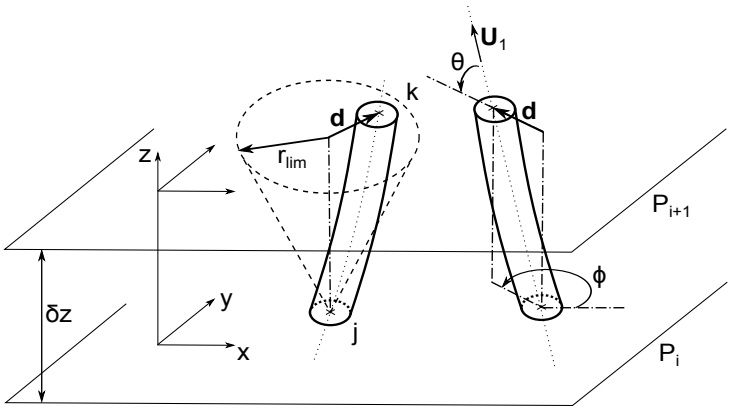

Figure 3.10: Detection of fibre with end points j and k from image slices P_i and P_{i+1}. Definition of local misalignment angles ϕ (in-plane) and θ (out-of-plane). Note that the local out-of-plane angle, θ, is determined according to the overall fibre undulation $\mathbf{U}_1$, see also Fig. 3.11. Sketch adopted from Paluch [40].

The distance between the image slices, see e.g. Fig. 3.10, is $\delta z = 1.6\mu$m, which is comparable to the resolution of the scan. This image resolution means that fibre diameters are not correctly identified, [P1]. Due to the relative low value of δz compared to the average fibre diameter (17μm), it is reasonable to set the limit exploration radius, r_{lim}, equal to the detected fibre radius, r_k. This means that a fibre is disregarded if $|\mathbf{d}| > r_k$. The in-plane location and radius for the fibres in each slice are determined using the circular Hough transformation, outlined in [P1]. The circle detection algorithm (Hough transformation) might miss a fibre detection in subsequent image slices during the analysis. If so, a fibre is still included in the analysis when the exploration criteria is met once/if the given fibre is rediscovered in a later image slice. The local in-plane misalignment angle with respect to the x-axis, ϕ, is determined as:

$$\begin{aligned} \mathbf{u} &= [\mathbf{d}(1) \quad \mathbf{d}(2) \quad \mathbf{d}(3)] \\ \mathbf{v} &= [1 \quad 0 \quad 0] \end{aligned} \qquad \Rightarrow \qquad \phi = \frac{\mathbf{u} \cdot \mathbf{v}}{\|\mathbf{u}\|\|\mathbf{v}\|} \tag{3.2}$$

where $\|\cdots\|$ is the norm of the argument, and $\cdot$ is the dot product. The local out-of-plane misalignment angle between each image slice, θ, with respect to the global fibre undulation with direction $\mathbf{U}_1$, is given by:

$$\begin{aligned} \mathbf{u} &= [\mathbf{d}(1) \quad \mathbf{d}(2) \quad \mathbf{d}(3)] \\ \mathbf{v} &= [\mathbf{U}_1(1) \quad \mathbf{U}_1(2) \quad \mathbf{U}_1(3)] \end{aligned} \qquad \Rightarrow \qquad \theta = \frac{\mathbf{u} \cdot \mathbf{v}}{\|\mathbf{u}\|\|\mathbf{v}\|} \tag{3.3}$$

The main undulation of the neutral axis of a fibre, is expressed in terms of the vectors $\mathbf{U}_i$, $i = 1, 2, 3$, as illustrated in Fig. 3.11.

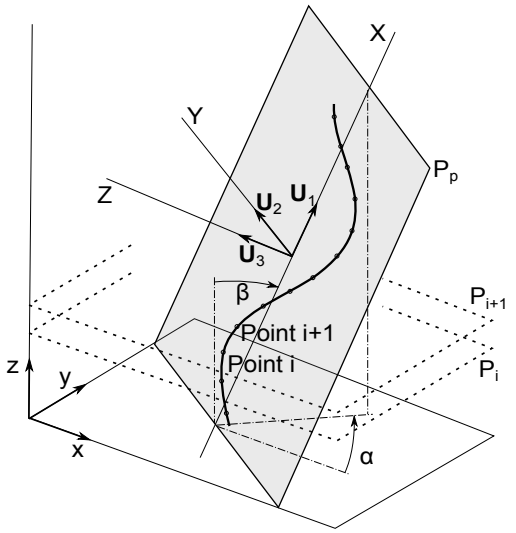

Figure 3.11: Main directions of fibre undulation, $\mathbf{U}_i$, along with inertia plane, P_p, associated to the entire detected fibre. Sketch adopted from Paluch [40].

Assuming that the fibre undulation is primarily restricted to a plane, P_p, defined as the centre of mass (inertia plane), see e.g. Fig. 3.11, the global fibre undulation $\mathbf{U}_i$ is determined as outlined by Paluch [40]. The spatial coordinates of the detected fibre along all image slices are collected in matrix format:

$$\mathbf{X} = \begin{bmatrix} x_1 & y_1 & z_1 \\ \vdots & \vdots & \vdots \\ x_N & y_N & z_N \end{bmatrix}$$

where N is the total number of slices considered. The matrix $\mathbf{g}$ associated with the centre of mass for the detected fibre coordinates, is:

$$\mathbf{g} = \mathbf{X}^{\mathrm{T}}\mathbf{D} \qquad \text{with} \qquad \mathbf{D} = \frac{1}{N}\mathbf{I}$$

whereas the variance-covariance matrix, $\mathbf{V}$, relative to the coordinates is equal to:

$$\mathbf{V} = \mathbf{X}^{\mathrm{T}}\mathbf{D}\mathbf{X} - \mathbf{g}\mathbf{g}^{\mathrm{T}}$$

In order to determine the main directions of the inertia plane P_p, spanned by the vectors $\mathbf{U}_i$, one needs to solve the eigenvalue problem of the form:

$$\mathbf{V}\mathbf{a} = \lambda\mathbf{a} \tag{3.4}$$

The eigenvectors associated to Eq. (3.4) give the main undulation directions of the fibre, $\mathbf{U}_i$. The global misalignment angles with respect to the coordinate axis, α and β, are then given by:

$$\begin{aligned} \mathbf{u} &= \begin{bmatrix} \mathbf{U}_1(1) & \mathbf{U}_1(2) & \mathbf{U}_1(3) \end{bmatrix} \\ \mathbf{v} &= \begin{bmatrix} 1 & 0 & 0 \end{bmatrix} \end{aligned} \qquad \Rightarrow \qquad \alpha = \frac{\mathbf{u}\cdot\mathbf{v}}{\|\mathbf{u}\|\|\mathbf{v}\|} \tag{3.5}$$

and

$$\begin{aligned} \mathbf{u} &= \begin{bmatrix} \mathbf{U}_1(1) & \mathbf{U}_1(2) & \mathbf{U}_1(3) \end{bmatrix} \\ \mathbf{v} &= \begin{bmatrix} 0 & 0 & 1 \end{bmatrix} \end{aligned} \qquad \Rightarrow \qquad \beta = \frac{\mathbf{u} \cdot \mathbf{v}}{\|\mathbf{u}\| \|\mathbf{v}\|} \tag{3.6}$$

with reference to Fig. 3.11. In the following, the local misalignment angles θ and ϕ are determined for all detected fibres between each image slice, and the global misalignment angles α and β are determined for each detected fibre.

3.3.3 Results and discussion

The fibre detection is based on a VOI sized $350 \times 1875\mu$m and height 3.36mm, which amounts to analysis of approximately 2100 images. In order only to analyse fibres the span somewhat across the VOI height, fibres and fibre segments that are less than 800μm in height are disregarded. This results in detection of 640 individual fibres, and 10 randomly selected reconstructed fibres are shown in Fig. 3.12. The accuracy of the fibre detection can be improved using a larger resolution of the micro CT-scanner.

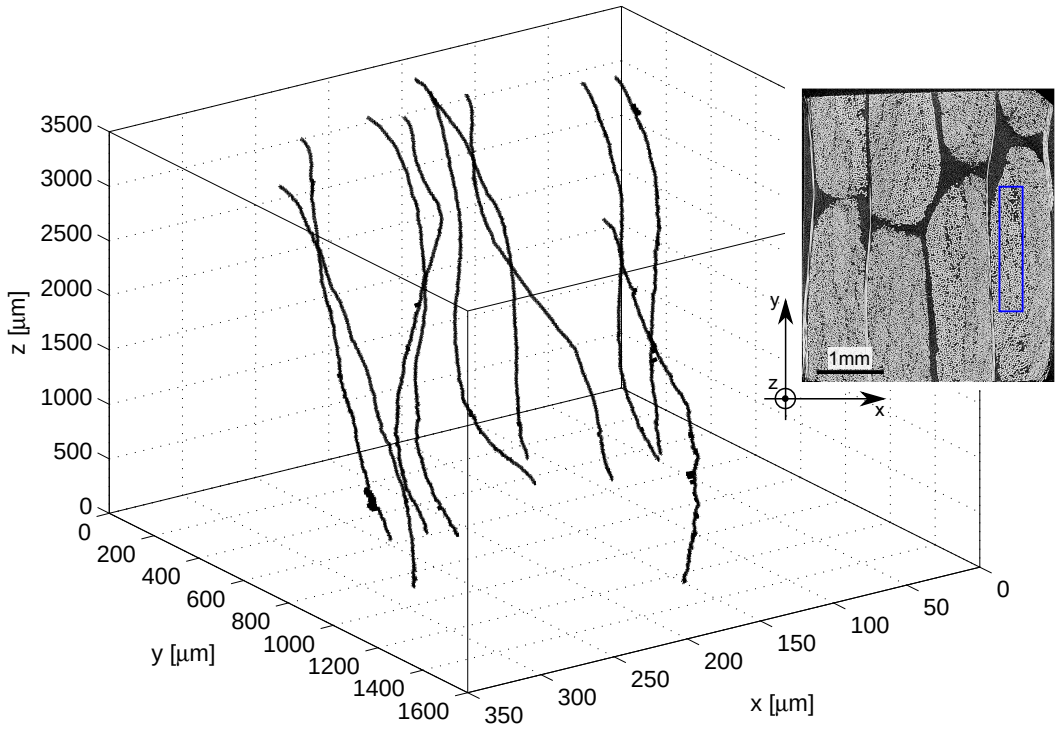

Figure 3.12: 3D reconstruction of selected fibres based on micro computed tomography and digital image analysis. Principal fibre direction follows the z-axis. A planar projection of the fibres is shown in Fig. 3.13. For visualisation, the axis are not scaled similarly. The insert shows the location within the sample.

The often used approximation of straight fibres in unidirectional materials is a crude simplification considering Fig. 3.12 where the fibres are obviously wavy and non-uniform. A projection of the fibres to the xz and yz-plane is shown in Fig. 3.13.

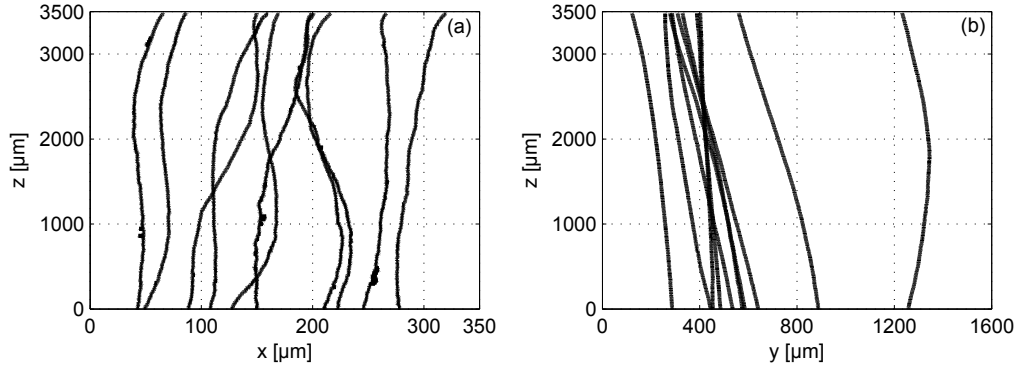

Figure 3.13: Projection of selected reconstructed fibres on axis-planes. For visualisation, the axis are not scaled similarly. (a) xz-plane. (b) yz-plane.

Fig. 3.13(a) shows the projection of the reconstructed fibres on the xz-plane, which is the fibre variation through the thickness of the sample (see e.g. insert in Fig. 3.12). It appears that the fibres undulate in a sinusoidal shaped way with a given wavelength and amplitude, which might be caused by the presence of a backing layer, see also Fig. 3.9. Note that the wavelength is much larger than the amplitude, which is a result of the figure axis scaling. The projection on the yz-plane, Fig. 3.13(b), suggest that the fibres are almost aligned and inclined with the same angle. However, the fibres might be wavy on a length scale larger than the specimen size analysed, or the inclination can be caused by the specimen cutting and a slightly tilted sample in the micro CT-scanner. The local fibre misalignment between each of the image slices, ϕ and θ, is presented in Fig. 3.14 in terms of the cumulative distribution function (CDF) and the probability density function (PDF).

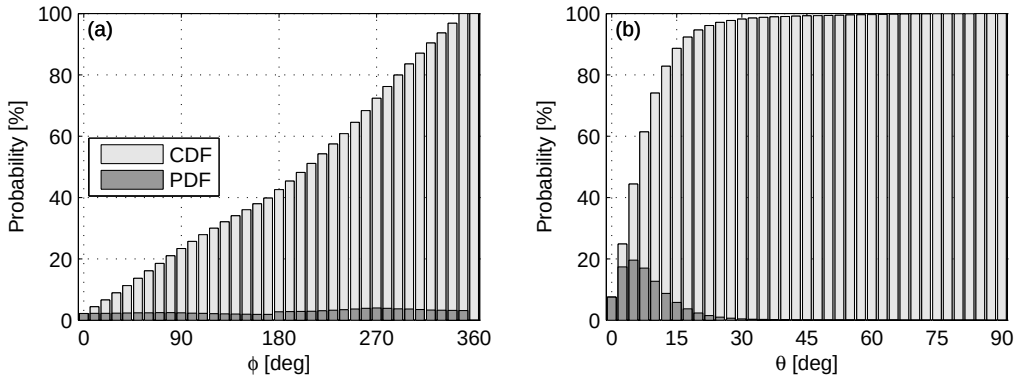

Figure 3.14: Local fibre misalignment between individual image slices in terms of the CDF and PDF. See Fig. 3.10 for definition of the angles. (a) In-plane misalignment, Eq. (3.2). (a) Out-of-plane misalignment, Eq. (3.3).

The local in-plane fibre misalignment between each image slice, Fig. 3.14(a), shows equal probability for all orientations. This means that each fibre at the microscale, is misaligned with a random in-plane orientation. The out-of-plane misalignment, Fig. 3.14(b), is a mea-

sure of the local microscale fibre variation with respect to the global fibre direction. A mean around $\theta = 10$deg and positive skewness are observed. Since the in-plane misalignment angle is random and the out-of-plane angle is rather well defined, this indicate that the fibre locally is 'spinning around' the global fibre direction. The global fibre undulation, expressed as α and β, is shown in Fig. 3.15 in terms of the cumulative distribution function and the probability density function.

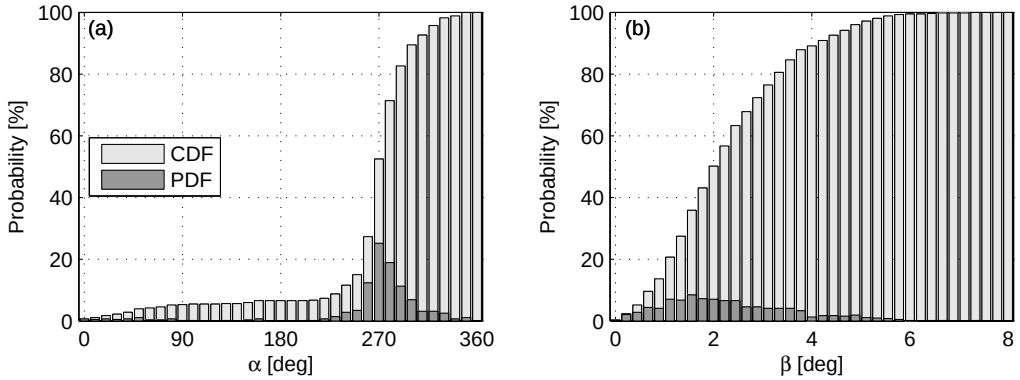

Figure 3.15: Global fibre undulation in terms of the CDF and PDF. See also Fig. 3.11 for definition of the angles. (a) In-plane undulation, Eq. (3.5). (a) Out-of-plane undulation, Eq. (3.6).

Fig. 3.15(a) shows that the global in-plane undulation has maximum probability at $\alpha = 270$deg, which indicates that the fibres drift in the transverse direction of the laminate. Fig. 3.15(b) presents the global out-of-plane undulation of the fibres with respect to the z-axis, and it shows that the fibres tend to incline with a somewhat well-defined angle around $\beta = 2$deg. This angle is coupled with the fibre variation in the yz-plane, presented in Fig. 3.13(b).

3.3.4 Summary

The fibre misalignment of a NCF has been determined based on micro computed tomography and digital image analysis. It is demonstrated that the fibres are approximately sinusoidal shaped in the thickness-wise direction of the laminate, and that the fibres are globally inclined in the transverse laminate direction. On the microscale, each fibre is 'spinning around' the global fibre direction. The observations presented are the first preliminary steps for a full 3D characterisation of non-crimp composites. The fibre architecture inside the bundles has been evaluated by simple means, and the next step is to characterise the bundle shapes and spatial variation. Also, further investigations are needed in order to document the effect of backing and stitching on the fibre misalignment as well as comparison to the misalignment in pure unidirectional composites like wound plates.

Chapter 4

Fatigue damage assessment

The second central theme in relation to present work is tension fatigue, which is addressed in the forthcoming chapter. First, the current status on materials research in relation to fatigue of composites is outlined. Then, three different experimental studies are presented where the fatigue life-time and the fibre architecture are linked together:

1. Investigation of the influence of fibre content on the life-time.
2. Identification of an appropriate stacking sequence of the preform.
3. The effect of specimen geometry on the fatigue life-time.

The chapter is closed with a numerical stress analysis using finite elements of the fatigue damaged composite, and a discussion for fibre architectural improvements with respect to tension-tension fatigue. Fatigue and fibre architecture are the themes of the appended paper [P4].

4.1 Literature survey

The aim of the literature survey is to confine and identify existing and recent work done within the field of fatigue damage mechanisms of non-crimp fabrics (NCF's), e.g. used for wind turbine rotor blades. For a general presentation on fatigue of composites, one should confront the references in Sec. 2.4. Fatigue life prediction and strength degradation mechanisms of composites used for wind turbine blades have been considered in the thorough and interesting work of Nijssen [26]. For wind turbine blade application, the SNL/MSU/DOE fatigue of composite materials database developed at Montana State University, [29], is a comprehensive and constant evolving information source within the field.

Even though the wide range of applications of NCF's, there is limited information available on the mechanical performance of these materials, especially in fatigue. A recent and elaborative review on fatigue of NCF's for wind turbine blade application, is found in Vallons et al. [58]. With reference to the automotive industry, Vallons [59] made a comprehensive study on the response of carbon fibre NCF's under various mechanical loadings. For static tensile loading, Edgren et al. [60] investigated the crack formation of a

cross-ply laminate manufactured of a NCF. In continuation to the study of Edgren et al., the same research group studied the compressive behaviour of NCF's with out-of-plane misalignment, Joffe et al. [61]. Later, Mattsson et al. [62] examined the effect of stiffness degradation and stacking sequence for the same NCF's. Lomov [49] gives an excellent introduction to the manufacturing, processing, mechanical performance, and application of NCF's. Discussions relevant to the present include: damage progression (by Asp et al.), fatigue (by Vallons), and application in wind turbine rotor blades (by Adolphs and Skinner). During tensile fatigue, Gagel et al. [63] considered the stiffness degradation, crack density evolution, and temperature development of a quasi-isotropic multiaxial NCF. The stiffness decrease was related to the crack density of the individual plies. In continuation to the experimental study, Gagel et al. [64] numerically investigated the fatigue behaviour of the same material. In a series of papers Adden and Horst, [65] and [66], used the same NCF as Gagel et al. in order to investigate the crack density and stiffness degradation of bi-axially fatigue-loaded tubes. Carvelli et al. [67] evaluated the impact of structural stitching (Z-reinforcement) on the fatigue and post fatigue behaviour of a biax NCF made of carbon fibres. They showed that the fatigue life-time for $R = 0.1$ improved in favour of the stitched laminate in the direction of the structural stitching whereas it reduced the life-time in the orthogonal direction.

Some of the above mentioned references also include numerical modelling of NCF materials, e.g. Edgren et al. [60], Joffe et al. [61], and Lomov [49]. Numerical predictions and evaluation of the damage in NCF's are typically based on the unit cell and/or representative volume element approaches (e.g. Drapier and Wisnom [68], Zhao et al. [69], and Tserpes and Labeas [70]). The multiscale modelling strategy is also common, see e.g. Ernst et al. [71] and LLorca et al. [72]. However, independent on the modelling strategy, the problem to model fatigue of NCF's is cumbersome and require large computational power. Therefore, most studies are focussed on the static behaviour, and more scientific effort is needed for the fatigue behaviour to be assessed properly.

4.2 Fatigue and fibre content[2]

4.2.1 Introduction and motivation

It has previously been demonstrated e.g. by Mandell et al. [23] that there is a connection between the fibre volume fraction and the fatigue life-time. In continuation to the observations done by Mandell and co-workers, the present section experimentally investigates the interplay between the FVF and tension-tension fatigue life-time.

4.2.2 Material and method

In an experimental study with tension-tension fatigue tests, stress-cycle curves are established for five different composite laminates with a varying fibre content. Selected microstructural parameters are examined based on the methodology presented in [P1],

[2]The content of the present section has been presented at the DFC-11/SI-5 conference held at Queens College, Cambridge University, 12-15 April, 2011.

and these parameters are linked to the fatigue life-time of the material. The chosen microstructural parameters considered are: the FVF inside the axial bundles, the number of contact points per fibre, and the nearest neighbour distance. Compared to the FVF, which is a global average characterisation parameter, these microstructural parameters are amongst those describing the internal structure of the material. It is believed that the parameters selected contribute to the fatigue life-time. Test details are presented in Table 4.1.

Table 4.1: Test overview for fatigue life-time and fibre content.

Category	Symbol	Unit	Value/comment
Test details			
Stress waveform	-	[-]	Sinusoidal
Stress ratio	R	[-]	0.1
Control mode	-	[-]	Stress
Monitoring	-	[-]	Extensometers
Frequency	f	[Hz]	5
Max. initial strain	$\varepsilon_{\max}$	[%]	Varying
Static preload	-	[-]	Yes
Test machine	-	[-]	Servo hydraulic Instron
Materials			
Fabric, UD	-	[-]	UD1322 (see e.g. Fig. 3.2 and Table 3.1)
Fabric, biax	-	[-]	BIAX450 (see e.g. Fig. 4.1 and Table 4.2)
Matrix	-	[-]	Unsaturated polyester
Processing method	-	[-]	VARTM
Number of layers	-	[-]	8
Stacking sequence	-	[-]	$[\pm 45_2, 0_2]_s$
Geometry	-	[-]	EN ISO 527-4:1997, [73]

The stacking sequence used is typical for testing of unidirectional composites at LM Wind Power. Fabric details for the BIAX450 NCF are shown in Fig. 4.1 and Table 4.2. Only one side of the fabric is shown in Fig. 4.1 since the other side is identical (reversed).

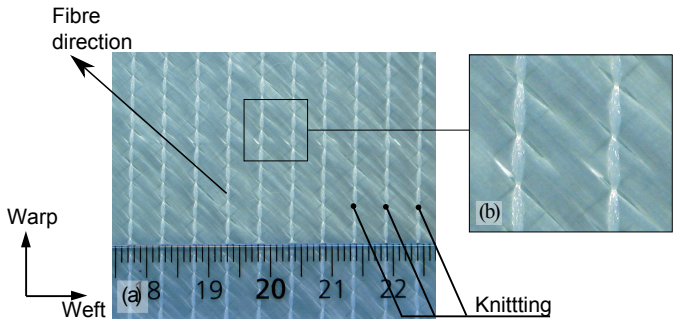

Figure 4.1: Fabric architecture of NCF BIAX450. Scale bar in units of cm. Stitching pattern: chain. (a) Fibre structure (both sides of the fabric are identical). (b) Magnification of 'fish eye'.

For biaxial NCF's, there is often a tendency to what is referred to as 'fish eyes', i.e. regions where the glass fibres are wavy due to the knitting, see Fig. 4.1(b). The 'fish eyes' cause resin rich pockets in the processed laminates. The size and distribution of these 'fish eyes' serve as a quantitative measure of the fabric quality, [49].

Table 4.2: Fabric specifications for commercially available BIAX450.

Category	Symbol	Biax	Stitching thread
Orientation	[deg]	± 45	N/A
Area weight	[g/m^2]	220 ± 10	6 ± 3
Linear density, roving	[tex]	160-420	7-9
Material	[-]	E-glass	Polyester
Avg. filament diameter	[μm]	≤ 19	N/A

The central gauge region of the test specimens has dimensions of $150 \times 25 \times t$ mm where the sample thickness, t, depends on the fibre content. The experimental Wöhler curves are determined for each experiment, and the SN-data for each test series are fitted to the Basquin equation:

$$\varepsilon(N) = aN^{-\frac{1}{m}} \tag{4.1}$$

thus presenting the data in a power law relation. The curve fits are performed according to the guidelines provided in ASTM E739-10, [74].

4.2.3 Results and discussion

The Wöhler-curves and the associated best-fits to the Basquin-equation for the five different samples considered are shown in Fig. 4.2.

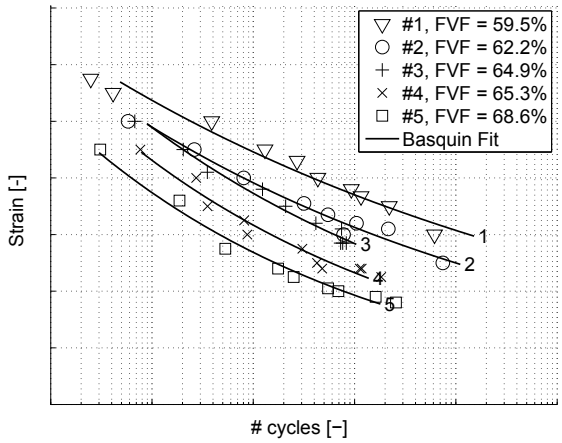

Figure 4.2: Experimental Wöhler curves for $[\pm 45_2, 0_2]_s$ composites with varying fibre content. Constants for the Basquin fits and selected microstructural parameters are presented in Table 4.3.[3]

[3] Axis are removed to avoid publication of LM Wind Power material values.

As seen from Fig. 4.2, the fatigue life is decreased for increasing fibre content, which was also observed by Mandell et al. [23]. The normalised constants for the Basquin fit are shown in Table 4.3 along with the selected microstructural parameters (number of contact points per fibre and the nearest fibre neighbour distance) obtained from a microscopic investigation of the samples. The methodology is outlined in [P1]. The FWF is determined by the loss ignition method, whereas the FVF is calculated inside the axial fibre bundles (bundle scale in Sec. 3.2) based on the threshold analysis in [P1].

Table 4.3: Normalised Basquin constants and result of the digital image analysis of glass fibre reinforced composite with varying fibre content exposed to tension fatigue.

		Fatigue data		Image analysis	
Sample #	FWF/FVF [%]	a/a_{mean} [-]	m/m_{mean} [-]	CP [a] [-]	NN [μm]
1	69.4 / 59.5	0.85	1.36	0.55	2.7/4.5
2	72.5 / 62.2	0.90	1.13	0.58	2.5/4.0
3	73.6 / 64.9	1.09	0.93	0.66	2.0/3.6
4	75.3 / 65.3	1.11	0.82	0.73	1.9/3.6
5	76.7 / 68.6	1.05	0.76	0.78	1.7/3.6

[a] CP Contact points per fibre
NN Nearest fibre neighbour distance, μ/σ

The fatigue slope, m, in Table 4.3 is affected by the different FVF's, and shows a decreasing tendency for increasing FVF, thus a poorer fatigue resistance. The intersection parameter, a, is somewhat independent on the FVF. A larger FVF implies a denser fibre packing, reflected in the increasing number of fibres in contact and the decreasing fibre-to-fibre distance. The fatigue exponent is plotted along with the number of contact points per fibre as a function of FVF in Fig. 4.3. Here, simulation results for the number of fibres in contact obtained from a numerical replication of the fibre architecture (see details in [P2]) are shown as well. The bandwidth indicates variations for different simulations.

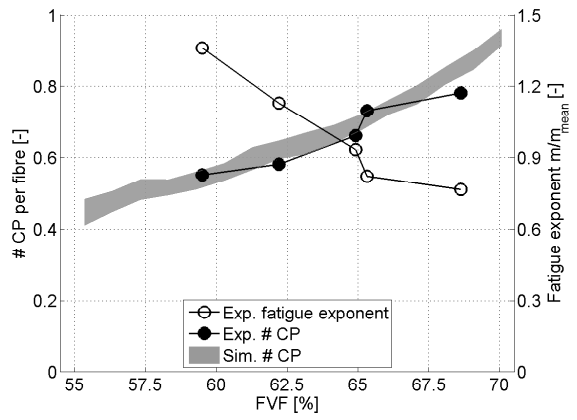

Figure 4.3: Fatigue life exponent and number of contact points as function of FVF.

From Fig. 4.3 it is observed that an increasing FVF gives a larger slope (smaller m) and steeper fatigue curve. The decrease in m is linked to the local interaction between fibres in contact, which is increasing as function of the FVF. A decreasing fatigue life exponent is also reported by Mandell et al. [23]; however, the FVF in the laminates used in their work, is fairly lower (from 30-55%) whereas the present is more realistic with respect to the application in focus. The drop in fatigue slope is related to the increasing number of fibres in contact. A numerical simulation of the fibre packing shows similar tendency as the experiments in relation to the number of contact points per fibre. It thus seem fair to use the simulated microstructure for future investigations of the effect of fibre architecture and fatigue life. Based on the conclusions from [P2], the fibre packing pattern (e.g. the Ripley's K-function and the number of neighbours) does not change as function of the FVF. Only, the fibres tend to pack more densely, e.g. reflected in the increasing number of contact points or decreasing fibre-to-fibre distance (see also Table 4.3). Since the fibre packing pattern does not change as function of the FVF, other factors like fibres in contact affect the fatigue life. For static loading, Kushch et al. [54] numerically showed a stress concentration in the vicinity of two neighbouring fibres. With reasonable confidence, the same (cyclic) stress concentration is present in fatigue as well, causing a reduction in life-time.

4.2.4 Summary

On the basis of the results presented above, it is concluded that there is an impact from the composite microstructure on the tension fatigue performance. The FVF is used as a simple measure of the microstructure, and linked to the experimental fatigue life-time diagrams. Increasing the FVF decreases the life-time, which is linked to the internal microstructure of the composite in terms of increasing number of fibres in contact and decreasing fibre-to-fibre separation. The explanation for the actual cause of the material degradation for varying FVF, is still unsettled.

4.3 Stacking sequence

4.3.1 Introduction and motivation

As shown in [P4], the transverse backing layer in the unidirectional NCF considered in the present, is critical regarding tension-tension fatigue performance since damage emerges from this layer. In continuation to the observations made in [P4], this section presents an experimental study on the effect of different stacking sequences of the unidirectional NCF UD1322 in relation to tension-tension fatigue. The effect of stacking sequence of cross-ply laminates manufactured of NCF's under tensile static loading has been investigated by different researchers, e.g. Mattsson et al. [62].

4.3.2 Material and method

Test details and material specifications are listed in Table 4.4. The material considered is the same used in Sec. 4.2.

Table 4.4: Test overview for stacking sequence and tension-tension fatigue.

Category	Symbol	Unit	Value/comment
Test details			
Stress waveform	-	[-]	Sinusoidal
Stress ratio	R	[-]	0.1
Control mode	-	[-]	Stress
Monitoring	-	[-]	Extensometers
Frequency	f	[Hz]	5
Max. initial strain	$\varepsilon_{\max}$	[%]	$[2 \times 0.6, 3 \times 0.8]$ per stacking sequence
Static preload	-	[-]	Yes
Test machine	-	[-]	Servo hydraulic Instron 8501
Material			
Fabric	-	[-]	UD1322 (see e.g. Fig. 3.2 and Table 3.1)
Matrix	-	[-]	Unsaturated polyester
Processing method	-	[-]	Closed mould, differential pressure
Number of layers	-	[-]	4
Average total thickness	t	[mm]	3.75
Stacking sequence	-	[-]	See Fig. 4.4
Geometry	-	[-]	EN ISO 527-4:1997, [73]

For each stacking sequence, two magnitudes of the maximum initial strain are considered, and the number of tests is shown in Table 4.4. All samples are tested to failure. Four different stacking sequences are investigated, and a sketch is shown in Fig. 4.4.

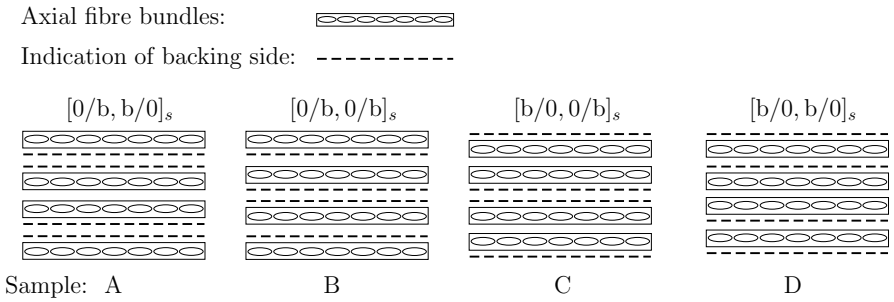

Figure 4.4: Illustration of the different stacking sequences of 4-layered unidirectional NCF tested in tension-tension fatigue. b denotes backing layer, and axial fibre direction is out of plane.

The average FVF on laminate scale, V_f, of the sample is determined using the relation:

$$t = \frac{nA_w}{\rho_f V_f} \tag{4.2}$$

Where t is the laminate thickness (Table 4.4) with n number of plies, A_w the area density of the fabric [g/m^2] (Table 3.1), and $\rho_f = 2610$kg/m^3 the fibre density. Evaluating Eq.

(4.2) yields $V_f \simeq 56.5\%$. The fatigue tests are carried out monitoring the stiffness loss and fatigue life-time, and these are compared for the different stacking sequences.

4.3.3 Results and discussion

Prior to the actual fatigue test, the specimens are preloaded in order to determine the static stiffness (and thereby set the initial fatigue load). The static stiffness and the average number of cycles to failure for the different specimens are shown in Table 4.5. Due to the limited number of specimens tested, only the mean value is presented for the life-times.

Table 4.5: Static stiffness and average number of cycles to failure (round off) for different stacking sequences.

Sample		A	B	C	D
Stacking		$[0/b, b/0]_s$	$[0/b, 0/b]_s$	$[b/0, 0/b]_s$	$[b/0, b/0]_s$
Static stiffness, E_0	[GPa]	49.0	48.5	48.1	47.6
Average no. cycles to failure, $\varepsilon_{\max} = 0.6\,\%$	[-]	67,700	57,100	81,800	111,000
Average no. cycles to failure, $\varepsilon_{\max} = 0.8\,\%$	[-]	23,100	13,300[a]	27,700	19,000

[a] Data sampling failed for one specimen.

As seen from Table 4.5, the variation of the static stiffness is within 3% meaning insignificant changes for the different stacking sequences, which is in accordance with simple ply theory. The fatigue life is affected by the stacking sequence. For the least loaded sample where the backing layer is 'a single layer' only, test D, the life-time is almost doubled compared to specimen B. Furthermore, if the backing layer is located towards the free surface of the specimen, the life-time is increased (specimens A and B vs. C and D). For the largest load, the observations are slightly different. Here, samples A-C still have the same life-time order as above, and sample D seems to fail premature. The stiffness degradation curves are shown in Fig. 4.5.

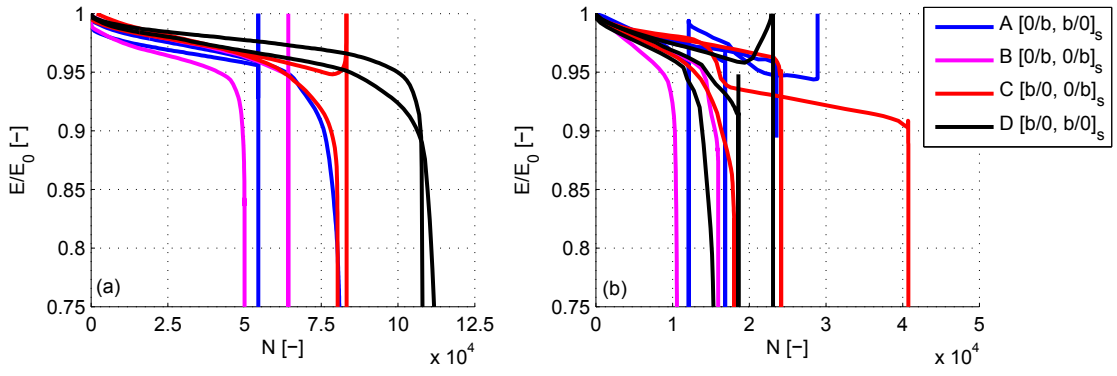

Figure 4.5: Stiffness degradation curves based on extensometer measurements for different stacking sequences. (a) $\varepsilon_{\max} = 0.6\,\%$. (b) $\varepsilon_{\max} = 0.8\,\%$.

From Fig. 4.5(a), it is observed that the stiffness decrease when entering fatigue stage III (see e.g. [P4]) close to final failure is in the order of 5%. This stiffness loss close to final failure is somewhat independent on the stacking sequence. Furthermore, the stiffness degradation rate increases for samples B and C compared to D. Specimens where the backing layers are placed in contact to each other (double transverse layer thickness) give a decrease in life-time (A, B and C). There does not seem to be any obvious explanation for lower life-time of sample D at the largest load level. Otherwise, the observations are similar as for the low load, but with larger scatter. One may argue whether the largest load, Fig. 4.5(b), causes other damage mechanisms than the least loaded samples, which is reflected in the irregular patterns of the stiffness degradation curves and relative few number of cycles to failure.

4.3.4 Summary

An experimental investigation on the effect of stacking sequence on the tension-tension fatigue life-time has been demonstrated. The transverse backing layer is critical with respect to fatigue damage propagation, [P4], and the location of the backing layer in the laminate affects the fatigue life-time. Even though a limited number of samples is tested, and the experiments show some anomalous behaviour for the largest load, the trend (and recommendation) is that future test laminates should be stacked as sample D, which is $[b/0, b/0]_s$.

4.4 Specimen geometry

4.4.1 Introduction and motivation

When performing experimental fatigue coupon testing of composite materials, there is often a scatter on the measured life-time even though the same load and material are used, see e.g. Table 4.5 and Fig. 4.5. In rotor blade design, this life-time variation is handled using statistical methodologies, partial safety factors, and linear damage accumulation rules to get a certain margin of safety to avoid failure, see e.g. the guidelines by Germanisher Lloyd [20]. The life-time scatter cannot solely be explained by variations in the microstructure, and other effects are present and should be taken into account, e.g. stress concentrations near end tabs (Aslan [75]), the effect of clamping force from the test machine (Mikkelsen & Bech [76]), and the design of the specimen geometry. The following section addresses the tension-tension fatigue life-time for different specimen designs. Two different test geometries from the same material batch are tested in tension fatigue, and the difference in life-time is discussed. Thermographic measurements are used as a tool for evaluation of the fatigue damage at a selected load level.

4.4.2 Material and method

The basic glass fibre fabric is same used in [P4] and the previous sections, namely the UD1322. Details on the experiment are seen in Table 4.6.

Table 4.6: Test overview for specimen geometry and tension-tension fatigue.

Category	Symbol	Unit	Value/comment
Test details			
Stress waveform	-	[-]	Sinusoidal
Stress ratio	R	[-]	0.1
Control mode	-	[-]	Stress
Monitoring	-	[-]	Extensometers and thermovision
Frequency	f	[Hz]	5
Max. initial strain	$\varepsilon_{\max}$	[%]	4×0.8 per geometry
Static preload	-	[-]	Yes
Test machine	-	[-]	Servo hydraulic Instron 8501
Material			
Fabric	-	[-]	UD1322 (see e.g. Fig. 3.2 and Table 3.1)
Matrix	-	[-]	Unsaturated polyester
Processing method	-	[-]	VARTM
Number of layers	-	[-]	4
Average total thickness	t	[mm]	3.87
Stacking sequence	-	[-]	$[\mathrm{b}/0, \mathrm{b}/0]_s$ (b is backing side)
Geometry	-	[-]	See Fig. 4.6

The test geometries investigated are the standard planar ISO527-4 [73] geometry, and an improved wedged fatigue geometry developed at DTU Wind Energy, Section of Composites and Material Mechanics. A total number of 12 specimens is manufactured, 6 of each geometry (4 of which are used in the present study). A sketch of the two specimen designs is presented in Fig. 4.6.

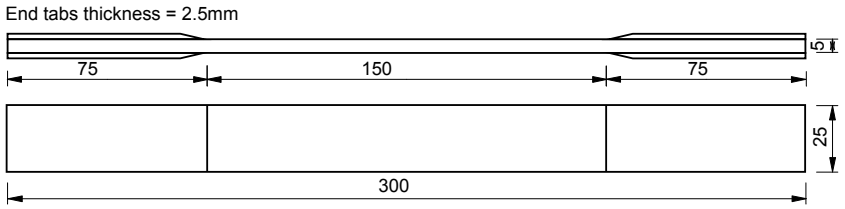

(a) Tension fatigue test geometry from ISO527-4, [73].

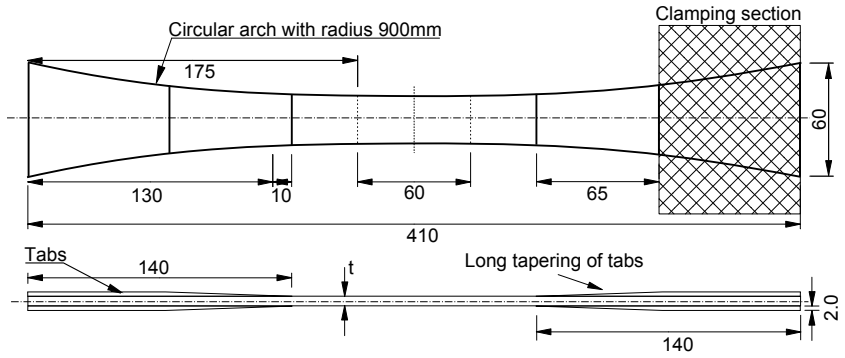

(b) Improved tension fatigue test geometry (butterfly) developed at DTU Wind Energy.

Figure 4.6: Specimen geometries tested in tension-tension fatigue. Geometries in mm.

The maximum initial strain $\varepsilon_{\max} = \sigma_{\max}/E_0 = 0.8\%$ is used as reference to investigate the life-time variation. The damage propagation is investigated using thermovision on one specimen from each geometry. A FLIR X6540sc thermographic camera equipped with a MWIR 50mm lens is used. The period for the thermographic image sampling is set to 30seconds, which means that the test frequency and image acquisition are out of phase. In order to reduce eventual unwanted temperature rise in the gauge region, a fan is mounted to ensure a constant airflow. Extensometers are kept in place with small steel springs. An image of the experimental setup is shown in Fig. 4.7.

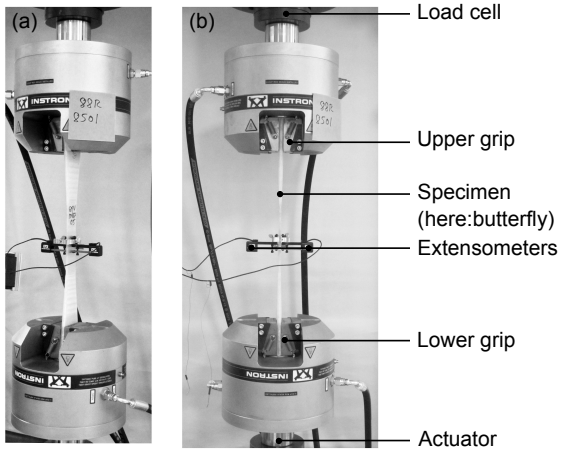

Figure 4.7: Experimental test setup for tension-tension fatigue tests of specimen design. (a) Side view. (b) Front view. Thermographic camera view.

4.4.3 Results and discussion

The stiffness degradation curves for the samples considered are shown in Fig. 4.8.

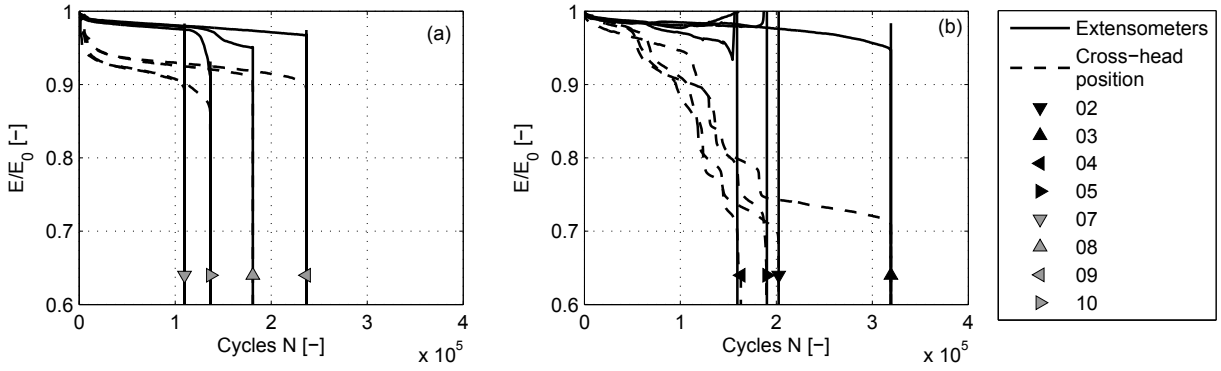

Figure 4.8: Normalised stiffness degradation curves for specimens loaded with an initial strain $\varepsilon_{\max} = 0.8\%$. Images of the fractured specimens are shown in Fig. 4.9. (a) ISO geometry, Fig. 4.6(a). (b) Butterfly geometry, Fig. 4.6(b).

The stiffness degradation curves measured by the extensometers in Fig. 4.8 show typical characteristics in terms of evolution: (i) stage I with a rapid decrease in stiffness within few cycles, (ii) stage II with a linear softening, and (iii) non-linear or sudden failure. It appears that the final stiffness loss measured by the extensometers close to failure is around 5 %, which is in similar range as observed in Sec. 4.3. For butterfly samples 02, 04 and 05, an artificial stiffness increase is observed on the extensometer measurements close to final failure. This increase is most likely due to a surface delamination, which entail an incorrect displacement measure of the extensometer since it slides on the specimen surface; thus, causing an artificial increase in the stiffness. The stiffness decrease measured by the cross-head on the butterfly samples shows a different behaviour in terms of gradually decreasing steps, which is investigated in further detail using thermovision. It is mentioned that the initial stiffness, E_0, of the cross-head often is larger than what is measured by the extensometers. The fractured specimens along with an objective estimate of the location/origin of fracture are presented in Fig. 4.9.

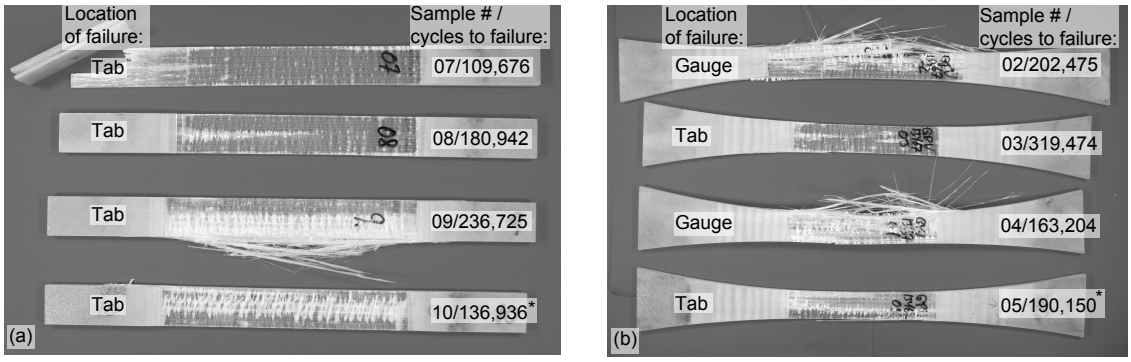

Figure 4.9: Images of broken specimens at $\varepsilon_{\max} = 0.8\%$. The stiffness degradation curves are seen in Fig. 4.8. The specimens marked with an asterisk (*) are used in the thermography analysis. (a) ISO geometry, Fig. 4.6(a). (b) Butterfly geometry, Fig. 4.6(b).

As seen from Fig. 4.9, the mode of failure for the different specimens is quite different. The ISO geometry, Fig. 4.9(a), primarily suffers from tab failure whereas some of the butterfly geometries (02 and 04) experience tearing of the fibres in the gauge region. Still, independent on the geometry, it seems difficult to mimic failure in the gauge region. The average number of cycles to failure is reported in Table 4.7.

Table 4.7: Comparison of life-times (round-off) at $\varepsilon_{\max} = 0.8\,\%$ between the different sample geometries considered. The individual number of cycles to failure is reported in Fig. 4.9. c_v denotes the coefficient of variation.

Sample shape	Reference	Cycles to failure		
		μ	σ	c_v
		[-]	[-]	[%]
ISO	Fig. 4.6(a)	166,000	56,000	33.4
Butterfly	Fig. 4.6(b)	219,000	69,000	31.6

The mean number of cycles to failure is approximately 30% larger for the improved butterfly geometry than the ISO geometry, see e.g. Table 4.7. The coefficient of variation, c_v, is in similar magnitude for the different geometries, indicating that the scatter range is approximately identical.

Samples number 10 (ISO) and 05 (butterfly) (see e.g. Figs. 4.8 and 4.9) are equipped with thermovision to monitor the temperature development as function of load-cycles. The results are shown in Figs. 4.10 and 4.11, respectively, and the camera view is seen in Fig. 4.7(b) for comparison. The rapid increase in cross-head compliance for the butterfly samples, Fig. 4.8(b), is explained by the thermographic observations.

The remaining page is intentionally left blank.

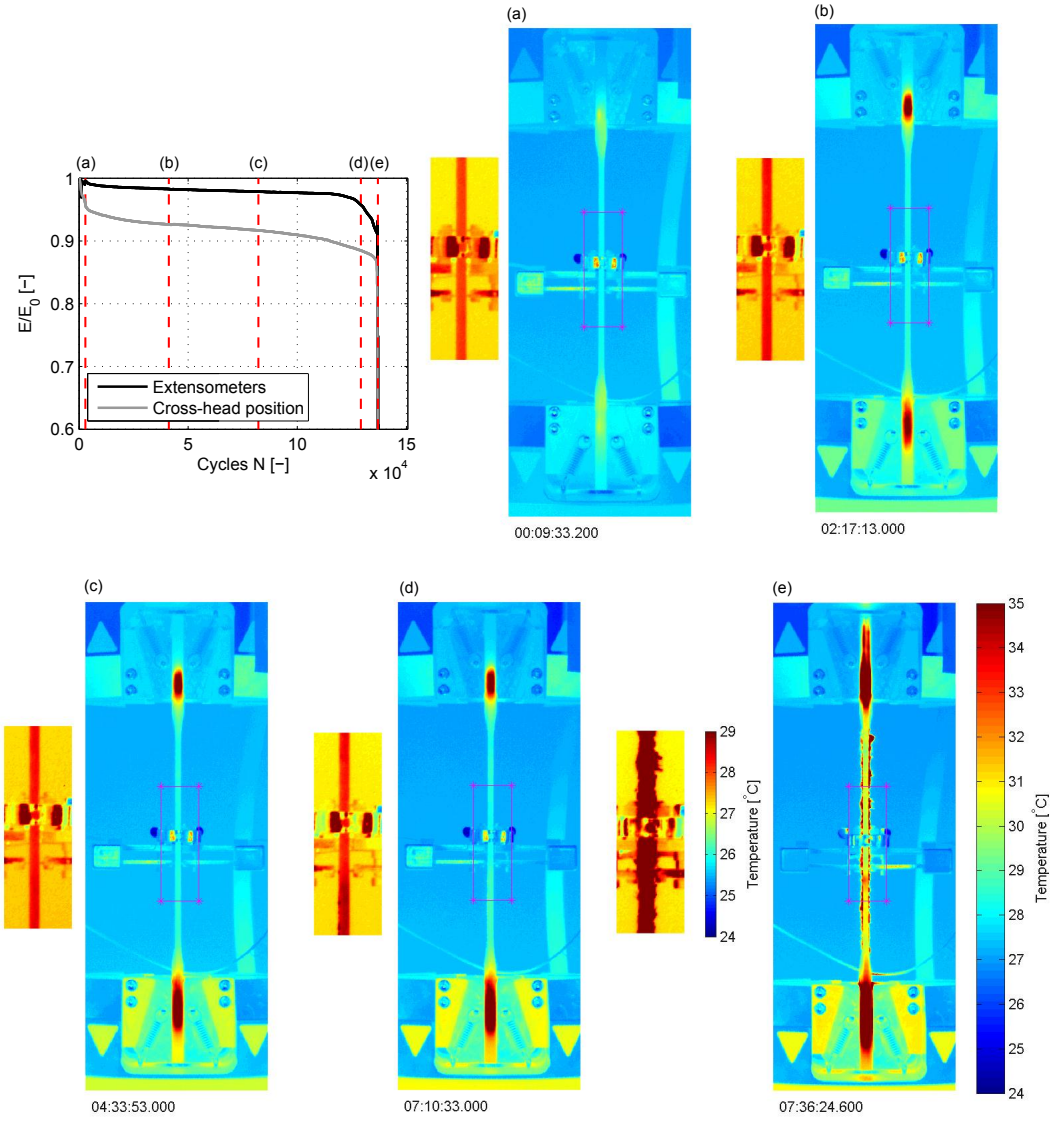

Figure 4.10: Global and local temperature development as function of stiffness degradation at selected load cycles for ISO geometry sample 10, Fig. 4.6(a). The gauge region is magnified, and the number below each global temperature image denotes the test time (hh:mm:sec). The temperature colourbar valid for all the global and local temperature variations, is shown in sub-figure (e). A movie clip entitled `JZAN_Temp_GPV_10_ISO` showing the temperature development as function of stiffness degradation can be found from the DTU Research Information System, Orbit. See footnote 1 on page 27 for description of the accessibility.

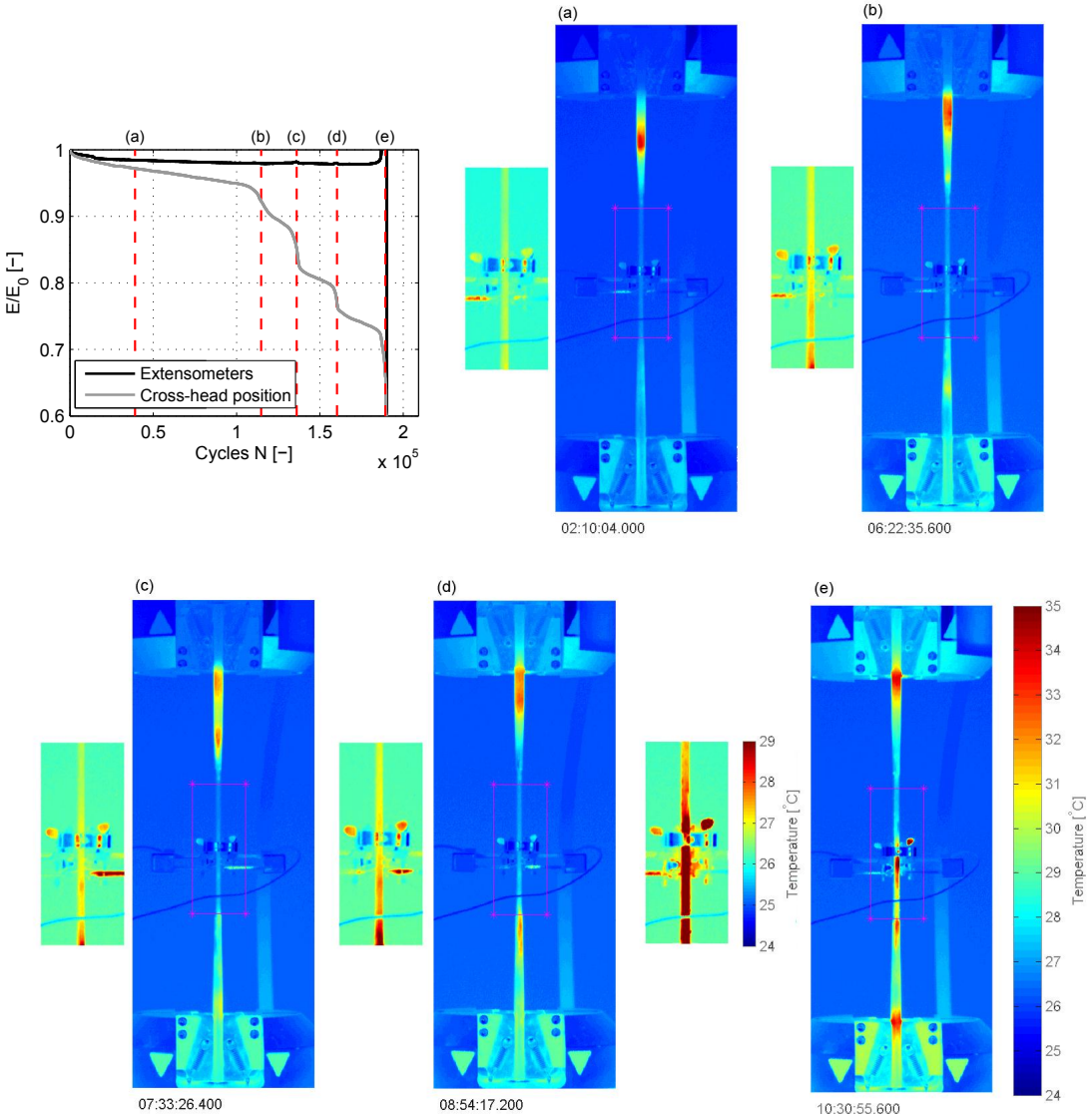

Figure 4.11: Global and local temperature development as function of stiffness degradation at selected load cycles for butterfly geometry sample 05, Fig. 4.6(b). The gauge region is magnified, and the number below each global temperature image denotes the test time (hh:mm:sec). The temperature colourbar valid for all the global and local temperature variations, is shown in sub-figure (e). A movie clip entitled `JZAN_Temp_GPV_05_Butterfly` showing the temperature development as function of stiffness degradation can be found from the DTU Research Information System, Orbit. See footnote 1 on page 27 for description of the accessibility.

A comparison between Figs. 4.10 and 4.11 yields that the temperature develops differently for the various geometries. The ISO geometry, Fig. 4.10, shows constant temperature and heating of the material inside the clamping section as a function of number of applied cycles. Since the material is constrained inside the clamps, it is likely that the heating (due to the damage) occurring inside the clamps cannot be monitored by the cross-head position, reflected in the smooth stiffness degradation curves in Fig. 4.8(a). On the other hand, the butterfly geometry, Fig. 4.11, shows a rapid increase in compliance occurring as a consequence of heating in the tab region outside the clamping section. The increase in compliance is consistent for all butterfly samples considered, see e.g. the stiffness degradation curves in Fig. 4.8(b). The rapid increase in compliance is related to propagating heat waves arising due to delamination and/or debonding in the tab region (more clearly seen on the movie clips). For both geometries, the temperature in the gauge region is somewhat constant. The temperature rise of the lower clamping device, is caused by the moving actuator. Selected regions of interest (ROI's) are analysed in order to investigate the local temperature development as function of load cycles. Fig. 4.12 shows the heat development within the clamps and in the gauge region as function of load-cycles. Post failure data is included to show the temperature drop after final failure.

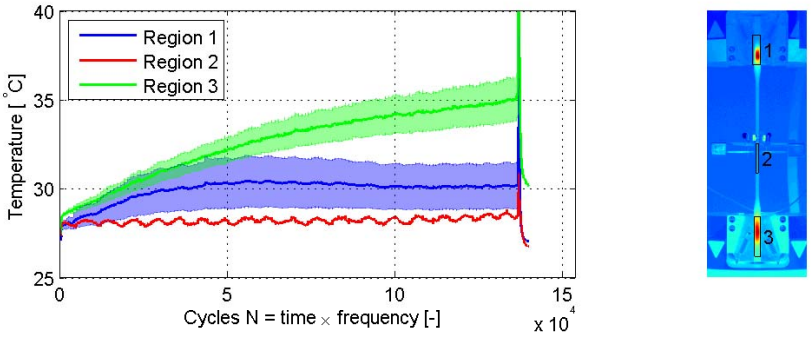

(a) ISO-geometry, Fig. 4.6(a).

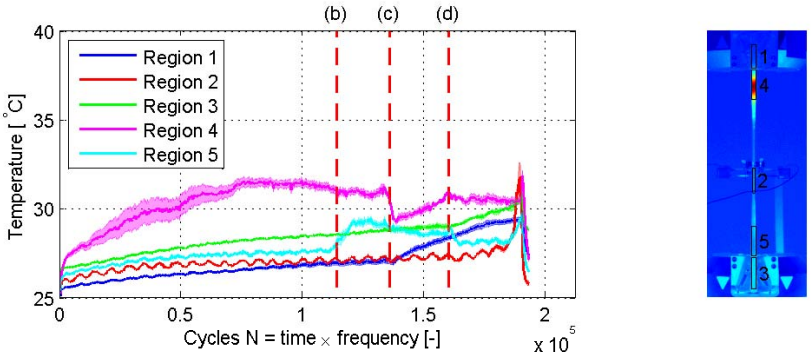

(b) Butterfly-geometry, Fig. 4.6(b). The dashed red lines marked (b)-(d) refer to the corresponding markers on the stiffness degradation curve shown in Fig. 4.11.

Figure 4.12: Temperature development in specific regions of interest as function of load cycles for different test geometries considered. Solid lines represent the mean temperature within the region, and the shaded region marks the measured standard deviation. Region 1: upper grip, region 2: gauge area, and region 3: lower grip. For the butterfly geometry, region 4: below upper grip, and region 5: above lower grip.

The ISO geometry, Fig. 4.12(a), shows continuous increasing heat development until failure in the lower clamp. The temperature in the ROI's in the gauge region and upper clamp seem to stagnate and remain constant as function of applied cycles. Considering the ROI's in the clamps for the butterfly geometry, Fig. 4.12(b), the temperature scatter is significantly reduced, and the heat development and maximum temperature are less compared to the ISO geometry. Near failure, the ROI in the upper clamp heats up. The butterfly geometry shows heating outside the grip section in the tab area, and these ROI's are shown as well in Fig. 4.12(b). With reference to Fig. 4.11, the locations for rapid increase in compliance are marked by the dashed red lines in Fig. 4.12(b). In Fig. 4.12(b), it is observed that the compliance increases are related to temperature variations outside the clamping section in the tab area (regions 4 and/or 5). Continuous surface temperature rise as function of load-cycles, as in Fig. 4.12(a), has also been reported by Gagel et al. [63].
When considering Fig. 4.12, one should keep in mind that temperature variations within the material are associated to two different mechanisms: (1) hysteresis, which is accumulated and irreversible, (2) thermoelastic effect, which is proportional to the load applied. For both geometries, the continuous temperature increase in the clamping section is related to hysteresis and irreversible damage, and final failure also occur in the tab region (see e.g. Fig. 4.9). The gauge region of the specimens (ROI 2 in Fig. 4.12) seems to experience a fluctuating temperature with constant mean as function of load cycles. This fluctuation is related to the thermoelastic response as a consequence of the applied stress. Due to the sampling period of the thermographic images, the wavelength appears larger than what is actually the case. According to Stanley & Chan [77], the temperature change in an orthotropic material as a consequence of the applied stress, is expressed as:

$$\Delta T = -\frac{T}{\rho\, C_p}(\alpha_1 \Delta\sigma_1 + \alpha_2 \Delta\sigma_2) \tag{4.3}$$

where ΔT is the temperature oscillation, T is the absolute surface temperature of the material, ρ is the material density, C_p is the specific heat capacity, α_i are the coefficients of thermal expansion in the two principal material directions $i = 1, 2$, and $\Delta\sigma_i$ are the amplitudes of the principal stresses. For the experiment analysed above using thermography, the only present stress range is $\Delta\sigma_1 = \sigma_{\max}(1-R) = E_0\varepsilon_{\max}(1-R) \simeq 47 \cdot 10^3\, 0.008(1-0.1) \simeq 338\,\text{MPa}$ with an average surface temperature, T, given in Fig. 4.12. Fruehmann et al. [78] considered a thermoelastic stress analysis based on a woven glass-fibre-reinforced epoxy composite, and came up with the following parameters: $\rho = 1980\,\text{kg/m}^3$, $C_p = 828\,\text{J/kg K}$, and $\alpha_1 = 8.54 \cdot 10^{-6}\,1/\text{K}$. It is noted that these parameters are valid for a woven composite, but assuming they can be used for the present material, Eq. (4.3) yields a temperature fluctuation in the range around $\Delta T = 0.5^\circ$ C. By comparison with the magnitude of the temperature oscillation of ROI 2 in Fig. 4.12, this value for ΔT seems to be in similar range where the oscillation is approximately $\Delta T \simeq 0.35^\circ$ C.

4.4.4 Summary

The life-time and damage (heat) evolution in tension-tension fatigue have been evaluated for two different test geometries. The exponent of the SN-curve varies in favour for the ISO geometry, which is most likely caused by the limited number of experiments.

Quantitative measurements using thermovision demonstrate the need for improving test geometries for tension-tension fatigue test since failure occurs outside the gauge region. The true life-time of the material is therefore not obtained. Even though an improved butterfly test specimen provides a larger life-time at the most frequent analysed maximum strain, it appears that failure still does not occur in the gauge section. The individual life-time scatter is caused by differences in the heat development during the test, and more research is needed to document this statement. In order to design a consistent test geometry that allows for the real material characteristics to be measured, the damage modes and origin of heat development of the specimen must be understood and described. For instance, the stress concentration near and between the end tab and the specimen has been analysed by Aslan [75]. Recently and ongoing research at the institute is focussed on numerical modelling and prediction of the stress field due to clamping, Mikkelsen and Bech [76]. Future studies will hopefully provide some of the answers to the problems related to the design of fatigue test specimens.

4.5 Stress analysis

4.5.1 Introduction and motivation

[P4] shows an experimental study on tension-tension fatigue damage propagation of a NCF, and the transverse backing layer is demonstrated to initialise fatigue failure. In order to evaluate the stress field causing transverse cracking in the backing bundle during fatigue, a simple stress analysis is carried out using finite elements for two different cases: un-cracked and cracked transverse backing bundle. The intention is to provide basic understanding regarding the stress distribution in the backing layer with regards to the damage modes observed in tension-tension fatigue. The finite element calculations are carried out in the commercial code ABAQUS 6.11.

4.5.2 Un-cracked backing bundle

The stress analysis of the un-cracked NCF material, is based on the unit cell approach. The discretised unit cell presented in [P4] is used to model the material, and a sketch of the unit cell is seen in Fig. 4.13.

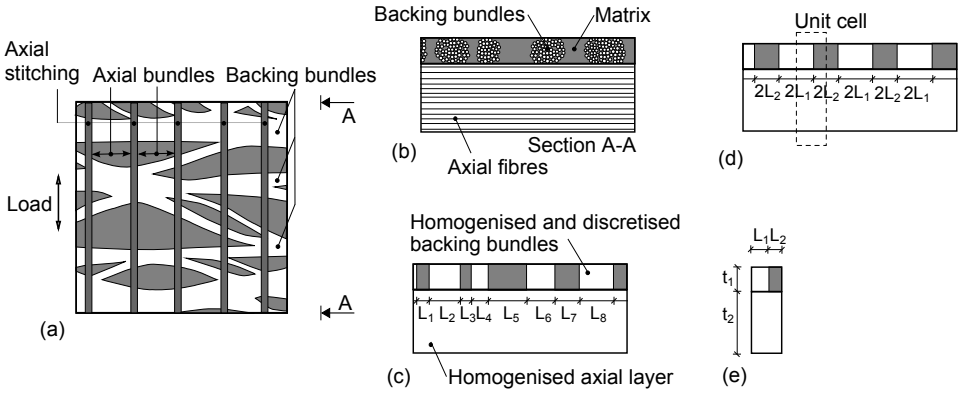

Figure 4.13: Homogenisation and sketch of unit cell representation of un-cracked non-crimp fabric (not to scale). (a) Top view of fabric architecture, cf. Fig. 3.2(b). (b) Longitudinal section. (c) Homogenisation of fibrous layers. (d) Generalisation and discretisation of geometry. (e) Unit cell representation.

The unit cell is based on homogenised properties of the fibrous layers, and discretised so that the backing bundles are separated with equidistant distance. However, by coupling several unit cells in series with different lengths, the non-discretised model, Fig. 4.13(c), can be replicated. The mechanical properties and boundary conditions of the unit cell are shown in Fig. 4.14.

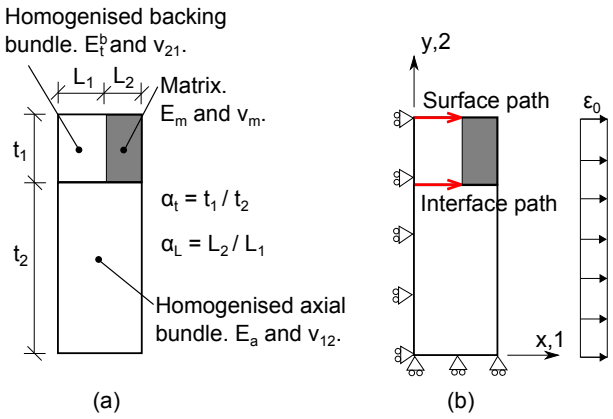

Figure 4.14: Unit cell for stress analysis of un-cracked backing bundle, see also [P4]. The axial fibres are oriented in horizontal direction, and transverse backing fibres are oriented out-of-plane. (a) Geometry and constituents. (b) Boundary conditions, load, and paths for determination of stresses.

It is chosen to consider a unit cell with the backing layer oriented towards a free surface, e.g. as the case for the surface bundles analysed in [P4]. This means that the boundary conditions are imposed as shown in Fig. 4.14(b). If the unit cell is surrounded by other material layers, e.g. as the interior bundles in [P4], the adjacent layers provide a constraint, and the boundary conditions must be re-evaluated. A uniform displacement (strain) is applied to the unit cell. The geometry of the unit cell is set up as follows. The thickness ratio, $\alpha_t = {}^{t_1}/_{t_2}$, is taken independent on the FVF, and is determined as the ratio between the area weight of the different fibre layers, i.e. $\alpha_t = 60/1322 = 0.05$ cf. Table 3.1. The thickness of the axial layer, t_2, is estimated using Eq. (4.2) on page 39 for a given FVF, and thereby $t_1 = t_2\alpha_t$. In order to determine the length of the backing bundle, L_1, the average fibre area, A_b, of the dry backing bundle is estimated by multiplication of the linear density of the backing bundle, L_d, (see Table 3.1) with the backing fibre density, ρ_f^b. Based on the assumption of similar fibre volume fraction in the axial and backing bundles, the length of the backing bundle is:

$$L_1 = \frac{A_b}{t_1\, V_f} = \frac{L_d\, \rho_f^b}{t_1\, V_f} \tag{4.4}$$

The length of the matrix between the backing bundles, L_2, follows from a given value of $\alpha_L = {}^{L_2}/_{L_1}$. In analogy with [P4], the homogenised stiffness of the axial bundle, E_a, and backing bundle, E_t^b, are predicted using the rule of mixtures and the Halphin Tsai equation, respectively. All materials are modelled linear elastic with Young's modulus and Poisson's ratio. The matrix stiffness is $E_m = 3.3\,\text{GPa}$, and the fibre stiffness is $E_f^a =$

87.5 GPa and $E_f^b = 70$ GPa for the axial and backing fibres, respectively. For simplicity, Poisson's ratio is taken independent on the volume fraction with magnitude $\nu_{12} = \nu_{21} = 0.3$ for the homogenised backing and axial bundles, and $\nu_m = 0.35$ for the matrix. The fibre density is $\rho_f^a = 2.61\,\mathrm{g/cm^3}$ (axial) and $\rho_f^b = 2.55\,\mathrm{g/cm^3}$ (backing). Inputs in setting up the geometry of the model are the fibre volume fraction, V_f, and the length ratio, α_L, and a sketch is shown in Fig. 4.15 for two different unit cells.

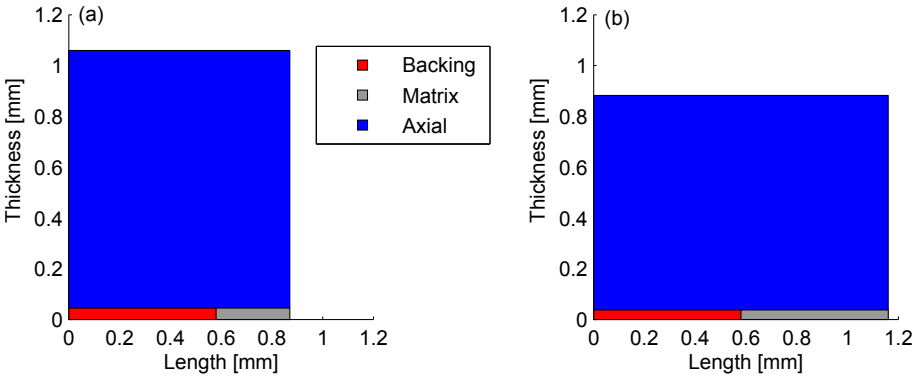

Figure 4.15: Sketch of unit cell geometries for varying fibre volume fraction and length. (a) $V_f = 50\,\%$, $\alpha_L = 0.5$. (b) $V_f = 60\,\%$, $\alpha_L = 1.0$.

Increasing the fibre volume fraction reduces the thickness of the unit cell, cf. Fig. 4.15. Due to the larger stiffness of the axial and backing bundles compared with the matrix, it is reasonable to assume that they provide an out-of-plane constraint on the less stiff matrix material. Thus, the matrix is modelled using a plane strain assumption (CPE4R, 4-node bilinear plane strain quadrilateral element with reduced integration and hourglass control) whereas the remaining materials are modelled under plane stress (CPS4R, 4-node bilinear plane stress quadrilateral element with reduced integration and hourglass control). A 2D model is used with increased mesh density in the vicinity between the different materials. The study is carried out as a linear static step, and no damage is included. The stress analysis is conducted for a varying length of the unit cell and fibre volume fraction considering the stress in the backing bundle, see e.g. the stress paths in Fig. 4.14(b). Along the interface between the backing and axial bundles, the following stresses are evaluated: normal (σ_{22}) due to the risk of interface debonding, shear (σ_{12}) due to the stress transfer between the layers, and axial (σ_{11}) due to the risk of transverse cracking. At the surface, the axial stress is also evaluated for comparison to the interfacial stress. The stress results are presented in Fig. 4.16 for a varying fibre volume fraction and length of the unit cell. The stress components are normalised with the far field stress in the axial bundle, $\sigma_0 = E_a\varepsilon_0$.

With reference to Fig. 4.16, the following observations are done. The shear stress, σ_{12}, along the interface has its maximum in the vicinity close to the matrix rich area in-between the backing bundles. Over a certain shear transfer length, the shear stress is transferred into axial stress in the backing bundle. The maximum shear stress increases for larger FVF, and is independent on the length of the unit cell. During tension fatigue, transverse cracks emerge in the backing bundle in a somewhat regular spaced pattern, [P4]. At some point, the shear transfer length becomes diminishing due to the crack spac-

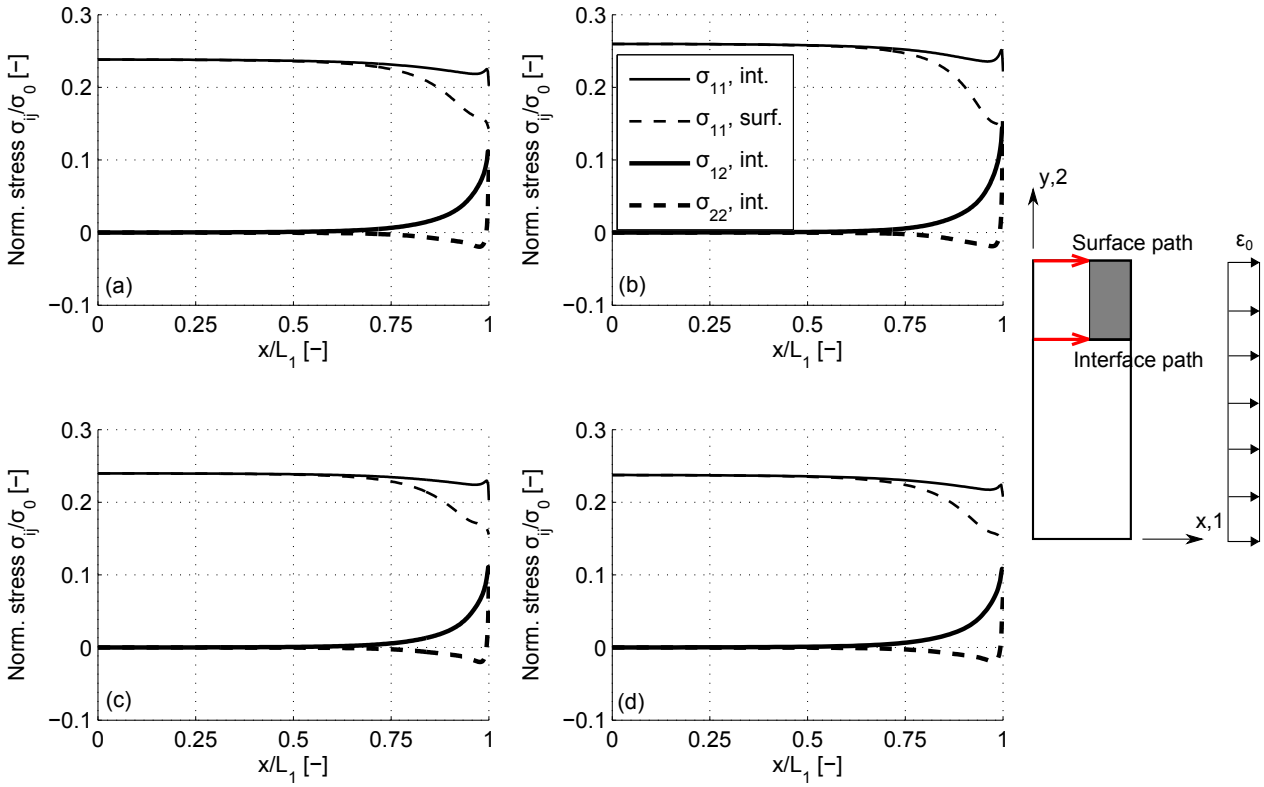

Figure 4.16: Selected stress components along the paths shown in Fig. 4.14(b) for varying fibre volume fraction and length of the unit cell. Results are normalised with the far field stress in the axial layer, $\sigma_0 = E_a\varepsilon_0$. (a) $V_f = 50\,\%$, $\alpha_L = 0.5$. (b) $V_f = 60\,\%$, $\alpha_L = 0.5$. (c) $V_f = 50\,\%$, $\alpha_L = 0.1$. (d) $V_f = 50\,\%$, $\alpha_L = 2.0$.

ing, and the shear stress cannot be transferred any loner; thus, a crack saturation level is reached. The stress field in the cracked unit cell is investigated in the next section. The normal stress, σ_{22}, is diminishing or compressive along the entire interface, but in the vicinity close to the matrix, the stress is tensile. Depending on the properties of the interface, this might cause interface delamination. The magnitude of the normal stress is in similar range independent on the FVF and unit cell length. The axial stress, σ_{11}, builds up towards the centre of the backing bundle until a steady value of approximately $0.25\sigma_0$, which is the magnitude of the stiffness ratio between the backing and axial bundles. Increasing the FVF, slightly increases the axial stress, and the influence of a varying length is infinitesimal. This observation is consistent both along the interface and at the surface. The transverse tensile strength of a unidirectional composite is typically much lower than the longitudinal (approximately within 5%, Soden et al. [79]), thus the risk of transverse cracking is increased for larger FVF's due to the increased axial stress. The shapes of the stress components along the different paths, Fig. 4.16, are similar to the ones presented by Alfredsson et al. [80] considering a different material system with the same unit cell.

Based on the simple stress analysis provided above, the following statements are presented:

- Stresses are transferred to the backing bundles through shear along the interface.
- Increasing the FVF gives larger axial stresses in the backing bundle, and an increased risk of transverse cracking.
- In order to obtain a more uniform stress state, it is advantageous to spread out the backing fibres more evenly.

It is noted that the present analysis is performed for a linear static loading, and the stress field changes if damage occurs. For a cyclic load with a given stress magnitude and amplitude, Fig. 4.16 can be used to estimate selected stress components for a given unit cell.

4.5.3 Cracked backing bundle

In continuation to the previous analysis, the subsequent situation to consider is the cracked backing bundle. As in the previous section, a surface layer is considered for evaluation of the stress field, and it is assumed that the transverse cracking happens sequentially as function of applied load cycles. This sequence is illustrated in Fig. 4.17.

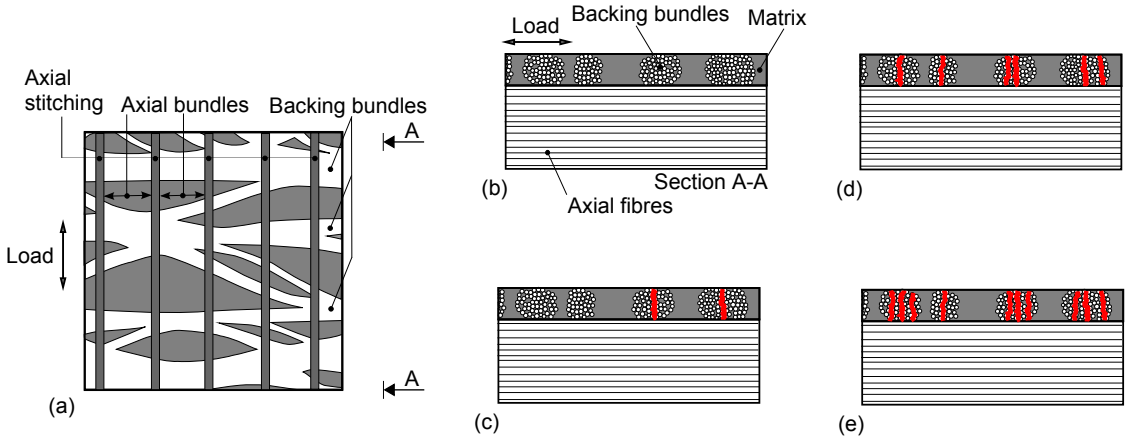

Figure 4.17: Sketch of transverse cracking sequence in backing bundle as a function of applied cycles, N, with $N_0 < N_1 < N_2 < N_3$. Transverse cracks are illustrated in red. (a) Top view of fabric architecture, see e.g. Fig. 3.2(b). (b) Intact, $N = N_0$. (c) Initialisation, $N = N_1$. (d) Propagation, $N = N_2$. (e) Saturation, $N = N_3$.

As shown schematically in Fig. 4.17, transverse cracking happens sequentially as function of applied cycles. The crack density increases as function of load cycles until a saturation level is reached. In order to model this behaviour numerically, a representative unit cell of the transverse cracking sequence is established, see Fig. 4.18. The cracked unit cell is somewhat similar to the ones used e.g. by Xia et al. [81] and Lundmark & Varna [82].

Idealised, transverse cracking occurs as a schematic sequence; thus, causing a systematic reduction in the length of the unit cell. Practically in the numerical model, this is achieved

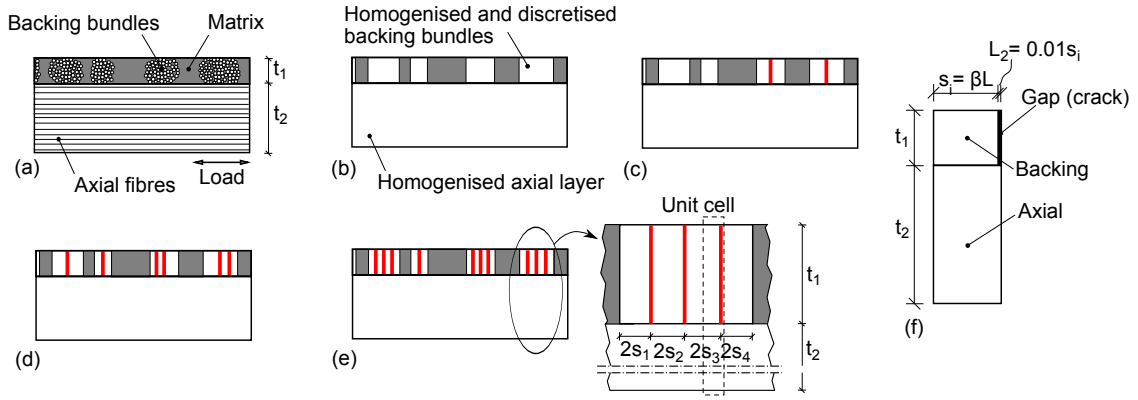

Figure 4.18: Sketch of unit cell representation of idealised transverse cracking sequence in backing bundle as a function of applied cycles, N, with $N_0 < N_1 < N_2 < N_3$. Transverse cracks are illustrated in red, see also Fig. 4.17 for comparison. (a) Longitudinal section of fabric architecture. (b) Homogenisation and discretisation. Intact, $N = N_0$. (c) Initialisation, $N = N_1$. (d) Propagation, $N = N_2$. (e) Saturation, $N = N_3$ and representative unit cell. (f) Unit cell geometry.

by introducing a length reduction factor, β, varying from 4 (large crack spacing, pseudo un-cracked) to 0.05 (small crack spacing, saturation). In the present investigation, it is chosen to fix the values for the material properties, and a FVF equal to 0.5 is used. The mechanical properties of the individual constituents are determined based on homogenisation techniques. The thickness t_1 and t_2, and initial length of the unit cell, L, are found as outlined in the previous section and in [P4]. This leads to an initial default length of the unit cell $L = 0.58\,\text{mm}$, which is comparable to the extension of the backing layer shown in Fig. 4.15(a). It is observed that the unit cell representation of the cracked configuration, Fig. 4.18(f), is remarkably similar to the un-cracked configuration, Fig. 4.14(a), if the length of the matrix is taken infinitesimal compared to the extension of the entire unit cell. In the numerical model, the transverse crack is modelled as a gap with properties, geometry, and boundary condition as shown in Fig. 4.19.

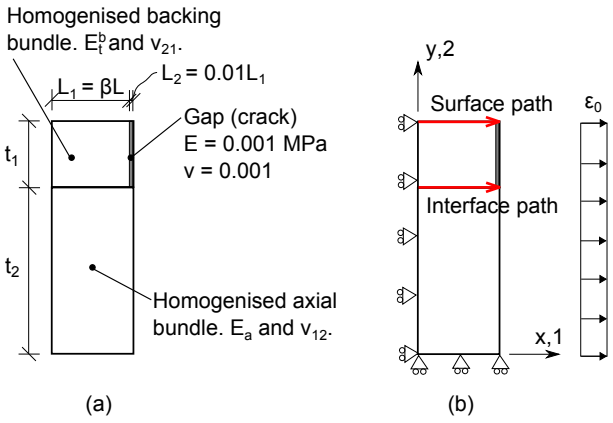

Figure 4.19: Unit cell for stress analysis of cracked backing bundle. The axial fibres are oriented in horizontal direction, and transverse backing fibres are oriented out-of-plane. (a) Geometry and constituents. (b) Boundary conditions, load, and paths for determination of stresses.

Two selected stress components are evaluated for the cracked unit cell along the different paths: the shear stress is determined in the vicinity of the interface between the two layers, and the axial stress along the surface. The axial stress at the surface is used since this causes transverse cracking. Furthermore, the compliance of the unit cell is determined numerically as function of crack density. The compliance is determined using a node-set along the boundary at $x = 0$ to extract the reaction force in the x-direction, which can be converted to compliance by Hooke's law and the magnitude of the applied strain. The result of the stress analysis is shown in Fig. 4.20.

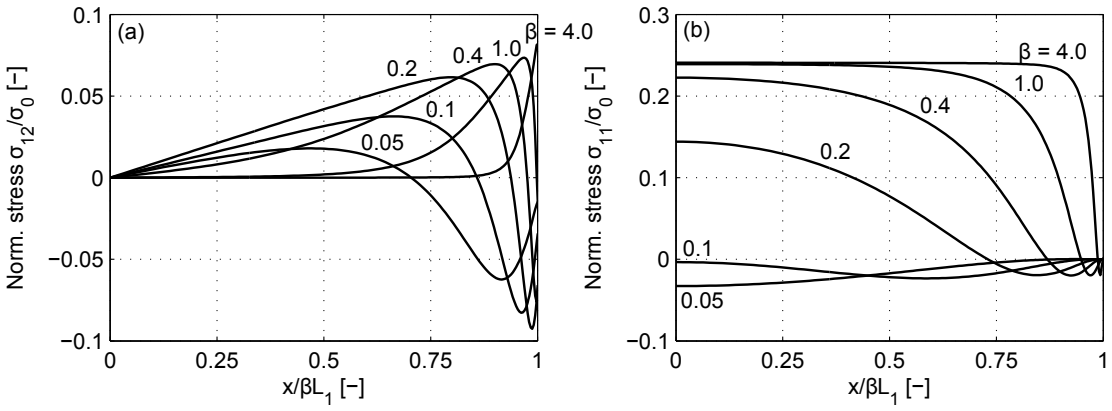

Figure 4.20: Stress analysis of cracked unit cell. The crack spacing is reflected in the length reduction factor β. Results are normalised with the far field stress in the axial layer, $\sigma_0 = E_a\varepsilon_0$. (a) Shear stress, σ_{12}, in the vicinity of the interface. (b) Axial stress, σ_{11}, along the surface path.

The shear stress along the interface for the cracked backing bundle, Fig. 4.20(a), shows that for a 'long' unit cell ($\beta > 1.0$) there is a certain shear transfer length that allows for the stress to build up in the backing bundle. For $\beta < 0.4$, the shear stress cannot be transferred completely into the backing bundle, and the shape of the shear stress curve changes and flattens. Fig. 4.20(b) shows that the axial stress at the surface in the centre of the bundle is diminishing for $\beta < 0.2$, otherwise constant. For this value of β it is therefore expected that no further cracking of the backing bundle can occur. For $\beta = 0.1$ and 0.2, the corresponding normalised crack density is in the range $s_{norm} = \frac{t_1}{2\beta L_1} \simeq 0.2 - 0.4$, which is in the same order of magnitude as reported experimentally in [P4] where $s_{norm} \simeq 0.3$ for a surface bundle.

The normalised compliance as function of normalised crack density is presented in Fig. 4.21. At crack saturation, the limit for the normalised compliance is determined as:

$$\frac{C}{C_0} = \frac{E_0}{E_{crack}} = \frac{E_a t_2 + E_t^b t_1}{t_1 + t_2} \frac{t_1 + t_2}{E_a t_2} = 1 + \frac{E_t^b}{E_a} \frac{t_1}{t_2} \tag{4.5}$$

where the stiffness and geometry terms are defined in Fig. 4.19. Eq. (4.5) is also referred to as the ply discount model, see Tsai [83] and for instance Mattsson et al. [62].

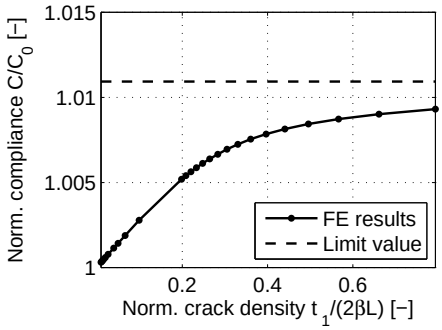

Figure 4.21: Numerical prediction of the unit cell compliance as function of normalised crack density.

For increasing crack spacing, Fig. 4.21 shows that the compliance increases; first in a linear manner, secondly in a non-linear manner. The shape of the curve seems to be in line with analytical predictions by Joffe & Varna [84] and Hansen [85]. Since the FE-model is elastic, there will always be some stress transfer between the layers, and the crack saturation level is likely never reached. Based on experimental fatigue tested samples, [P4] determined the normalised crack spacing at saturation in the range around 0.3-0.4. Taken into account the simplistic FE-model, idealisation and variations of the material properties, and the statistical variations in the crack spacing measurements, there seems to be agreement between the predicted compliance in Fig. 4.21 and the experimentally measured crack saturation level.

4.5.4 Prediction of transverse crack spacing

The spring model developed in [P4] to analyse the stiffness of the unit cell shown in Fig. 4.14(a), is in the following used to predict the transverse crack spacing for different fibre volume fractions of the composite laminate. As explained in [P4], the spring model is used to estimate the compliance of the laminate at full crack saturation. The compliance (or stiffness decrease) predicted by the spring model seems to correlate with the experimentally observed stiffness degradation during stage I of a fatigue experiment, [P4]. If the stiffness of the backing bundle in Fig. 4.14(a) is lost, this corresponds to crack saturation of the layer. Using the spring model to describe this behaviour, the associated normalised compliance is plotted in Fig. 4.22 as function of the FVF.

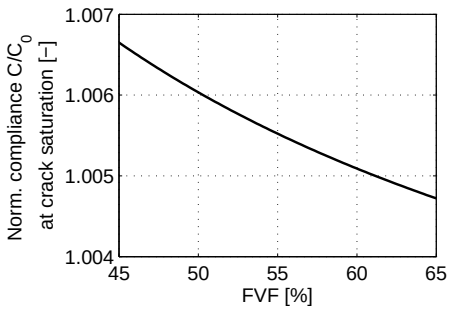

Figure 4.22: Spring model prediction of unit cell compliance at crack saturation as function of fibre volume fraction.

Assuming that the normalised compliance obtained from the spring model, Fig. 4.22, can be coupled to the generic numerical prediction for the transverse crack spacing, Fig. 4.21, it is possible to obtain an estimate on the normalised transverse crack spacing for a varying fibre volume fraction of the laminate. The estimate is shown in Fig. 4.23.

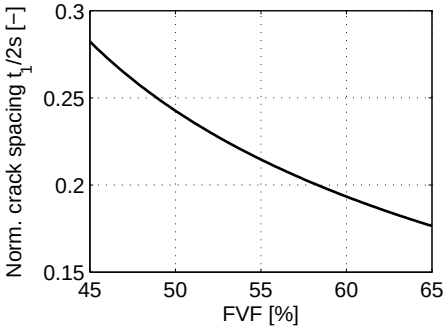

Figure 4.23: Estimate of normalised transverse crack spacing at saturation as function of fibre volume fraction.

The crack spacing at saturation is decreasing as function of the fibre volume fraction, Fig. 4.23, which is likely caused by the increase in stiffness of the constituents, see also Hansen [85]. The result presented in Fig. 4.23 serves a first estimate on the crack spacing at saturation for a surface bundle, and additional experimental or advanced numerical calculations should be used to verify the estimate.

4.5.5 Summary

A simple stress analysis using finite elements is used to investigate the stress field of an un-cracked and cracked backing bundle in a NCF composite in order to describe the damage onset observed in tension-tension fatigue experiments. Stresses are transferred from the stiff axial fibre bundle into the backing bundle through shear along the interface. Depending on the extension of the backing bundle, axial stresses build up towards the centre of the bundle. These axial stresses cause transverse cracking of the bundle, and it is demonstrated that the axial stresses are diminishing as the crack spacing is decreased. The compliance of the cracked unit cell is used to provide an estimate on the saturated crack spacing as function of the fibre volume fraction of the laminate. Even though simplistic finite element models are used, the transverse cracking sequence can be predicted with reasonable accuracy in comparison to the experimental data available. Due to the lack of reliable and suitable material properties for the composite analysed, it has not been possible to evaluate the transverse cracking using analytical models like for instance Joffe & Varna [84] or Hansen [85].

4.6 Discussion on fibre architecture

The previous sections have investigated different aspects of tension fatigue damage in unidirectional materials made of NCF's for wind turbine blades. Transverse cracking of

the backing bundle is demonstrated to be the first mode of failure in tension-tension fatigue, [P4], and it is thus important to overcome this damage mode. The following section is based on ideas and observations made during the study, and should be taken as instructive regarding future improvements of the fibre architecture of NCF's in relation to tension-tension fatigue.

Interlaminar shear stresses and the transverse crack density are reduced if an interleaf is applied between the transverse backing and axial layers, see e.g. Hansen [85] and Gillespie & Hansen [86]. Application of an interleaf can be difficult to overcome in a practical fabric design, but is accomplished if a thin compliant sheet is placed in-between the backing and axial layer.

Transverse cracking of the backing bundle is related to the stiffness and thickness of the layer, and an increased stiffness of the transverse layer decrease the onset stress of transverse cracking, Hansen [85]. Thus, it is recommended to use a more compliant material for the backing fibres. The onset strain of transverse cracking may also be lowered if the thickness of the layer is reduced. However, the improvement of a reduced thickness is minor, and can be difficult to accomplish in reality (see also discussion in [P5]).

For the present material used, the backing fibres are oriented in ± 80 deg, and it is likely that there exists an optimum orientation of the backing fibres in order to minimise transverse cracking. Opening stresses causing transverse cracking are reduced if the orientation is $\theta = \pm 45$ deg, and finding the optimum orientation requires a more thorough study since the damage mode for an off-axis ply might be different compared to cross-ply. Vinogradov & Hashin [87] recently proposed an approach based on variational calculus to deal with the stiffness reduction of cracked off-axis laminates.

Using the material data from the commercially available AS4/3501-6 unidirectional carbon/epoxy prepreg composite, Nairn [88], investigated transverse crack density development for static loading of cross-ply laminates with different layer thickness. The main results are reproduced in Fig. 4.24.

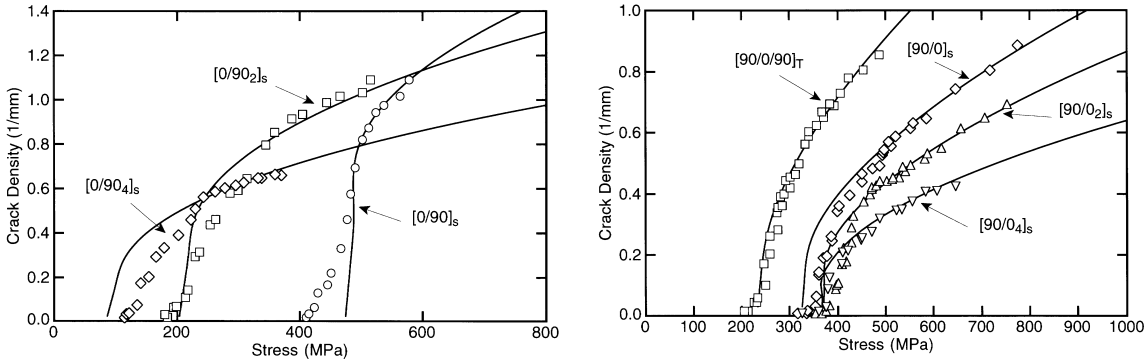

(a) $[0/90_m]_s$. (b) $[90/0_m]_s$.

Figure 4.24: Transverse crack density as function of macroscopic stress. The material is AS4/3501-6 with different laminate configurations. Solid lines denote the model predictions using a variational approach, Nairn [89] and Nairn and Hu [90]. From [88].

Depending on the stacking sequence and thickness of the cross-ply laminate, the crack evolution is different in terms of the applied macroscopic stress. For $[0/90_m]_s$ laminates, Fig. 4.24(a), the initiation stress drops when the thickness of the transverse layer is increasing, and the crack density at saturation is less for larger thickness of the 90deg ply (inversely related to the thickness). However, one should keep in mind that the results change if the crack density is plotted against applied strain, which will likely collapse the curves in Fig. 4.24(a) due to the varying stiffness. For $[90/0_m]_s$ laminates, Fig. 4.24(b), the onset of transverse cracking is almost identical with slower propagation, indicating that transverse cracking is somewhat unaffected by the increase in stiffness of the UD layer.

The stacking sequence of the unidirectional NCF influences the tension-tension fatigue behaviour (see also Sec. 4.3 on page 38). This is likely linked to the onset of transverse cracking presented in Fig. 4.24. The recommendations with regards to the stacking sequence are therefore, both in relation to static and cyclic loading;

- backing layers should not be placed in contact to each other,
- the backing layer should be located symmetrically around the centre orientated towards the free surface of the specimen,
- the initiation stress for transverse cracking is dependent on the backing bundle thickness, and the thickness of the backing bundle should be minimized.

In addition, new tension-tension fatigue test geometries and methodologies are needed in order to avoid unwanted failure occurring outside the gauge region.

Transverse cracking of the backing layer is not controlled by the stiffness of the unidirectional axial layer, see e.g. Hansen [85]. Thus, the stiffness of the axial fibres can be altered, e.g. by an improved glass type, without a significant impact on the transverse cracking.

The bonding between fibre and matrix should be altered to allow for more energy to be dissipated during fatigue. This can be done by a tailored sizing that is designed to the specific fibre-matrix system. Residual stresses (volumetric shrinkage of the matrix) and fibre debonding are critical concerning the onset of transverse cracking in polyester based matrices, see also [P4].

Chapter 5

Conclusion

The present thesis has explored the effects of fibre architecture on the tension-tension fatigue life-time of unidirectional glass fibre reinforced composite materials used in the main laminate of a wind turbine rotor blade. Studies on the fibre architecture and fatigue life-time are the two consistent central themes throughout the thesis.

A new methodology is developed to characterise the internal microstructure of fibre bundles in a non-crimp fabric composite. This methodology is applied to analysis of composite laminates, and a numerical tool for generation and simulation of statistically representative volume elements of composite microstructures is developed. The microstructure generator is shown to produce statistically equivalent microstructures. Through a parametric variation of the fibre radii distribution, it is demonstrated that the spatial statistics of the fibre packing pattern are unaffected by any variations in the fibre radii distribution. The microstructure generator is used to determine the minimum size of a statistically representative volume element based on the spatial point pattern statistics of the fibres. As a practical example, the characterisation methodology developed, is utilised to examine the hierarchical microstructure of a non-crimp fabric in terms of variations in the fibre volume fraction at different material length scales. It is illustrated that the fibre volume fraction is dependent on the length scale considered, and the fibre volume fractions at the different length scales are interconnected. The non-destructive technique of micro computed tomography, is utilised in a preliminary study to evaluate the three dimensional fibre misalignment in the unidirectional fibre composite. Both fibre misalignment and waviness are present, and these imperfections have an unfavourable effect on the mechanical properties, which must be further explored.

The experimental framework of the thesis consists of different configurations where the fibre architecture and fatigue life-time are linked together. The major finding is that fatigue damage initialisation and propagation of non-crimp fabrics are identified and explained. Damage initiates as cracks in the transverse backing bundles, which cause a stress singularity in the axial load-carrying fibres leading to cyclic damage propagation, eventually causing failure. The onset of fatigue damage, in terms of transverse cracking, is clarified by a stress analysis using a linear elastic finite element simulation. The influence of fibre content, stacking sequence, and test specimen geometry on the fatigue

life-time, is examined in experimental studies. It is shown that increasing the fibre content reduces the life-time, which is coupled to the internal microstructure of the material. Recommendations regarding the stacking sequence of the individual plies are provided in order to obtain improved life-time. Thermovision is used as a measuring technique to quantify the scatter and difference in fatigue life-time for various test geometries. The often observed life-time scatter in composites fatigue testing, is explained in terms of different heat developments during the fatigue experiment. It is also high-lighted that improvements in the test geometry are needed.

Throughout the thesis, insight is provided regarding the microstructure, fibre architecture, and tension fatigue characteristics of non-crimp composite materials. The knowledge acquired, is collected in a survey covering the design process of a non-crimp fabric composite preform suitable for wind turbine rotor blade application.

The findings of the present work serve as a step on the way for development of more fatigue resistant composite materials for future wind turbine rotor blades. Advanced quantification tools and methodologies are provided as well as a comprehensive presentation of tension fatigue experiments. The perspective of the study is to implement an improved fabric architecture in future non-crimp preforms.

5.1 Outlook

The study leaves out a number of unsettled points for future work, and this section lists some ideas for coming research efforts related to the present.

Fatigue of composites

The study has investigated and clarified tension-tension fatigue damage evolution of unidirectional glass fibre reinforced composites manufactured of non-crimp fabrics. A natural extension to the present work, is to consider the fatigue life-time with respect to: the assessment of load ratios (R-ratio, stress level), load conditions (test frequency, load waveform, varying amplitude/block loading, block sequence dependency), load type (tension-compression, compression-compression, multiaxial), high-cycle characteristics, different layups and fabrics, and climatic test conditions . Even though much scientific effort has already been put in these fields, an unified overview and explanation remain for the actual cause of fatigue damage of composites.

Unit cell modelling

The numerical microstructure generator developed and the three dimensional microstructural characterisation serve as obvious candidates for assistance in numerical finite element modelling of statistically representative volume elements. Using the unit cell approach, fatigue damage propagation can be modelled by cyclic cohesive laws for the fibre/matrix interface, stochastic strength properties for the constituents, and damage and non-linear material behaviour. On top of this, one can add the suggestions provided above with respect to fatigue, which complicate the problem even further. Numerical

modelling of fatigue of composites is a cumbersome and challenging task, which requires tremendous computational efforts, and a proper modelling strategy still remains. This raises the interesting question whether it is better to perform experiments that are difficult to make but easy to model and interpret, rather than experiments that are easy to make and difficult to model.

Materials and design

A long way is still to come before the knowledge gained can be adopted in common wind turbine blade design. Based on the ideas for a new modified non-crimp fabric architecture, the fabric must be designed completely, manufactured, tested, evaluated, and certified. Then, implemented in the current blade technology, and tested in full scale. Along the way, there are many obstacles; for instance, the manufacturing and processing defects, material imperfections, and inhomogeneities, which must be described and understood.

At current, new material systems like composite hybrids are entering the blade industry, and it is of interest to explore the potential of these new systems. For instance, carbon fibres are prone to microbucking in compression, and the fibre misalignment is therefore important.

Guidelines for blade materials today prescribe design in the linear range of the materials, and there is an unexplored potential of the load capacity outside the linear region (or even to consider non-linear elasticity). Furthermore, the stochastic nature of composite properties is handled with the outmoded method of partial safety factors. With the computational capacity present, it is likely that probabilistic methods form the basis for future wind turbine rotor blade designs.

Bibliography

[1] European Wind Energy Association. Pure power - wind energy targets for 2020 and 2030. *EWEA*, 2009.

[2] T. K. Jacobsen. Materials technology for large wind turbine rotor blades - limits and challenges. In *Proceedings of the 32nd Risø International Symposium on Materials Science*, pages 35–45, Risø DTU, 2011.

[3] Z. Hashin. Analysis of composite materials. *Journal of applied mechanics*, 50(2):481–505, 1983.

[4] R. M. Jones. *Mechanics of composite materials*. Taylor & Francis, 2nd edition, 1999.

[5] A. R Bunsell and J. Renard. *Fundamentals of fibre reinforced composite materials*. Institute of Physics Publishing, 1st edition, 2005.

[6] T. W. Chou. *Microstructural design of fiber composites*. Cambridge University Press, 2005.

[7] C. Decolon. *Analysis of Composite Structures*. Kogan Page Science, 2002.

[8] B. W. Rosen. Mechanics of composite strengthening. In *Fiber composite materials*, pages 37–65. American Society for Metals Seminar, 1965.

[9] S. M. de Azeredo Lopes. *Statistical analysis of particle distributions in composite materials*. PhD thesis, University of Sheffield, 2000.

[10] S. Ghosh, Z. Nowak, and K. Lee. Quantitative characterization and modeling of composite microstructures by voronoi cells. *Acta materialia*, 45(6):2215–2234, 1997.

[11] R. Pyrz. Quantitative description of the microstructure of composites. Part I: Morphology of unidirectional composite systems. *Composites science and technology*, 50(2):197–208, 1994.

[12] J. Summerscales. *Microstructural characterisation of fibre-reinforced composites*. Woodhead Publishing, 1998.

[13] J. G. McGowan, R. W. Hyers, K. L. Sullivan, J. F. Manwell, S. V. Nair, B. McNiff, and B. C. Syrett. A review of materials degradation in utility scale wind turbines. *Energy materials: materials science and engineering for energy systems*, 2(1):41–64, 2007.

[14] B. Hayman, J. Wedel-Heinen, and P. Brøndsted. Materials challenges in present and future wind energy. *Warrendale: materials research society*, 33(4):343–535, 2008.

[15] P. J. Schubel and R. J. Crossley. Wind turbine blade design review. *Wind engineering*, 36(4):365–388, 2012.

[16] G. Galilei. *Discorsi e dimostrazioni matematiche, intorno à due nuove scienze*. 1638.

[17] P. Brøndsted, H. Lilholt, and A. Lystrup. Composite materials for wind power turbine blades. *Annual review of materials research*, 35:505–538, 2005.

[18] P. S. Veers, T. D. Ashwill, H. J. Sutherland, D. L. Laird, D. W. Lobitz, D. A. Griffin, J. F. Mandell, W. D. Musial, K. Jackson, and M. Zuteck. Trends in the design, manufacture and evaluation of wind turbine blades. *Wind energy*, 6(3):245–259, 2003.

[19] J. F. Manwell, J. G. McGowan, and A. L. Rogers. *Wind energy explained: theory, design and application*. John Wiley & Sons, 2010.

[20] Germanischer Lloyd. Guideline for the certification of wind turbines, 2010.

[21] R. P. L. Nijssen, A. M. van Wingerde, and D. R. V. van Delft. The OptiDAT materials fatigue database.

In *27th Risø International Symposium on Materials Science: Polymer Composite Materials for Wind Power Turbines*, pages 257–262, Risø National Laboratory, Roskilde, Denmark, 2006.

[22] http://www.wmc.eu/optimatblades_optidat.php. Knowledge centre WMC - optidat database, June 2013.

[23] J. F. Mandell, D. D. Samborsky, and D. Cairns. Fatigue of composite materials and substructures for wind turbine blades. Technical report, Sandia National Laboratories, 2002.

[24] J. Lemaitre and R. Desmorat. *Engineering damage mechanics: ductile, creep, fatigue and brittle failures*. Springer, 2005.

[25] P. Brøndsted, S. I. Andersen, and H. Lilholt. Fatigue performance of glass/polyester laminates and the monitoring of material degradation. *Mechanics of composite materials*, 32(1):21–29, 1996.

[26] R. P. L. Nijssen. *Fatigue life prediction and strength degradation of wind turbine rotor blade composites*. PhD thesis, Delft University of Technology, 2006.

[27] C. W. Kensche. Fatigue of composites for wind turbines. *International journal of fatigue*, 28(10):1363–1374, 2006.

[28] J. C. Marín, A. Barroso, F. París, and J. Cañas. Study of fatigue damage in wind turbine blades. *Engineering failure analysis*, 16(2):656–668, 2009.

[29] J. F. Mandell, D. D. Samborsky, P. Agastra, A. T. Sears, and T. J. Wilson. Analysis of SNL/MSU/DOE fatigue database trends for wind turbine blade materials. *Sandia Contractor Report, Sandia National Laboratories*, 2009.

[30] R. Talreja. Fatigue of composite materials: damage mechanisms and fatigue-life diagrams. *Proceedings of the royal society of London. Series A, mathematical and physical sciences*, 378(1775):461–475, 1981.

[31] R. M. McMeeking and A. G. Evans. Matrix fatigue cracking in fiber composites. *Mechanics of materials*, 9(3):217–227, 1990.

[32] H. El Kadi and F. Ellyin. Effect of stress ratio on the fatigue of unidirectional glass fibre/epoxy composite laminae. *Composites*, 25(10):917–924, 1994.

[33] E. K. Gamstedt and R. Talreja. Fatigue damage mechanisms in unidirectional carbon-fibre-reinforced plastics. *Journal of materials science*, 34(11):2535–2546, 1999.

[34] J. Degrieck and W. Van Paepegem. Fatigue damage modeling of fibre-reinforced composite materials: review. *Applied mechanics reviews*, 54(4):279–300, 2001.

[35] H. Mao and S. Mahadevan. Fatigue damage modelling of composite materials. *Composite structures*, 58(4):405–410, 2002.

[36] A. P. Vassilopoulos and T. Keller. *Fatigue of fiber-reinforced composites*. Springer, 2011.

[37] S. Torquato. Statistical description of microstructures. *Annual review of materials research*, 32(1):77–111, 2002.

[38] M. Kachanov and I. Sevostianov. On quantitative characterization of microstructures and effective properties. *International journal of solids and structures*, 42(2):309–336, 2005.

[39] S. W. Yurgartis. Techniques for the quantification of composite mesostructure. *Composites science and technology*, 53(2):145–154, 1995.

[40] B. Paluch. Analysis of geometric imperfections affecting the fibers in unidirectional composites. *Journal of composite materials*, 30(4):454, 1996.

[41] B. D. Ripley. The second-order analysis of stationary point processes. *Journal of applied probability*, 13(2):255–266, 1976.

[42] P. M. Dixon. Ripley's K function. In *Encyclopedia of environmetrics*. John Wiley & Sons, Ltd, 2006.

[43] R. Pyrz. Correlation of microstructure variability and local stress field in two-phase materials. *Materials science and engineering: A*, 177(1–2):253–259, 1994.

[44] P. Louis and A. M. Gokhale. Application of image analysis for characterization of spatial arrangements of features in microstructure. *Metallurgical and materials transactions A*, 26(6):1449–1456, 1995.

[45] Z. Shan and A. M. Gokhale. Representative volume element for non-uniform micro-structure. *Computational materials science*, 24(3):361–379, 2002.

[46] S. Swaminathan, S. Ghosh, and N. J. Pagano. Statistically equivalent representative volume elements for unidirectional composite microstructures: Part I-without damage. *Journal of composite materials*,

40(7):583, 2006.

[47] S. Swaminathan and S. Ghosh. Statistically equivalent representative volume elements for unidirectional composite microstructures: Part II-With interfacial debonding. *Journal of composite materials*, 40(7):605, 2006.

[48] D. Mattsson, R. Joffe, and J. Varna. Methodology for characterization of internal structure parameters governing performance in NCF composites. *Composites part B: engineering*, 38(1):44–57, 2007.

[49] S. V. Lomov. *Non-Crimp Fabric Composites: Manufacturing, Properties and Applications*. Woodhead Publishing, 2011.

[50] Y. Wei and J. Zhang. Characterization of microstructure in stitched unidirectional composite laminates. *Composites part A: applied science and manufacturing*, 39(5):815–824, 2008.

[51] I. Verpoest and S. V. Lomov. Virtual textile composites software WiseTex: integration with micromechanical, permeability and structural analysis. *Composites science and technology*, 65(15–16):2563–2574, 2005.

[52] N. Tessitore and A. Riccio. A novel FEM model for biaxial non-crimp fabric composite materials under tension. *Computers & structures*, 84(19–20):1200–1207, 2006.

[53] A. Petriccione, D. Annicchiarico, V. Antonucci, M. Giordano, A. Riccio, F. Scaramuzzino, and M. Zarrelli. A stiffness volume averaging based approach to model non-crimp fabric reinforced composites. *Composites science and technology*, 72(2):360–369, 2012.

[54] V. I. Kushch, S. V. Shmegera, P. Brøndsted, and L. Mishnaevsky. Numerical simulation of progressive debonding in fiber reinforced composite under transverse loading. *International journal of engineering science*, 49(1):17–29, 2011.

[55] M. R. Wisnom. The effect of fibre misalignment on the compressive strength of unidirectional carbon fibre/epoxy. *Composites*, 21(5):403–407, 1990.

[56] B. Budiansky and N. A. Fleck. Compressive failure of fibre composites. *Journal of the mechanics and physics of solids*, 41(1):183–211, 1993.

[57] S. W. Yurgartis. Measurement of small angle fiber misalignments in continuous fiber composites. *Composites science and technology*, 30(4):279–293, 1987.

[58] K. Vallons, G. Adolphs, P. Lucas, S. V. Lomov, and I. Verpoest. Quasi-UD glass fibre NCF composites for wind energy applications: a review of requirements and existing fatigue data for blade materials. *Mechanics & industry*, 14(3):175–189, 2013.

[59] K. Vallons. *The behaviour of carbon fibre-epoxy NCF composites under various mechanical loading conditions*. PhD thesis, Katholieke Universiteit Leuven, 2009.

[60] F. Edgren, D. Mattsson, L. E. Asp, and J. Varna. Formation of damage and its effects on non-crimp fabric reinforced composites loaded in tension. *Composites science and technology*, 64(5):675–692, 2004.

[61] R. Joffe, D. Mattsson, J. Modniks, and J. Varna. Compressive failure analysis of non-crimp fabric composites with large out-of-plane misalignment of fiber bundles. *Composites part A: applied science and manufacturing*, 36(8):1030–1046, 2005.

[62] D. Mattsson, R. Joffe, and J. Varna. Damage in NCF composites under tension: effect of layer stacking sequence. *Engineering fracture mechanics*, 75(9):2666–2682, 2008.

[63] A. Gagel, D. Lange, and K. Schulte. On the relation between crack densities, stiffness degradation, and surface temperature distribution of tensile fatigue loaded glass-fibre non-crimp-fabric reinforced epoxy. *Composites part A: applied science and manufacturing*, 37(2):222–228, 2006.

[64] A. Gagel, B. Fiedler, and K. Schulte. On modelling the mechanical degradation of fatigue loaded glass-fibre non-crimp fabric reinforced epoxy laminates. *Composites science and technology*, 66(5):657–664, 2006.

[65] S. Adden and P. Horst. Damage propagation in non-crimp fabrics under bi-axial static and fatigue loading. *Composites science and technology*, 66(5):626–633, 2006.

[66] S. Adden and P. Horst. Stiffness degradation under fatigue in multiaxially loaded non-crimped-fabrics. *International journal of fatigue*, 32(1):108–122, 2010.

[67] V. Carvelli, V. N. Tomaselli, S. V. Lomov, I. Verpoest, V. Witzel, and B. Van den Broucke. Fatigue and post-fatigue tensile behaviour of non-crimp stitched and unstitched carbon/epoxy composites. *Composites science and technology*, 70(15):2216–2224, 2010.

[68] S. Drapier and M. Wisnom. Finite-element investigation of the compressive strength of non-crimp-

fabric-based composites. *Composites science and technology*, 59(8):1287–1297, 1999.

[69] L. G. Zhao, N. A. Warrior, and A. C. Long. Finite element modelling of damage progression in non-crimp fabric reinforced composites. *Composites science and technology*, 66(1):36–50, 2006.

[70] K. I. Tserpes and G. N. Labeas. Mesomechanical analysis of non-crimp fabric composite structural parts. *Composite structures*, 87(4):358–369, 2009.

[71] G. Ernst, M. Vogler, C. Hühne, and R. Rolfes. Multiscale progressive failure analysis of textile composites. *Composites science and technology*, 70(1):61–72, 2010.

[72] J. LLorca, C. González, J. M. Molina-Aldareguía, J. Segurado, R. Seltzer, F. Sket, M. Rodríguez, S. Sádaba, R. Muñoz, and L. P. Canal. Multiscale modeling of composite materials: a roadmap towards virtual testing. *Advanced materials*, 44(23):5130–5147, 2011.

[73] EN ISO. 527-4: 1997 (E) Plastics-determination of tensile properties, Part 4. *Test conditions for isotropic and orthotropic fibre-reinforced plastic composites*, 1997.

[74] ASTM International. Practice for statistical analysis of linear or linearized stress-life (S-N) and strain-life (-N) fatigue data. Technical Report ASTM E739 - 10, ASTM International, 2010.

[75] M. Aslan. *Characterisation of flax fibres and flax fibre composites*. PhD thesis, Technical University of Denmark, DTU Wind Energy, 2012.

[76] L. Mikkelsen and J. Bech. Secondary stress effects during load introduction into unidirectional composite test coupons. In *CompTest 2013 - Book of Abstracts*, Aalborg University, 2013.

[77] P. Stanley and W. K. Chan. The application of thermoelastic stress analysis techniques to composite materials. *The journal of strain analysis for engineering design*, 23(3):137–143, 1988.

[78] R. K. Fruehmann, J. M. Dulieu-Barton, and S. Quinn. On the thermoelastic response of woven composite materials. *The journal of strain analysis for engineering design*, 43(6):435–450, 2008.

[79] P. D. Soden, M. J. Hinton, and A. S. Kaddour. Lamina properties, lay-up configurations and loading conditions for a range of fibre-reinforced composite laminates. *Composites science and technology*, 58(7):1011–1022, 1998.

[80] K. S. Alfredsson, A. A. Gawandi, J. W. Gillespie Jr., L. A. Carlsson, and T. A. Bogetti. Stress analysis of axially and thermally loaded discontinuous tile core sandwich with and without adhesive filled core gaps. *Composite structures*, 93(7):1621–1630, 2011.

[81] Z. C. Xia, R. R. Carr, and J. W. Hutchinson. Transverse cracking in fiber-reinforced brittle matrix, cross-ply laminates. *Acta metallurgica et materialia*, 41(8):2365–2376, 1993.

[82] P. Lundmark and J. Varna. Constitutive relationships for laminates with ply cracks in in-plane loading. *International journal of damage mechanics*, 14(3):235–259, 2005.

[83] S. W. Tsai. Strength theories of filamentary structures. In *Fundamental aspects of fiber reinforced plastic composites*, pages 3–11. Wiley Interscience, New York, 1968.

[84] R. Joffe and J. Varna. Analytical modeling of stiffness reduction in symmetric and balanced laminates due to cracks in 90 layers. *Composites science and technology*, 59(11):1641–1652, 1999.

[85] U. Hansen. *Transverse cracking of laminated composite materials with interleaves*. PhD thesis, University of Delaware - Center for Composite Materials, 1996.

[86] J.W. Gillespie Jr. and U. Hansen. Transverse cracking of composite laminates with interleaves: a variational approach. *Journal of reinforced plastics and composites*, 16(12):1066–1092, 1997.

[87] V. Vinogradov and Z. Hashin. Variational analysis of cracked angle-ply laminates. *Composites science and technology*, 70(4):638–646, 2010.

[88] J. A. Nairn. Matrix microcracking in composites. In *Comprehensive Composite Materials*, volume 2, pages 403–432. Elsevier science Ltd., Oxford, 2000.

[89] J. A. Nairn. The strain energy release rate of composite microcracking: a variational approach. *Journal of composite materials*, 23(11):1106–1129, 1989.

[90] J. A. Nairn and S. Hu. The formation and effect of outer-ply microcracks in cross-ply laminates: a variational approach. *Engineering fracture mechanics*, 41(2):203–221, 1992.

Appendix A

Appended papers

Included to the thesis are the following journal papers.

[P1] Zangenberg J., Larsen J.B., Østergaard R.C., and Brøndsted P. Methodology for characterisation of glass fibre composite architecture, *Plastics, Rubber and Composites*, **41(4/5)**, pp. 187-193 (2012).

[P2] Zangenberg J. and Brøndsted P. Quantitative study on the statistical properties of fibre architecture of genuine and numerical composite microstructures, *Composites Part A: Applied Science and Manufacturing*, **47**, pp. 124-134 (2013).

[P3] Zangenberg J. and Brøndsted P. Determination of the minimum size of a statistical representative volume element from a fibre-reinforced composite based on point pattern statistics, *Scripta Materialia*, **68**, pp. 503-505, (2013).

[P4] Zangenberg J., Brøndsted P., and Gillespie J.W. Jr. Fatigue damage propagation in unidirectional glass fibre reinforced composites made of a non-crimp fabric, *Journal of Composite Materials*, **Accepted**, (2013).

[P5] Zangenberg J., Brøndsted P., and Koefoed M. Design of a fibrous composite preform for wind turbine rotor blades, *Materials & Design*, **Submitted**, (2013).

[P1]

Zangenberg J., Larsen J.B., Østergaard R.C., and Brøndsted P.

METHODOLOGY FOR CHARACTERISATION
OF GLASS FIBRE COMPOSITE ARCHITECTURE

Plastics, Rubber and Composites, **41(4/5)**, pp. 187-193 (2012).

Methodology for characterisation of glass fibre composite architecture

J. Zangenberg*[1,2], J. B. Larsen[2], R. C. Østergaard[2] and P. Brøndsted[1]

The present study outlines a methodology for microstructural characterisation of fibre reinforced composites containing circular fibres. Digital micrographs of polished cross-sections are used as input to a numerical image processing tool that determines spatial mapping and radii detection of the fibres. The information is used for different analyses to investigate and characterise the fibre architecture. As an example, the methodology is applied to glass fibre reinforced composites with varying fibre contents. The different fibre volume fractions (FVFs) affect the number of contact points per fibre, the communal fibre distance and the local FVF. The fibre diameter distribution and packing pattern remain somewhat similar for the considered materials. The methodology is a step towards a better understanding of the composite microstructure and can be used to evaluate the interconnection between fibre architecture and composite properties.

Keywords: Glass fibres, Scanning electron microscopy, Composite microstructure, Microstructural characterisation

This paper is part of a special issue on Deformation and fracture of polymers and their composites

Introduction

The fibre volume fraction (FVF) is considered as the most crucial microstructural parameter for describing fibre reinforced composites. The parameter forms the basis for the well known rule of mixtures for determining the in-plane stiffness of a composite material, *see* e.g. Jones.[1] Commonly, the FVF is determined on the basis of the weight fractions and the densities of the individual constituents and yields an average laminate parameter for the entire composite. However, on a local scale, the FVF attains larger values, e.g. inside individual bundles where the fibre concentration is enlarged.

It is evident that there exists other microstructural parameters that characterise a fibre reinforced composite, e.g. packing pattern, neighbouring distance, clustering, etc. Information about these parameters can be extracted from measurements on cross-sections of the given composite. Digital image analysis and processing are tools to be used to identify the material microstructure. Attempts have been made in order to characterise the full three-dimensional (3D) structure of (glass) fibre composites (FVF, fibre misalignment, waviness, fibre curvature, etc.) using a sectioning approach based on microscope images. This analysis requires great accuracy in the sectioning process and in identifying the individual fibres. The method is time consuming but serves well in order to describe the local appearance of the microstructure. This 3D characterisation has been carried out by several researchers, *see* for instance, Paluch[2] or Clarke *et al.* [3] These studies also include the determination of the fibre misalignment angle inspired by the ideas of Yurgartis,[4] where the misalignment angle is determined by measurements of the elliptical fibre shape that appears on an inclined cross-section compared to the principal fibre direction. Using numerical routines, Creighton *et al.*[5] and Kratmann *et al.*[6] determined the misalignment angle for much lower resolution images and thus saving the processing time. The difference between two-dimensional (2D) and 3D characterisation is outlined in the, to some extent, personal account of Exner.[7]

Based on digital micrographs of a planar and polished cross-section of a unidirectional fibre composite, this study presents a methodology which detects the spatial distribution and radii of the fibres. This mapping of the fibres is used to define a number of parameters that are considered relevant for the microstructural characterisation of fibre reinforced composites. The method is capable of analysing local regions as well as entire bundles or cross-sections. For illustrating the applicability, the methodology is applied to different glass fibre reinforced composites with varying fibre contents. The ideas presented are inspired by the review work of Guild and Summerscales,[8] who discuss a number of different approaches for image analysis of fibre composites, Pyrz,[9] who quantitatively investigated the composite microstructure by statistical tools, and Paluch,[2] who made 3D characterisation based on 2D image techniques. This stereological approach for investigating the 3D microstructure based on 2D images has been used extensively, but it seems that the methods and ideas have not been brought to any practical experience. For instance, when the composite microstructure is investigated numerically using representative volume elements, general assumptions are made on the fibre distribution and packing pattern, communal fibre distance,

[1]Materials Research Division, Risø DTU, Frederiksborgvej 399, Roskilde 4000, Denmark
[2]LM Wind Power, Jupitervej 6, Kolding 6000, Denmark

*Corresponding author, email jzan@risoe.dtu.dk

Published by Maney on behalf of the Institute
Received 14 October 2011; accepted 27 November 2011
DOI 10.1179/1743289811Y.0000000067

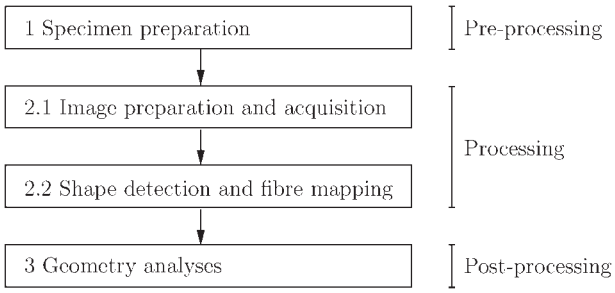

1 Flowchart for detection of composite microstructure

boundary conditions, etc. Wongsto and Li[10] investigated the effect of boundary condition on the representative volume element and made numerical simulation of a random distributed fibre arrangement. The fibre randomness was further investigated by Melro *et al.*,[11] who developed a statistically characterised algorithm to generate random composite cross-sections. The predictions from the algorithm in terms of effective composite properties agreed well with the experimental data. The idea of random fibre distribution was also used by Mishnaevsky and Brøndsted,[12] who, in a numerical study, considered fatigue damage of unidirectional fibre reinforced composites. Ongoing work will extend the knowledge of the interplay between fatigue damage and fibre architecture since details in the fibre architecture has proven to be detrimental for fatigue performance.

Method

Shape detection algorithms are well known within the field of digital image analysis, and there exists numerous algorithms depending on the purpose. A common procedure is the Hough transformation by Hough,[13] who came up with the idea of shape detection of lines based on parameter space. The work was further developed by Duda and Hart,[14] where the shape detection was extended to include circular objects. This method is commonly referred to as the circular Hough transformation, and a more profound presentation can be found in the work of Shapiro and Stockman.[15] The magnitude of the parameter space for shape detection depends on the shapes considered. For instance, line detection uses a two-parameter space (slope and intersection), circle detection 3 [centre (x,y) and radius] and ellipses 5 [minor/major axis, centre (x,y) and orientation]. Increasing the parameter space heavily increases the computational requirements. The current method is based on the circular Hough transformation for detection of circular shapes.

The analysis is split up into three different steps: preprocessing, processing and post-processing, as presented in Fig. 1 and the following subsections.

Preprocessing

The preparation of the test samples is crucial in order to obtain the best possible image quality. Standard microscope specimens are used, where a representative material sample of the composite laminate is cut and cast in an epoxy resin to form a cylinder with a diameter of 30 mm. Thereupon, the specimens are polished in a grinder with abrasive paper varying from no. 250 to 4000 in grain size. The polishing time is adjusted according to the grain size. It is evident that the sample surface appears as plane and smooth as possible.

Processing

To obtain the best image quality, it is recommended to use a scanning electron microscope (SEM), an environmental SEM or a low vacuum SEM for image acquisition. If an SEM is used, the specimens need to be coated due to their non-conducting surface. It is possible to use an optical microscope, but this requires even more sensitivity in the preprocessing step due to the lower resolution, lower depth of field and poorer lighting conditions in an optical microscope compared to an electron microscope. In the present work, a low vacuum SEM is used.

The magnification of the microscope should be adjusted so the misinterpretation in the radii detection is reduced (*see* further discussion in the section on 'Implementation'). To minimise computational requirements, the shape detection is based on 8 bit greyscale images. Upon acquisition of the micrographs, the shape detection is divided into two independent steps: a Canny edge detection of the image[16] and a circle detection based on these edges using the circular Hough transformation. The Canny edge detection locates edges by searching for a local maxima of the colour gradient within the considered image. An example is illustrated in Fig. 2, where the grey level intensity is illustrated along a given path in the image. It is evident that the edges of the fibres are detectable due to the obvious colour gradient.

Once the edges of the fibres are detected, the circular Hough transformation is applied by a voting procedure to identify the best matching circles. The input parameters for the transformation can be adjusted depending on the image quality (threshold level, search

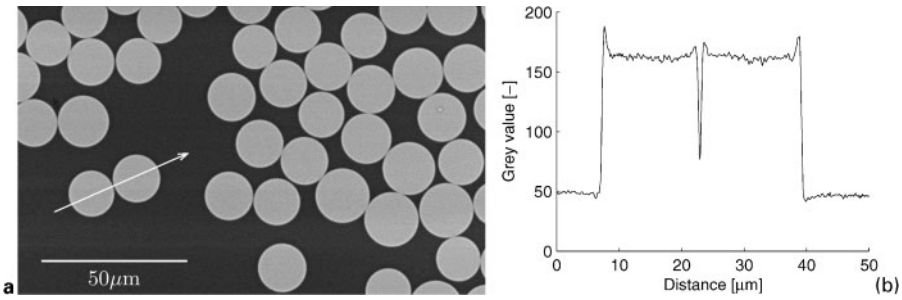

a SEM image of glass fibres (light part) and matrix (darker part) in UD reinforced composite: arrow indicates direction for grey level intensity in *b*1; *b* grey level intensity along path shown in *a*: white level is 255, black is 0. Note that interfacial region gives rise to larger grey value than fibre

2 Identification of fibre edges in unidirectional (UD) fibre reinforced composite based on SEM image

range and magnitude of search filter). The results of the detection are the in-plane fibre location (x, y coordinates) and the fibre radius r.

Owing to the numerical processing power, there is a limit for the image size that can be analysed by the circular Hough transformation. Therefore, for larger image sizes (approximately larger than 1000×1000 pixels), the entire image is split up into a number of user defined segments that are analysed separately, and the results are stored for each segment. An average value for the entire image is evaluated once all the segments have been analysed. The segmentation procedure can also be used to characterise the microstructure across a fibre bundle, the effects of clustering due to stitching tension, etc.

Post-processing

Circle sets on a plane are defined if the positions and radii of the circles are known. Characterising these circle sets requires knowledge about the number of circles, circle diameter distribution, communal distance between the circles, clustering, packing pattern and circles in contact. When these parameters are known, it is possible to make a full characterisation of the circle set. The following analyses are considered based on the fibre centre and radii obtained from the circular Hough transformation:

(i) global FVF
(ii) void content
(iii) fibre diameter distribution
(iv) number of contact points per fibre
(v) nearest neighbour distance
(vi) fibre clustering parameter
(vii) number of neighbours and local FVF.

Each of the above analyses is outlined in the following.

(i) The FVF is considered a fundamental parameter, which is used in characterising and calculating the mechanical properties of fibre reinforced composites. In the present work, the FVF is determined using three distinct procedures:

1. knowing the individual fibre radii and the total image size, it is possible to determine the FVF of the detected fibres. It is assumed that the position and diameter of the fibres do not vary in the normal direction of the fibres. Hence, the FVF is determined as

$$\mathrm{FVF} = \frac{\sum_{i=1}^{N} V_{i,\mathrm{fibre}}}{V_{\mathrm{total}}} = \frac{\sum_{i=1}^{N} A_{i,\mathrm{fibre}}}{A_{\mathrm{image}}} = \frac{\pi \sum_{i=1}^{N} r_i^2}{A_{\mathrm{image}}} \quad (1)$$

   where V is the volume, A is the area, N is the number of fibres and r_i is the individual fibre radius. This procedure for determining the FVF is referred to as FVF1
2. a simple procedure to evaluate the FVF is by threshold analysis. The image is transformed into a black/white image, whereas the resin appears as black pixels and the fibres as white pixels. The FVF is found as the ratio between the white pixels and the total number of pixels. This procedure is referred to as FVF2
3. it is likely that the circular Hough transformation does not detect every fibre in the cross-section, especially near the image boundary where the fibres are cut off. This procedure simply removes the detected fibres (used in procedure 1) and performs a threshold analysis (as in procedure 2) on the remaining undetected fibres. This procedure is referred to as FVF3.

It is given that the sum of the FVFs from procedures 1 and 3 should match procedure 2.

(ii) Voids may be present in the materials, and these voids are known to influence the mechanical properties. Since voids appear as black regions in the micrographs, these are identified if a pixel value is lower than a user defined threshold. The total void content is found as the sum of these pixels in relation to the total number of pixels.

(iii) It is often assumed in numerical analyses of fibre reinforced composites that the fibre diameter distribution is uniform, which is often not the case in practice. The fibre diameter is measured by the circular Hough transformation and assumed normal distributed, meaning that it is characterised by the mean value and the standard deviation.

(iv) Contact between surfaces leads to stress concentrations; therefore, contact between fibres is considered as a potential zone for crack initiation, *see* e.g. Wongsto and Li.[10] A contact condition between two circles (fibres) is defined if the centre to centre distance between two adjacent circles i and j d_{ij} is less than the sum of their individual radii $r_i + r_j$. However, due to fibre surface roughness, interface and inaccuracy in the circle detection, the contact condition is given as $d_{ij} \leqslant (r_i + r_j)\alpha$, where the factor $\alpha = 1{\cdot}01$ follows from the work of Mishnaevsky and Brøndsted.[12] Denoting the total number of circle contact conditions as c, the total number of contact points CP_{total} is determined as

$$CP_{\mathrm{total}} = \frac{c - N}{2} \quad (2)$$

where the factor of 2 is included to avoid repeated contact points.

Since the total number of contact points in equation (2) is dependent on the number of inclusions, the total number of contact points is normalised with the number of detected fibres N in order to get the number of contact points per fibre CP. For two common fibre packing patterns, the number of contact points per fibre and FVF is illustrated in Fig. 3 for an infinite fibre array.

(v) Separation distance between the fibres may minimise the stress concentration, and this analysis determines the distance to the nearest neighbour. The neighbouring distance between fibres i and j is defined as $ND_{ij} = d_{ij} - r_i - r_j$, and the shortest distance is found by the solution to the classical travelling salesman problem (TSP) using a TSP algorithm. Further information on the TSP can be found from Lawler *et al.*[17] The result of the analysis is the 'shortest route' through all fibres and thereby the nearest neighbouring distances (NNDs). For quantification, the NND is assumed to follow a log normal behaviour with mean μ and standard deviation σ, meaning that the limits are expressed as $\exp[\log(\mu) \pm \log(\sigma)]$.

(vi) Clustering of fibres leads to regions that influence the mechanical behaviour. In order to estimate the fibre clustering, the simple relation from Clark and Evans[18] is used as a measure for fibre clustering. Originally, the theory was used in terms of spatial relations in populations, but it is directly applied in the current

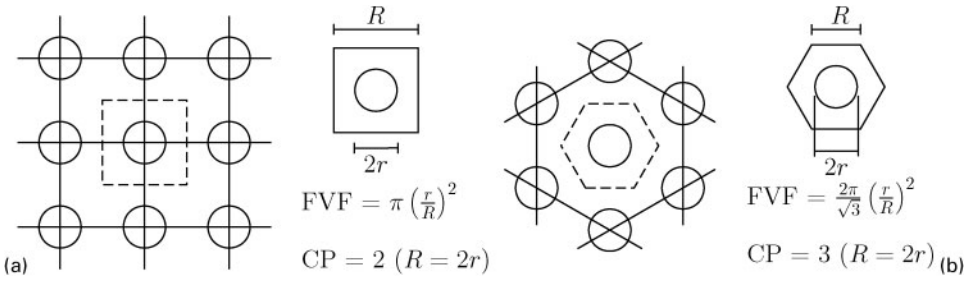

a square array; *b* hexagonal array

3 Typical fibre packing patterns in unidirectional composite along with FVF and number of contact points per fibre (CP)

study even though there are some limitations. The clustering parameter R is expressed as

$$R = \frac{\bar{r}_A}{\bar{r}_E}, \quad \bar{r}_A = \frac{\sum \mathrm{NND}}{N} \quad \text{and} \quad \bar{r}_E = \frac{1}{2\rho^{1/2}} \tag{3}$$

with $\bar{r}_A$ being the mean of the series of distances to the nearest neighbour, and $\bar{r}_E$ is the mean distance to the nearest neighbour expected in an infinitely large random distribution with density ρ. In the current case, the sum of the NNDs ΣNND is found as the ''shortest route'' between fibre centre mentioned above. The fibre density is found as $\rho = N/A_{\mathrm{image}}$.

The convenient thing about the clustering parameter is its easily accessible interpretation since it is bound by the limits $0 \leqslant R \leqslant 2{\cdot}15$, where the lower limit follows from an intermediate neighbouring distance equal to 0 (fully clustered), and the upper limit is for a hexagonal array with equidistant distance to other neighbours. For $R = 1$, the packing pattern is random.

(vii) Often, when modelling the composite microstructure, an idealised fibre packing pattern is assumed to be in the arrays shown in Fig. 3. These packing patterns are seldomly found in practice, and the following analysis estimates the packing pattern in terms of the number of neighbours and a local FVF. More sophisticated methods may be used to characterise the packing pattern, e.g. the second order intensity function as proposed by Pyrz[9] and Ghosh *et al.*[19]

The number of neighbours is found from a Delaunay triangulation of the fibre centre points, and the local FVF is determined as the fibre area in relation to the area of Voronoi cell associated to each fibre. In brief, a Voronoi tessellation is a decomposition of a scatter (in this case points on the plane) into a cell structure each containing exactly 1 point. The property of the cell is that any point inside the cell is closer to that point than to any other site. A Delaunay triangulation, on the other hand, is sort of the dual problem to the Voronoi tessellation such that no point sets are inside the circumcircle of any triangle. The two principles are illustrated for a generated fibre arrangement in Fig. 4. For a more profound presentation, *see* Okabe.[20]

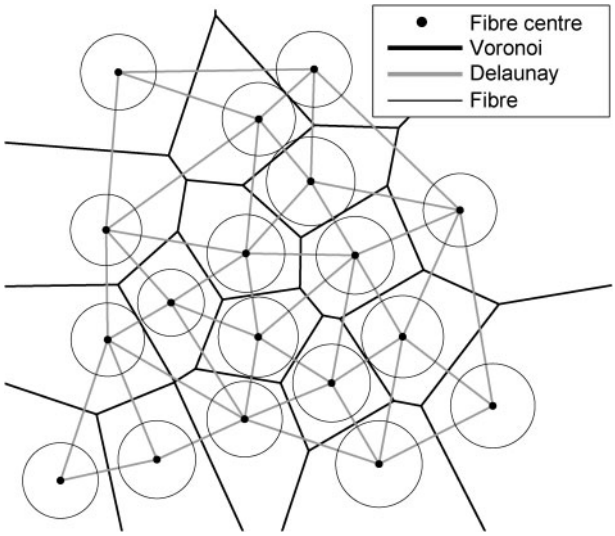

4 Sketch of Voronoi tessellation and Delaunay triangulation for random point set in plane

In the present analysis, the Voronoi cells are used to determine a local FVF (referred to FVF4) for each fibre since the area of the cell A_{Voronoi} can be considered as an 'area parameter' associated to each fibre with area A_{fibre}. Thereby, the local FVF is determined as $A_{\mathrm{fibre}}/A_{\mathrm{voronoi}}$. The area of the Voronoi cells along the image boundary cannot be evaluated explicitly, which is why the boundary fibres are disregarded. The local FVF is assumed to follow a normal distribution described by the mean value and the standard deviation. The centre points of the detected fibres are used as input for the triangulation in order to find the number of neighbours, here presented as the mean value and standard deviation respectively. Similar analyses have been used previously, e.g. in the work of Paluch.[2]

Implementation

The programming language MATLAB is used for the implementation of the methodology. The circular Hough transformation and the TSP algorithm can be found at the MathWorks File Exchange.[21]

The algorithm and implementation have been tested on two selected fibres on several images with different microscope magnifications in order to estimate the accuracy of circle detection. The fibres are shown in Fig. 5a, where fibre A is completely isolated, and fibre B is surrounded by several others. The result from the analysis is shown in Fig. 5b, where the detected fibre diameter is plotted as a function of microscope magnification.

For low magnification images below 5 pixels/μm, there is a scatter in the measured fibre diameters. However, in order to get sufficient accuracy and amount of fibres per image, a value of 1·64 pixels/μm is used in the following well aware that this gives rise to a non-negligible deviation in the determination of the FVF in procedure FVF1 mentioned above.

Depending on the image shape, image size and number of fibres, the number of contact points is affected. Therefore, a test is carried out to investigate the image shape/size sensitivity. The test is carried out for a square fibre packing arrangement with no intermediate

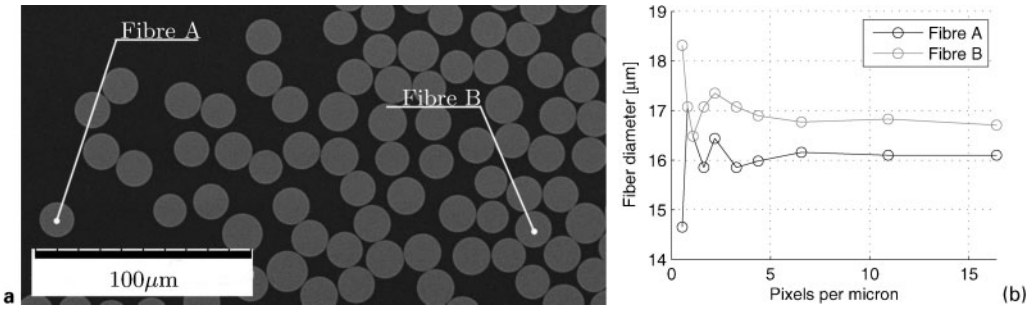

a fibres considered in accuracy analysis; *b* detected fibre diameter as function of microscope magnification

5 Accuracy analysis for detection of fibre radius

distance between the fibres. For a varying image shape/size, it turns out that for a 'low' number of fibres (say, <50 fibres in a narrow shaped image), the number of contact points is affected.

Application

Two-layered glass/polyester composites with varying fibre contents were manufactured using the vacuum assisted resin transfer moulding process, and the specimens are analysed by the methodology outlined in the section on 'Method'. All the images are acquired within a bundle without any resin rich zones near the edges. A typical result of the circle detection is presented in Fig. 6.

A close examination of the detected circles shown in Fig. 6 reveals that the algorithm detects a number of non-existing fibres; nonetheless, these fibres are removed in the post-processing step by evaluation of the grey level intensity at the centre of the (mis)detected fibre. The post-processing analyses are carried out as mentioned in the previous section, and the results are presented in Table 1 and Figs. 7 and 8. μ and σ denote the mean value and standard deviation respectively, and all data are assumed to be normal/log normal distributed and independent. Table 1 presents the number of detected fibres and the fibre diameter distribution.

Figure 7 presents the obtained FVFs for the different analyses, and the results are normalised with the value from FVF3 (threshold analysis) in sample 1.

Figure 8 shows the number of contact points per fibre *CP*, the nearest neighbour distance *NN*, the clustering parameter *ClP* and the number of neighbours *NoN* as a function of the obtained FVF. Again, the FVF is normalised with the value from FVF3 (threshold analysis) in sample 1.

The variation in fibre diameters is small, and the measurements are almost constant in the range around $d_f \simeq 17$ μm, which is also the prescribed diameter by the manufacturer.

As mentioned in the previous section, the sum of the FVFs determined from procedures FVF1 and FVF2 should be equal to the FVF determined by procedure FVF3. This is illustrated in Fig. 7, where the deviation between the methods is within $\pm 1{\cdot}2\%$, which is regarded as a sufficient accuracy in the shape detection. It is worth noticing that the local FVF, i.e. FVF4, is consistently larger than the FVFs determined from the other analyses. No voids are found in the samples investigated.

For a heavier fibre compaction, it is found that the number of contact points per fibre *CP* increases and the nearest neighbour distance *NN* decreases (*see* Fig. 8). The packing pattern remains the same independent of the FVF, which is reflected in the number of neighbours *NoN* and the clustering parameter *ClP* approaching the upper limit of 2·15. This means that the packing pattern converges against a pseudohexagonal array.

Discussion

From the number of fibres detected (*see* e.g. Table 1) and the image sizes used, the image size sensitivity in relation to the number of contact points per fibre is limited for the samples considered. The number of contact points per fibre increases for increasing FVF, which is in accordance to what is reported by Mishnaevsky and Brøndsted[12] in a numerical study.

Even though the actual fibre packing in Fig. 6 does not appear to be systematic, the fibres tend to arrange in what is referred to as a pseudohexagonal packing pattern. Using the Delaunay triangulation, Paluch[2]

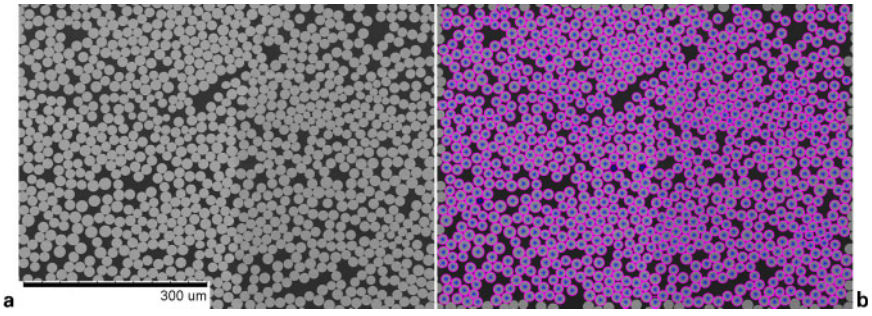

a basis for image analysis: SEM image of polished cross-section; *b* spatial mapping of fibres with detected radii using circular Hough transformation

6 Typical images for analysing microstructure of unidirectional glass fibre reinforced composite: presented images are segments of analysed images

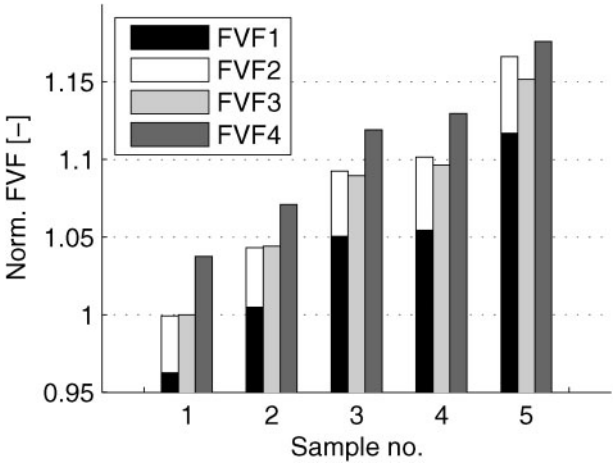

7 Results of image analyses: FVF based on different procedures: FVF1, radii of fibres; FVF2, boundary analysis; FVF3, threshold analysis; FVF4, local (Voronoi)

made a similar conclusion in relation to the packing pattern.

Pyrz[9] carried out a quantitative study on the microstructure of composites based on statistical analyses. In specific, a probability investigation was made between the NND for different FVFs. The trend is obviously that the larger FVF is, the smaller the mean NND and standard deviation is observed. The same findings are concluded in the present study.

The clustering parameter described in the work of Clark and Evans[18] is determined based on the fibre centre without information regarding the fibre radius. Therefore, the basis of using this analysis is misleading since the underlying statistical theory is based on point sets rather than circles. It has not been possible at this stage of the study to find a suitable description for clustering of circles where the individual radii are included.

It is apparent that it would be more accurate to determine the Voronoi diagrams in terms of circle sets on a plane rather than points due to the circular cross-section of the fibres, *see* e.g. presentation by Kim *et al.*[22] However, based on the work of Paluch[2] and to ease the implementation, the presented method is considered to be sufficient.

The local FVF (FVF4) predicts a larger value compared to the global FVF, which is in contradiction to what could be expected from the idealised fibre arrangements in Fig. 3 that produce similar results for local and global FVFs. Still, the magnitudes of the deviation are in similar range to what is found from Ghosh *et al.*[19] based on simulations of uniform fibre distributions with FVF in the range up to 32·4%.

The optimum solution to the TSP has been investigated by several researchers, and there exist numerous

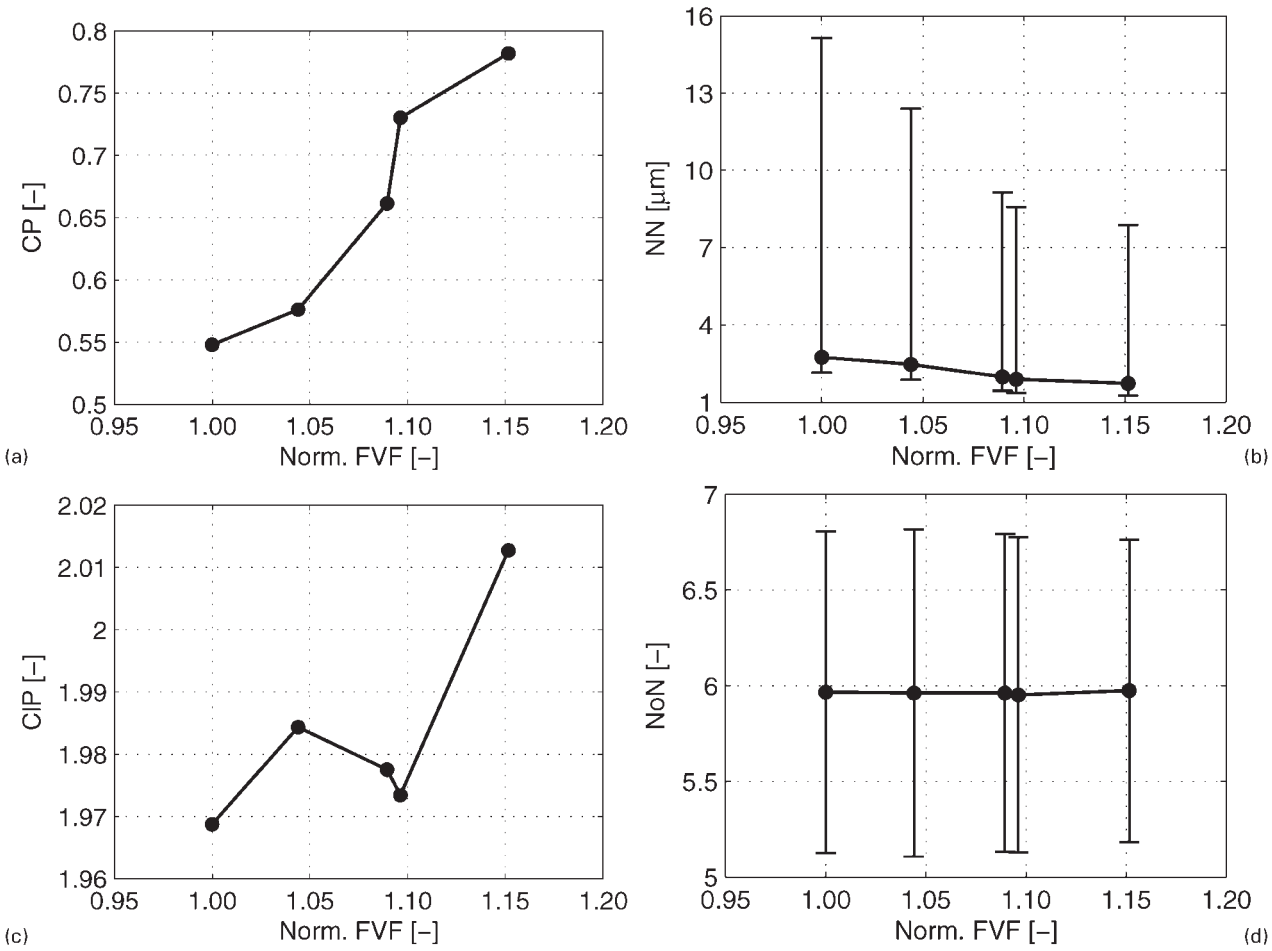

a contact points per fibre *CP*; *b* nearest neighbour distance *NN*; *c* clustering parameter *ClP*; *d* number of neighbours *NoN*

8 Results of image analyses for different FVFs

Table 1 Result of image analysis: number of detected fibres and fibre diameter distribution (mean μ and standard deviation σ)*

No.	NoF	FD [μ/σ] / [μm/μm]
1	4745	17·19/1·46
2	4605	17·17/1·45
3	4797	17·21/1·57
4	3335	16·96/1·44
5	7679	17·32/1·50

*NoF: number of fibres; FD: fibre diameter.

different solution techniques for the problem. However, the problem of finding the optimum solution is far from trivial. In the case of N fibres, the number of different routes is given as $(N-1)!/2$, which indicates the increasing problem complexity for large N. Therefore, approximated methods are often used where the route might not be the optimum one but somewhat close to. Such an algorithm is used in the present, and as a result, the shortest route might not be the optimum.

Conclusions

A new methodology is presented dealing with shape detection and microstructural analysis of composite materials containing circular fibres. Based on digital micrographs and numerical image processing, the fibre architecture/microstructure is evaluated for a number of different parameters. For demonstration, the methodology is shown useful to identify and compare microstructural parameters for different glass fibre reinforced composites with varying fibre contents. The following microstructural parameters are affected by changes in the FVF: the number of contact points per fibre, nearest neighbour distance and the local FVF (the fibre area in relation to the area of the associated Voronoi cell). For increasing FVF, the number of contact point per fibre increases, whereas the nearest neighbour distance decreases. The local FVF is somewhat larger than the global FVF. Voids are not found in the samples. Independent of the FVF, the fibres are arranged in a pseudohexagonal array with approximately six neighbours per fibre.

References

1. R. M. Jones: 'Mechanics of composite materials'; 1999, New York, Hemisphere Pub.
2. B. Paluch: 'Analysis of geometric imperfections affecting the fibers in unidirectional composites', *J. Compos. Mater.*, 1996, **30**, (4), 454.
3. A. R. Clarke, G. Archenhold and N. C. Davidson: 'A novel technique for determining the 3D spatial distribution of glass fibres in polymer composites', *Compos. Sci. Technol.*, 1995, **55**, (1), 75–91.
4. S. W. Yurgartis: 'Techniques for the quantification of composite mesostructure', *Compos. Sci. Technol.*, 1995, **53**, (2), 145–154.
5. C. J. Creighton, M. P. F. Sutcliffe and T. W. Clyne: 'A multiple field image analysis procedure for characterisation of fibre alignment in composites', *Composites Part A: Appl. Sci. Manuf.*, 2001, **32A**, (2), 221–229.
6. K. K. Kratmann, M. P. F. Sutcliffe, L. T. Lilleheden, R. Pyrz and O. T. Thomsen: 'A novel image analysis procedure for measuring fibre misalignment in unidirectional fibre composites', *Compos. Sci. Technol.*, 2009, **69**, (2), 228–238.
7. H. E. Exner: 'Stereology and 3D microscopy: useful alternatives or competitors in the quantitative analysis of microstructures?', *Image Anal. Stereol.*, 2004, **23**, (2), 73–82.
8. F. J. Guild and J. Summerscales: 'Microstructural image analysis applied to fibre composite materials: a review', *Composites*, 1993, **24**, (5), 383–393.
9. R. Pyrz: 'Quantitative description of the microstructure of composites. Part I: morphology of unidirectional composite systems', *Compos. Sci. Technol.*, 1994, **50**, (2), 197–208.
10. A. Wongsto and S. Li: 'Micromechanical FE analysis of UD fibre-reinforced composites with fibres distributed at random over the transverse cross-section', *Composites A: Appl. Sci. Manuf.*, 2005, **36A**, (9), 1246–1266.
11. A. R. Melro, P. P. Camanho and S. T. Pinho: 'Generation of random distribution of fibres in long-fibre reinforced composites', *Compos. Sci. Technol.*, 2008, **68**, (9), 2092–2102.
12. L. Mishnaevsky, Jr and P. Brøndsted: 'Statistical modelling of compression and fatigue damage of unidirectional fiber reinforced composites', *Compos. Sci. Technol.*, 2009, **69**, (3–4), 477–484.
13. P. V. C. Hough: 'Method and means for recognizing complex patterns', Technical report, US Patent 3,069,654, 1962.
14. R. O. Duda and P. E. Hart: 'Use of the Hough transformation to detect lines and curves in pictures', *Commun. ACM*, 1972, **15**, (1), 11–15.
15. L. G. Shapiro and G. C. Stockman: 'Computer vision'; 2000, Upper Saddle River, NJ, Prentice Hall.
16. J. Canny: 'A computational approach to edge detection', in 'Readings in computer vision: issues, problems, principles, and paradigms', (ed. M. A. Fischler and O. Firschein), Vol. 184, 87–116; 1987, Los Altos, CA, Morgan Kaufmann.
17. E. L. Lawler, A. H. Rinnooy-Kan, J. K. Lenstra and D. B. Shmoys: 'The traveling salesman problem: a guided tour of combinatorial optimization', Vol. 3; 1985, New York, Wiley.
18. P. J. Clark and F. C. Evans: 'Distance to nearest neighbor as a measure of spatial relationships in populations', *Ecology*, 1954, **35**, (4), 445–453.
19. S. Ghosh, Z. Nowak and K. Lee: 'Quantitative characterization and modeling of composite microstructures by Voronoi cells', *Acta Mater.*, 1997, **45**, (6), 2215–2234.
20. A. Okabe: 'Spatial tessellations: concepts and applications of Voronoi diagrams'; 2000, New York, John Wiley & Sons Inc.
21. MathWorks Inc.: 'MATLAB central files'; 2011, Natick, MA, MathWorks Inc.
22. D. S. Kim, D. Kim and K. Sugihara: 'Voronoi diagram of a circle set from Voronoi diagram of a point set: II. Geometry', *Comput.-Aided Geom. Des.*, 2001, **18**, (6), 563–585.

[P2]

Zangenberg J. and Brøndsted P.

QUANTITATIVE STUDY ON THE STATISTICAL PROPERTIES OF FIBRE ARCHITECTURE OF GENUINE AND NUMERICAL COMPOSITE MICROSTRUCTURES

Composites Part A: Applied Science and Manufacturing, **47**, pp. 124-134 (2013).

Composites: Part A 47 (2013) 124–134

Contents lists available at SciVerse ScienceDirect

Composites: Part A

journal homepage: www.elsevier.com/locate/compositesa

Quantitative study on the statistical properties of fibre architecture of genuine and numerical composite microstructures

J. Zangenberg [a,b,*], P. Brøndsted [b]

[a] LM Wind Power Blades, Composite Mechanics, Jupitervej 6, DK-6000 Kolding, Denmark
[b] Department of Wind Energy, Section of Composites and Materials Mechanics, Technical University of Denmark, Risø Campus, Frederiksborgvej 399, DK-4000 Roskilde, Denmark

ARTICLE INFO

Article history:
Received 23 April 2012
Received in revised form 22 October 2012
Accepted 23 November 2012
Available online 20 December 2012

Keywords:
A. Glass fibres
A. Laminate
B. Microstructures
C. Statistical properties/methods

ABSTRACT

A quantitative study is carried out regarding the statistical properties of the fibre architecture found in composite laminates and that generated numerically using Statistical Representative Volume Elements (SRVE's). The aim is to determine the reliability and consistency of SRVE's for representation of the composite microstructure as well as investigate the effect of a varying fibre radii distribution on the fibre architecture. Based on digital image analysis, the fibre architecture of unidirectional glass fibre composites with varying fibre content is recognised. The fibre architecture found is compared to a numerical microstructure generator using Monte Carlo simulations. It is shown that the numerical microstructure generator produces fibre arrangements that are statistically similar to the observed, which indicates a reliable and consistent SRVE. The microstructural effects of a parametric variation of the parameters for fibre radii distribution are simulated, and the influence on the fibre architecture is investigated.

1. Introduction

A Statistical Representative Volume Element (SRVE) is characterised as the smallest volume element in which the composite microstructure can be statistically described (or somewhat close to), Swaminathan and Ghosh [1]. Numerical simulation of the fibre architecture in composite materials has been studied extensively to generate SRVE's. Wongsto and Li [2] investigated (S)RVE properties based on a predefined fibre structure with equal radius followed by an arbitrary stirring to ensure a more random packing. Melro et al. [3] compared the work of Wongsto and Li to a hard-core generator with a sophisticated stirring criteria, and found similar behaviour based on statistical descriptors e.g. the Ripley's *K*-function. Based on experimental measurements of the fibre geometry, Thomas et al. [4] used a hard-core process to generate microstructures that were able to catch the anisotropic nature of the materials considered. Trias et al. [5,6] studied different aspects of a SRVE using the hard-core generator and an even radius distribution. Vaughan and McCartny [7] made a nearest neighbour algorithm that assigns the fibres according to the first and second nearest neighbour distribution found from an image analysis on composite laminates. The fibre radii distribution was modelled as log-normal, and they were able to generate microstructures that matched the laminates quite accurately. Common for these studies are that the generated microstructures are not compared in depth to observations made on genuine composites.

Through analysis of SRVE's and virtual testing, numerical investigations are often coupled to the mechanical performance of composites. In order to improve the performance one must understand and be able to describe the influential factors that govern the mechanical behaviour. Optimising the mechanical performance of fibre reinforced composites is generally a two fold process: either to improve the properties of the materials used and/or to change the composition of the microstructure. The motivation for the present study is to focus on the latter of these in order to understand the influence of fibre radii distribution on the spatial statistics of the fibre packing pattern. For a SRVE to be trustworthy and reliable, it is an essential requirement that it actually replicates the real composite microstructure, which is also a central focus in the present study. The study provides a profound investigation on the fibre architecture in composite laminates and numerical simulations, and the roadmap consists of four steps (see Fig. 1): (a) using digital image analysis, several composite laminates with different fibre content are analysed to describe the fibre architecture. (b) A numerical microstructure generator is developed that produces SRVE's of a fibre reinforced composite containing circular fibres with uneven radii distribution. (c) Based on Monte Carlo simulations, the generated fibre architectures are compared to the observations made on the genuine composite laminates. (d) A parametric study is conducted for a varying fibre radii distribution

* Corresponding author at: Department of Wind Energy, Section of Composites and Materials Mechanics, Technical University of Denmark, Risø Campus, Frederiksborgvej 399, DK-4000 Roskilde, Denmark. Tel.: +45 5138 8407; fax: +45 4677 5758.
E-mail addresses: jzan@dtu.dk, jezh@lmwindpower.com (J. Zangenberg), pobr@dtu.dk (P. Brøndsted).

1359-835X/$ - see front matter © 2012 Elsevier Ltd. All rights reserved.
http://dx.doi.org/10.1016/j.compositesa.2012.11.015

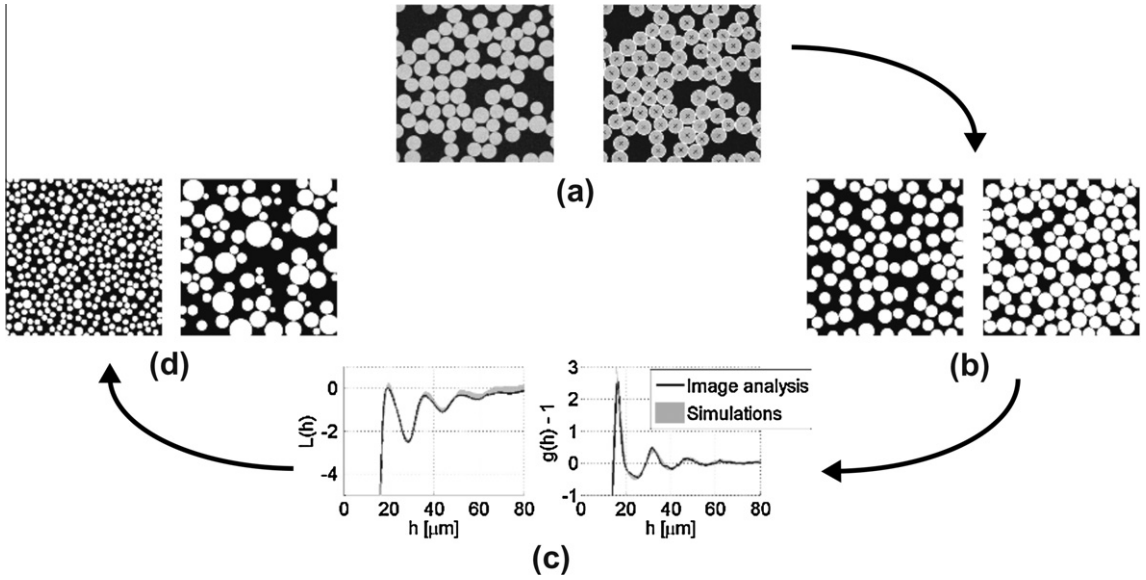

Fig. 1. Roadmap for comparing the fibre architecture between genuine composite laminates and a numerical microstructure generator: (a) digital image analysis: mapping of fibres; (b) numerical microstructure generator; (c) comparison of microstructure; and (d) parametric variation of fibre radii distribution.

to investigate the influence on the fibre architecture. Each step shown in Fig. 1 is explained in further detail in Section 2. The scope of the work is to demonstrate the statistical representativeness of the fibre packing pattern for a SRVE, and to investigate the fibre architecture for different variations in the fibre radii distribution. The work is the first step on the way for a better understanding of the interconnection between composite microstructure and mechanical performance.

1.1. Background

The following section presents the statistical tools and parameters that are used in order to characterise and compare the different composite microstructures.

1.1.1. Statistical descriptors for point pattern analysis

Statistical point pattern analysis is extensively used in order to describe the fibre architecture of composite materials, and the second order intensity function (or the Ripley *K*-function, Ripley [8]) has proven to be a powerful descriptor, Pyrz [9] and Ghosh et al. [10]. Unlike first order measures (such as the nearest neighbour distance) that often analyse short range distances, the *K*-function provides information regarding the point pattern at several distances. This means that the *K*-function can distinguish differences such as clustering or regularity in a point pattern (e.g. unidirectional fibres in a transverse cross section). The *K*-function is characterised as the number of expected further inclusions (fibres) found within a circle with radius h from any point considered divided by the inclusion density, λ. Mathematically this is defined as, Dixon [11]:

$$K(h) = \frac{1}{\lambda}\sum_i\sum_j \frac{I(d_{ij} < h)}{N}\frac{1}{w_{ij}}, \tag{1}$$

where N is the number of inclusions, $\lambda = N/A$ is the inclusion density in the study region with area A, $I(d_{ij} < h)$ is the indicator function (d_{ij} is the distance between points i and j), and w_{ij} is a weighting function that provides the edge correction. The indicator function attains the value of 1 if the argument is true, and 0 otherwise. The weighting function is included to avoid any bias near the boundary of the study region, and different estimators are described in the literature. The basic methods are illustrated in Fig. 2, Lopes [12] and Yamada and Rogerson [13].

Yamada and Rogerson [13] tested the different edge corrections shown in Fig. 2, and found that the circumference edge estimator performed well compared to the other methods. Therefore, this

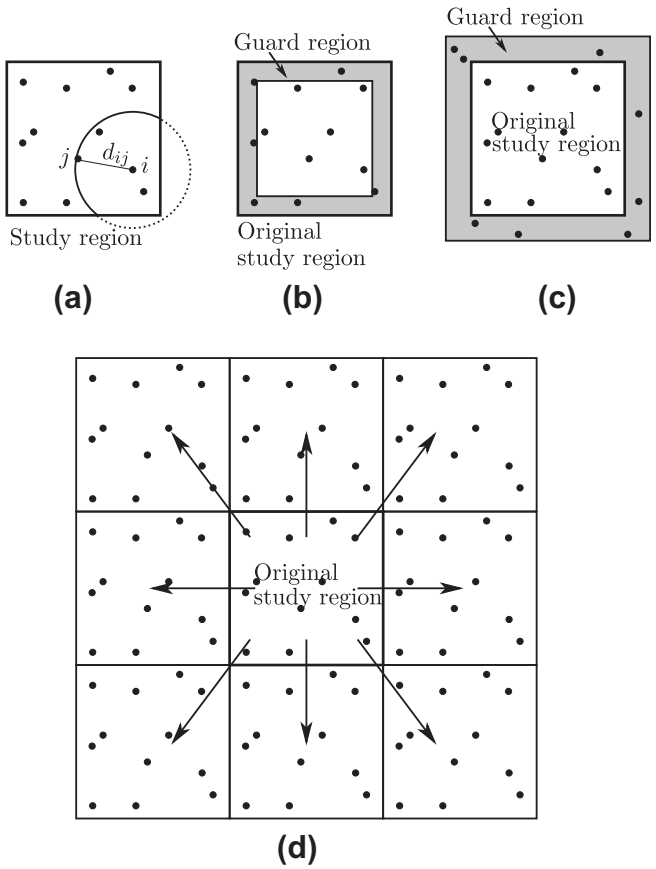

Fig. 2. Different edge correction methods: (a) circumference edge estimator; (b) inner guard region; (c) outer guard region; and (d) toroidal.

method is used in the following. This commonly used estimator has a value of 1 when the circle centered at point i with radius d_{ij} is entirely inside the study region. If a part of the circle falls outside the study region, then w_{ij} is equal to the ratio between the circumference of the circle that is inside the region and the circumference of the entire circle, see Fig. 2a. Explicit formulas for the circumference edge correction are found in Goreaud and Pelissier [14].

In order to evaluate the point pattern obtained from Eq. (1), the fibre architecture is tested against the state of Complete Spatial Randomness (CSR) (or the Poisson process). For CSR the inclusions are randomly located in the study region, and the K-function is given by, Dixon [11]:

$$\widehat{K}(h) = \pi h^2. \tag{2}$$

A common way to test the deviation from the CSR configuration is achieved by equating Eqs. (1) and (2):

$$L(h) = \sqrt{\frac{K(h)}{\pi}} - h, \tag{3}$$

which is referred to as the L-function. CSR gives a value of $\widehat{L} = 0$, and a typical approach is to test the deviation from CSR using Eq. (3) for all values of h.

Fig. 3a shows the L-function for common packing packing patterns (square, hexagonal, random, 2 clusters, 4 clusters). It is seen that periodic patterns (hexagonal or square) give rise to a characteristic saw-tooth shape for $L(h)$ when h is equal to the characteristic distances in the pattern, e.g. $h = 75,\ \sqrt{2}\cdot 75, 2\cdot 75, \sqrt{5}\cdot 75$, etc. for the square array. For a given value of h, positive peak values of $L(h)$ indicate clustering in the point pattern while negative imply some degree of regularity. To evaluate the differences in the fibre architecture, Eq. (1) is calculated numerically using MATLAB for the different fibre arrangements, and Eq. (3) is used to evaluate the deviation from CSR.

In order to test the statistical significance regarding the condition of CSR, Getis and Franklin [15] have stated that the 95% confidence interval, CI_{95}, of the Poisson process can be approximated as:

$$CI_{95} = \pm 1.42\frac{\sqrt{A}}{N-1}, \tag{4}$$

with A being the area of the study region, and N is the number of inclusions. Eq. (4) will be used to test whether the fibre packing patterns can be characterised as random.

The pair distribution function, $g(h)$, is a measure for the probability $g(h)\,dh$ of finding another inclusion within a circular annulus with thickness dh. The definition is, Ghosh et al. [10]:

$$g(h) = \frac{1}{2\pi h}\frac{dK(h)}{dh}, \tag{5}$$

where $K(h)$ follows from Eq. (1). The K-function can discriminate different point patterns whereas the pair distribution function can distinguish characteristic distances within the point pattern. This means that peak values of the function correspond to the most frequent distances between the inclusions. The pair distribution function for typical point patterns is shown in Fig. 3b. In the case of CSR, the pair distribution function is equal to unity. In order to evaluate the deviation from CSR, the pair distribution is therefore presented as $g(h) - 1$. The derivative of $K(h)$ in Eq. (5) is found using numerical differentiation and a central difference scheme.

The two functions $L(h)$, Eq. (3), and $g(h) - 1$, Eq. (5), will be used to compare the spatial point patterns for the laminates and the simulated microstructures, tested against the condition of CSR using Eq. (4). It is noted that the presented tools serve as a description of the spatial statistic of the point pattern, and it is expected that there is a connection to physical and mechanical properties.

1.1.2. Parameters for describing the composite architecture

Characterisation of a glass fibre reinforced composite based on digital image analysis was presented in a previous study, see Zangenberg et al. [16]. Composite laminates with unidirectional fibres

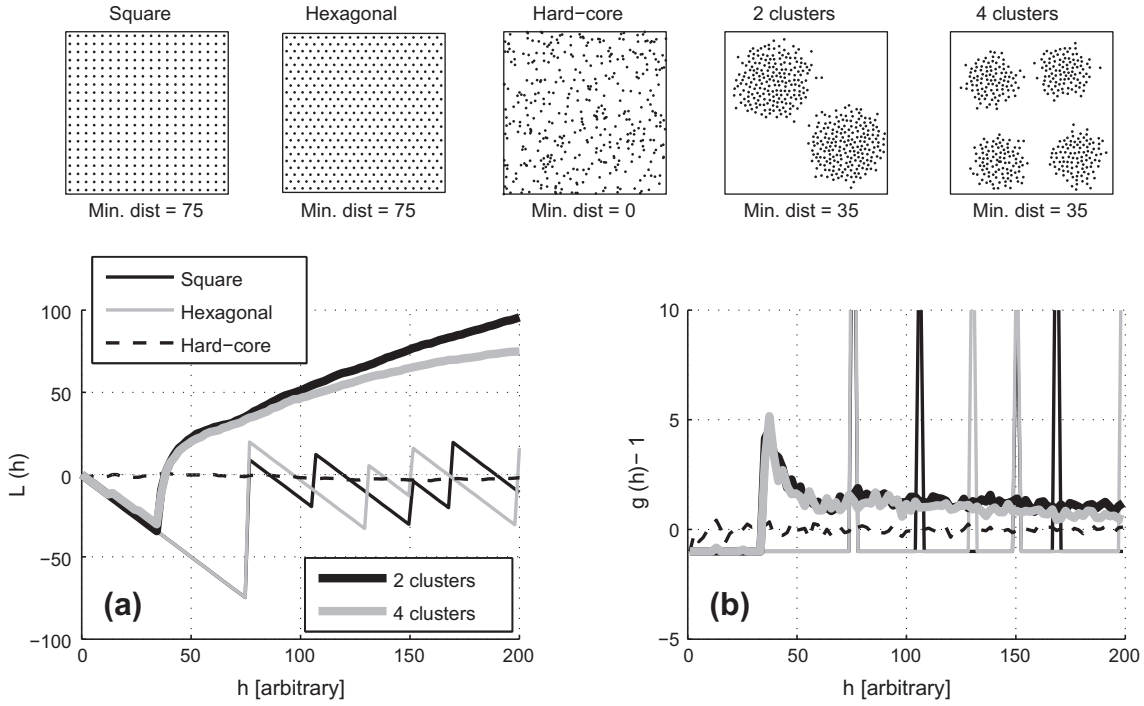

Fig. 3. Second order statistics for typical packing patterns. It is noted that the hard-core process is analogous to the Poisson pattern; (a) the L-function, Eq. (3) and (b) pair distribution function, Eq. (5).

and different fibre content were investigated, and the parameters that turned out to characterise the microstructure were: (i) number of neighbours, (ii) nearest neighbour distance, (iii) contact points per fibre, and (iv) local fibre volume fraction (area fraction between fibre and the corresponding Voronoi cell). These parameters will be used to measure the agreement between the laminates and the simulated composite microstructures.

2. Method

The following section introduces the four steps shown in Fig. 1, namely: (a) fibre architecture of laminates based on digital image analysis, (b) development of a numerical microstructure generator, (c) comparison of microstructure based on laminates and microstructure generator, and (d) parametric variation of fibre radii distribution.

2.1. Fibre architecture based on laminates

Twenty-nine different glass fibre reinforced laminates with varying fibre content were manufactured using the vacuum assisted resin transfer moulding process and a polyester resin. Representative material samples were cut from the cured laminates, encapsulated in epoxy, ground and polished. Micrographs were captured with a LVSEM, and the resulting fibre architecture was mapped using the circular Hough transformation. A post-processing step was applied to measure the different microstructural descriptors mentioned in Section 1.1. For a full presentation of the methodology, see Zangenberg et al. [16]. The fibre volume fraction (FVF) of the samples is determined by a threshold analysis where the micrographs are binarized, and the FVF is calculated as the ratio between white pixels (fibres) and the total number of pixels. The FVF is determined within a bundle and is not representative for the entire composite laminate. The bundle structure is illustrated in Fig. 4.

2.2. Numerical microstructure generator

A numerical microstructure generator is programmed in MATLAB with the following input: the fibre radii distribution (mean, standard deviation, and skewness), required FVF, and the size of the domain. The routine is based on a hard-core allocation followed by a stirring process, and is implemented as:

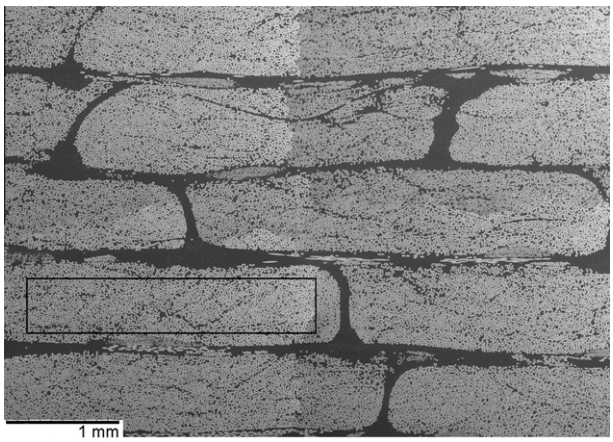

Fig. 4. Typical micrograph of bundle structure observed in glass fibre reinforced composites. Window marks the region where the fibre architecture and FVF are evaluated.

(i) Fibres are allocated using a random number generator, and the individual fibre radius is assigned according to a discretised skew-normal distribution as discussed in the following sections. The compatibility is checked for each new fibre. There are no restrictions on the minimum free distance between the fibres due to the comparison to genuine composite laminates.
(ii) To gain more free space for fibre allocation, the fibres are compacted. Starting with a random fibre, the closest neighbours are moved towards the considered one by a random fraction of the free distance between the considered fibre and its neighbours. Increments (i) and (ii) are iterated until the required FVF has been reached.
(iii) The final stirring is a combination of (ii) and a stirring based the shortest path through all fibres found from the solution to the Travelling Salesman Problem (TSP), see e.g. Lawler et al. [17]. The TSP-path gives the shortest route through all the fibres in the domain, and the stirring is performed by moving the fibres along the direction to the next fibre in the TSP-path. The procedure is repeated three times to get a more consistent fibre packing.

To avoid jamming, the allocation process, (i), is changed for FVF > 60%. To find the empty regions in the domain, a Delaunay triangulation is made, see also Okabe [18]. The area of each Delaunay triangle is determined since there will be an increased probability for free space the larger the area of the Delaunay triangle. A subdomain is generated at the largest areas where the fibres are sought allocated. For the larger volume fractions the final stirring criteria, (iii), is included in the compaction step within the iteration process, (ii). Outputs from the algorithm are the fibre locations (x,y), fibre radius, and the fibre area that falls inside the domain.

2.3. Replication and comparison of fibre architecture

It is evident that the microstructure generator replicates the statistics of the fibre radii distribution. As a general input to the algorithm, the fibre distribution is based on the average values from the 29 analysed images. The size of the SRVE must be large enough to catch the correct statistics of the point pattern and, at the same time, be as small as possible e.g. to maximise the computational efficiency in a finite element program. It has been chosen to model the domain as a square with side lengths $L = 800\ \mu m$. Ongoing studies will identify the minimum size of the SRVE needed in order to satisfy the spatial statistics in the point pattern.

To get a statistical foundation and reproduce any variations in the microstructure, a scatter of different microstructures are simulated (Monte Carlo simulation). It is chosen to generate 8 different FVF's uniformly distributed in the range $55 - 70\%$. For each FVF, 20 different microstructures are generated.

2.4. Parametric variation of fibre radii distribution

A parametric study is conducted in order to investigate any changes in the fibre architecture due to the fibre radii distribution. Since the volume element is size independent, the different fibre radii statistics are normalised and presented in Table 1. Case 1

Table 1
Input data for a parametric variation of the fibre radii distribution.

Case	1	2	3	4	5	6	7	8	9
Mean radius	1	0.5	2	1	1	1	1	1	1
Std. deviation	1	1	1	1.5	0.5	1	1	1	0
Skewness	1	1	1	1	1	0	0.5	2	0

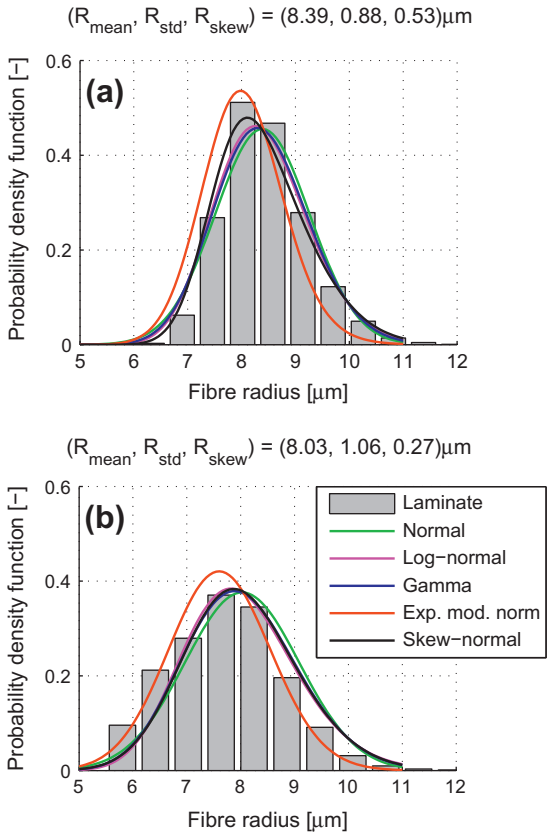

Fig. 5. Two typically observed fibre radii variations in composite laminates, and fit to common probability distributions. The following average parameters for the fibre radii-statistics are obtained from the 29 analysed images (mean, standard deviation, skewness): $(r_{mean}, r_{std}, r_{skew}) = (8.59, 0.74, 0.35)$ µm. (For interpretation of the references to color in this figure legend, the reader is referred to the web version of this article.)

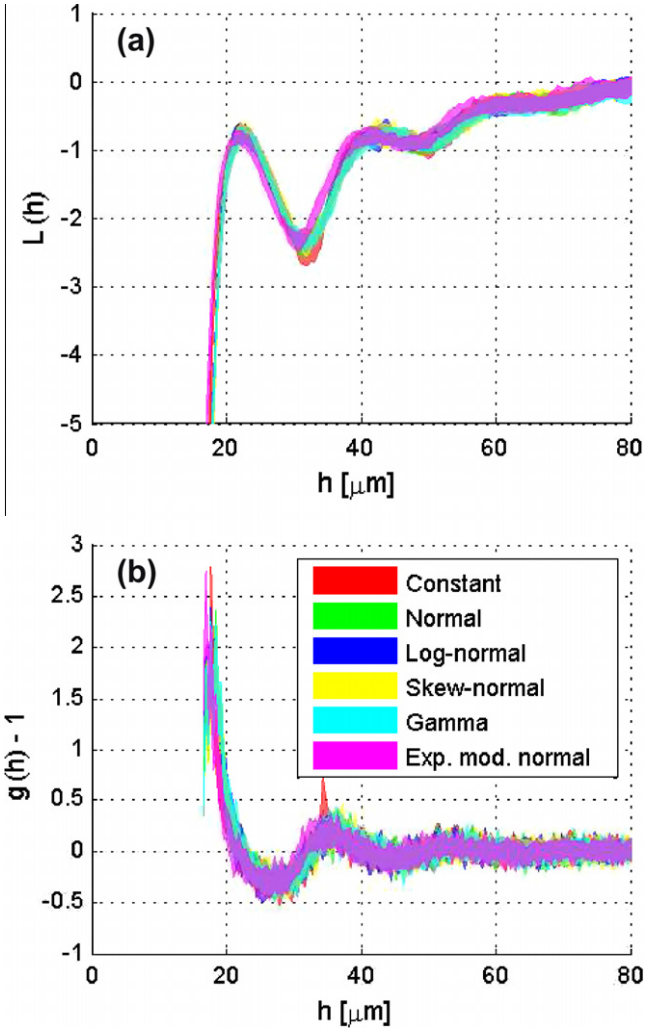

Fig. 6. Second order statistics for different types of fibre radii distribution based on a numerically generated SRVE. The results are presented as deviation from the Poisson pattern with $\hat{L}(h) = \hat{g}(h) - 1 = 0$: (a) the L-function, Eq. (3) and (b) pair distribution function, Eq. (5). (For interpretation of the references to color in this figure legend, the reader is referred to the web version of this article.)

serves as a reference, case 6 is a normal-distribution, and case 9 is with uniform fibre radius. The size of the SRVE is normalised accordingly.

The composite microstructure is investigated for 8 different FVF's uniformly distributed in the range $55 - 70\%$ with 20 different generated microstructures for each FVF.

3. Results

3.1. Fibre architecture based on laminates

A typical result of the fibre detection has been shown in Fig. 1a. The fibres crossing the image boundary of the micrographs remain undetected due to the incomplete shape, and are not being used in the post processing. In the simulations, the fibres that are located closer than a fibre radius away from the boundary are therefore disregarded when determining the L- and g-functions to get consistency. Even though an edge correction is used, this affects the results. The number of mapped fibres varies between 1800 and 8600 (mean 4600) depending on the image size. The image sizes are rectangular shaped, but approximating the shape to a square gives side lengths in the range from 780 µm to 1690 µm (mean 1270 µm), which is slightly larger than the size of the simulated SRVE's. The image size and number of fibres are used to evaluate the statistical significance regarding the K-function, Eq. (4). A typical observed variation in the fibre radii is presented in Fig. 5 along with common probability distributions (normal, log-normal, gamma, exponentially modified normal, and skew-normal).

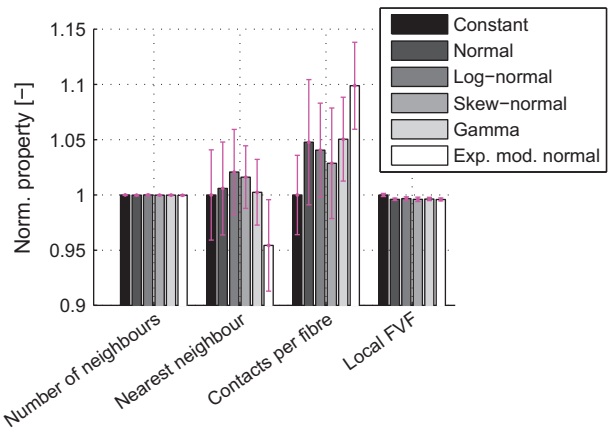

Fig. 7. The effect of fibre radii distribution on selected microstructural parameters based on a numerically generated SRVE. The bar reflects the mean value of the 20 different analyses while the errorbar reflects the standard deviation. (For interpretation of the references to color in this figure legend, the reader is referred to the web version of this article.)

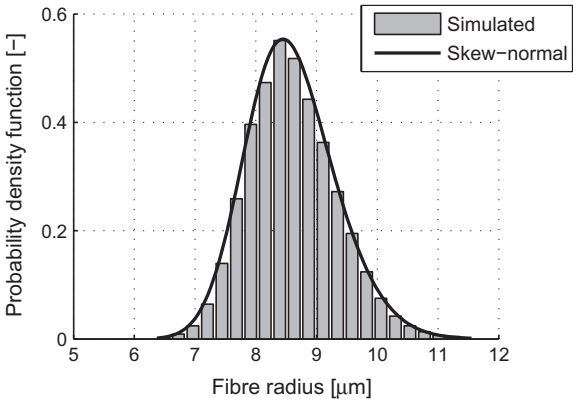

Fig. 8. Example of a discretised radii distribution used as input for the microstructure generator. The skew-normal distribution is plotted for the radii parameters shown in the caption of Fig. 5 for a FVF = 65%.

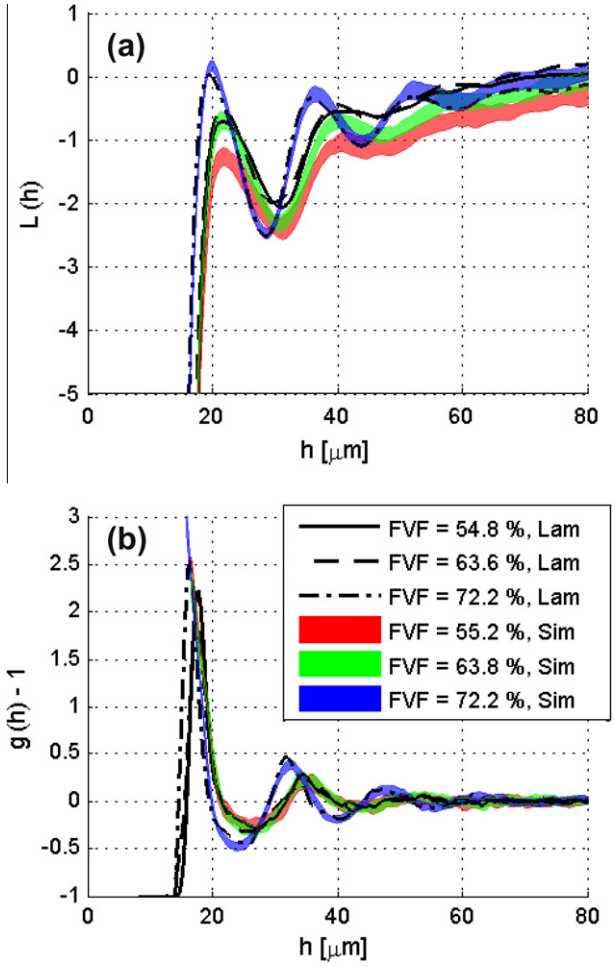

Fig. 9. Comparison of the fibre architecture for different FVF's based on image analysis of composite laminates (Lam) and numerical simulations (Sim). The results are presented as deviation from the Poisson pattern with $\hat{L}(h) = \hat{g}(h) - 1 = 0$: (a) the L-function, Eq. (3) and (b) pair distribution function, Eq. (5). (For interpretation of the references to color in this figure legend, the reader is referred to the web version of this article.)

A positive skewness (right-skewed distribution compared to the normal distribution) is observed for the variation in the fibre radii. Depending on the magnitude of the skewness, the outcome of which distribution provides the best fit, is different. For increasing values of the skewness, cf. Fig. 5a and b, the trend is that the skew-normal distribution gives a better fit compared to the remaining distributions. The exponentially modified normal distribution detects the peak around the mean, but provides a poor fit for radii larger than the mean. The impact of radii distribution on the fibre packing is investigated in Section 3.2.

3.2. Fibre architecture based on numerical simulation

The influence of fibre radii distribution on the fibre packing pattern is investigated by a numerical study using the numerical microstructure generator. Different types of the fibre radii distribution (constant, normal, log-normal, skew-normal, gamma, and exponentially modified normal) are used, and the difference in fibre architecture is addressed. 20 different SRVE's are generated for each type of the fibre radii distribution. The SRVE size is $L \times L = 800 \times 800$ μm, and the requested FVF is 60%. The fibre radii statistics follow from the average parameters in Fig. 5, and the second order statistics are presented in Fig. 6 for the various radii distributions considered.

It is observed from Fig. 6 that there is a small difference between the various fibre radii distributions and the second order statistics since the different analyses fall on top of each other. The number of neighbours, the nearest neighbour distance, the number of contact points per fibre, and the local FVF is shown in Fig. 7 for the different fibre radii distributions. To ease the result presentation, the respective properties in Fig. 7 are normalised with the value obtained from the analysis with constant fibre radius.

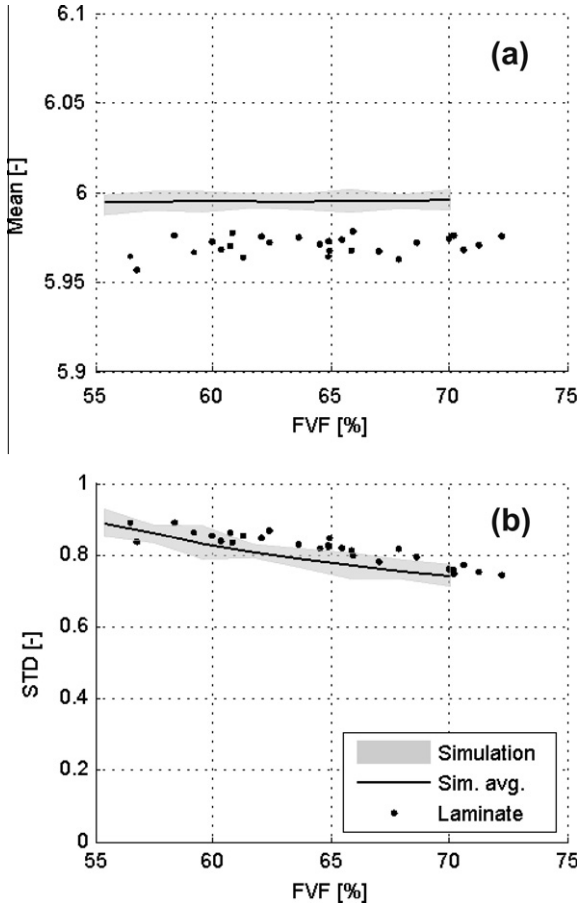

Fig. 10. Comparison of composite laminates and numerical microstructure generator for the number of neighbours as a function of FVF: (a) mean and (b) standard deviation.

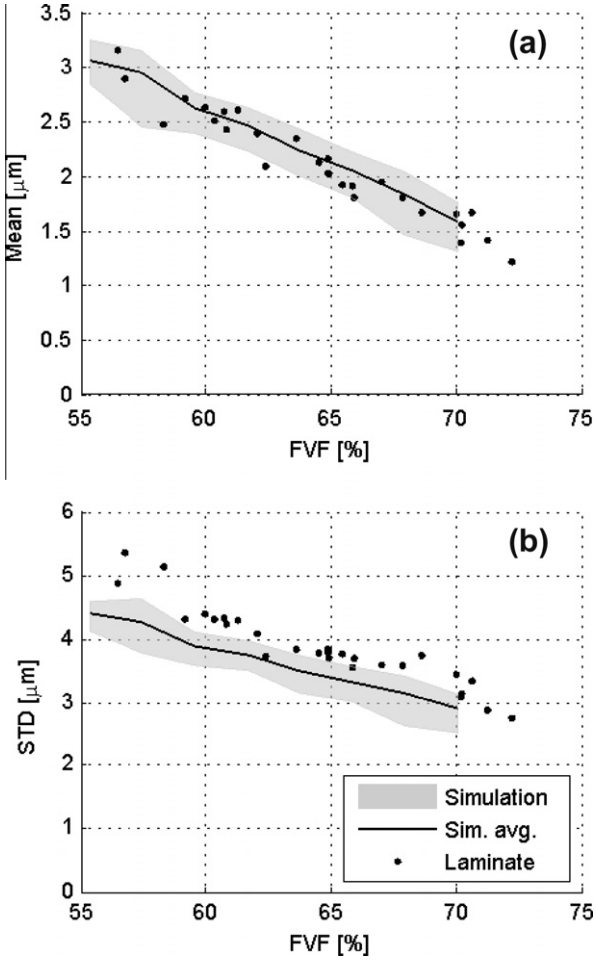

Fig. 11. Comparison of composite laminates and numerical microstructure generator for the nearest neighbour distance as a function of FVF: (a) mean and (b) standard deviation.

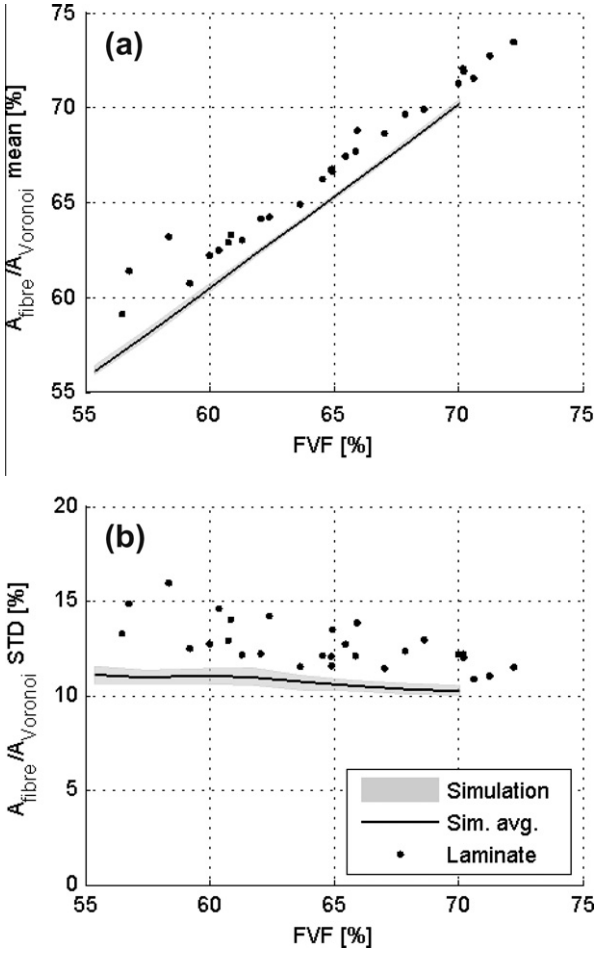

Fig. 13. Comparison of composite laminates and numerical microstructure generator for the local FVF as a function of global FVF: (a) mean and (b) standard deviation.

The number of neighbours and the local FVF, Fig. 7, are unaffected by the different fibre radii distributions, but there is a variation for the nearest neighbour distance and the number of contact points per fibre. This is also to be expected since smaller and larger fibres are included for these distributions, which imply a different and closer packing. Even though there is limited variation in the fibre packing pattern depending on the different probability distributions, the skew-normal distribution is chosen to model the fibre radii statistics. The reason for doing so is discussed in further detail in Section 4.1.

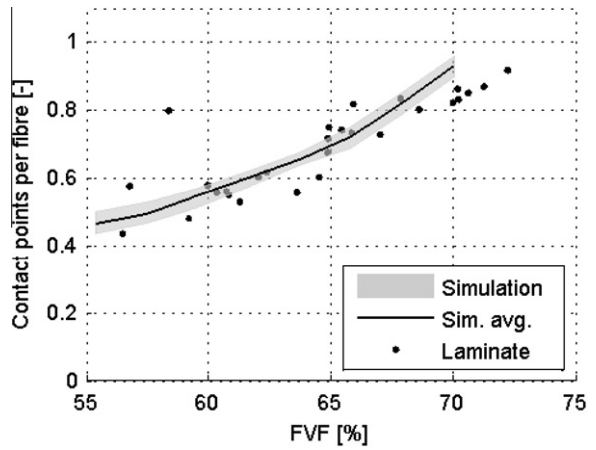

Fig. 12. Comparison of composite laminates and numerical microstructure generator for the number of contact points per fibre as a function of FVF.

A typical example of a simulated microstructure has been presented in Fig. 1b. For all simulations, the number of fibres in each SRVE varies from approximately 1500–2000 for the FVF's in the range from 55% to 70%. An input example of a discretised fibre radii distribution for the numerical microstructure generator is shown in Fig. 8. It is seen that the simulated radii distribution in Fig. 8 provides a reasonable fit to the skew-normal distribution.

3.3. Comparison of fibre architecture from laminates and numerical simulation

Three selected laminates with different FVF's are used to compare the packing pattern with the simulated microstructures. As a representation for the observed microstructures, the configurations with the lowest and largest FVF in the laminates are chosen along with a FVF that falls in-between. In order to get consistency, the fibre radii distribution obtained from the respective laminates is used as input to the numerical microstructure generator. A total number of 30 analyses are run for each FVF, and Fig. 9a shows the L-function, Eq. (3), and Fig. 9b the pair distribution function, Eq. (5), in terms of a scatter curves presenting the respective ranges.

Comparison of the fibre packing pattern in the laminates and the simulations, Fig. 9, reveals that there seems to be similar trends

regarding the clustering distances. The confidence intervals from Eq. (4) are evaluated based on the simulations. For a square domain with side length $L = 800$ μm, and $N = 1500 - 2000$, Eq. (4) yields $CI_{95} = \pm[0.76: 0.57]$. The confidence intervals are directly comparable to the L-function in Fig. 9a, and by comparison it is seen that the fibre arrangements can be regarded as random for $h \gtrsim 60$ μm.

The number of neighbours for each FVF in the composite laminates and simulations is shown in Fig. 10. For the simulated fibre arrangements, the average value is plotted along with the respective minimum/maximum ranges. Skewness is ignored, and all results are assumed to follow normal behaviour described by a mean value and standard deviation.

The fibres tend to arrange in a pseudo-hexagonal pattern where each fibre is associated with approximately six neighbours. This packing tendency is consistent and independent of the FVF. The standard deviation of the number of neighbours, Fig. 10b, is decreasing for increasing FVF meaning that the fibres pack more consistently towards a hexagonal array. The nearest neighbour distance is presented in Fig. 11.

The mean nearest neighbour distance and standard deviation, presented in Fig. 11, decrease for increasing FVF, which seems reasonable for a larger degree of compaction when increasing the FVF. Both trends seem to follow a linear behaviour. The number of contact points per fibre is depicted in Fig. 12.

The number of contact points per fibre, Fig. 12, is an increasing function for increasing FVF. There is an approximately linear tendency between the number of contact points as function of FVF. The local FVF is defined as the area fraction between the fibre and the associated Voronoi cell, and the results are presented in Fig. 13.

The local FVF for the laminates is larger than the global FVF, but with equal magnitude for the simulated microstructures. This is discussed in the following section. Both seem to dependent linearly on the global FVF. The standard deviation seems to be constant and independent of the FVF.

3.4. Parametric variation of fibre radii distribution

Based on the findings in the previous sections, it is believed that the microstructure generator can be used to simulate fibre architectures in a composite material, and a parametric variation of the parameters for the fibre radii distribution seems to be

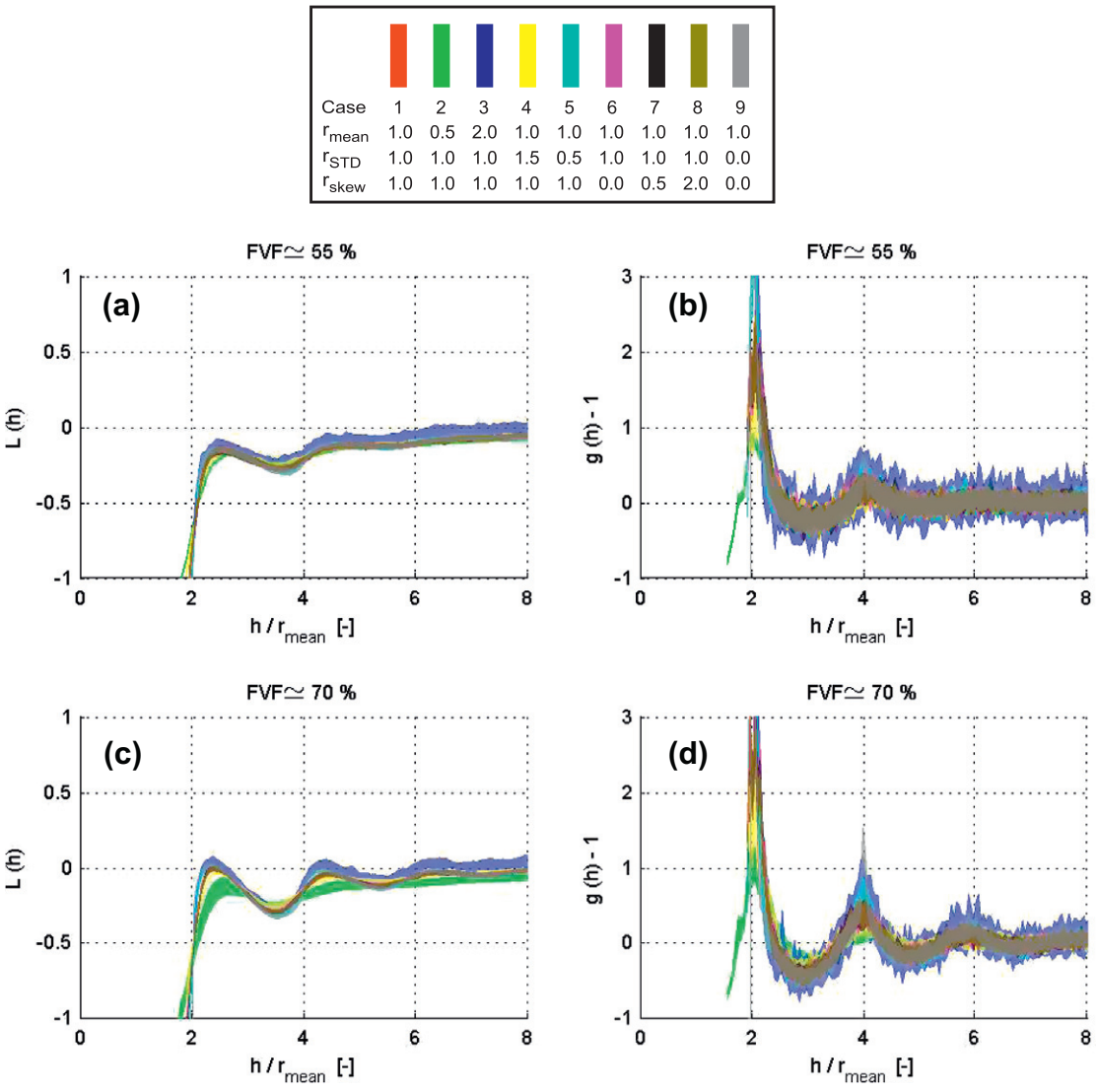

Fig. 14. Second order statistics for two different FVF's for different variations in the fibre radii distribution. (a) and (c): the L-function. (b) and (d): pair distribution function. Top row, (a) and (b): FVF ≃ 55%. Bottom row, (c) and (d): FVF ≃ 70%. (For interpretation of the references to color in this figure legend, the reader is referred to the web version of this article.)

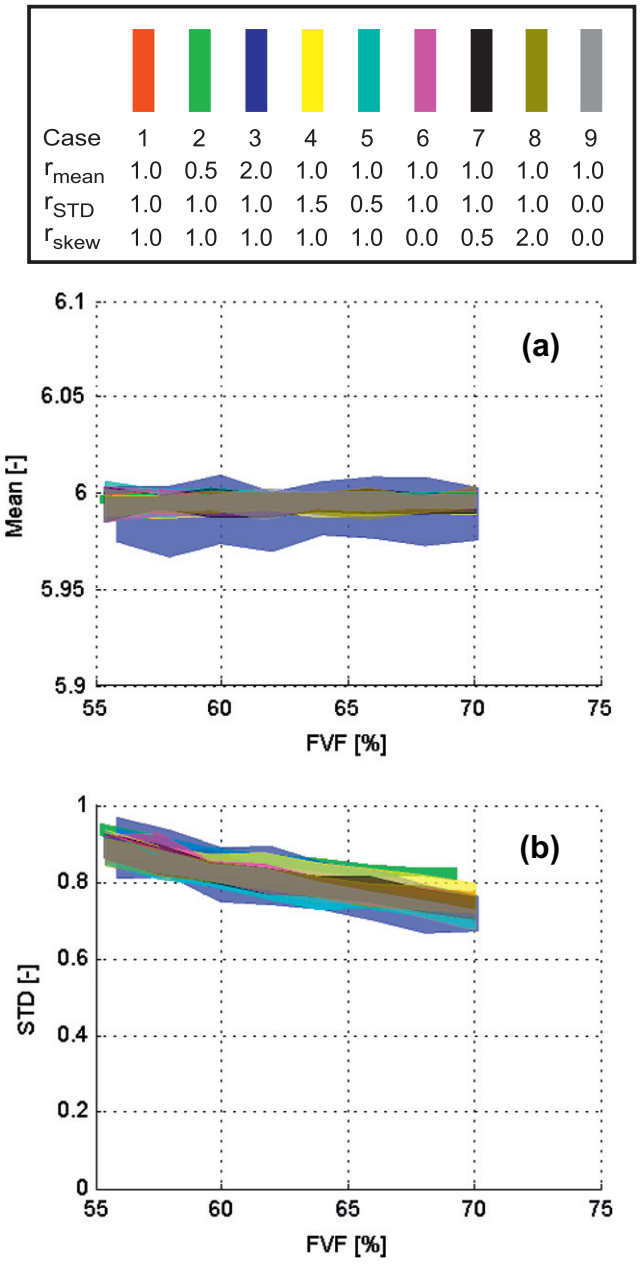

Fig. 15. Number of neighbours as a function of FVF for different variations in the fibre radii distribution: (a) mean and (b) standard deviation. (For interpretation of the references to color in this figure legend, the reader is referred to the web version of this article.)

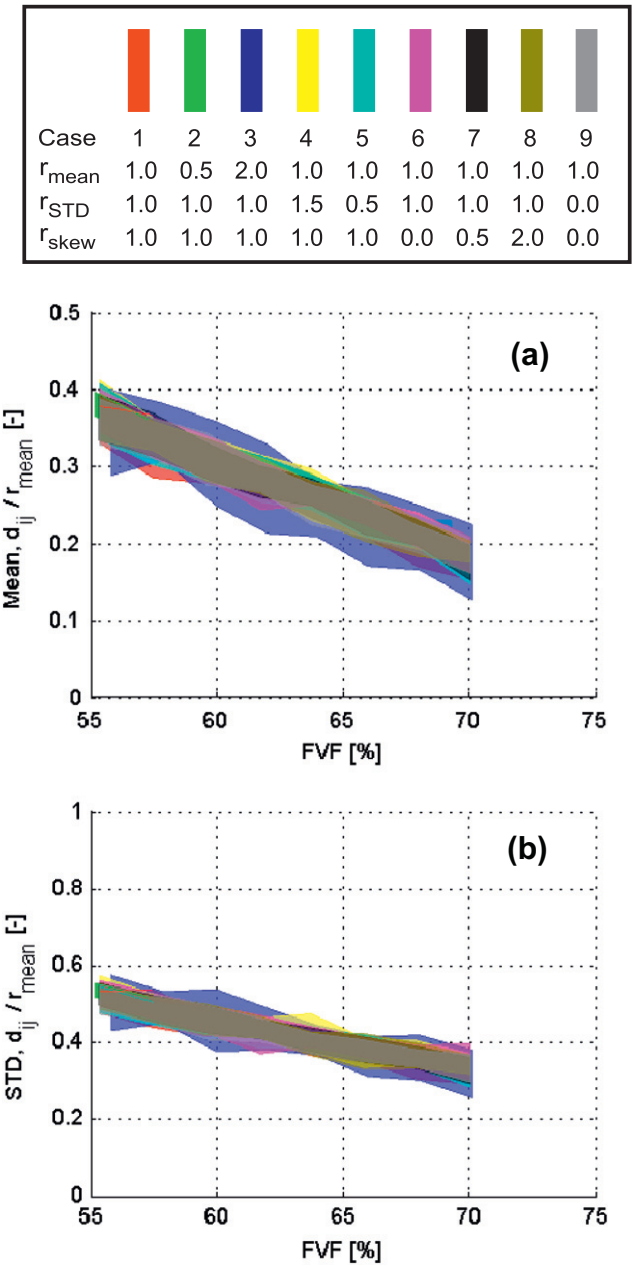

Fig. 16. Nearest neighbour distance, d_{ij}, as a function of FVF for different variations in the fibre radii distribution: (a) mean and (b) standard deviation. (For interpretation of the references to color in this figure legend, the reader is referred to the web version of this article.)

trustworthy. The radii distribution is again modelled as skew-normal. A normalised SRVE is used in the analysis, and to ease the visuality the average data are omitted, and only the respective minimum/maximum ranges are presented. Results are presented in similar format as the previous section, and can be found in Figs. 14–18. For two different FVF's (55% and 70%) the differences in fibre packing patterns are reflected in the *L*-function, Eq. (3), and pair distribution function, Eq. (5), presented in Fig. 14.

Independent on the parameters of the fibre radii distribution, there seems to be an agreement between the fibre packing patterns, and similar behaviour is observed for both FVF's. Again, the confidence intervals from Eq. (4) indicate that that packing patterns tend towards a random configuration for increasing *h*. The number of neighbours is presented in Fig. 15.

The number of neighbours per fibre, Fig. 15, is seen to be unaffected by variations in the fibre radii distribution; nonetheless, with a slight variation on individual simulations for a larger mean radius (blue curve). The nearest neighbour distance is depicted in Fig. 16.

The nearest neighbour distance, shown in Fig. 16, is unaffected by the parameters of the fibre radii distribution. Fig. 17 shows the number of contact points per fibre as a function of FVF.

The number of contact points per fibre, Fig. 17, is independent on the parameters of the fibre radii distribution; however, there seems to be a slightly larger variation for different mean fibre radii. Fig. 18 shows the local FVF as a function of the global FVF.

The local FVF, Fig. 18, is also independent on variations of the fibre radii distribution, but the standard deviation of the local

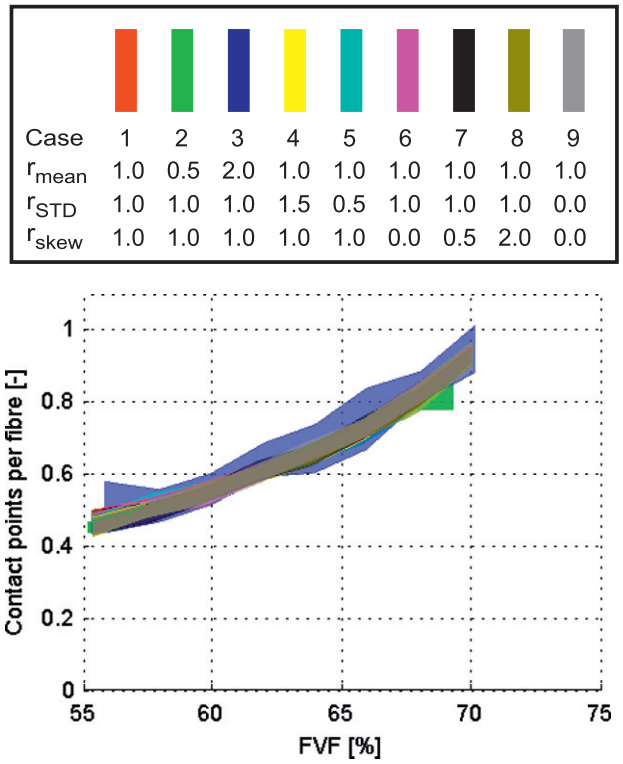

Fig. 17. Contact points per fibre as a function of FVF for different variations in the fibre radii distribution. (For interpretation of the references to color in this figure legend, the reader is referred to the web version of this article.)

FVF changes when the mean value or standard deviation of the fibre radii are varied.

4. Discussions

4.1. Fibre architecture from laminates and numerical simulation

Due to the glass fibre manufacturing process there will be a minimum fibre radius, which is caused by the fact that the smallest fibres tend to break during processing. This means a tendency for a right-skewed fibre radii distribution, e.g. as shown in Fig. 5. It is seen from Figs. 6 and 7 that the fibre packing pattern is not affected significantly by the different fibre radii distributions considered. Thus, in order to be able to model a wider- and skew-radii distribution, and to get as close as possible to the observations made in genuine laminates, it is chosen to use the skew-normal distribution for the fibre radii variation. Even though the fibre packing pattern does not change significantly depending on the fibre radii distribution, see e.g. Figs. 6 and 7, there is a connection to the mechanical properties. For instance, fibres in contact are severe regarding local stress concentrations, see e.g. Kushch et al. [19]. It is seen from Fig. 7 that the number of contact points per fibre increase with approximately 10% if the fibre radii distribution is modelled as skew. Therefore, it is recommended to use a distribution that models skewness (e.g. as the skew-normal distribution used in the present) even though the fibre packing pattern remains somewhat unchanged.

It is likely that the fibre radii distribution from the laminates should be continuous rather than discrete as presented in Fig. 5, but since the observed radii statistics are determined based on pixels values with finites size, the distribution is discrete.

Fig. 9 shows the differences in the fibre packing pattern in terms of the L- and g-functions for different FVF's. Both show characteristic peaks in multiples of the (mean) fibre diameter plus the

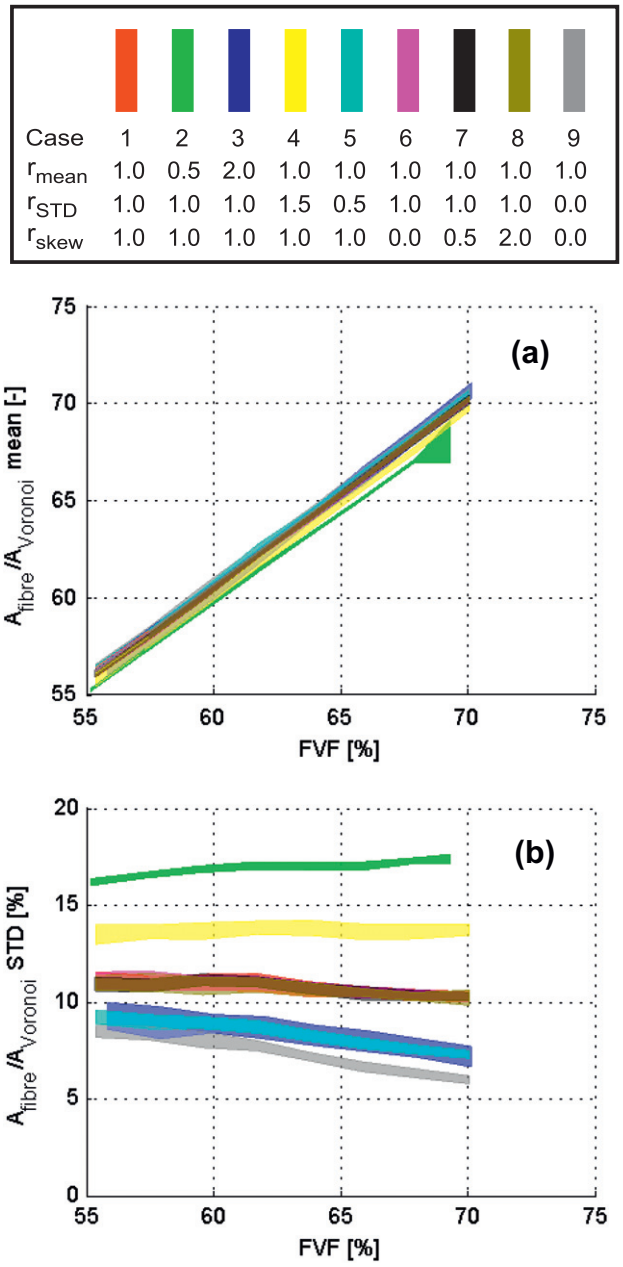

Fig. 18. Local FVF as a function of global FVF for different variations in the fibre radii distribution: (a) mean and (b) standard deviation. (For interpretation of the references to color in this figure legend, the reader is referred to the web version of this article.)

nearest neighbour distance meaning that there is a certain degree of clustering/regularity at these distances. This tendency is most pronounced for values of h approximately <60 μm. The confidence intervals from Eq. (4) show that the point pattern can be regarded as random for $h \gtrsim 60\ \mu m \simeq 7r_{mean}$, which is in similar magnitude as reported by Melro et al. [3]. Since the FVF is an average characterisation parameter for the study region, an increasing FVF means a more compact fibre packing. As it is seen from both the L- and g-functions, an increasing FVF does not change the fibre packing pattern significantly, but ensures a tighter packing. This is reflected in a horizontal shift to the left in the functions meaning that a tighter fibre packing is present for increasing FVF.

For all considered descriptive parameters (number of neighbours, nearest neighbour distance, contact points per fibre, and local FVF), the simulations seem to match the statistical point

pattern behaviour in the laminates quite accurately. All parameters appear to be linear related to the FVF. The simulations of the mean local FVF predict a lower value compared to the laminates, which is due to inaccuracies in the circle detection algorithm for the considered microscope magnification, see e.g. Zangenberg et al. [16]. Due to the characteristics of the circle detection, it is likely that the fibre radius detected by the Hough algorithm will be larger than the actual fibre radius, leading to an increased value of the local FVF. Still, the slope of the two curves in Fig. 13a is somewhat alike.

A parametric variation of the fibre radii distribution reveals that a varying mean fibre radius does not change the fibre architecture, which is due to the fact that the SRVE is a dimensionless quantity and scales with the fibre radius.

4.2. Fibre radii distribution and mechanical properties

The influence of variations in the fibre radii distribution on mechanical properties is outside the scope of this work, but other studies have shown that a change in fibre radius have an effect on the mechanical laminate properties. Adams and Short [20] (long glass fibres/polyester matrix, flexure and torsion experiments) as well as Ramsteiner and Theysohn [21] (short glass fibre reinforced polyamide, tension and impact experiments) studied the relation between the (mean) fibre radius and mechanical properties, and found that the longitudinal Young's modulus of the composite was independent on the fibre radius. This is also what could be expected using the rule of mixtures. Adams and Short [20] also found an increase in interlaminar shear strength for decreasing fibre radius, and Ramsteiner and Theysohn showed an increase in composite failure strength for a smaller mean fibre radius. They also found that the interfacial shear strength was independent on fibre radius, which is in contradiction to the work of Moon et al. [22] (glass fibre/epoxy matrix, pullout experiments) who reported and increase in strength for a decrease in fibre radius. Unfortunately, no references are found for the influence of fibre radii statistics on the fatigue performance. The above presentation illustrates that there is at least an interconnection between fibre radius and the static mechanical composite properties. It is shown in the present study that the fibre radii distribution has limited effect on the fibre architecture, but it is still an open question which fibre radii distribution is ideal to ensure optimum mechanical properties, thermal behaviour, damage tolerance, and fatigue performance.

5. Conclusion

Statistical Representative Volume Element's (SRVE's) of Glass Fibre Reinforced Polymers (GFRP's) have gained interest due to their feasibility in numerical simulations, but it is essential that the SRVE replicates the microstructure of the materials considered. A quantitative study relates the fibre architecture found in composite laminates to a SRVE. Digital image analysis of polished cross-sections of a unidirectional GFRP has been used to characterise the fibre architecture and compare it to numerically generated SRVE's.

From the analysed laminates, it is shown that the fibre radii variation is best described by a right skewed distribution. In order to replicate the correct statistics of the fibre radii variation, it is recommended to use the skew-normal distribution well aware that the fibre packing pattern remains unchanged if another probability distribution is used.

A numerical microstructure generator demonstrates that the spatial statistics in the fibre architecture can be replicated, and that a reliable and statistically consistent SRVE can be simulated. Based on Monte Carlo simulations, the microstructure generator simulates fibre architectures that are statistically similar to the GFRP's. It is shown that the fibre packing pattern is random on a length scale approximately larger than $7r_{mean}$ where r_{mean} is the mean fibre radius.

A parametric variation of the fibre radii distribution (mean, standard deviation, and skewness) shows that the fibre architecture is unaffected by any changes of the parameters considered. This is an important property that can be used in future numerical studies to optimise the mechanical performance of GFRP's with respect to fibre geometry.

Acknowledgements

The authors thank Antonio Melro from the University of Porto for inspiring to the current work as well as providing the foundation for the developed algorithm.

References

[1] Swaminathan S, Ghosh S. Statistically equivalent representative volume elements for unidirectional composite microstructures: Part II – with interfacial debonding. J Compos Mater 2006;40:605.
[2] Wongsto A, Li S. Micromechanical FE analysis of UD fibre-reinforced composites with fibres distributed at random over the transverse cross-section. Compos A: Appl Sci Manuf 2005;36:1246–66.
[3] Melro A, Camanho P, Pinho S. Generation of random distribution of fibres in long-fibre reinforced composites. Compos Sci Technol 2008;68:2092–102.
[4] Thomas M, Boyard N, Perez L, Jarny Y, Delaunay D. Representative volume element of anisotropic unidirectional carbon-epoxy composite with high-fibre volume fraction. Compos Sci Technol 2008;68:3184–92.
[5] Trias D, Costa J, Turon A, Hurtado J. Determination of the critical size of a statistical representative volume element (SRVE) for carbon reinforced polymers. Acta Mater 2006;54:3471–84.
[6] Trias D, Costa J, Mayugo J, Hurtado J. Random models versus periodic models for fibre reinforced composites. Computat Mater Sci 2006;38:316–24.
[7] Vaughan T, McCarthy C. A combined experimental-numerical approach for generating statistically equivalent fibre distributions for high strength laminated composite materials. Compos Sci Technol 2010;70:291–7.
[8] Ripley BD. The second-order analysis of stationary point processes. J Appl Probab 1976:255–66.
[9] Pyrz R. Quantitative description of the microstructure of composites. Part I: morphology of unidirectional composite systems. Compos Sci Technol 1994;50:197–208.
[10] Ghosh S, Nowak Z, Lee K. Quantitative characterization and modeling of composite microstructures by Voronoi cells. Acta Mater 1997;45:2215–34.
[11] Dixon PM. Ripley's k function. In: Encyclopedia of environmetrics. John Wiley & Sons, Ltd; 2006. p. 1796–803.
[12] de Azeredo Lopes SM. Statistical analysis of particle distributions in composite materials. Ph.D. thesis. University of Sheffield; 2000.
[13] Yamada I, Rogerson PA. An empirical comparison of edge effect correction methods applied to k-function analysis. Geogr Anal 2003;35:97–109.
[14] Goreaud F, Pelissier R. On explicit formulas of edge effect correction for ripley's k-function. J Veg Sci 1999:433–8.
[15] Getis A, Franklin J. Second-order neighborhood analysis of mapped point patterns. Ecology 1987;68:473.
[16] Zangenberg J, Larsen JB, Østergaard RC, Brøndsted P. Methodology for characterisation of glass fibre composite architecture. Plast Rubber Compos 2012;41 4:187–93.
[17] Lawler EL, Rinnooy-Kan AH, Lenstra JK, Shmoys DB. The traveling salesman problem: a guided tour of combinatorial optimization, vol. 3. New York: Wiley; 1985.
[18] Okabe A. Spatial tessellations: concepts and applications of Voronoi diagrams. John Wiley & Sons Inc; 2000.
[19] Kushch V, Shmegera S, Brøndsted P, Mishnaevsky Jr L. Numerical simulation of progressive debonding in fiber reinforced composite under transverse loading. Int J Eng Sci 2011;49:17–29.
[20] Adams RD, Short D. The effect of fibre diameter on the dynamic properties of glass-fibre-reinforced polyester resin. J Phys D: Appl Phys 1973;6:1032–9.
[21] Ramsteiner F, Theysohn R. The influence of fibre diameter on the tensile behaviour of short-glass-fibre reinforced polymers. Compos Sci Technol 1985;24:231–40.
[22] Moon CK, Lee J-O, Cho HH, Kim KS. Effect of diameter and surface treatment of fiber on interfacial shear strength in glass fiber/epoxy and HDPE. J Appl Polym Sci 1992;45:443–50.

[P3]

Zangenberg J. and Brøndsted P.

DETERMINATION OF THE MINIMUM SIZE OF A STATISTICAL REPRESENTATIVE VOLUME ELEMENT FROM A FIBRE-REINFORCED COMPOSITE BASED ON POINT PATTERN STATISTICS

Scripta Materialia, **68**, pp. 503-505, (2013).

Available online at www.sciencedirect.com

SciVerse ScienceDirect

Scripta Materialia 68 (2013) 503–505

Scripta MATERIALIA

www.elsevier.com/locate/scriptamat

Determination of the minimum size of a statistical representative volume element from a fibre-reinforced composite based on point pattern statistics

J. Zangenberg[a,b,*] and P. Brøndsted[b]

[a]LM Wind Power Blades, Composite Mechanics, Jupitervej 6, DK-6000 Kolding, Denmark
[b]Department of Wind Energy, Section of Composites and Materials Mechanics, Technical University of Denmark, Risø Campus, Frederiksborgvej 399, DK-4000 Roskilde, Denmark

Received 1 October 2012; revised 26 November 2012; accepted 27 November 2012
Available online 6 December 2012

In a previous study, Trias et al. [1] determined the minimum size of a statistical representative volume element (SRVE) of a unidirectional fibre-reinforced composite primarily based on numerical analyses of the stress/strain field. In continuation of this, the present study determines the minimum size of an SRVE based on a statistical analysis on the spatial statistics of the fibre packing patterns found in genuine laminates, and those generated numerically using a microstructure generator.

Keywords: 2-D quantitative analysis; Scanning electron microscopy (SEM); Fibre-reinforced composites; Glass fibre; Monte Carlo simulation

In order to numerically investigate mechanical properties and damage evolution of fibre-reinforced composites, statistical representative volume elements (SRVEs) are widely used (see e.g. [1–3] for a general presentation). The size of the SRVE is fundamental since it must be large enough to catch the correct stress/strain fields and spatial statistics of the fibre packing pattern. At the same time, the SRVE must be as small as possible to minimize the computational effort in a finite element context. For transverse cross-sections of unidirectional fibre-reinforced composites, limited information is available regarding the minimum size of the SRVE; however, Trias et al. [1] have determined the minimum SRVE size based on different mechanical analyses (e.g. stress/strain field, effective properties, and energy) of generated microstructures made of a carbon/epoxy system. In order to replicate the evaluation parameters considered with reasonable reliability, the minimum side length obtained is $L = 50\,r$ for a square-shaped SRVE with uniform fibre radius r. They did not consider any comparisons to actual microstructures found in genuine composite laminates, and as continuation of the work of Trias et al., the present study determines the minimum size of an SRVE with non-uniform fibre radii distribution considering only the spatial point pattern statistics. For varying size of the square-shaped SRVE, a comparison is made between the fibre packing patterns found in genuine composite laminates and that produced numerically using a microstructure generator.

The fibre packing pattern of three different unidirectional composite laminates with varying fibre volume fraction (FVF) is analysed using digital image analysis. The laminates (glass fibres/polyester matrix) are manufactured using the VARTM process, and micrographs of the microstructure are captured from transverse cross-sections using a scanning electron microscope. The fibre architecture is mapped by the circular Hough transformation, which yields the fibre location and the individual fibre radii [4]. The obtained fibre radii statistics (mean, standard deviation and skewness) from the analysed laminates are: $r_{mean} = 8.59$ μm, $r_{std} = 0.74$ μm, and $r_{skew} = 0.35$ μm. These fibre radii statistics are used as input to a numerical microstructure generator to replicate the fibre architecture. The microstructure generator is inspired by the work of Melro et al. [2] and is based on a hard-core generator with a sophisticated stirring criteria to ensure the fibre packing, especially

* Corresponding author at: Department of Wind Energy, Section of Composites and Materials Mechanics, Technical University of Denmark, Risø Campus, Frederiksborgvej 399, DK-4000 Roskilde, Denmark. Tel.: +45 5138 8407; fax: +45 4677 5758.; e-mail addresses: jzan@dtu.dk; jezh@lmwindpower.com; pobr@dtu.dk

1359-6462/$ - see front matter
http://dx.doi.org/10.1016/j.scriptamat.2012.11.032

for fibre volume fractions above 60%. The fibre stirring criteria is a combination of a compaction step of the closest fibre neighbours and the shortest path through all fibres. Fibre allocation for fibre volume fractions above 60% is ensured using a sub-domain allocation based on the area of the largest Delaunay triangles. By comparison between genuine laminates and generated microstructures, it is found that the numerical microstructure generator is capable of producing statistically similar fibre architectures with respect to the point pattern, and thus it is suitable for numerical generation of SRVEs [5]. These two tools are used in the present to study the minimum size of the SRVE that can be used to replicate the spatial statistics of the composite microstructure. Five different sizes of the square-shaped SRVE ($L \times L$, varying from $L = 300$–700 μm) are simulated, and selected microstructural parameters are used to evaluate the consistency. For each size of the SRVE, different FVFs are generated, matching those found in the laminates. Five different microstructures are generated for each FVF to identify individual variations. The microstructural characterization parameters are: the number of neighbours per fibre, the nearest neighbour distance, the number of contact points per fibre and the local FVF (fibre area in relation to the area of the associated Voronoi cell; see e.g. [5]). These parameters are described by the mean value obtained from the different analyses. The spatial point pattern is evaluated for a single FVF using a second-order statistical analysis based on the Ripley K-function, $K(h)$, and the pair distribution function, $g(h)$ [5–8]. The second-order statistics are presented as the deviation from complete spatial randomness (CSR) in terms of the expressions $L(h) = \sqrt{K(h)/\pi} - h$ and $g(h) - 1$, which for the case of CSR yields $L(h) = g(h) - 1 = 0$ [5,6,8]. Fibre centres are used as input for the determination of the second-order statistics.

The FVFs obtained in the laminates are [60.4, 65.4, 70.2]%, and the simulated microstructures are chosen to be with FVF = [60, 65, 70]%. The number of neighbours per fibre, the nearest neighbour distance, the number of contact points per fibre and the local FVF are presented in Figure 1 for the different sizes of the SRVE. For each FVF presented, the respective property is normalized with the associated value from the corresponding laminate. This means that an identical replication of the microstructure is obtained for the properties equal to unity. From Figure 1 it is observed that the number of neighbours per fibre, the nearest neighbour distance, the number of contact points per fibre and the local FVF are all unaffected by the size of the SRVE; nonetheless, there is a larger individual scatter for smaller sizes of the SRVE (larger magnitude of the errorbar). Figure 2 shows the deviation between the requested and obtained FVFs from the microstructure generator. According to Figure 2, a smaller SRVE size and a lower requested FVF imply a larger deviation in the obtained FVF in the simulations. Furthermore, there seems to be an

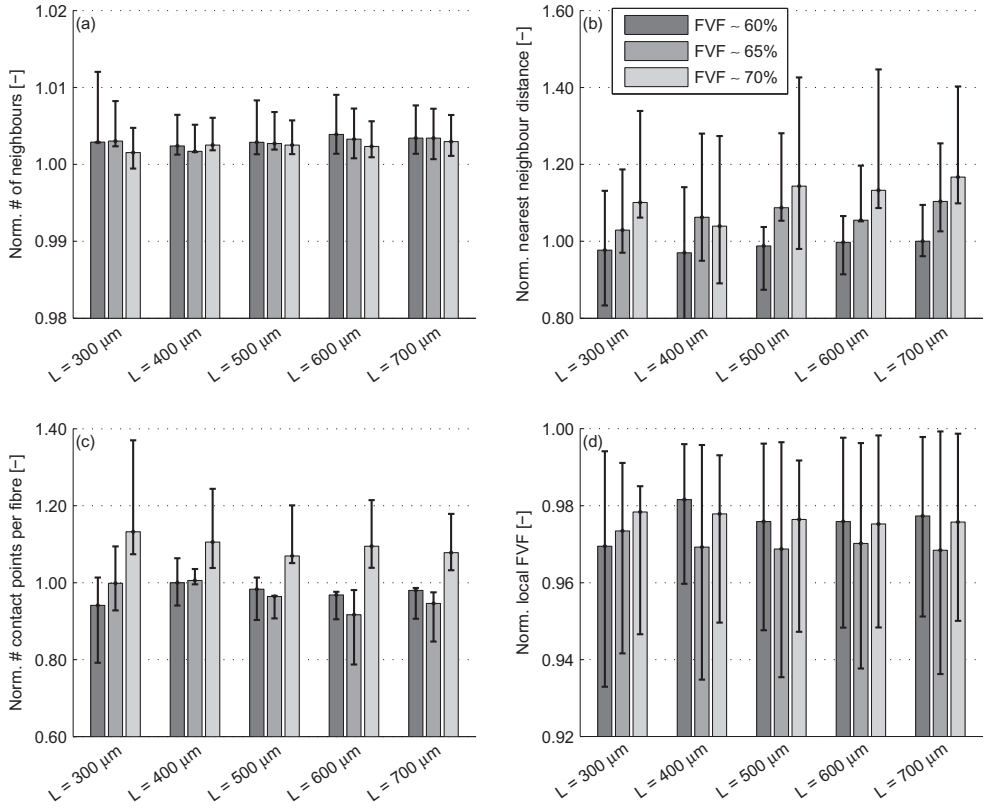

Figure 1. Differences between the fibre packing pattern for a numerically generated SRVE and composite laminates. The SRVE is square shaped, with side length L. Results are normalized with the value obtained from the respective composite laminate with the same FVF, and the error bar reflects the minimum/maximum value obtained in the simulation. (a) Number of neighbours. (b) Nearest neighbour distance. (c) Number of contact points per fibre. (d) Local FVF.

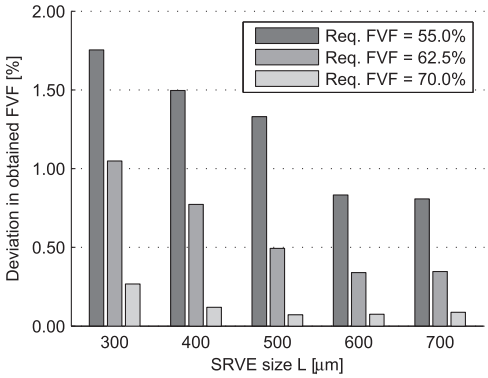

Figure 2. Deviation in the requested and obtained fibre volume fraction from the numerical microstructure generator.

asymtotic behaviour for $L \geqslant 600$ μm. Therefore, in order to obtain the least deviation on the required FVF and to reduce individual scattering, the side length should be at least $L = 600$ μm. The second-order statistics are presented in Figure 3 for a selected FVF, namely FVF = 65%. In Figure 3 the functions show characteristic peaks in multiples of the mean fibre diameter plus the communal fibre-to-fibre distance. This means an increased probability of clustering for these distances. For increasing values of h, the packing pattern tends towards CSR, with $L(h) = g(h) - 1 = 0$. It is noted from Figure 3 that the packing pattern of the laminate follows a CSR pattern if $h \gtrsim 60\ \mu\text{m} \simeq 7r_{mean}$. This means that the size of the SRVE must be larger than $7r_{mean}$ in order to replicate the CSR pattern. This observation is in accordance with that of Zangenberg and Brøndsted [5]. For the smaller side lengths of the SRVE, the second-order statistics cannot be replicated due to the small amount of fibres, which is reflected in the deviating patterns, especially distinct for $L < 600$ μm, see also the magnified image in Figure 3(a). For $L < 600$ μm the functions seem to drift away from the laminate data, while, by inspection and comparison to the genuine laminate, it is found that the deviation is reduced for $L \geqslant 600$ μm. Therefore, $L \geqslant 600$ μm appears to be a suitable minimum side length for the SRVE.

If the fibre radii distribution is assumed to follow a normal behaviour, then 99+% of the distribution is covered within the range of $r_{mean} \pm 3r_{std}$. Since larger radii imply a more difficult fibre allocation in the simulations, an equivalent radius, r_{eq}, accounting for the non-uniformity of the radii distribution, is proposed as: $r_{eq} = r_{mean} + 3r_{std}$. Trias et al. [1] found that a normalized side length equal to $\delta = L/r = 50$ for a square-shaped SRVE with uniform fibre radius, r, would be sufficient to replicate the correct stress/strain field. Using this notation with the equivalent radius and $L = 600$ μm, it is found that $\delta = L/r_{eq} = 56$ is sufficient for the spatial point pattern statistics to be satisfied. Following the conclusion from Trias et al., it is noted that, for this value of δ, the stress and strain fields will also be satisfied. Therefore, the spatial point pattern statistic of the fibre microstructure can be replicated for approximately the same size of the SRVE.

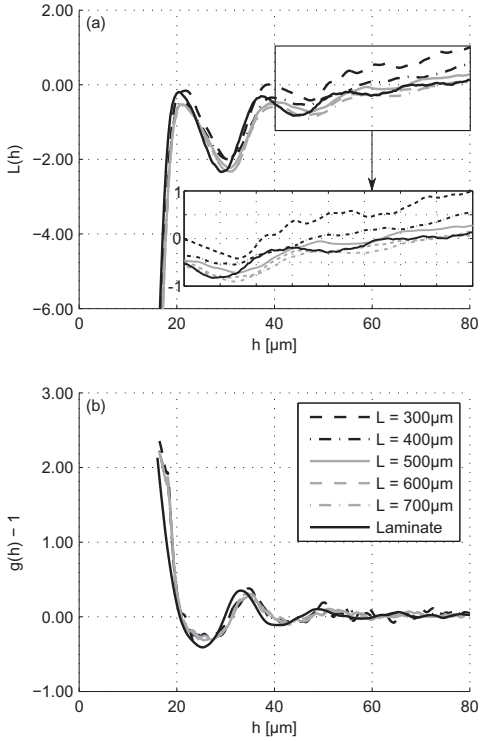

Figure 3. Second-order statistics of composite architecture from genuine laminates and simulated microstructures. Results are shown for FVF = 65%. The SRVE is square shaped, with side length L. (a) The L-function. (b) Pair distribution function.

In summary, the minimum size of an SRVE of a transverse cross-section from a unidirectional fibre-reinforced composite with non-uniform fibre radii distribution is investigated using point pattern statistics. Numerical microstructures are generated for different sizes of the volume element, and the resulting fibre packing pattern is compared to that found in genuine composite laminates. For side lengths of the square-shaped SRVE $L > 600$ μm, all considered evaluation parameters are met. Introducing an equivalent fibre radius $r_{eq} = r_{mean} + 3r_{std}$, the point pattern statistics are replicated for $\delta = L/r_{eq} = 56$. This value corresponds to the findings by Trias et al. [1] considering numerically generated SRVEs and the mechanical performance.

[1] D. Trias, J. Costa, A. Turon, J. Hurtado, Acta Mater. 54 (2006) 3471.
[2] A. Melro, P. Camanho, S. Pinho, Compos. Sci. Technol. 68 (2008) 2092.
[3] Z. Shan, A.M. Gokhale, Comput. Mater. Sci. 24 (2002) 361.
[4] J. Zangenberg, J.B. Larsen, R.C. Østergaard, P. Brøndsted, Plast. Rubber Compos. 41 (2012) 187.
[5] J. Zangenberg, P. Brøndsted, Compos. A – Appl. Sci. Accepted (2012) XX.
[6] P.M. Dixon, Encyclopedia of Environmetrics, third ed., John Wiley & Sons, Ltd., Chichester, 2002.
[7] R. Pyrz, Compos. Sci. Technol. 50 (1994) 197.
[8] S. Ghosh, Z. Nowak, K. Lee, Acta Mater. 45 (1997) 2215.

[P4]

Zangenberg J., Brøndsted P, and Gillespie J.W. Jr.

FATIGUE DAMAGE PROPAGATION IN UNIDIRECTIONAL GLASS FIBRE REINFORCED COMPOSITES MADE OF A NON-CRIMP FABRIC

Journal of Composite Materials, **Accepted**, (2013).

Fatigue damage propagation in unidirectional glass fibre reinforced composites made of a non-crimp fabric

Jens ZANGENBERG [1, 2 *], Povl BRØNDSTED [2], John W. GILLESPIE Jr. [3]

[1]*LM Wind Power Blades, Composite Mechanics, Jupitervej 6, DK-6000 Kolding, Denmark*
[2]*Department of Wind Energy, Section of Composites and Materials Mechanics, Technical University of Denmark, Risø Campus, Frederiksborgvej 399, DK-4000 Roskilde, Denmark*
[3]*Center for Composite Materials, Department of Materials Science and Engineering, Department of Civil and Environmental Engineering, Department of Mechanical Engineering, University of Delaware, Newark, Delaware 19716, USA*
** Corresponding author: Jens Zangenberg, e-mail: jzan@dtu.dk, tel: +45 5138 8407, fax. +45 4677 5758.*

ABSTRACT: Damage progression in unidirectional glass fibre reinforced composites manufactured of a non-crimp fabric subjected to tension-tension fatigue is investigated, and a quantitative explanation is given for the experimentally observed stiffness degradation. The underlying damage-mechanisms are examined using three distinct microscopic analyses, and the transverse crack density is measured. It is documented that the stiffness loss in fatigue is directly related to fibre fractures in the load-carrying axial fibre bundles, initialised by interface debonding and cracking in the transverse backing bundles. A simple stiffness spring model validates the stiffness loss observed. A fatigue damage scheme is presented, which suggests that damage initiates due to failure of the backing bundle causing a stress concentration in the axial load carrying fibres. This stress concentration, along with fretting fatigue, gives rise to axial fibre fractures and a loss of stiffness, eventually leading to final failure. The uniqueness of the present work is identification of the mechanisms associated with tension fatigue failure of unidirectional non-crimp fabrics used for wind turbine blades. The observed damage mechanisms need further attention and understanding in order to improve the fatigue life-time of unidirectional glass fibre reinforced non-crimp fabrics.

KEYWORDS: Fatigue damage; glass fibre reinforced composite; microscopy; fibre fracture; stiffness degradation; non-crimp fabric.

INTRODUCTION

Stiffness degradation of unidirectional Glass Fibre Reinforced Polymers (GFRP's) under tension fatigue loading is a well-known observation.[1-5] Nonetheless, there has not been any unambiguous explanation for what mechanisms cause this stiffness loss in the unidirectional GFRP's made of a non-crimp fabric (NCF). However, for regular cross-ply (or angle-ply) laminates, the damage mechanisms are well described both for static and cyclic loading.[6-10] Simple calculations using the rule-of-mixtures show that the stiffness loss of the unidirectional composite cannot be solely explained by loss of matrix stiffness alone; hence, fractures of individual axial load-carrying fibres must occur. This fact has been reported by different researchers e.g. Gamstedt & Talreja.[11] A typical tension-tension fatigue process for a unidirectional GFRP under constant stress is sketched in Figure 1(a) showing two different common types of observable damage: degradation of stiffness and/or increase in material damping (increasing size of the hysteresis loop). Continuous monitoring of these damage variables during a fatigue experiment enables a quantitative measurement of the damage evolution as function of load cycles, Figure 1(b). The damage progression in Figure 1(b) is typically characterised by a non-linear initiation stage (stage I), a stage of uniform linear damage propagation (stage II), and finally stage III where damage is localised and leads to final failure.[1] The magnitude and evolution of the stiffness loss is dependent on loading type, loading magnitude, layup sequence, and material properties. Often, the global stiffness loss

leads to localisation before the entire stiffness of the composite is lost.[3, 10] Monitoring stiffness loss (or damping) can therefore be used to determine the damage level in a GFRP.[12]

[Figure 1 around here]

The application focus of the present study is wind turbine rotor blades manufactured of a GFRP. Two dimensioning factors in modern blade design are fatigue in relation to life-lime, and stiffness in relation to tower clearance. Stiffness degradation is therefore an important mechanism to understand and describe in order to maintain sufficient tower clearance during the blade life (typically 20-25 years). Traditionally, composites for blade application are made of non-crimp fabrics where straight fibres in bundles with different orientation are stitched together to form a preform. Lomov[13] gives an introduction to NCF technology. For large single or double curved moulded composite structures (like rotor blades), transverse backing fibres are used to support the fabric and maintain fibre alignment while handling/draping the fabric in the mould. Limited information is available in relation to damage progression for these non-crimp materials. This is especially true for unidirectional GFRP's with backing fibres where there does not seem to be a definitive explanation for the mechanisms related to fatigue damage. Samborsky et al.[14] reported an influence of backing layers on the mechanical fatigue performance, but they did not investigate the associated damage mechanisms. For static loading only, Edgren et al.[15] investigated transverse cracking in a $[0/90]_s$ non-crimp material in terms of crack density and numerical studies. Gagel et al.[16] investigated the fatigue behaviour of a multiaxial NCF based on crack density. The present study is a quantitative analysis of the tension fatigue damage mechanisms that govern the life-time of a non-crimp GFRP; thus, the focus is on identifying the specific mechanism of stiffness reduction. Tension-tension fatigue experiments are conducted at selected representative load-levels to characterise the material stiffness degradation during fatigue. Based on the obtained stiffness degradation curves, an additional experiment is carried out and stopped in stage II at a predefined damage level, and the obtained material damage is analysed using different microscopic techniques. A simple analytical linear spring model is used to analyse the stiffness loss. Using the experimental observations, a damage sequence in relation to tension-tension fatigue is postulated. The associated damage modes are investigated for two different load levels. The materials used, fatigue characteristics, and load-magnitude and -ratio are typical for the design of the main laminate in a wind turbine blade.

MATERIALS AND METHOD

The material used in the present study is a unidirectional non-crimp glass fibre fabric with backing. Details on the fabric architecture can be found in Table 1.

[Table 1 around here]

The backing bundles are placed on top of the axial bundles and stitched together using a polyester thread; thus, the backing bundles are in direct contact with the axial fibres. During the stitching process, the backing bundles are separated and form a somewhat entangled and irregular spaced pattern, which causes a transverse in-plane waviness of the layer. In the following, the terminology intertwining region will be used to refer to this region, see Figure 2(b). The two sides of the dry un-infused fabric are illustrated in Figure 2 where the axial bundles and the sewing thread (polyester) are visible on one side, and the backing fibres on the other.

[Figure 2 around here]

The fabrics are stacked as $[b/0, b/0]_s$ where b indicates the backing layer, i.e. with the backing layers oriented symmetrically towards the free edges. Panels are manufactured using a closed mould with a differential vacuum pressure and a thermoset unsaturated polyester resin. End tabs are mounted, and planar test specimens are cut according to ISO 527-4[18] with a gauge region of 150 x 25 x t mm where t is the specimen thickness. A servo hydraulic Instron 8501 test machine is used for the experiment, and two extensometers are placed back-to-back in the central part of the specimen to measure the axial strain. Prior to the fatigue testing, the specimens are preloaded in order to determine the initial stiffness, E_0. Load-controlled, constant amplitude, tension-tension fatigue experiments are conducted. The load waveform follows a sinusoidal pattern with a frequency of 5Hz. Tension-tension fatigue is most important to blade design, and a characteristic load ratio $R = \sigma_{min}/\sigma_{max} = 0.1$ is used in the present study. Two different magnitudes of the maximum initial strain are used, namely $\varepsilon_{max} = \sigma_{max}/E_0 = 0.6\%$ and $\varepsilon_{max} = 0.8\%$. In order to mimic the fatigue damage, the experiments tested at the largest load serve as a validation for the observed damage mechanisms in the least loaded specimen. For the least loaded sample, full life-time stiffness degradation curves, similar to Figure 1(b), are established for the material in order to gain information about the life-time and the stiffness-loss of the composite. Subsequently, the fatigue test is stopped in stage II when the maximum strain reaches a preset value of 0.64%. At this strain level, a certain amount of fatigue damage is accumulated in the material. Three procedures are then used for fatigue damage inspection: (i) specimen surface using optical polarised light microscopy, (ii) interior of specimen considering a longitudinal section and electron microscopy, and (iii) removing the resin by burning and inspect for broken axial fibres by optical microscopy. The different inspection sites are illustrated in Figure 3. In order to examine for eventual initial damage due to residual stresses (shrinkage of resin), inspection site (ii) is also analysed in the unloaded part of the specimen (the tab region).

[Figure 3 around here]

Based on the longitudinal sections of the fatigue tested composite, the transverse crack density in the backing layer (both surface and interior) is inspected and measured microscopically. In the present investigation, a transverse crack is defined if the backing fibres are debonded from the matrix along a somewhat straight line through the entire layer thickness. The transverse crack spacing, s, is measured and related to the equivalent layer thickness, t_{eq}. The equivalent thickness is determined by measurement of the area (volume) encapsulated between to cracks divided with the crack spacing. The transverse crack density is dependent on the layer thickness, Hutchinson and Suo[19], and it is thus suitable to investigate the normalised crack spacing t_{eq}/s. The underlying mechanisms that cause the material damage during the fatigue experiments are analysed quantitatively, and a damage scheme is presented. The results presented are limited to a single fibre volume fraction, tested at different initial strain levels. The fibre volume fraction used is representative for typical materials used in wind turbine blades. It is of interest to investigate other volume fractions in relation to fatigue damage, but with regards to the industrial application, the FVF considered is adequate.The mass of the fibre and matrix is measured by the ignition loss method, and the fibre weight fraction of the present sample is calculated to be 73.6% with a standard deviation of 1.21% (fibre volume fraction, FVF = 55.1%, standard deviation 1.52%). The mean porosity content is 0.54% with a standard deviation of 0.04%.

RESULTS

Stiffness Loss during Fatigue

The fatigue damage evolution is presented in Figure 4 along with the associated normalised stiffness degradation. The data shown in Figure 4(a) is for one of the least loaded samples that is run to failure, and the plot is normalised with the maximum number of cycles for that particular sample, N_{max}.

[Figure 4 around here]

Since the experiment is conducted in load-controlled mode, the stress remains constant and the strain increases (stiffness decreases) as function of normalised cycles, c.f. Fig 4(a). Figure 4(b) shows the stiffness degradation curves for the two tested initial strain levels. As seen, there is small variability in the stiffness degradation curves, which suggest an adequate consistency in the experiments. Similar magnitude of the stiffness loss is reported in the different stages independent on the initial load-level; however, with an increasing progression rate for increased initial strain. The mean initial stiffness is determined as $E_0 = 48.0$GPa with a coefficient of variation $c_v = 1.53\%$. The experiment with $\varepsilon_{max} = 0.6\%$ is used for inspection of damage, and those with $\varepsilon_{max} = 0.8\%$ are used as validation of the observed mechanisms. For $\varepsilon_{max} = 0.6\%$, two initial tests are conducted in order to measure the fatigue life-time and corresponding stiffness degradation curve for the material. Based on these curves, test parameters for an additional experiment are set i.e. when the test is to be stopped at a predefined damage level (stiffness loss) in order to inspect for damage. The normalised stiffness has reached a level $E/E_0 = 0.958$ when the test is stopped. The fatigue damage mechanisms are investigated in further detail in the following sections for the sample that is stopped before final failure.

Surface Damage

Polarised optical microscopy is used to inspect for fatigue damage on the specimen surface, see e.g. Figure 3(i). A typical micrograph showing the fatigue damage of a specimen loaded with an initial strain $\varepsilon_{max} = 0.6\%$ is shown in Figure 5. Figures 5(b)-(c) are produced using image stitching of several individual micrographs. Note that the micrographs appear in better quality in the digital version of the manuscript.

[Figure 5 around here]

A considerable amount of fatigue damage is observed, and a closer examination reveals that the damage is concentrated in consistent crack bands in the backing bundles; especially, in the intertwining regions, see e.g. magnification in Figure 5(b). The cracks bands are believed to be transverse or interface cracks orientated in the direction along the backing fibres. Beneath the backing fibres in the intertwining regions, an extensive amount of fibre debonding is found in the axial load-carrying fibre bundles, see Figure 5(c). Cracks or damage in the resin rich (intermediate) region between the backing bundles are apparently not present.

Interior Damage

A typical longitudinal section (cf. Figure 3(ii)) with constituents is shown in Figure 6.

[Figure 6 around here]

It is observed from Figure 6 that the axial fibres are not completely aligned in the loading direction, but with a small degree of waviness. The backing bundles are either located near the specimen surface or in the interior of the sample, and Figures 7 and 8 show a magnification of typical backing bundles at these two locations. For both locations, similar damage types are found: (i) interface delamination of the backing fibres, (ii) transverse cracks, and (iii) axial

fibre fractures. Examples on these are highlighted in the figures as well. The micrographs are created using image stitching of several individual images.

[Figure 7 around here]

Figure 7 presents the fatigue damage associated to the surface bundles, and it confirms that the crack bands seen on the specimen surface in Figure 5 are related to transverse cracking and fibre debonding/interface delamination in the backing bundle. By measurement, it is found that the axial fibres are broken until a distance approximately equal to 200μm inside the axial layer, which is roughly around 20% of the thickness of the axial layer. This gives a notable contribution to the decrease in axial stiffness. Figure 8 shows the fatigue damage for a bundle located inside the sample.

[Figure 8 around here]

As for the surface bundles, damage in the interior of the specimen is characterised by fibre debonding and transverse cracking along the backing fibre interfaces. It is remarkable that no matrix cracks are found in the resin rich (intermediate) regions in the sample. It is also observed that axial fibre fractures are primarily found in the axial layer to which the backing bundle is stitched. The extension of the fractures in the axial fibres is in this case approximately equal to 400μm, which is around 40% of the axial layer thickness.
Selected details of the damaged composite are shown in Figure 9 for two interior and one surface bundle.

[Figure 9 around here]

As seen from Figure 9, the damage modes are complex, but with common characteristics: an extensive amount of fibre debonding in the backing layer leading to a transverse crack in the axial layer. Furthermore, Figures 9(b)-(c) suggest that the crack initiates within the backing bundle and propagate towards the axial layer. Depending on the thickness of the resin layer between the backing bundle and the axial layer, the crack may be arrested. This is due to a decrease in the energy release rate for a crack in a compliant material approaching a stiffer material. This problem is analogous to cracking of thin films, analysed by Beuth[20]. The transverse crack either gives rise to axial fibre breaks, Figure 7(b), or, as shown in Figure 9(a), leads to debonding along the interface in the axial layer.
In order to examine for eventual initial fibre debonding in the backing layer due to residual stresses or chemical shrinkage, the unloaded tab region is inspected. This is shown in Figure 10 for both a surface and interior bundle.

[Figure 10 around here]

In general, the adhesion between backing fibres and resin is relatively good, Figure 10(a) and (c), but regions are found where there is an initial fibre/interface debonding caused by residual stresses or chemical shrinkage, Figure 10(b) and (d). This is critical since damage initiates in these regions.Two bundles (surface and interior) are selected for measurement of the transverse crack densities, and can be seen in Figures 11 and 12.

[Figure 11 around here]

[Figure 12 around here]

The measurements of the normalised crack spacing for both bundle types are shown in Table 2. It is noted that measurements are assigned an uncertainty due to determination of the exact location of the transverse cracks and the equivalent bundle thickness.

[Table 2 around here]

It is observed from Table 2 that the surface bundles have a lower crack density compared with the interior bundles.

Damage in Axial Fibres

The resin is burned away in an oven, and broken fibres are found in the axial bundles in the regions of contact to the backing fibres. A top view of a typical specimen (initial strain ε_{max} = 0.6%) after burning the resin is shown in Figure 13(a). The polyester sewing thread is also burned off.

[Figure 13 around here]

After carefully removing the backing fibres at the same location, Figure 13(b), it is found that there is a severe concentration of broken axial fibres underneath the backing bundles, Figure 13(c). These broken axial fibres contribute significantly to the axial stiffness loss of the composite. In order to highlight the statement regarding axial fibre fractures, an image overlay of Figure 13(a) and 13(b) is presented in Figure 14. Here, it is obvious that axial fibre fractures occur underneath the backing bundles; especially, in the intertwining region.

[Figure 14 around here]

Damage at Larger Initial Strain Level

The previous sections have presented a thorough microscopic investigation on the damage sequence in the specimen loaded with an initial strain ε_{max} = 0.6%. In order to validate the damage mechanisms observed, similar analyses are performed on a sample loaded to failure with an initial strain ε_{max} = 0.8%. The final damage mode is dominated by tearing (longitudinal splitting and intralaminar delamination) and not a single localised sharp crack, see example in Figure 15.

[Figure 15 around here]

As above, the damage consists of transverse cracks (fibre debonding) in the backing layer extending into the axial load-carrying fibres. The extension of the broken axial fibres amounts to approximately 45% and 30% of the layer thickness for interior and surface bundles respectively before they form an intralaminar delamination as shown in Figure 15. These values are slightly larger than the sample analysed above, which is a result of the sample being loaded to failure. The normalised crack spacing is measured and presented in Table 2; however, only for the interior bundle.

DISCUSSION

Observations

As seen from Table 2, the saturated crack spacing is almost twice for the surface bundles compared with the interior bundles. Surface cracks behave more like layers with double thickness, which is due to the free surface in comparison with the constrained interior bundles. This observation seems to be consistent with other studies e.g. Nairn and Hu[21] and Gillespie and Hansen[22]. It is left to a future study to analyse and investigate the transverse cracking in fatigue e.g. based on a variational principles[21,22], stress analysis, or finite elements.

For the largest loaded specimen, it turned out to be complicated to inspect for transverse cracks in the surface bundles since the debonded backing fibres could not be inspected in the microscope (pure matrix cracks remained open and visible). It is believed that the cracks encircling the debonded fibres in the surface bundles are closed upon failure due to the release of internal stresses. For the interior bundles, the adjacent axial layers provide a constraint that limits the stress release, and enables the measurement of the transverse crack density. Still, independent on the maximum initial strain, the normalised crack spacing is in similar magnitude (Table 2), which indicates that the transverse crack spacing has reached saturation for the least loaded sample. The damage propagation modes observed are similar for both load levels considered.

Edgren et al.[15] studied transverse cracking in axial static loading of a carbon fibre reinforced NCF's with a stacking sequence $[0/90]_s$. Observations were similar damage modes as shown in the present: cracking of transverse bundles; however, without a discussion on the damage mechanisms. Using a unidirectional non-crimp fabric with backing strands (PPG-Devold L1200/G30-E07), Samborsky et al.[14] investigated the effect of different resins (epoxy and unsaturated polyester) in tension fatigue (R = 0.1). They showed that the million cycle tensile strain differed with a factor of two in favour of the epoxy-based composites. Based on the observations in the present study, the difference between resins and fatigue life is linked to the shrinkage (thermal and chemical) of the resin, which initiate the transverse cracks. Previous studies determined the volumetric shrinkage strain as 3-7% for epoxy (e.g. Li et al.[23]) and 6-10% for unsaturated polyester (e.g. Bogetti and Gillespie[23]), see also Nielsen[25]. Based on the volumetric shrinkage, and the fact that transverse cracks initialise as a consequence of residual stresses, it is thus expected that epoxy resins show better resistance in fatigue when fabrics with backing are considered. Furthermore, Samborsky et al.[14] performed a tension fatigue experiment (R = 0.1) where the backing strands where removed in order to investigate the effect of these. No effect was reported for the case of an epoxy resin. For the polyester resin, the fatigue exponent on the SN-curve remained somewhat unchanged, but the intersection parameter increased with almost 20% when removing the backing strands. This means a significant improvement in the fatigue behaviour. For polyester resin, it is thus decisive to understand the damage mechanisms in fatigue associated with the backing layer in order to make a future material improvement.

Stiffness Degradation Model

A simple unit cell spring model is developed in order to predict the axial stiffness of the material considered, see Appendix. This model is used to evaluate the stiffness decrease for a fully cracked backing layer as well as a prediction on the stiffness loss as function of further fractures of the axial fibres. The predicted stiffness for the fibre volume fraction used in the experiments is E_0 = 47.6GPa, which is in accordance with the experimentally observed ones E_0 = 48.0GPa. As seen from Figure A.2(b), the stiffness contribution from the backing bundle is limited, and for the present sample the contribution is 0.542% (see also Figures A.2(b) and 16). By comparison with the experimental stiffness degradation curves, Figure 4(b), the stiffness loss associated with transverse cracking of the backing layer accounts for stage I of

the fatigue stiffness loss. Upon further applied cyclic load, transverse cracks from the backing bundles propagate into the axial layer, which gives a further stiffness decrease caused by the reduced layer thickness. Axial fibre debonding does not affect the stiffness loss significantly, but affects the damping characteristics. The experimentally observed reduction in axial layer thickness is in the order of 20-40%, and the simple spring model can be used to describe this. By introducing a stiffness reduction factor on the axial layer thickness, t_2, varying from 0 (fully cracked specimen, failed) to 1 (undamaged axial layer), it is possible to describe the stiffness loss as a function of reduction in axial layer thickness (a basic assumption is that all unit cell elements have the same thickness reduction). The result is shown in Figure 16 along with the stiffness loss observed for the least loaded fatigue sample that is used in the microscopic investigation above.

[Figure 16 around here]

From Figure 16 an initial stiffness loss corresponding to cracking of the backing bundles is predicted, and as the crack propagates into the axial layer a further decrease in stiffness is observed. Finally, the stiffness drops when the sample fails. A layer thickness reduction of 45% is predicted by the model, which is in similar magnitude as observed experimentally.
It is remarkable the shape of the curve in Figure 16 is similar to the stiffness degradation curve in Figure 4. In a fatigue experiment, the thickness reduction factor is actually a function of applied cycles. If it is possible to determine the thickness reduction factor as function of cycles (e.g. by tension fatigue test of the single edge notch test specimen), this can be coupled with the stiffness prediction to obtain an estimate of the stiffness degradation curve and fatigue life-time. Even though the model is quite simple, it is able to predict the stiffness loss with reasonable accuracy. Of course, other mechanisms are present such as stress redistribution due to cracking, stress concentration, etc., but these must be evaluated using finite elements.

Fatigue Damage Scheme

The fatigue damage process in stage II is investigated, and it is shown that damage initiates in the intertwining regions of backing bundles and then propagates to the axial fibres. Distinguishing between the different fatigue damage stages presented in Figure 1(b), an explanation for the mechanisms of tensile fatigue damage failure in an axially loaded unidirectional NCF with backing, is given in the following. It is noted that the scheme is only valid for material systems containing some kind of fibre backing arrangement, and not for pure unidirectional samples without backing. For pure unidirectional samples, the fatigue life is improved compared to the present material system, and is only governed by differences in the fibre architecture (packing pattern, touching fibres, local clustering, waviness, etc.) and the properties of the constituents (fibre, matrix, and interface), see e.g. Samborsky et al.[14] Obviously, these characteristics are also essential for the present material, but they are not the detrimental cause of fatigue failure. A graphical presentation of the proposed fatigue damage process can be seen in Figures 17 and 18.

[Figure 17 around here]

Stage I: Typical observed stiffness loss is within a few percent, and damage is characterised by transverse cracking/failure of the backing bundles causing delamination within the backing bundle and along the fibre/matrix interface, see e.g. Figure 18(b). Fibre adhesion and

intralaminar properties are believed to be essential for this stage. Release of internal residual stress due to curing is an important issue that needs further attention.
Stage II: Lasting most of the life-time with a somewhat constant stiffness degradation rate, damage consists of local stress concentrations around - and sliding friction (fretting, rubbing) between - the backing bundles and the axial fibres; especially, in the intertwining regions, see e.g. Figure 2(b). As the cyclic load is continuously applied, the fretting mechanisms along with stress concentrations cause fibre fractures in the axial bundles. Because of the stress concentration at the broken fibre ends in the load-carrying bundles, fibre debonding occurs and propagates along the axial direction. Fibre fracture and debonding continues throughout the stage, and cause both a loss of stiffness and an increase in material damping due to the friction. Interfacial fibre/matrix properties are considered crucial. The damage process is presented in Figure 18(c).
Stage III: Near the end of the life-time of the GFRP, damage progression of stage 2 is localised in terms of longitudinal splitting (intralaminar failure) and leads to final failure. Final failure can often be observed near the end tabs where the local stress distribution is more complex. The associated damage mode close to final failure is illustrated in Figure 18(d).

[Figure 18 around here]

It is believed that the transverse cracks originate from the inside of the backing bundle, and then propagate towards the axial layers or the sample surface. These transverse cracks may cause axial fibre fractures due to stress-concentrations or delamination along the interface between the axial- and backing-layer. Upon sufficient number of load-cycles, a crack saturation level is reached in the backing bundles, and the stiffness/strength of this layer is lost; hence, the entire load is carried by the axial bundles. During further cycling, the axial layers will slide on top of the backing bundles, which cause a fretting/rubbing fatigue mechanism and fibre fractures in the axial bundles.

Reflections and Future Aspects
Since the backing layer is not directly designed to contribute to the strength/stiffness of the composite, but is primarily necessary in order to handle the fabric, one can imagine possible solutions to the problem presented above:
(i) optimise the fibre arrangement of the backing layer,
(ii) change the backing fibres to a more compliant material to reduce the interfacial stresses and stiffness mismatch between the layers,
(iii) apply a soft and thin interleaf (tackifier) between the axial bundles and the backing (see e.g. Tsotsis[265], or Hillermeier & Seferis[27]). A soft interleaf has previously been demonstrated to reduce the interlaminar stresses in cross-ply laminates for static loading, Gillespie & Hansen.[22] A soft interleaf can e.g. be made in combination with (ii),
(iv) develop new stitching patterns that can stabilise and support the fabric so the backing layer can be avoided.
The postulated fatigue damage sequence is based on quantitative observations, and a numerical investigation would be beneficial in order to investigate the influence of the backing layer during fatigue. In relation to numerical studies, the damage modes presented require large computational efforts as well as a methodology for fatigue damage evaluation, especially of the fibre/matrix interface. Static damage propagation of the fibre-matrix interface has been studied extensively both on single fibre and unit cell level, see e.g. Kushch et al.[28] or Wang et al.[29] but to mention a few. However, at least to the author's knowledge, no useful and consistent models/methodologies are available at present to describe the interface

properties in fatigue. Besides the unit cell approach, concepts of virtual testing and multi-scale modelling (see e.g. the work of Ladavéze[30] or LLorca et al.[31]) are promising modelling strategies for numerical design and evaluation of composite materials. Future research efforts should be put in establishing a link between the experimentalists and numerics in order for virtual testing to be meaningful. The present work has contributed in the sense that tension fatigue damage mechanisms in non-crimp fabrics are discovered and assessed. Future work is focussed on describing the observed phenomena using different modelling strategies.

CONCLUSIONS

Despite the fact that unidirectional fibre reinforced composites is the simplest kind of laminated materials, the fatigue failure mechanisms are complicated and not understood in detail. Using three distinct quantitative procedures, tension fatigue damage in unidirectional glass fibre composites made of a non-crimp fabric with backing has been assessed and documented. The experimentally observed stiffness loss during fatigue is caused by an initial failure of the backing bundles forming a stress concentration, and a fretting/rubbing mechanism that gives rise to broken fibres in the axial load-carrying bundles. Upon further cyclic loading, these mechanisms cause fibre debonding near the ends of the broken axial fibres and further loss of stiffness. Damage is finally localised and failure occurs. A simple spring model is used to express and verify the stiffness loss as function of reduction in axial layer thickness.

ACKNOWLEDGMENTS

The author gratefully acknowledges the funding from the Danish Council for Strategic Research for its support via the Danish Centre for Composite Structures and Materials for Wind Turbines (DCCSM) (contract number 09-067212).

REFERENCES

1. Brøndsted P, Andersen S, and Lilholt H. (1996). Fatigue performance of glass/polyester laminates and the monitoring of material degradation. *Mech Compos Mater*, **32**(1): 21-29.
2. Beaumont PWR, Dimant R, and Shercliff H. (2006). Failure processes in composite materials: getting physical. *J Mater Sci*, **41**(20): 6526-6546.
3. Nijssen RPL. (2006). Fatigue life prediction and strength degradation of wind turbine rotor blade composites. PhD Thesis, Delft University of Technology, NL.
4. Demers CE. (1998). Tension–tension Axial Fatigue of E-glass Fiber-reinforced Polymeric Composites: Tensile Fatigue Modulus. *Constr Build Mater*, **12**(1): 51-58.
5. Brøndsted P, Lilholt H, and Lystrup A. (2005). Composite Materials for Wind Power Turbine Blades. *Annu Rev Mater Res*, **35**: 505-538.
6. Garrett K, and Bailey J. (1977). Multiple transverse fracture in 90 cross-ply laminates of a glass fibre-reinforced polyester. *J Mater Sci*, **12**(1): 157-168.
7. Reifsnider K. (1980). Fatigue behavior of composite materials. *Int J Fracture*, **16**(6): 563-583.
8. Wang A, Kishore N, and Li C. (1985). Crack development in graphite–epoxy cross-ply laminates under uniaxial tension. *Compos Sci Technol*, **24**(1): 1-31.
9. Lafarie-Frenot M, Henaff-Gardin C, and Gamby D. (2001). Matrix cracking induced by cyclic ply stresses in composite laminates. *Compos Sci Technol*, **61**(15): 2327-2336.
10. Mao H, and Mahadevan S. (2002). Fatigue damage modelling of composite materials. *Compos Struc*, **58**(4): 405-410.
11. Gamstedt EK, and Talreja R. (1999). Fatigue damage mechanisms in unidirectional carbon-fibre-reinforced plastics. *J Mater Sci*, **34**(11): 2535-2546.

12. Zhang Z, and Hartwig G. (2002). Relation of damping and fatigue damage of unidirectional fibre composites. *Int J Fatigue*, **24**(7): 713-718.
13. Lomov SV. (2011). *Non-Crimp Fabric Composites: Manufacturing, Properties and Applications*, **1st edt**, Woodhead Publishing, ISBN: 978-1-84569-762-4.
14. Samborsky DD, Mandell JF, and Miller D. The SNL/MSU/DOE Fatigue of Composite Materials Database: Recent Trends, In: *53rd AIAA/ASME/ASCE/AHS/ASC Structures, Structural Dynamics and Materials Conference*, Honolulu, Hawaii, USA, 23-26 April 2012, AIAA-2012-1573.
15. Edgren F, Mattsson D, Asp LE, Varna J. (2004). Formation of damage and its effects on non-crimp fabric reinforced composites loaded in tension. *Compos Sci Technol*, **64**(5), 675–692.
16. Gagel A, Lange D, Schulte K. (2006). On the relation between crack densities, stiffness degradation, and surface temperature distribution of tensile fatigue loaded glass-fibre non-crimp-fabric reinforced epoxy. *Compos part A - Appl S*, **37**(2), 222–228.
17. Owens Corning. (2011). Composite solutions reinforcement guide.
18. ISO, ENN.d. 527-4:1997 (E) Plastics–Determination of Tensile Properties, Part 4. Test Conditions for Isotropic and Orthotropic Fibre-reinforced Plastic Composites.
19. Hutchinson JW, and Suo Z. (1992). Mixed mode cracking in layered materials. *Adv Appl Mech*, **29**, 62-191.
20. Beuth JL. (1992). Cracking of thin bonded films in residual tension. *Int J Solids Struc*, **29**: 1657-1675.
21. Nairn JA, and Hu S. (1992). The formation and effect of outer-ply microcracks in cross-ply laminates: a variational approach. *Eng Frac Mech*, **41**(2), 203–221.
22. Gillespie JW Jr, and Hansen U. (1997). Transverse cracking of composite laminates with interleaves: a variational approach. *J Reinf Plast Comp*, **16**(12): 1066-1092.
23. Li C, Potter K, Wisnom MR, and Stringer G. (2004). In-situ measurement of chemical shrinkage of MY750 epoxy resin by a novel gravimetric method. *Compos Sci Technol*, **64**(1), 55–64.
24. Bogetti TA, and Gillespie JW Jr. (1992). Process-induced stress and deformation in thick-section thermoset composite laminates. *J Compos Mat*, **26**(5), 626–660.
25. Nielsen MW. (2013). *Prediction of process induced shape distortions and residual stresses in large fibre reinforced composite laminates*. PhD thesis. Technical University of Denmark.
26. Tsotsis TK. (2009). Interlayer toughening of composite materials. *Polym Compos*, **30**(1): 70–86.
27. Hillermeier R, and Seferis J. (2001). Interlayer toughening of resin transfer molding composites. *Compos part A - Appl S*, **32**(5): 721-729.
28. Kushch VI, Shmegera SV, Brøndsted P, and Mishnaevsky Jr. L. (2011). Numerical simulation of progressive debonding in fiber reinforced composite under transverse loading. *Int J Eng Sci*, **49**(1), 17–29.
29. Wang HW, Zhou HW, Mishnaevsky Jr. L, Brøndsted P, and Wang LN. (2009). Single fibre and multifibre unit cell analysis of strength and cracking of unidirectional composites. *Comp Mat Sci*, **46**(4), 810–820.
30. Ladevéze P. (2004). Multiscale modelling and computational strategies for composites. *Int J Numer Meth Eng*, **60**(1), 233–253.
31. LLorca J, González C, Molina-Aldareguía JM, Segurado J, Seltzer R, Sket F, Rodríguez M, Sádaba S, Muñoz R, and Cana LP. (2011). Multiscale modeling of composite materials: a roadmap towards virtual testing. *Adv Mater*, **23**(44), 5130–5147.
32. Jones RM. (1999). *Mechanics of composite materials*, **2nd edt**, Hemisphere Pub., ISBN: 1-56032-712-X.

APPENDIX

Stiffness model

In order to estimate the stiffness loss associated to cracking of the transverse backing layer, a simple spring model of the material is considered. A representative unit cell is established, see Figure A.1, and the axial stiffness is evaluated for the unit cell. Eventual fibre waviness, fibre debonding, and defects are neglected.

[Figure A.1 around here]

The unit cell is based on homogenised properties of the fibrous layers, and discretised so that the backing bundles are separated with equidistant distance. However, by coupling several unit cells in series with different lengths, the non-discretised model, Figure A.1(c), can be replicated. The stiffness of the axial layer, E_a, is determined using the rule of mixtures:

$$E_a = V_f E_f^a + (1 - V_f) E_m \qquad \text{(A.1)}$$

With V_f being the FVF [-], and E_f^a and E_m are the Young's moduli of the fibre (axial layer) and matrix, respectively. The transverse stiffness of the backing bundles, E_t^b, is predicted using the Halphin-Tsai equation, Jones[32]:

$$E_t^b = E_m \frac{1 + \xi \eta V_f}{1 - \eta V_f} \qquad \text{with} \qquad \eta = \frac{E_f^b / E_m - 1}{E_f^b / E_m + \xi} \qquad \text{(A.2)}$$

where E_t^b is transverse stiffness of the backing bundle. E_f^b and E_m refer to the corresponding fibre (backing bundle) and matrix properties, respectively. A value of $\xi = 2$ is suggested for the transverse stiffness, Jones.[32] If the backing layer is assumed continuous rather than discrete, then the stiffness of the backing layer, E_t, including the intermediate resin region, is expressed as:

$$E_t = \frac{E_t^b E_m}{E_t^b \alpha_L + E_m}(1 + \alpha_L) \qquad \text{with} \qquad \alpha_L = \frac{L_2}{L_1} \qquad \text{(A.3)}$$

The axial stiffness of the entire unit cell, E, in Figure A.1(e) is finally expressed as:

$$E = \frac{\alpha_t E_t + E_a}{1 + \alpha_t} \qquad \text{with} \qquad \alpha_t = \frac{t_1}{t_2} \qquad \text{(A.4)}$$

Comparing the unit cell, Figure A.1, with the picture of the fabric, Figure 2(b), it is observed that the length ratio, α_L, is a varying parameter. In order to get a reasonable representation of the actual material, the unit cell is coupled in series with a random length ratio in the range from 0 to 2. For the present analysis, 1000 unit cell elements in series are used with a varying random length ratio. It is reasonable to assume that the thickness ratio, α_t, is independent on the FVF since the individual layers are compressed equally when the FVF is varied (different applied vacuum pressure). The thickness ratio is taken as the fraction between the area weight of the different layers, i.e. $\alpha_t = t_1/t_2 = 60/1322 = 0.05$, cf. Table 1.

For simplicity, it is assumed that the volume fraction of the backing bundles and axial layer is similar, and the corresponding fibre stiffness is given in Table 1. Matrix properties are similar

for the entire unit cell, and the resin modulus is E_m = 3.3GPa. If the stiffness of the backing bundle is set to zero, $E_t^b = 0$, this corresponds to full crack saturation of the backing bundle.

The stiffness prediction of the model is shown in Figure A.2(a) for different fibre volume fractions, and compared with the rule of mixtures. The stiffness contribution from the backing bundle is shown in Figure A.2(b).

[Figure A.2 around here]

As seen from Figure A.2, the rule of mixtures overestimates the stiffness prediction with approximately 4%. The effect from the backing bundle is limited, and the stiffness contribution is in the order of 0.5%.

Table 1. Properties of the fibres in the non-crimp fabric considered.

	Axial fibres	Backing fibres
Diameter [μm]	17 or 24	9
Roving size [tex]	2400	68
Nominal area weight [g/m^2]	1322	60
Orientation [deg]	0	±80
Glass type[17]	High performance, WindStrand	E-glass
Young's modulus[17]	87.5	70
Density[17] [g/cm^3]	2.61	2.56

Table 2. Normalised crack spacing for fibre bundles located near the specimen surface or the interior of the sample. t_{eq} is the equivalent bundle thickness measured between two adjacent cracks with spacing, s.

	ε_{max} [%]	t_{eq}/s mean [-]	t_{eq}/s std [-]
Surface bundle	0.6	0.31	0.13
Interior bundle	0.6	0.51	0.18
Surface bundle	0.8	N/A	N/A
Interior bundle	0.8	0.40	0.18

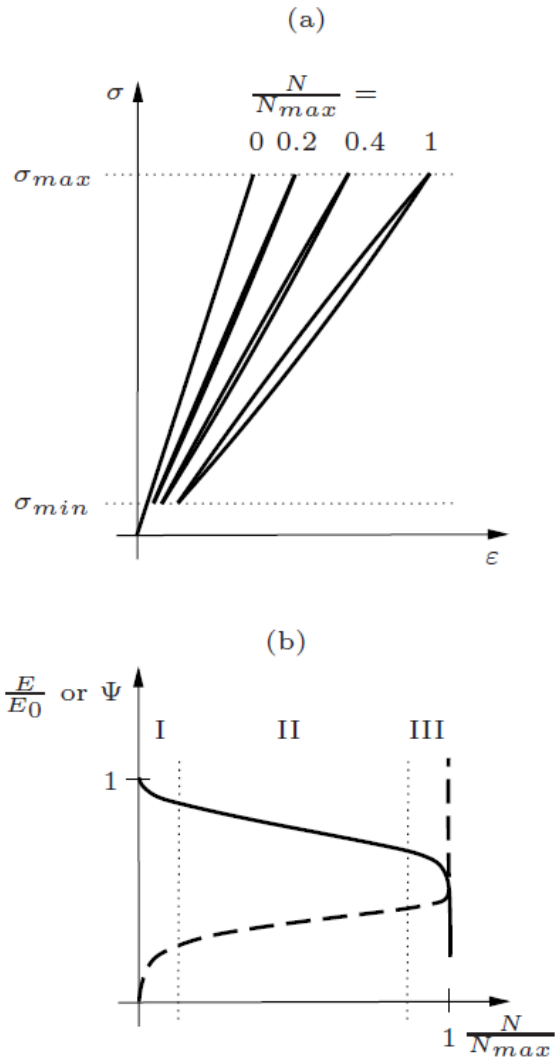

Figure 1. Sketch of a typical tension-tension fatigue process observed in a glass fibre reinforced composite. (a) Stress/strain relation for a stress controlled fatigue test showing evolution of damage as function of normalised number of cycles. (b) Stiffness degradation (-) and damping propagation (--) as function of normalised load cycles.

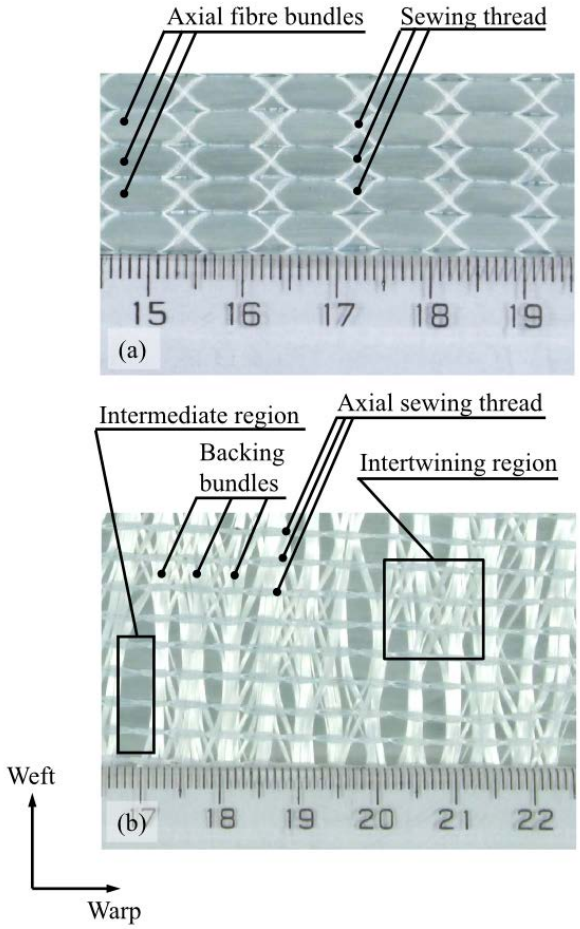

Figure 2. Illustration of dry fabric. Ruler with units of cm. (a) Axial face. Axial bundles and double equal pillar tricot stitching. (b) Backing face. Axial bundles are placed underneath the backing in horizontal direction.

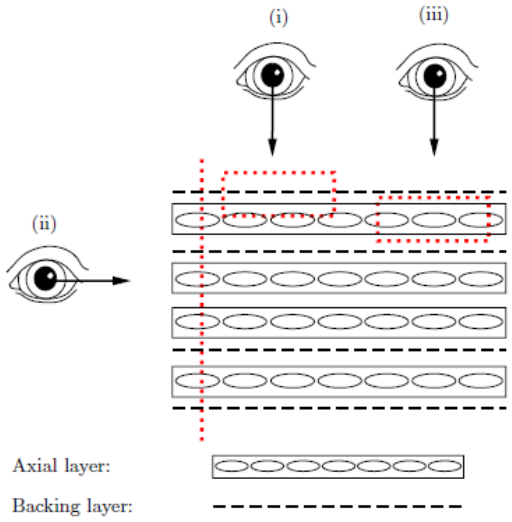

Figure 3. Sketch of the considered locations for damage inspection. Axial fibre direction is out-of-plane. (i) Surface inspection using polarised light microscopy. (ii) Interior inspection by electron microscopy and a polished and surface coated longitudinal section. (iii) Axial fibre bundles by burning the resin and removing the backing fibres.

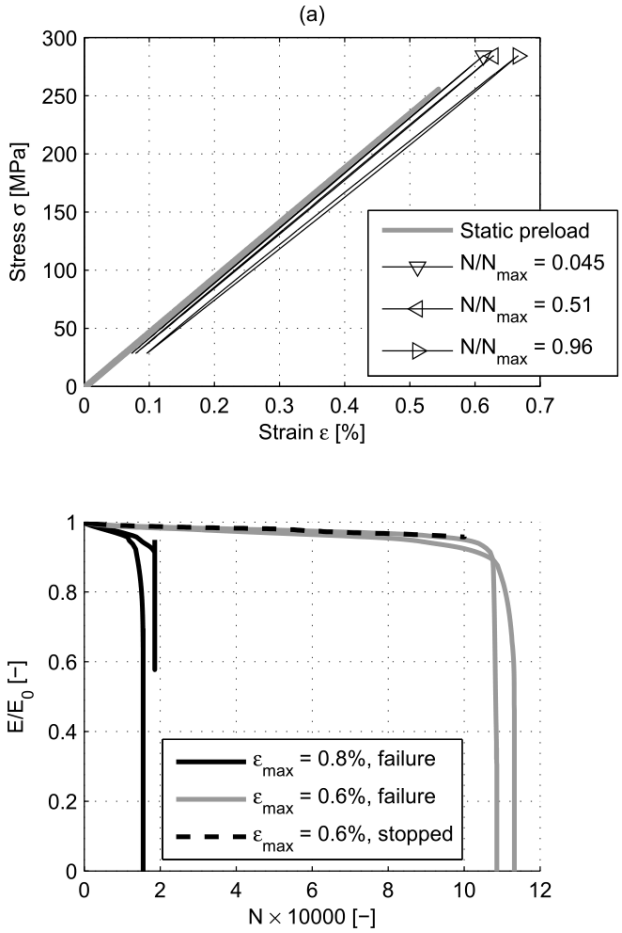

Figure 4. Result of fatigue experiment of a GFRP. (a) Stress-strain diagram during fatigue for an initial strain equal to 0.6%. Indication of stiffness loss and material damping (increasing size of hysteresis loop) as function of normalised load cycles. (b) Normalised stiffness as function of average of normalised load cycles.

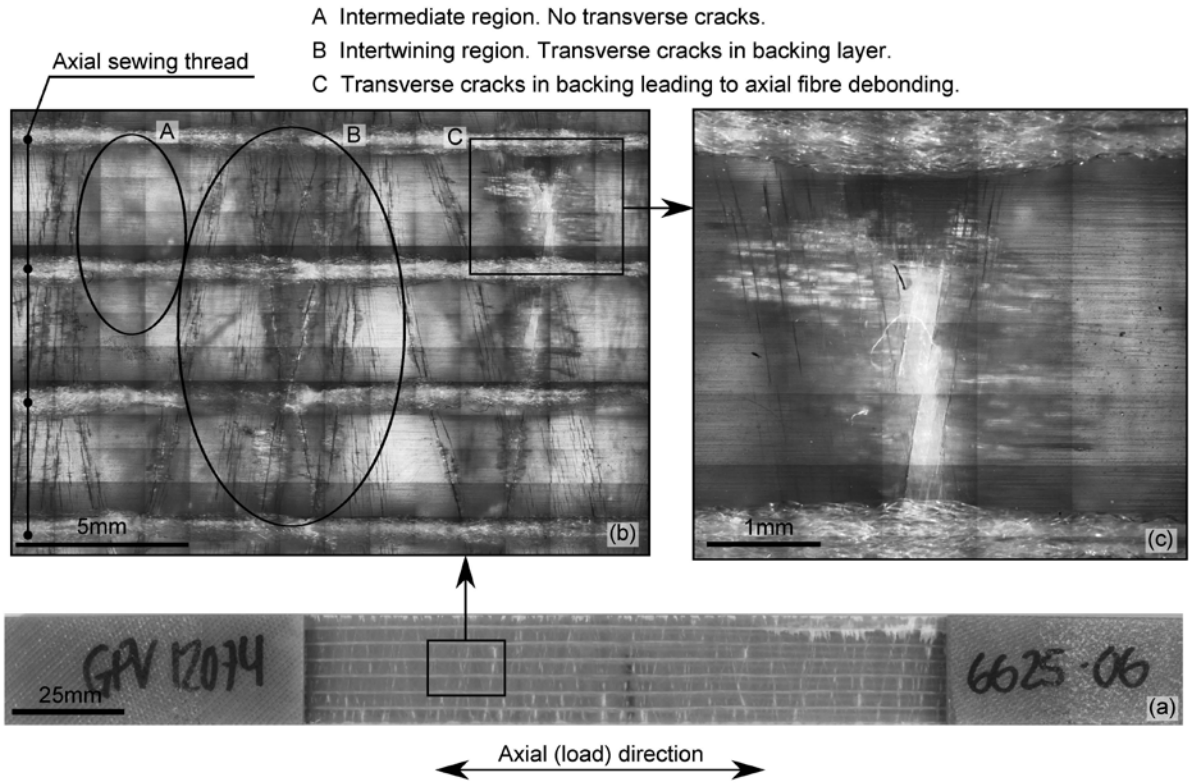

Figure 5. Surface image of fatigue damage in a unidirectional GFRP, cf. Figure 2 for the fabric architecture. (a) Fatigue tested specimen with initial strain ε_{max} = 0.6%. (b) Surface damage in backing layer. (c) Damage in backing layer causing axial fibre debonding.

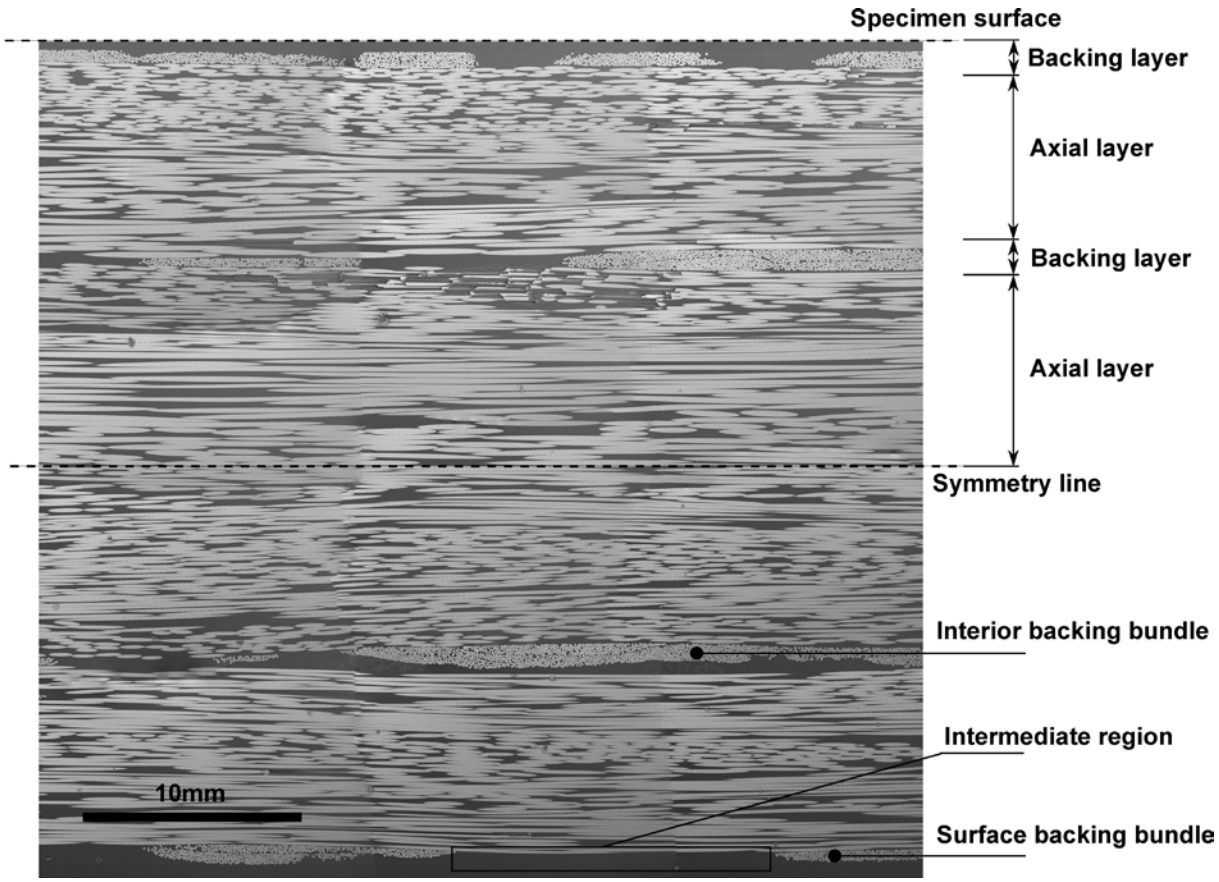

Figure 6. Longitudinal section of specimen with indication of stacking sequence and constituents.

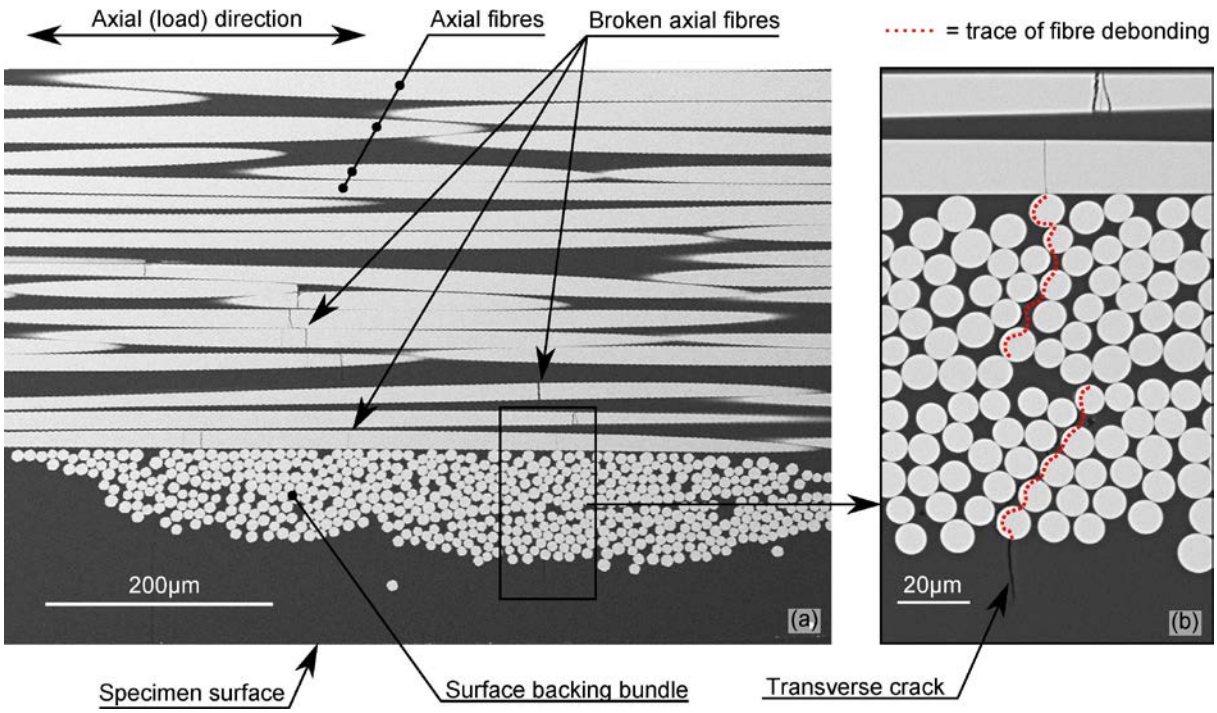

Figure 7. Fatigue damage (initial strain ε_{max} = 0.6%) in axial fibres near a surface backing bundle located towards the mould side of the specimen. (a) Overview. (b) Magnification.

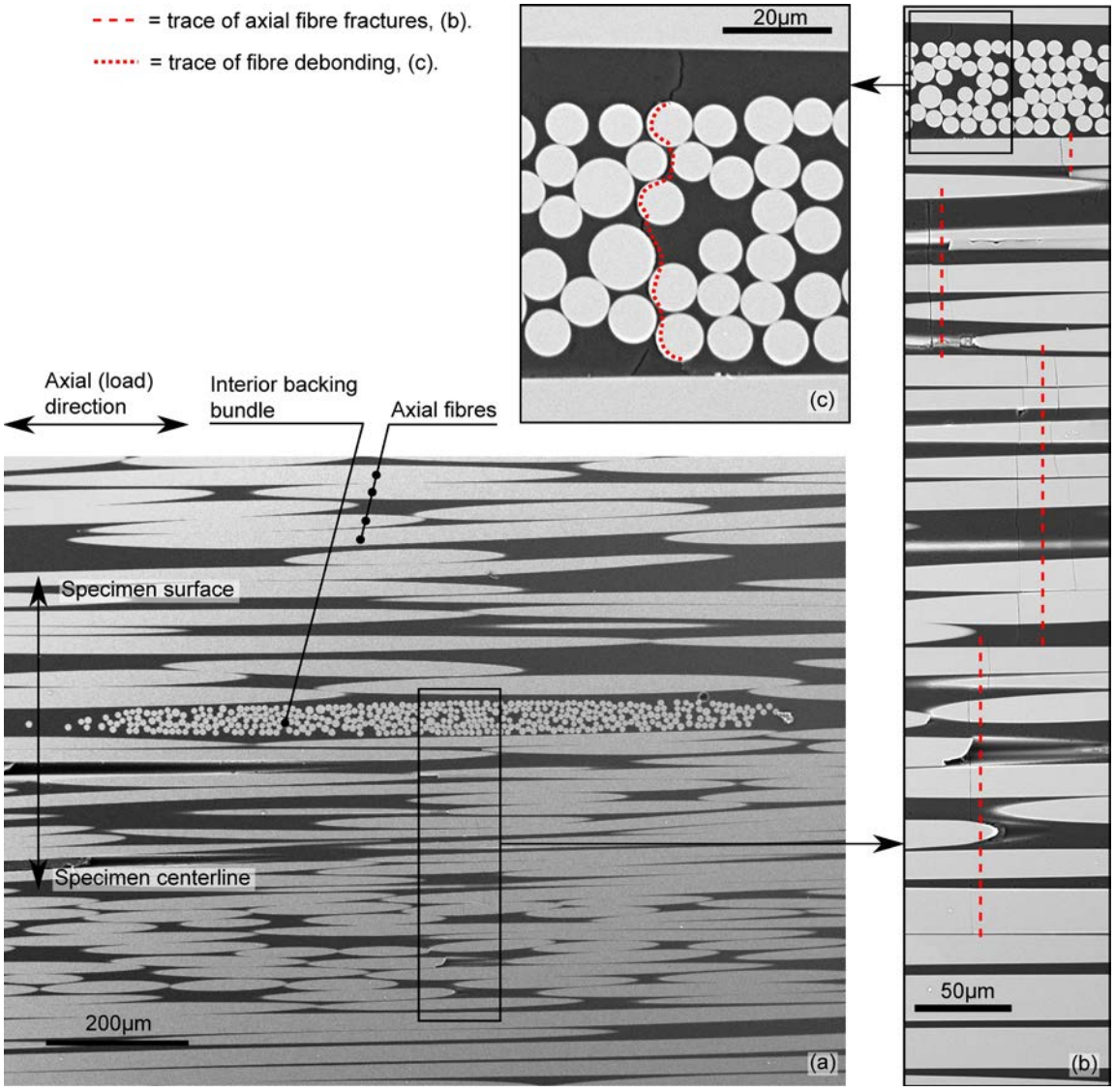

Figure 8. Fatigue damage (initial strain ε_{max} = 0.6%) in interior backing bundle located inside the specimen. The backing bundle is stitched to the lower axial layer in the figure. (a) Overview. (b) Magnification of axial fibre fractures. (c) Magnification of fibre debonding in the backing layer (transverse crack).

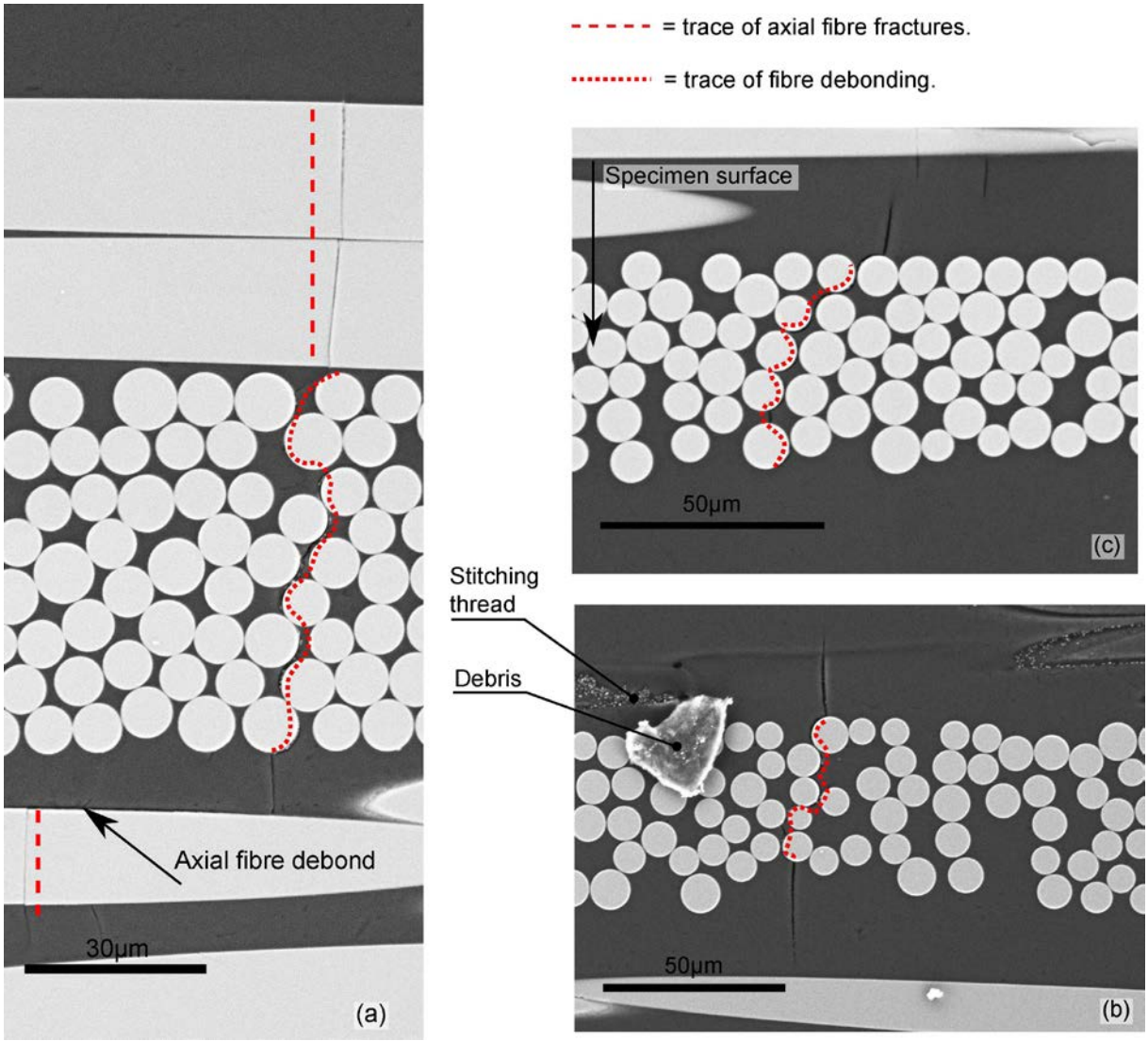

Figure 9. Details of fatigue damage (initial strain ε_{max} = 0.6%). (a) Transverse crack, axial fibre debonds, and axial fibre breaks in interior backing bundle. (b) Transverse crack in interior backing bundle propagating towards the axial layer. (c) Transverse crack in surface bundle propagating towards the axial layer.

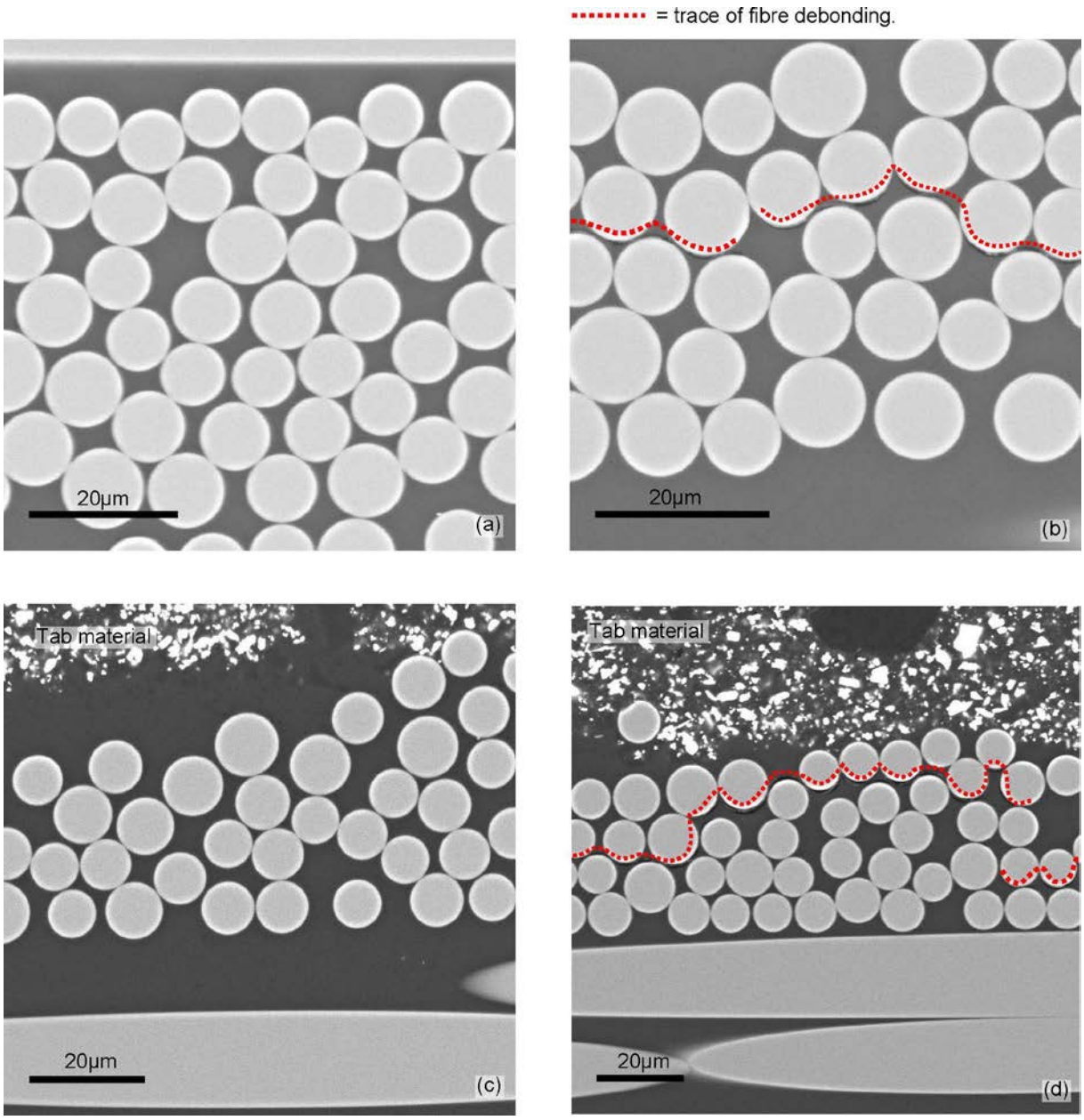

Figure 10. Adhesion between backing fibres and resin in unloaded tab region from specimen with initial strain ε_{max} = 0.6%. (a) Interior bundle, good adhesion. (b) Interior bundle, poor adhesion and fibre debonding. (c) Surface bundle, good adhesion. (d) Surface bundle, poor adhesion and fibre debonding.

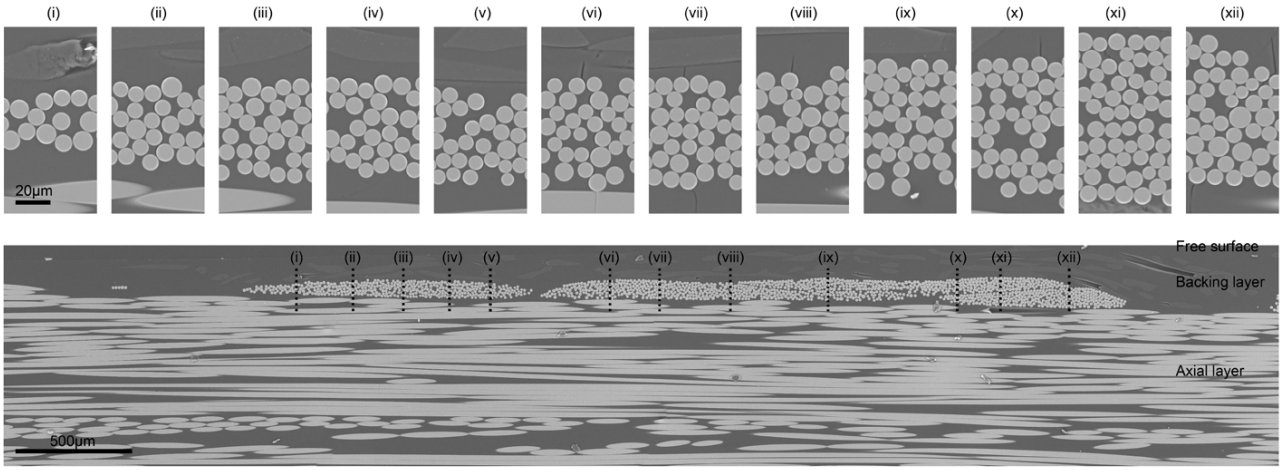

Figure 11. Micrograph of transverse cracks in surface bundle: overview and crack details. Fatigue tested with initial strain ε_{max} = 0.6%. Values for the crack spacing are given in Table 2.

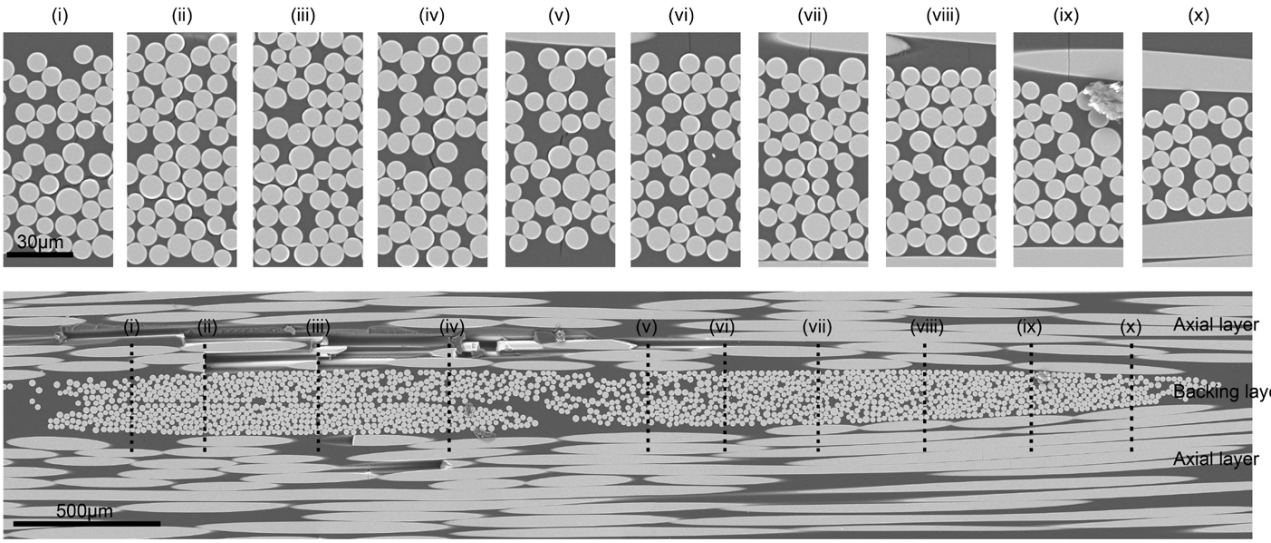

Figure 12. Micrograph of transverse cracks in interior bundle: overview and crack details. Fatigue tested with initial strain ε_{max} = 0.6%. Values for the crack spacing are given in Table 2.

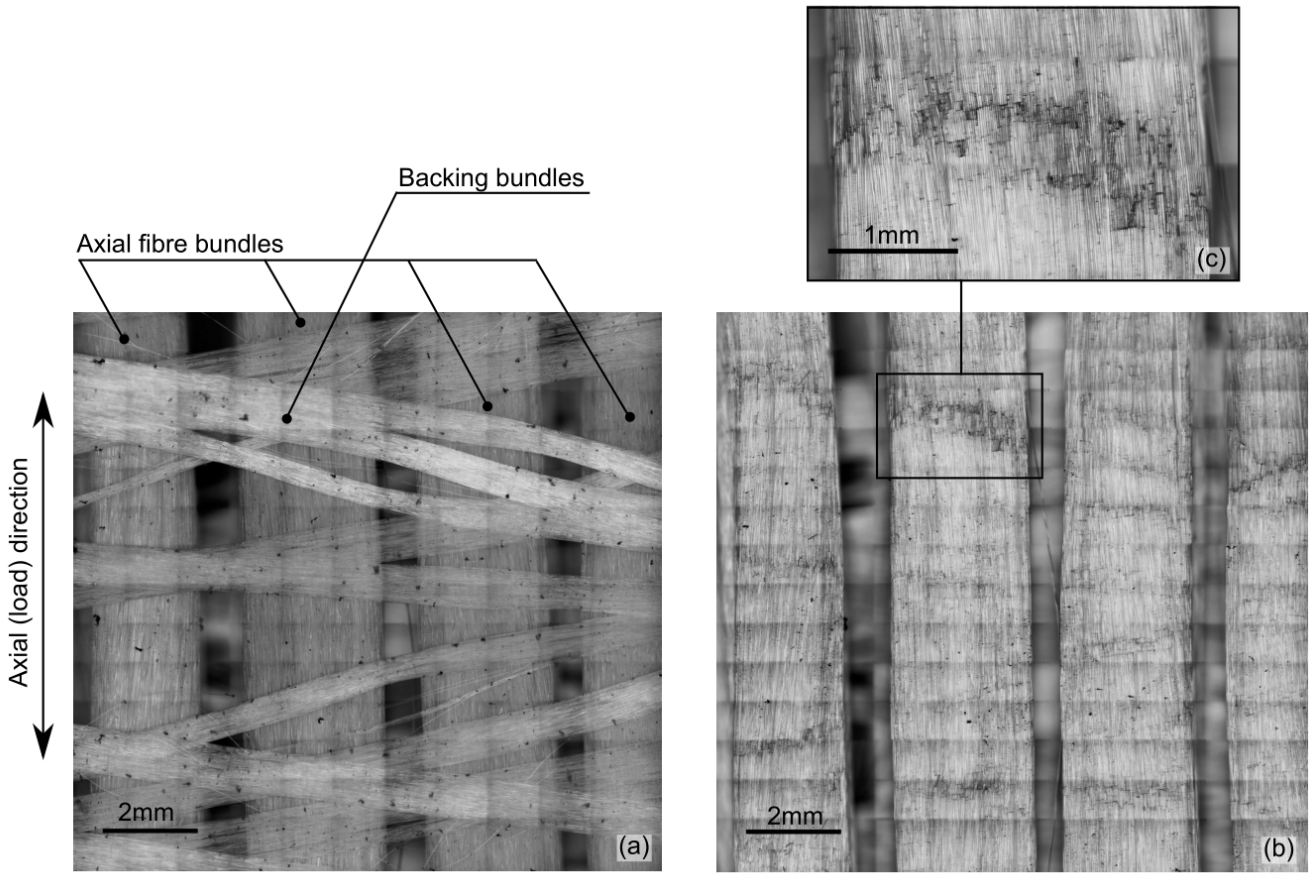

Figure 13. Specimen after removal of the resin (initial strain $\varepsilon_{max} = 0.6$). (a) With backing fibres. Axial fibres are located beneath the backing fibres in the vertical direction. (b) Without backing fibres. Note the extensive amount of axial fibre fractures beneath the backing. (c) Magnification of axial fibre breaks.

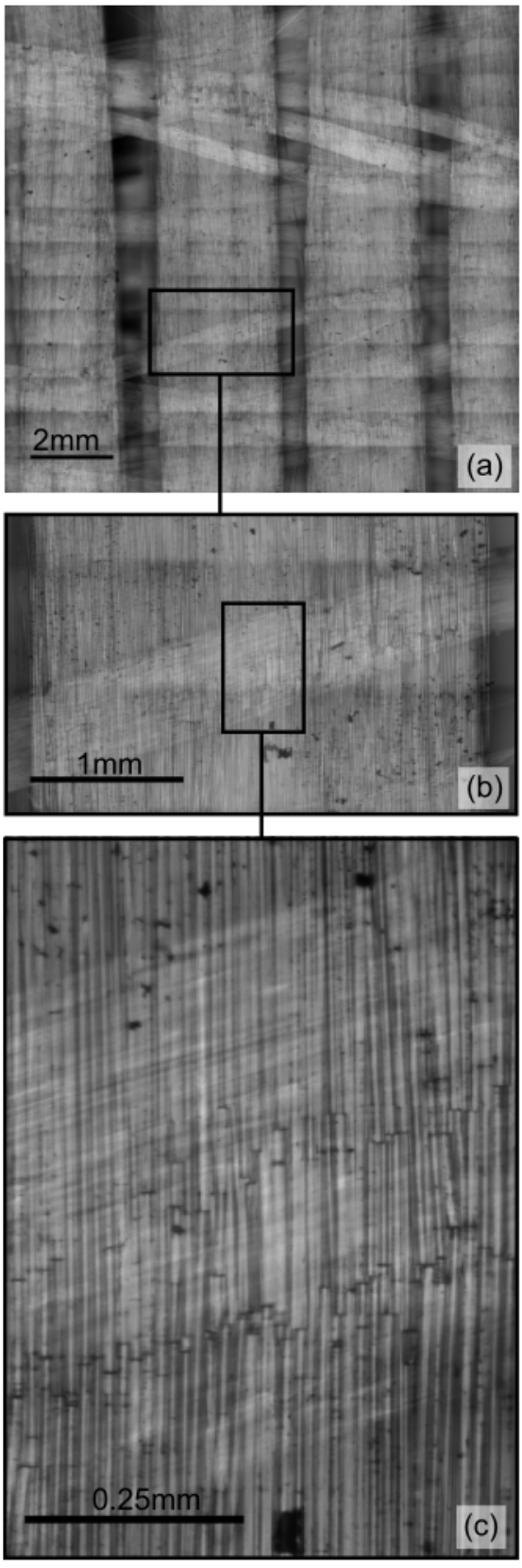

Figure 14. (a) Image overlay of the micrographs presented in Figure 13(a) and (b). (b-c) Magnification of axial fibre fractures beneath backing.

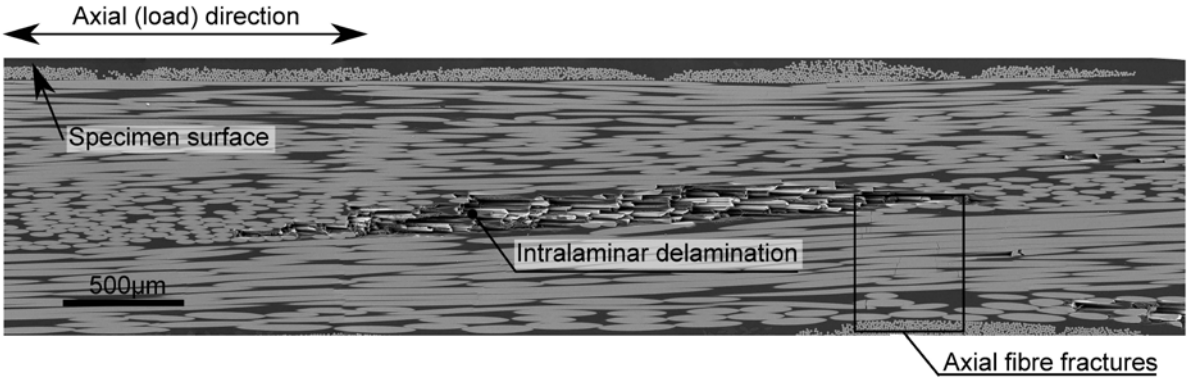

Figure 15. Example on intralaminar delamination caused by initial cracking of transverse layer followed by axial fibre fractures.

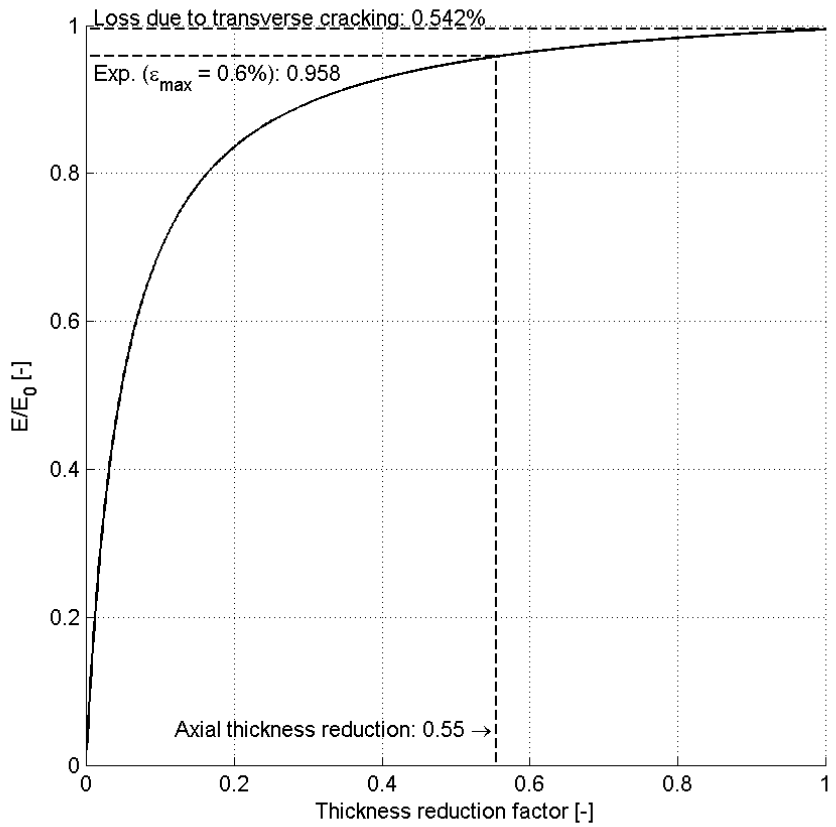

Figure 16. Spring model prediction of stiffness loss as a function of thickness reduction in axial fibre layer. Experimental stiffness loss is shown along with the predicted thickness reduction.

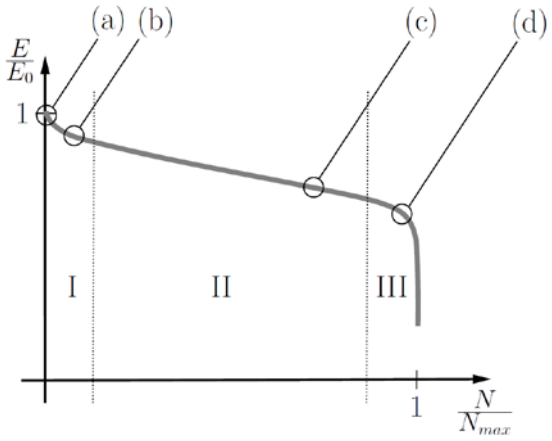

Figure 17. Stiffness degradation curve with different damage states. The damage states (a) - (d) are illustrated in Figure 18.

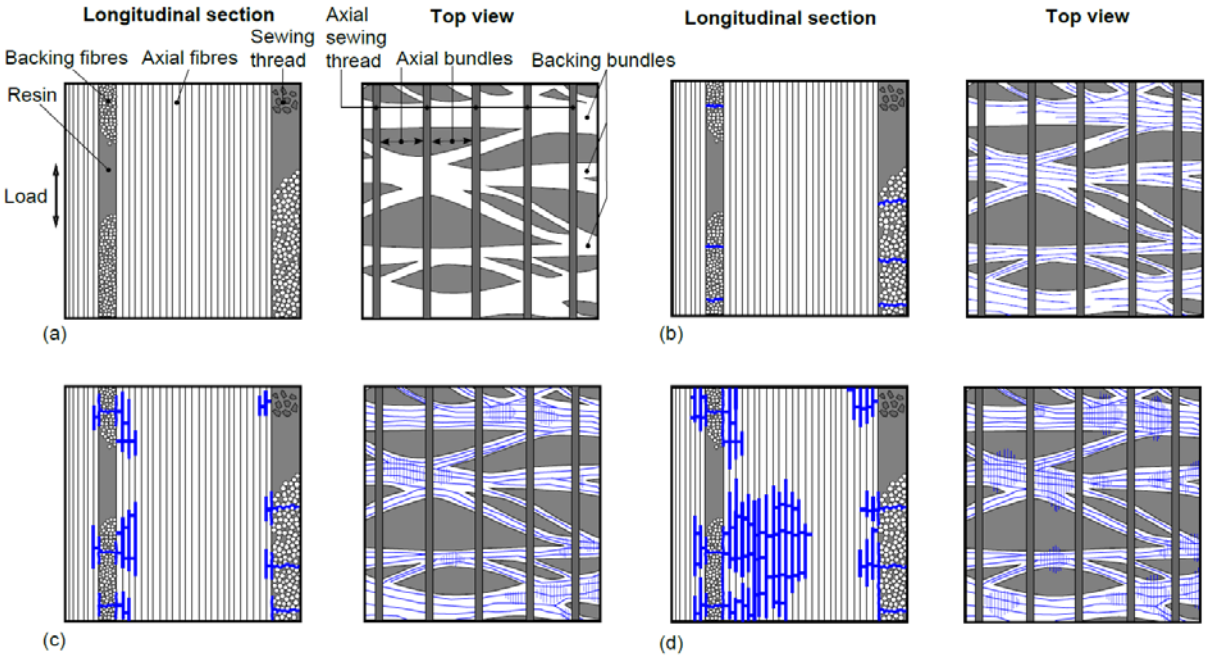

Figure 18. Postulated tension fatigue damage scheme for unidirectional glass fibre reinforced composites with backing layer. The different damage states are shown in the stiffness degradation curve in Figure 17. (a) Unloaded. (b) Stage I, damage initiation. (c) Stage II, damage propagation. (d) Stage III, localisation and failure.

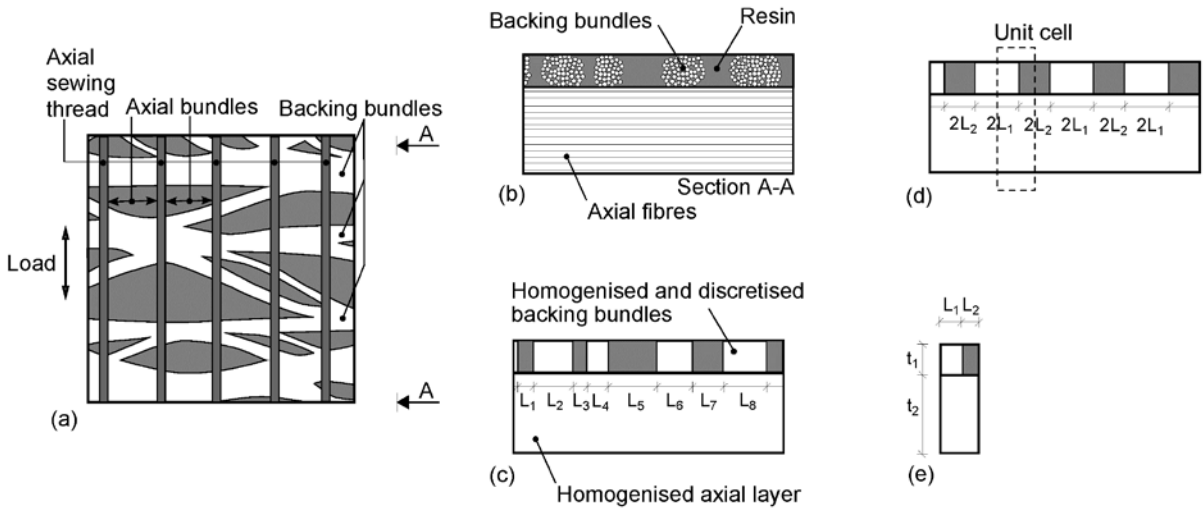

Figure A.1. Homogenisation and sketch of unit cell representation of un-cracked non-crimp fabric (not to scale). (a) Top view of fabric architecture, cf. Figure 2(b). (b) Longitudinal section. (c) Homogenisation of fibrous layers. (d) Generalisation and discretisation of geometry. (e) Unit cell representation.

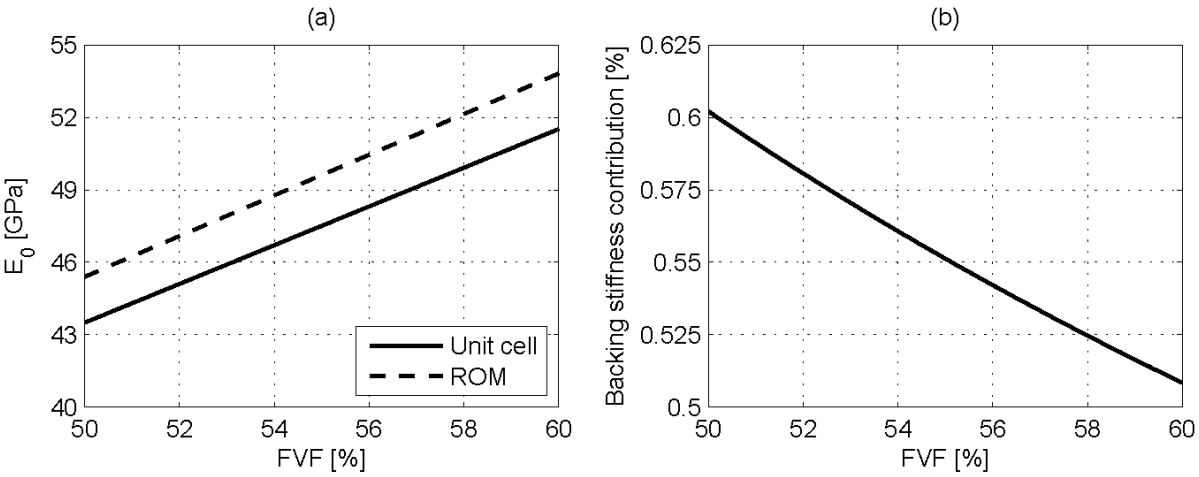

Figure A.2. Stiffness prediction as a function of FVF using unit cell spring model. (a) Axial stiffness, Equation (A.4) and rule of mixtures (ROM), Equation (A.1). (b) Stiffness contribution from backing layer.

[P5]

Zangenberg J., Brøndsted P., and Koefoed M.

DESIGN OF A FIBROUS COMPOSITE PREFORM FOR WIND TURBINE ROTOR BLADES

Materials & Design, **Submitted**, (2013).

Design of a fibrous composite preform for wind turbine rotor blades

J. Zangenberg[a,b,*], P. Brøndsted[b], M. Koefoed[a]

[a]*LM Wind Power Blades, Materials and Processes, Jupitervej 6, DK-6000 Kolding, Denmark*

[b]*Department of Wind Energy, Section of Composites and Materials Mechanics, Technical University of Denmark, Risø Campus, Frederiksborgvej 399, DK-4000 Roskilde, Denmark*

Abstract

The present work addresses the different factors and challenges one must cope with in the design process of a composite preform used for the load-carrying main laminate of a wind turbine rotor blade. The design process is split up into different key elements, each of which are presented and discussed separately. The key elements are all interconnected, which complicate the design process and involves an iterative procedure. The aim is to provide an overview of the process that governs the design of composite preforms for wind turbine blades. The survey can be used as an information source on composite preform manufacturing. Basic knowledge on wind turbine blade technology and composites is assumed.

Keywords: Composite, Preform design, Wind turbine blade, Non-crimp fabric, Glass fibre

*Corresponding author. Tel.: +45 5138 8407; fax. +45 4677 5758.

Email addresses: jzan@dtu.dk (J. Zangenberg), jzan@lmwindpower.com (J. Zangenberg), pobr@dtu.dk (P. Brøndsted), mko@lmwindpower.com (M. Koefoed)

1. Introduction

Fibre reinforced composites are the natural material selection for wind turbine rotor blades due to their large strength and stiffness to weight ratio compared with conventional structural materials [1]. During the recent decade, the rotor blade size development has increased rapidly, as illustrated in Fig. 1. In turn, much effort has been put on the improvement of the mechanical properties of these composite materials in order to reduce the blade weight by materials savings.

[Figure 1 about here.]

The processed composite in the blade consists of resin encapsulated fibres arranged in a preform. A composite preform is defined as the unconsolidated assemblage of dry fibres, yarns, and/or fabrics [2]. Edwards [3] presents a general overview on the present composite technology including preforms. The design of a composite preform is by far a trivial task, and involves many different engineering aspects. In the following, the design process for a composite preform used in the main laminate of a wind turbine rotor blade, is outlined. The location of the main laminate in a blade is shown in Fig. 2.

[Figure 2 about here.]

A simplified interaction scheme showing the key elements regarding the preform design process, is presented in Fig. 3.

[Figure 3 about here.]

In order to design a suitable preform, one must be aware of all the elements mentioned in Fig. 3, and it is noted that the elements in the design process are interconnected in a non-coherent manner. For instance, choosing a certain filament diameter affects mechanical and processing properties, and in order for the preform to be certified for blade use there might be restrictions on the allowable fibre diameter. Therefore, the scheme presented in Fig. 3 is iterative, and requires control of all the different elements. The preform must also be designed according to a number of business and regulation requirements, e.g. cost and a certain required strength. The general requirements for future composites used in wind turbine blades are: enhanced mechanical properties (especially stiffness and fatigue), improved processing time, lower (or at least similar) cost as conventional fabrics, and improved reliability. In turn, a given preform must be designed to meet these requirements.

In the following survey, each of the key elements presented in Fig. 3 are introduced and discussed in relation to preforms for wind turbine blades. The survey is limited to an introduction and discussion of the key elements, and should be considered as an information source on preform design for wind turbine blades. The structure of the survey is that each key element is presented separately following the progress in Fig. 3. For each key element, the common factors in blade manufacturing are outlined, and the most widely used is passed on to the next key element. For instance, choosing the basic fibre material forms the basis for a presentation of the next key element, namely the filament. Using this format, the preform design process is gradually outlined following Fig. 3.

2. Material

The traditional baseline material selection for fibres used in wind turbine rotor blades is glass, which has been used since the early days of blade manufacturing. In recent years as blades are getting longer (c.f. Fig. 1), the need for a stiffer and stronger fibre material has emerged. Carbon is the most obvious choice, but the increase in mechanical performance compared with glass needs to be balanced with the additional cost, [4]. Hybrid materials (intelligent combinations of both glass and carbon) where the best properties from each material are utilised, are coming into play. However, more research and knowledge are required on hybrid composites before the material can enter as a common material for blade use. The most obvious candidate for additional fibre materials is natural fibres, and an instructive comparison between natural, glass, and carbon fibre materials, is shown in Table 1. Table 1 serves as an instructive indication and comparison of the various materials since there exists different material grades within each category.

[Table 1 about here.]

As seen from Table 1, there is a large variation in properties for the different fibre materials. From a blade manufacturer's point of view, the choice of baseline material is dependent on tradition, current technology, blade design, industrial collaboration, and know-how. The majority of existing blade technology is founded on glass fibres, and glass fibres are typically manufactured of E-glass. However, superior types with improved mechanical properties like S-glass or high-performance glass types (e.g.

Owens Corning's H-glass) have also gained recent interest. Different fibre materials are presented in further detail in the work of Edwards [3]. Compatibility with different resin systems should also be considered when choosing the baseline material.

3. Filament

Having chosen the baseline material in terms of glass, the next step is to discuss the filament. A filament is the smallest unit of a fibrous material, and is often referred to as a fibre. Fibres are used rather than particles due to the blade manufacturing process and the fact that fibres can redistribute the load if a filament fails. During the glass fibre manufacturing processing, several thousand circular filaments are drawn from a platinum spinneret or bushing, collected to form a direct roving/tow, and spun into a bobbin. In order to improve the fibre surface topology, increase the adhesion between fibre and resin, reduce the risk of moisture ingress, and improve wetting with the resin, the glass fibres are sized with a silane based solution before they are collected in the roving. The sizing is chemically modified to suit a specific resin type (polyester, epoxy, etc.). The roving can either consist of twisted or un-twisted filaments (twisted rovings are often referred to as a yarn), but since fibre waviness reduces the compression strength of the composite, un-twisted rovings are the most widespread. Yarns (twisted rovings) are often employed when dealing with natural fibres whereas un-twisted rovings are used for carbon or glass. The number of filaments in the roving can be varied by changing the spinneret, but there exist different standard sizes for the spinneret that limits the number of filaments. The

bobbin can either be used directly in filament winding or sewn/woven to form a preform. When manufacturing the preform, several rovings can be collected into a bundle that form the basic unit of the material. The size of the roving or bundle is classified as the linear density (mass per unit length, unit of tex [g/km]). The linear density affects different properties, e.g. drapeability, resulting preform thickness, wetting and permeability, and lay-up time. Larger fibre bundles reduce the drapeability, wetting properties, and the lay-up time, but the increased thickness is critical concerning intralaminar properties such as delamination.

Selection of the filament diameter is dependent on the spinneret used for the fibre manufacturing, and the fibre diameter is to a great extent based on tradition. Nonetheless, some considerations can be made in relation to the fibre diameter. For instance, since the amount of surface defects in glass fibres is proportional to the volume considered (Weibull size effect), it is advantageous to use fibres with a relative small diameter compared with the critical crack length, a_c. By choosing a relative small diameter, the probability that the fibre contains a flaw that is beyond the critical crack length, is therefore less. The Griffith criterion for crack growth of the critical crack length, a_c, at a fracture stress, σ_c, is expressed as, [5]:

$$\sigma_c = \sqrt{\frac{EG_c}{\pi a_c}} \quad \Rightarrow \quad a_c = \frac{EG_c}{\pi \sigma_c^2} = \left(\frac{K_{Ic}}{\sigma_c}\right)^2 \frac{1}{\pi} \tag{1}$$

where E is Young's modulus, G_c is the strain energy release rate, and K_{Ic} is the mode I fracture toughness. The latter equation is valid under plane stress. Typical values for glass are (assigned with a some uncertainty): $K_{Ic} \simeq 0.8\,\mathrm{MPa}\sqrt{\mathrm{m}}$ and $\sigma_c \simeq 2000\,\mathrm{MPa}$, which yields a critical crack length in the order of $a_c \simeq 0.05\,\mu\mathrm{m}$. Traditionally in glass fibre manufacturing, the

choice has been on fibres with a diameter around 17 μm. This value originates from experience and tradition from the glass fibre manufacturer, and the fact of a profitable production process. For instance, larger fibre diameters have the benefit of increasing production mass frequency compared to smaller. However, as seen from Eq. (1), a smaller fibre diameter is advantageous, but one can imagine that the risk of fibre breakage during manufacturing is increased for decreasing diameter. Relative thick fibres improve the infusion time/wet out, but reduces the perimeter to area ratio which is beneficial in relation to shear stress transfer along the fibre interface.

4. Architecture

In order to position the glass fibres in the blade mould, the fibre (bundles) must be assembled in a given architecture. The fibre architecture defines the type of preform, and different common types are presented in Table 2 and Fig. 4.

[Table 2 about here.]

[Figure 4 about here.]

The different preforms mentioned in Table 2 are characterised by an increasing cost and complexity for the larger dimensionality. For application in wind turbine blades, 2D preforms offer the best characteristics when balanced between cost, processing, and mechanical performance. The optimum mechanical solution would be a filament wound preform; nonetheless, this is not practical possible due to the blade

manufacturing technology. Prepregs (and to some extend tapes) offer better mechanical performance than unconsolidated fabrics, but require a heated mould (or autoclave) in order to be processed. Woven, braided, and knitted preforms are relatively cheap since the preform is mechanically interlocked by the fibre bundles. However, in-plane properties (e.g. compression strength) are reduced compared to straight preforms due to the crimp. On the other hand, these preforms offer high resistance against delamination. Many different weaving types are present e.g. plain, satin, and twill weave. Woven textiles are characterised by high crimp and low drapeability. The optimum for the fibre architecture with regards to the application is achieved by non-woven preforms where the fibres are straight with low crimp. Fibres are arranged in straight bundles that are held together using a thread or glue, and these preform types are referred to as non-crimp fabrics (NCF's), see e.g. Fig. 4(b). NCF's are also referred to multiaxial warp-knitted fabrics due to the fact that several individual layers with different orientation are stacked and sewn together. For a NCF, straight fibrous layers with different orientation are placed on top of each other and not interlaced e.g. as in woven composites. NCF's are dry fabrics, and can be processed using autoclave, hot/cold pressing, or (vacuum assisted) resin transfer moulding with almost any kind of resin. A typical commercially available unidirectional non-crimp fabrics used in the blade industry is the so-called Combi 1250 fabric, which is illustrated in Fig. 5. The number 1250 designates the total amount (area weight, $^{g}/_{m^2}$) of glass fibres in preform. The fabric consists of a uni-axial layer (1150 $^{g}/_{m^2}$), transverse backing strands (50 $^{g}/_{m^2}$), and a chopped strand mat (CSM) (50 $^{g}/_{m^2}$).

Layers are held together using a stitching thread.

[Figure 5 about here.]

Issues in relation to the design of NCF's are: size and shape of the bundles, number of filaments in the bundle, stitching tension applied to the bundles, stitching pattern, and the methodology for stabilising the preform, e.g. backing fibres, chop, or tackifier. The cost of NCF's is relatively low, and they offer a fine drapeability and permeability compared to woven preforms. The texture of NCF's means that it is a hierarchical material since single fibres are arranged in bundles that are organised in layers. A typical example of a processed non-crimp fabric used for wind turbine blades, is illustrated in Fig. 6. A comprehensive presentation and discussion on non-crimp fabrics in relation to manufacturing, properties, and application, is given in the work of Lomov [6].

[Figure 6 about here.]

Having chosen the overall architecture in terms of glass fibres and NCF's, the next step is to consider the dominant fibre orientation. The main action on the blade material is bending (consider the rotor blade as a simple cantilevered beam model with a distributed load). The bending action requires large amounts of reinforcement in the longitudinal/lengthwise direction of the blade in the main laminate, see e.g. Fig. 2. Therefore, the preform should have a predominant amount of unidirectional fibres in the warp direction. The unidirectional fibres are arranged in bundles, which set the constraint on the preform thickness. A relative thick preform (large

bundle size) is beneficial in terms of saving layup time. On the other hand, the drapeability is lowered for increasing thickness, and there is a risk of unsaturated regions inside the bundles. Furthermore, delamination due to ply-drops is sensitive to the laminate thickness, and the delamination strength is decreasing for increasing thickness of the laminate.
In order to provide some transverse stiffness/strength and to stabilise the fabric, transverse weft fibres are employed, see also Fig. 5. The transverse fibres can either be one or several separate transverse layer(s) oriented in a certain angle with respect to the axial fibres, or a chopped strand mat (CSM). This layer improves the static transverse properties, but has a negative influence on the fatigue performance [7]. In order to avoid wrinkle formation and gaps of the unidirectional fibres, it is advantageous to place the supporting layer at an inclined angle (such that the transverse fibres are commingled) instead of perpendicular to the unidirectional bundles. In relation to the geometry of the weft layer, the same considerations as the unidirectional layer should be considered, e.g. fibre material used, appropriate fibre diameter, bundle size, etc. Traditionally, the supporting transverse layers are stitched to the unidirectional layer using a polyester thread. For tension and compression tests dominated by inter-fibre failure perpendicular to the principal fibre direction, the certifying agency Germanischer Lloyd [8] prescribes that the maximum fibre weight parallel to the load direction is not allowed to exceed 5 %, which may limit the amount of transverse material in the weft direction in specific tests.

5. Mechanical

When the architecture of the preform is in place, the processed properties of the composite should be evaluated. However, the mechanical properties should still be considered and kept in mind in the previous stages of the preform design phase. Mechanical properties of the processed preform are decisive with regard to the application, and it is evident that the material resists the actions without failure. The average tension strain level due to the applied actions on a turbine blade is relatively low ($\leq 1.0\%$), and therefore strength issues are in general not of major concern. In compression; however, material instability might be prevailing. Expansion due to moisture ingress or by temperature fluctuations are also to be evaluated as a part of the mechanical considerations during the fabric design phase. Independent of the baseline material used, the composite needs to sustain the given action with a certain margin of safety as prescribed by the certifying agencies [8, 9, 10]. For larger blades (say > 40m), the blade design is generally based on primarily two factors, [11, 12]:

- Tower clearance of the blade (stiffness driven design)
- Life-time of the blade (fatigue resistance)

Stiffness can be altered by changing the baseline material (see e.g. Table 1) or by adding layers to the composite. Fatigue resistance can be improved by a better material understanding, or by lowering the actions on the material (e.g. by smart design, or by adding layers in the laminate - which in turn will increase the blade weight). Blades are typically designed for a 20 years

lifetime [8, 10] and will be exposed to more than 10^8 to 10^9 load cycles during the lifetime [1]. Thus, there is a need for a fatigue resistant material. Stiffness and static properties are primarily affected by the amount and individual properties of the filaments, whereas fatigue is closely related to the architecture, see e.g. Zangenberg et al. [7] and Mandell et al. [13]. Here, it is reported that damage due to the transverse layer is a detrimental cause of failure in fatigue, and it is therefore suggested to optimise the fabric architecture to get a better fatigue resistance. Ply-drops and delamination are factors that should be considered in the mechanical design phase of a fabric both regarding static and fatigue actions. Ply-drops and delamination are sensitive to thickness variation of the layers, and can set a limiting size on the preform thickness. A way to improve delamination resistance is by through-thickness reinforcement (see e.g. Fig. 4(c)); however, this has a side effect since localised fibre damage and changes in microstructure occur near the additional reinforcement. Furthermore, there is a negative influence on the in-plane mechanical properties.

6. Processing

It is important that the preform can be processed in a reasonable time that allows for fast manufacturing of the structure. It is therefore required to have a high permeability and, at the same time, ensure a sufficient wetting between fibre and resin. The wetting is affected by the choice of sizing, but information on sizing properties is often kept confidential by the glass fibre manufacturers. The permeability is linked to the size (tex value) and shape of the fibre bundles, compaction of the bundles due to the stitching tension,

intermediate bundle distance (see Fig. 7), and the architecture of the attached transverse layer. Infusion of a blade shell typically happens perpendicular to the warp direction of the preform, and a sketch of the infusion process is seen in Fig. 7.

[Figure 7 about here.]

As illustrated in Fig. 7, the resin flow front is moving in the channels in-between the axial bundles and in the intermediate region between the transverse bundles. The inter-bundle saturation happens as the flow front passes by, but if the axial bundles are too large for the resin to enter due to the loss of pressure, there is a risk of dry glass within the bundle. This fact should be taken into account when determining the proper linear density and shape of the axial bundles. The intermediate bundle distance is important to ensure proper wetting along the axial fibre direction. It is advantageous to increase the thickness (area weight) of the transverse layer in order to speed up the infusion process; however, this has a side effect on the weight increase and fatigue performance. The stitching thread employed to keep the axial bundles together can be used to adjust the permeability within the bundles by varying the stitching tension; nonetheless, one should keep in mind that a densely packed bundle with many fibres in contact leads to stress concentrations in the processed laminate. This stress concentration gives rise to damage initiation, see e.g. Kushch et al. [14]. With regards to handling of the preform, relative heavy (large area weight) fabrics save the lay-up time, but can be difficult to process due the risk of dry glass as illustrated in Fig. 7. Furthermore, for

heavy preforms, the curved geometry of the blade shell causes wrinkle formation in the axial layers that decrease the compression strength. Lundström [15] present an overview and simple modelling technique for evaluation of the permeability of non-crimp fabrics.

7. Cost

From a business point of view, the cost of the preform is by far the most important factor. One way to adjust the cost is by proper selection of the baseline material, see e.g. Table 1. Others are the actual manufacturing cost of the preform, and the tradition and technology available for the fibre manufacturers. For instance, the fibre manufactures have different standardised bushings for controlling the roving size and fibre diameter, which limit the design space. Of course, new bushing can be acquired but these are fairly expensive, so the choice is often on standard solutions. Another example where cost is a constraining factor, is in relation to the orientation of the transverse supporting layer. Often, this layer is placed in the weft direction orthogonal to the axial bundles, which is easy to manufacture since it only requires a lay-up machine that moves sideways compared to the warp direction. If the supporting weft layer is inclined with respect to the axial bundles, the lay-up machine should move inclined as well. Depending on the fabric width, this can give complications (and raise the cost) if the angle between warp and weft fibres deviates much from 90°. Not only the cost of the preform itself is essential, but the entire cost-route of the preform is of interest. For instance, improved wetting, mechanical performance, and permeability might be achieved if a better (read:more

expensive) sizing is used, which increases the preform cost. On the other hand, the processing time is lowered and the mould time is thus reduced. Therefore, by considering the entire cost route, overall savings might emerge even though the preform cost is increased.

8. Quality

For a blade manufacturers perspective, the preform is designed according to the above mentioned key elements, and it is essential that the end product meet the expectations set by the blade manufacturer. In order to achieve the requested product quality, the blade manufacturer set up different demands in relation to the preform quality, e.g. straightness, size and extend of allowable defects, formability, shelf-life, etc. Deficiencies and defect in the preform must be prevented, which require a certain quality control. This quality control implies standardised procedures for inspection of incoming preforms as well as methods for evaluation of the quality. At present, this is left to the consumer of the preform to evaluate the quality, and quality standards might be a way for improving the interaction between supplier and customer.

9. Certification

Limited information is available regarding regulations and guidelines for manufacturing of preforms for wind turbine blades. Nonetheless, there is a number of certifying agencies dealing with the overall design of wind turbine blades. The most relevant of these are, along with the respective standard:

- Det Norske Veritas (DNV) [9]

- International Electrotechnical Commission [10]
- Germanischer Lloyd [8]

These standards are mostly engaged with the processed properties of the preform for blade design purposes, e.g. statistical variation and design values for strength, stiffness, and fatigue. Since these parameters are indirectly functions of the preform design, it is worth keeping them in mind during the preform design process. As an example is mentioned the transitions between different thickness of a laminate mentioned in Germanischer Lloyd [8] that is relevant in relation to ply-drops, thus the laminate (preform) thickness.

10. Summary

As illustrated in the above survey, it is a complex and challenging task to design a composite preform for a wind turbine rotor blade. The design involves many different iterative steps that are joint together in a non-coherent manner. The pre-design of a fabric can be made based on experience and knowledge e.g. regarding failure modes, manufacturing technology, and processing. However, in order to manufacture, test, certify, and implement a new fabric, many different stakeholders need to be involved. The stakeholders all have different approaches and interests in making the ultimate preform, but it is a balance between numerous factors.

11. Acknowledgements

The author gratefully acknowledges the funding from the Danish Council for Strategic Research for its support via the Danish Centre for Composite

Structures and Materials for Wind Turbines (DCCSM) (contract number 09-067212).

12. References

[1] P. Brøndsted, H. Lilholt, A. Lystrup, Composite materials for wind power turbine blades, Annu. Rev. Mater. Res. 35 (2005) 505–538.

[2] P. M. Wambua, R. Anandjiwala, A review of preforms for the composites industry, Journal of Industrial Textiles 40 (2011) 310–333.

[3] K. L. Edwards, An overview of the technology of fibre-reinforced plastics for design purposes, Materials & design 19 (1998) 1–10.

[4] P. S. Veers, T. D. Ashwill, H. J. Sutherland, D. L. Laird, D. W. Lobitz, D. A. Griffin, J. F. Mandell, W. D. Musial, K. Jackson, M. Zuteck, Trends in the design, manufacture and evaluation of wind turbine blades, Wind energy 6 (2003) 245–259.

[5] A. A. Griffith, The phenomena of rupture and flow in solids, Philosophical Transactions of the Royal Society of London. Series A, Containing Papers of a Mathematical or Physical Character 221 (1921) 163–198. ArticleType: research-article / Full publication date: 1921 / Copyright © 1921 The Royal Society.

[6] S. V. Lomov, Non-Crimp Fabric Composites: Manufacturing, Properties and Applications, Woodhead Publishing, 2011.

[7] J. Zangenberg, P. Brøndsted, J. Gillespie Jr, Fatigue damage propagation in unidirectional glass fibre reinforced composites, Journal of Composite Materials - submitted (2013).

[8] Germanischer Lloyd, Guideline for the certification of wind turbines, 2010.

[9] Det Norske Veritas, Design and manufacture of wind turbine blades, offshore and onshore wind turbines:, DNV-DS-J102 (2010).

[10] International Electrotechnical Committee, IEC 61400-1: Wind turbines part 1: Design requirements, International Electrotechnical Commission (2005).

[11] P. J. Schubel, R. J. Crossley, Wind turbine blade design review, Wind Engineering 36 (2012) 365–388.

[12] J. G. McGowan, R. W. Hyers, K. L. Sullivan, J. F. Manwell, S. V. Nair, B. McNiff, B. C. Syrett, A review of materials degradation in utility scale wind turbines, Energy Materials: Materials Science and Engineering for Energy Systems 2 (2007) 41–64.

[13] J. Mandell, D. Samborsky, D. Miller, The SNL/MSU/DOE fatigue of composite materials database: Recent trends, AIAA-2012-1573, Honolulu, Hawaii, 2012.

[14] V. I. Kushch, S. V. Shmegera, P. Brøndsted, L. Mishnaevsky, Numerical simulation of progressive debonding in fiber reinforced composite under transverse loading, International Journal of Engineering Science 49 (2011) 17–29.

[15] T. S. Lundström, The permeability of non-crimp stitched fabrics, Composites Part A: Applied Science and Manufacturing 31 (2000) 1345–1353.

[16] P. Wambua, J. Ivens, I. Verpoest, Natural fibres: can they replace glass in fibre reinforced plastics?, Composites Science and Technology 63 (2003) 1259–1264.

[17] P. Soden, M. Hinton, A. Kaddour, Lamina properties, lay-up configurations and loading conditions for a range of fibre-reinforced composite laminates, Composites Science and Technology 58 (1998) 1011–1022.

List of Figures

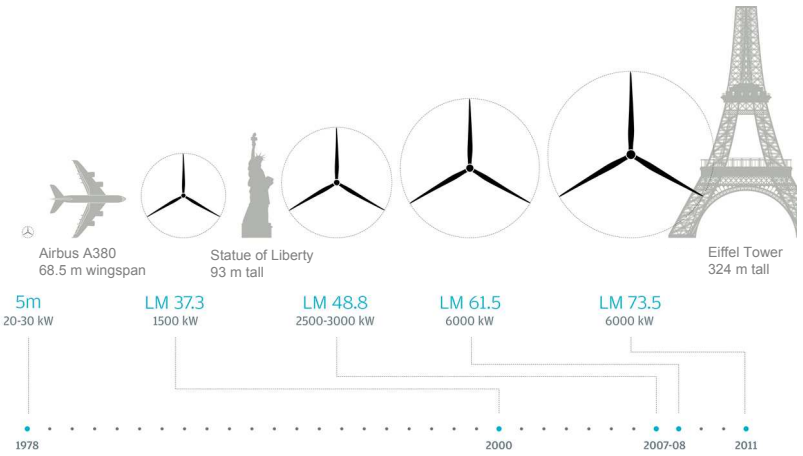

Figure 1: Size development of LM Wind Power blades during the last decades. The number LM XX denotes the blade length in meters, and the number below the associated electrical power output from the turbine.

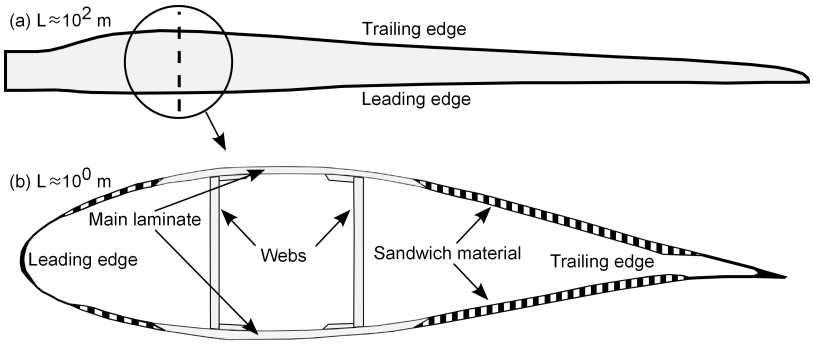

Figure 2: Sketch of a wind turbine rotor blade along with main components. (a) Overview. (b) Cross-section.

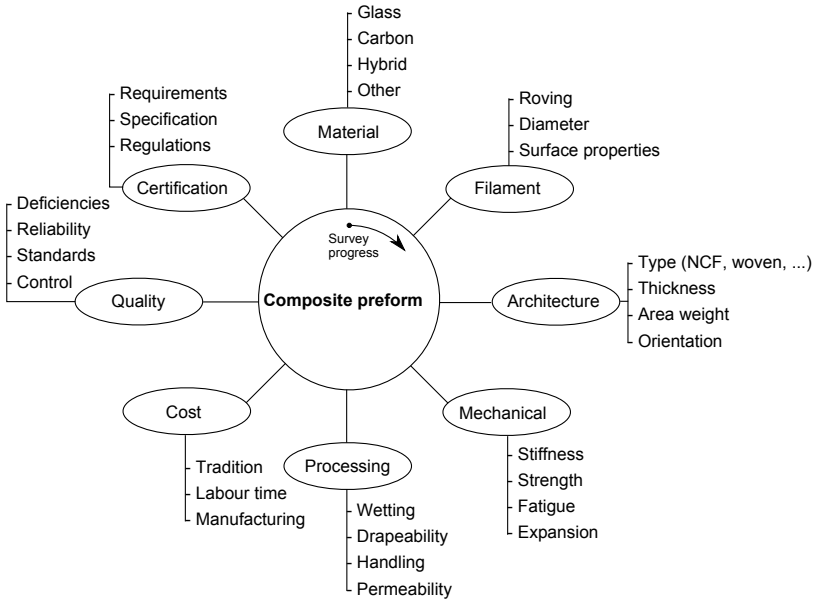

Figure 3: Interaction scheme with key elements and associated influential factors for consideration in the design of a composite preform for wind turbine blades. The key elements are encircled by an ellipse, and selected influential factors are mentioned in connection to these.

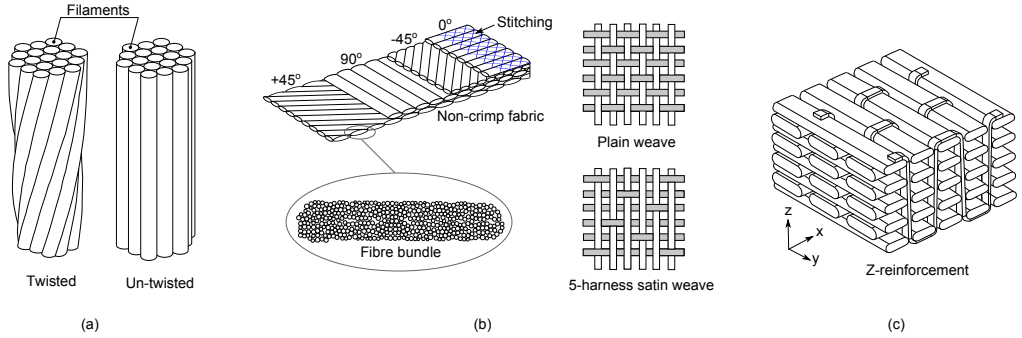

Figure 4: Sketch of selected fibre preforms depending on dimensionality. (a) 1D, roving. (b) 2D, fabrics: NCF and woven. (c) 3D, Z-reinforcement.

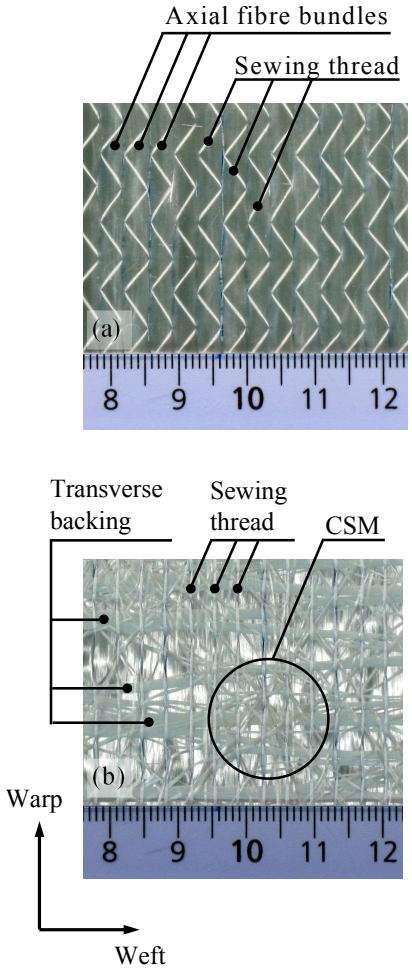

Figure 5: Image of the fibre architecture of the commercially available unidirectional non-crimp preform Combi 1250 often used in the wind turbine blade industry. Scale bars in units of cm. (a) Front face. Axial bundles and stitching pattern. (b) Back face. Axial fibre bundles are placed in the vertical direction underneath the backing and chopped strand mat (CSM).

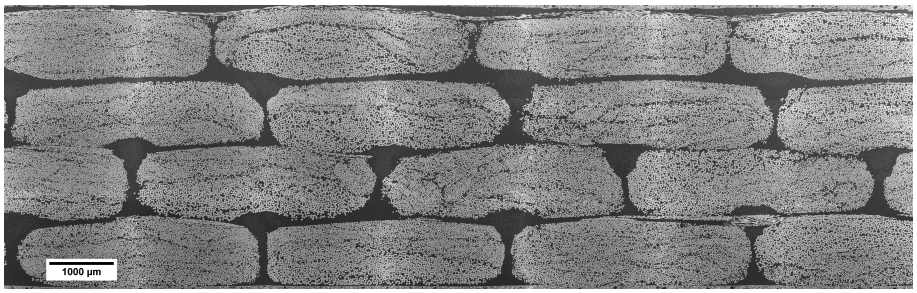

Figure 6: Example of the hierarchical microstructure observed in a glass fibre composite manufactured using a non-crimp fabric: fibres arranged in bundles, and bundles organised in layers. Unidirectional (warp) fibre direction is out-of-plane in the image. Note the relative thin horizontal transverse backing layer (weft) between the bundles.

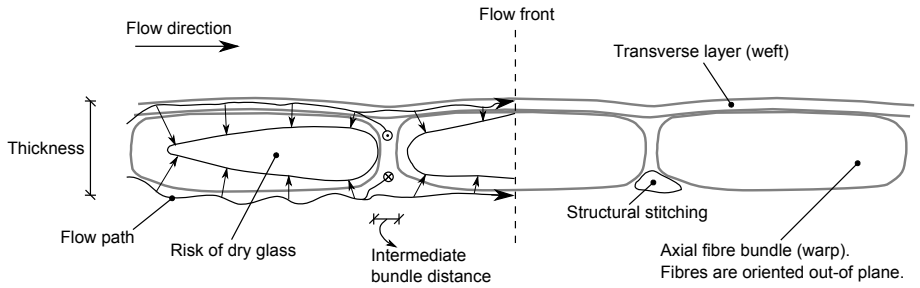

Figure 7: Transverse cross-section of the vacuum infusion process in a single-layered non-crimp fabric with a stabilising backing layer. See Fig. 6 for a micrograph for comparison.

List of Tables

Table 1: Instructive comparison between different fibre materials. Inspiration from [16] and [17].

	Natural fibres	Glass fibres	Carbon fibres
Density	Low	High	Moderate
Stiffness	Low	Moderate	High
Tensile strength	Low	Moderate	High
Compression strength	Low	High	Moderate
Fatigue resistance	Moderate/high	Moderate/high	High
Cost	Low	Low/moderate	High
Energy consumption	Low	Moderate	High
Renewability	Yes	No	No
Recyclability	Yes	No	No
Accessibility	High	High	Moderate
Distribution	Moderate	Wide	Moderate
Disposal	Degradable	Non-degradable	Non-degradable

Table 2: Different preforms depending on the dimensionality. For details on the different types, see e.g. Wambua & Anandjiwala [2]. Selected types are shown graphically in Fig. 4.

Dimensionality	1D	2D	3D	Higher
Examples	Yarn	Tapes	Sandwich fabrics	Polar coordinate preform
	Roving	Prepreg	Solid fabrics	Diagonally reinforcement
		Woven		
		Non-woven		
		Braids		
		Filament winding		
		Mats		
		Knitting		

DTU Wind Energy is a department of the Technical University of Denmark with a unique integration of research, education, innovation and public/private sector consulting in the field of wind energy. Our activities develop new opportunities and technology for the global and Danish exploitation of wind energy. Research focuses on key technical-scientific fields, which are central for the development, innovation and use of wind energy and provides the basis for advanced education at the university.

DTU Wind Energy
Section of Composites and Materials Mechanics
Technical University of Denmark

DTU Risø Campus
Building 118
Frederiksborgvej 399
DK-4000 Roskilde

www.vindenergi.dtu.dk